

University of Windsor

## Scholarship at UWindor

---

Electronic Theses and Dissertations

Theses, Dissertations, and Major Papers

---

6-1-2023

# Control and Protection Solutions for Resilient Protective Relaying of Modern Power Systems

Abdallah Alaa Mohieldien Aboelnaga  
*University of Windsor*

Follow this and additional works at: <https://scholar.uwindsor.ca/etd>



Part of the [Electrical and Computer Engineering Commons](#)

---

### Recommended Citation

Aboelnaga, Abdallah Alaa Mohieldien, "Control and Protection Solutions for Resilient Protective Relaying of Modern Power Systems" (2023). *Electronic Theses and Dissertations*. 9361.  
<https://scholar.uwindsor.ca/etd/9361>

This online database contains the full-text of PhD dissertations and Masters' theses of University of Windsor students from 1954 forward. These documents are made available for personal study and research purposes only, in accordance with the Canadian Copyright Act and the Creative Commons license—CC BY-NC-ND (Attribution, Non-Commercial, No Derivative Works). Under this license, works must always be attributed to the copyright holder (original author), cannot be used for any commercial purposes, and may not be altered. Any other use would require the permission of the copyright holder. Students may inquire about withdrawing their dissertation and/or thesis from this database. For additional inquiries, please contact the repository administrator via email ([scholarship@uwindsor.ca](mailto:scholarship@uwindsor.ca)) or by telephone at 519-253-3000ext. 3208.

# **Control and Protection Solutions for Resilient Protective Relaying of Modern Power Systems**

By

Abdallah Aboelnaga

A Dissertation

Submitted to the Faculty of Graduate Studies  
through the Department of Electrical and Computer Engineering  
in Partial Fulfillment of the Requirements for  
the Degree of Doctor of Philosophy  
at the University of Windsor

Windsor, Ontario, Canada

2023

© 2023 Abdallah Aboelnaga

Control and Protection Solutions for Resilient Protective Relaying of Modern Power  
Systems

by

Abdallah Aboelnaga

APPROVED BY:

---

W. Morsi, External Examiner  
Ontario Tech University

---

A. Azab  
Department of Mechanical, Automotive and Materials Engineering

---

N. Kar  
Department of Electrical and Computer Engineering

---

B. Balasingam  
Department of Electrical and Computer Engineering

---

M. Azzouz, Advisor  
Department of Electrical and Computer Engineering

April 24, 2023

# **DECLARATION OF CO-AUTHORSHIP / PREVIOUS PUBLICATION**

## **I. Co-Authorship**

I hereby declare that this thesis incorporates material that is the result of joint research as follows:

- Chapter 3 of the thesis includes the outcome of publications co-authored with Dr. Maher Azzouz, who provided supervision and guidance during the research writing process and manuscript editing.
- Chapters 4 and 6 incorporate unpublished materials co-authored with Dr. Maher Azzouz, who provided supervision and guidance during the research writing process and manuscript editing.
- Chapter 5 of the thesis includes the outcome of publications co-authored with Dr. Maher Azzouz, Dr. Hatem Sindi, and Dr. Ahmed Awad. Dr. Azzouz provided guidance and feedback on refining ideas and editing the manuscript; Dr. Hatem Sindi and Dr. Ahmed Awad contributed feedback on improving ideas. The key ideas, primary contributions, data analysis, interpretation, and writing were performed by the author.

I am aware of the University of Windsor Senate Policy on Authorship, and I certify that I have properly acknowledged the contribution of other researchers to my thesis and have obtained written permission from each of the co-author(s) to include the above material(s) in my thesis.

I certify that, with the above qualification, this thesis, and the research to which it refers, is the product of my own work.

## **II. Previous Publication**

This thesis includes three original journal papers, two conference papers, and two patents that have been previously published/submitted to journals for publication, as follows:



Thesis Chapter	Publication title/full citation	Publication status
Chapter 3	A. A. Aboelnaga and M. A. Azzouz, "Adaptive current-angle-based phase selection for microgrids with inverter-interfaced renewable energy sources," in <i>IEEE Transactions on Smart Grid</i> , vol. 13, no. 1, pp. 417-428, Jan. 2022, doi: 10.1109/TSG.2021.3112664.	Published
Chapter 4	A. A. Aboelnaga, M. A. Azzouz, "A modified voltage-angle-based classifier for reliable operation during different advanced control functions and varied arc resistances. <i>IEEE Transactions on Power Delivery</i> .	Submitted
Chapter 5	<ul style="list-style-type: none"> <li>• A. A. Aboelnaga, M. A. Azzouz, H. F. Sindi and A. S. A. Awad, "Fault ride through of inverter-interfaced renewable energy sources for enhanced resiliency and grid code compliance," in <i>IEEE Transactions on Sustainable Energy</i>, vol. 13, no. 4, pp. 2275-2290, Oct. 2022, doi: 10.1109/TSTE.2022.3191631.</li> <li>• A. A. Aboelnaga, H. Sindi, and M. A. Azzouz. "Dual current controller of inverter interfaced renewable energy sources for accurate phase selection method and grid codes compliance," <i>U.S. Patent</i> No. 11,114,854. 7 Sep. 2021.</li> <li>• A. A. Aboelnaga, H. Sindi, and M. A. Azzouz, "Dual current controller of inverter interfaced renewable energy sources for accurate phase selection method and grid codes compliance," <i>U.S. Patent</i> No. 11,374,407. 28 Jun. 2022.</li> <li>• A. A. Aboelnaga and M. A. Azzouz, "Dual stationery frame control of inverter-based resources for reliable phase selection," <i>2021 IEEE 19th International Conference on Industrial Informatics (INDIN)</i>, Palma de Mallorca, Spain, 2021, pp. 1-6, doi: 10.1109/INDIN45523.2021.9557510.</li> <li>• A. A. Aboelnaga, M. A. Azzouz, H. F. Sindi and A. S. A. Awad, "Dual current control of inverter-based resources for enhanced resilience and complying grid codes," <i>2023 IEEE ISGT-Middle East Conference</i>, Mar. 2023.</li> </ul>	Published

---

Chapter 6	A. A. Aboelnaga, M. A. Azzouz, “Dual current controller for enhanced resiliency and complying with fault ride-through imposing negative-sequence current requirements,” <i>IEEE Transactions on Sustainable Energy</i> .	To be submitted
-----------	--	-----------------

---

I certify that I have obtained written permission from the copyright owner(s) to include the above-published material(s) in my thesis. I certify that the above material describes work completed during my registration as a graduate student at the University of Windsor.

### III. General

I declare that, to the best of my knowledge, my thesis does not infringe upon anyone’s copyright nor violate any proprietary rights and that any ideas, techniques, quotations, or any other material from the work of other people included in my thesis, published or otherwise, are fully acknowledged in accordance with the standard referencing practices. Furthermore, to the extent that I have included copyrighted material that surpasses the bounds of fair dealing within the meaning of the Canada Copyright Act, I certify that I have obtained written permission from the copyright owner(s) to include such material(s) in my thesis.

I declare that this is a true copy of my thesis, including any final revisions, as approved by my thesis committee and the Graduate Studies office and that this thesis has not been submitted for a higher degree to any other University or Institution.

## ABSTRACT

Renewable energy sources (RESs) are permeating the power grid due to their importance in reducing air pollution and fuel consumption. These sources require synchronization with the power grid using inverters that must meet grid code (GC) requirements. During fault conditions, GCs enforce inverter interfaced RESs (IIRESs) to follow reactive current generation (RCG) requirements to enhance grid stability. However, it could adversely affect protection functions, e.g., phase selection methods (PSMs), operations.

The main objective of this dissertation is to enhance the power system resiliency by determining the faulty phase(s) accurately. This is achieved by investigating the root causes behind the failure of the commercial PSMs when fault currents are supplied from IIRESs. Consequently, accurate PSMs are achieved by two approaches. The first approach is enhancing the relay algorithm to guarantee correct faulty phase determination during different IIRES controllers. The second approach is fulfilled by controlling IIRESs to achieve PSM and RCG requirements, simultaneously.

Short-circuit analysis is performed to investigate the effect of various fault conditions, including arc resistances, on phase selection. Hence, A new current-angle-based PSM that adaptively adjusts the conventional zone bisectors is proposed to confront the exotic IIRES fault current signatures. Compensation angles are added to the zone bisectors to mitigate any differences in the sequence impedance angles affecting relays emanating from IIRESs. In addition, new zone boundaries are proposed to cope with various fault resistances.

Furthermore, a comprehensive analysis is performed to determine the effect of various IIRES controllers on the relative angles between sequence voltages measured at the fault

and relay locations due to the voltage drop occurred on the transmission line. Thereafter, a comprehensive PSM based on comparing the angles of sequence voltages is proposed. In the proposed method, new zones are defined to guarantee precise phase selection during various fault conditions.

On the other hand, two dual-current controllers (DCCs) are designed to secure a correct operation of the conventional PSM and meet positive-sequence RCG requirements. First, initial reference angles of the negative- and positive-sequence currents are determined according to the grid-side zero-sequence current angle and RCG requirements, respectively. Then, these angles are adjusted to secure correct operation of PSM without violating RCG requirements. Thereafter, the reference currents are calculated to achieve the reference current angles and keep the current magnitude within permissible limits.

Lastly, the current-angle-based PSM is analyzed when the IRESs follow GCs with positive- and negative-sequence RCG requirements, which reveals their inability to ensure correct PSM operation. Consequently, a new DCC is designed to guarantee the correct operation of commercial PSM without violating these GCs and achieve maximum current limit requirements. First, the negative-sequence-current angle is designed to guarantee injecting the minimum negative-sequence active current that ensures correct PSM based on the relative angle between the negative- and zero-sequence currents. Subsequently, the positive-sequence current angle is designed to allow maximum positive-sequence active current injection without violating PSM requirements. Finally, the positive- and negative-sequence current magnitudes are determined to inject the maximum current limit.

## DEDICATION

*To my beloved parents, Alaa and Zainab, beloved wife, Omnia, and  
my dear siblings Mona and Mohamed.*

## ACKNOWLEDGEMENTS

First and foremost, I would like to thank God whose guidance has led me this far.

I extend my heartfelt appreciation to my advisor, Dr. Maher Azzouz, for providing me with expert guidance, invaluable advice, constant support, and continual encouragement through my Ph.D. My appreciation and thanks are extended to my Ph.D. committee members: Dr. Naryan Kar, Dr. Balakumar Balasingam, and Dr. Ahmed Azab. Thanks, are also extended to my external examiner, Dr. Walid Morsi.

My profound gratitude and boundless appreciation go to my parents, Mr. Alaa Aboelnaga and Mrs. Zainab Abdelrahman. Their unwavering support, constant encouragement, and heartfelt prayers were instrumental in making my research possible, and I am forever thankful to them.

My most profound appreciation to my wife, Omnia Yasser, for her support and encouragement during my study. I would like to thank my siblings, Mona Aboelnaga and Mohamed Aboelnaga, for their continuous support and prayers.

Last but not least, I want to express my appreciation to my previous advisor, Professor Mostafa Marei, for guiding me throughout my M.Sc. studies at Ain Shams University and for supporting me and recommending me to pursue my Ph.D. at the University of Windsor.

# TABLE OF CONTENTS

<b>DECLARATION OF CO-AUTHORSHIP / PREVIOUS PUBLICATION.....</b>	<b>iii</b>
<b>ABSTRACT.....</b>	<b>vi</b>
<b>DEDICATION.....</b>	<b>viii</b>
<b>ACKNOWLEDGEMENTS .....</b>	<b>ix</b>
<b>LIST OF TABLES .....</b>	<b>xv</b>
<b>LIST OF FIGURES .....</b>	<b>xvii</b>
<b>LIST OF ABBREVIATIONS .....</b>	<b>xxiii</b>
<b>LIST OF SYMBOLS .....</b>	<b>xxv</b>
<b>Chapter 1 Introduction.....</b>	<b>1</b>
1.1 Preface.....	1
1.2 Research Motivations.....	2
1.3 Research Objectives .....	3
1.4 Dissertation Outline .....	4
<b>Chapter 2 Background and Literature Review .....</b>	<b>6</b>
2.1 Modeling of VSCs.....	6
2.2 Inverter Control .....	8
2.2.1 Inner Control Loop.....	8
2.2.2 Outer Control Loop .....	15
2.3 Phase Selection.....	17
2.3.1 Conventional PSMs.....	18
2.3.2 Relay Modifications for Precise PSM.....	19
2.3.3 DCC Modifications to Guarantee Correct Operation of Conventional PSM .....	20

2.4 Discussion .....	21
<b>Chapter 3 Adaptive Current-Angle-Based Phase Selection for Microgrids with Inverter-Interfaced Renewable Energy Sources.....</b>	<b>23</b>
3.1 Introduction .....	23
3.2 Phase Selection Analysis.....	23
3.2.1 Current-Angle-Based PSM .....	23
3.2.2 Voltage-Angle-Based PSM.....	29
3.3 Assessing Current and Voltage-Angle-Based PSMs .....	32
3.4 Adaptive Current-Angle-Based PSM.....	36
3.4.1 Adaptive Zones of $\delta_l^0$ .....	37
3.4.2 Adaptive Zones of $\delta_l^+$ .....	38
3.5 Performance Evaluation .....	39
3.5.1 Effect of Fault Resistances.....	40
3.5.2 Grid-Connected Mode of CIGRE Benchmark System .....	45
3.5.3 Islanded Mode of CIGRE Benchmark System .....	49
3.5.4 Performance Against Different IRES Controllers .....	51
3.6 Conclusions .....	52
<b>Chapter 4 Reliable Phase Selection for Transmission Networks Considering Arc Resistances and Various Control Functions of Renewable Energy Sources .....</b>	<b>54</b>
4.1 Introduction .....	54
4.2 Analysis of Relative Angles between Sequence Fault Voltages.....	55
4.2.1 SLG Fault Analysis .....	55
4.2.2 LLG Fault Analysis.....	57
4.2.3 LL Fault Analysis.....	59
4.3 Analysis of Phase Shifts between Sequence Voltages.....	60



4.3.1 Zero-sequence Voltage.....	61
4.3.2 Negative- and Positive-sequence Voltages .....	62
4.4 Proposed Voltage-Angle-Based PSM .....	70
4.4.1 Modified Zones of $\delta_V^0$ .....	71
4.4.2 Modified Zones of $\delta_V^+$ .....	72
4.4.3 Pinpoint the Fault Type .....	72
4.5 Performance Evaluation .....	73
4.5.1 Compatibility with Conventional Controllers .....	73
4.5.2 Compatibility with Recent Grid Codes .....	76
4.5.3 Compatibility with Active and Reactive Power Ripple Mitigation .....	78
4.6 Conclusions .....	81
<b>Chapter 5 Fault Ride Through of Inverter-Interfaced Renewable Energy Sources for Enhanced Resiliency and Grid Code Compliance.....</b>	<b>82</b>
5.1 Introduction .....	82
5.2 Problem Statement .....	82
5.3 Proposed Dual Current Controller for PSM and GC Compliance .....	86
5.3.1 Stage I. Initial Values of $\delta_{ref}^0$ and $\delta_{ref}^+$ .....	87
5.3.2 Stage II. Initial Reference Angle of the Negative-Sequence Current .....	87
5.3.3 Stage III. Initial Reference Angle of the Positive-Sequence Current .....	89
5.3.4 Stage IV. Reference Angles of the Negative- and Positive-Sequence Currents .....	90
5.3.5 Stage V. Inverter's $\alpha\beta$ Reference Currents: .....	95
5.4 Performance Evaluation of DCC1 .....	97
5.4.1 Response at Different Fault Locations .....	98
5.4.2 Compatibility with Various GCs.....	102

5.4.3	Compatibility with the NERC Reliability guidelines.....	104
5.4.4	Comparison with Other DCCs .....	107
5.4.5	Further Results .....	108
5.4.6	Real-time Simulations .....	110
5.5	Proposed Dual Current Controller for Enhanced PSM Security and Compliance with RCG Requirements .....	113
5.5.1	Determining the Initial Positive-Sequence Current Angle at POI .....	114
5.5.2	Determining the Initial Negative-Sequence Current Angle at POI.....	115
5.5.3	Determining the Negative- and Positive-Sequence Current Angles at POI .....	115
5.5.4	Determining and Controlling the Negative- and Positive-Sequence Current References at the IRES .....	117
5.6	Performance Evaluation of DCC2 .....	118
5.6.1	Compatibility with GCs Imposing Constant Power Factor.....	118
5.6.2	Compatibility with GCs Imposing Reactive Current Relative to Voltage Drop .....	120
5.7	Conclusions .....	122
<b>Chapter 6 Dual Current Control of IRESs for Phase Selection and Compliance with Recent Negative-Sequence RCG .....</b>		<b>123</b>
6.1	Introduction .....	123
6.2	Problem Statement .....	123
6.2.1	SLG Faults.....	127
6.2.2	LLG Faults .....	128
6.2.3	LL Faults .....	130
6.3	Assessing Current-Angle-Based PSM when IRES Follows VDE-AR-N 4120-GC .....	130

6.4 The Proposed Dual Current Controller .....	133
6.4.1 Stage I. The Referential Angle of the Negative-Sequence Current Angle .....	133
6.4.2 Stage II. The Reference of the Negative-Sequence Current .....	134
6.4.3 Stage III. The Referential Angle of the Positive-Sequence Current Angle .....	135
6.4.4 Stage IV. The Initial Reference of the Positive-Sequence Current Angle .....	135
6.4.5 Stage V. The Reference Positive-Sequence Current .....	137
6.4.6 Stage VI. The Reference Positive- and Negative-Sequence Currents in $dq$ Frame .....	139
6.5 Performance Evaluation .....	140
6.5.1 Response under Different Fault Resistances .....	140
6.5.2 Compatibility with Various X/R Ratios of the Transmission Line .....	149
6.6 Conclusions .....	151
<b>Chapter 7 Conclusions.....</b>	<b>153</b>
7.1 Conclusions .....	153
7.2 Contributions .....	155
7.3 Future Work .....	156
<b>Bibliography .....</b>	<b>157</b>
<b>Appendices.....</b>	<b>164</b>
Appendix A Data of Test Networks .....	164
Appendix B Verification of the negative-sequence current magnitude equation ...	165
<b>Vita Auctoris.....</b>	<b>168</b>

## LIST OF TABLES

Table 3.1. Sample system measurements at different fault resistances .....	41
Table 3.2. Sample system measurements for LL faults .....	44
Table 3.3. IIRES-side relay ( $R_{83}$ ) measurements in the grid-connected CIGRE benchmark system .....	45
Table 3.4. IG-side relay ( $R_{65}$ ) measurement in grid-connected CIGRE benchmark system .....	47
Table 3.5. IIRES-side relay ( $R_{83}$ ) measurement in islanded CIGRE benchmark system .....	50
Table 3.6. IG-side relay ( $R_{65}$ ) measurement in islanded CIGRE benchmark system .....	50
Table 3.7. IIRES-side relay ( $R_{83}$ ) measurement when the IIRES is controlled to mitigate active power ripples .....	51
Table 3.8. IIRES-side relay ( $R_{83}$ ) measurement when the IIRES is controlled to mitigate reactive power ripples .....	52
Table 4.1. Range of $\Delta\delta_{RF}^+$ and $\Delta\delta_{RF}^0$ in conventional control .....	64
Table 4.2. Range of $\Delta\delta_{RF}^+$ and $\Delta\delta_{RF}^0$ when IIRES follows the new grid codes .....	66
Table 4.3. Range of $\Delta\delta_{RF}^+$ and $\Delta\delta_{RF}^0$ when the IIRES is controlled to eliminate active-power ripples .....	70
Table 4.4. Range of $\Delta\delta_{RF}^+$ and $\Delta\delta_{RF}^0$ when the IIRES is controlled to eliminate reactive-power ripples .....	70
Table 4.5. Range of $\delta_R^+$ and $\delta_R^0$ for faults fed by IIRES .....	71
Table 4.6. Active power generation during conventional controller .....	74
Table 4.7. Reactive power generation during conventional controller .....	75
Table 4.8. IIRES's controller following the German grid code, when $K = 6$ .....	76
Table 4.9 IIRES's controller following the German grid code, when $K = 2$ .....	77

Table 4.10. Active and reactive-power ripple mitigation when the positive-sequence current is injecting active current.....	79
Table 4.11. Active and reactive-power ripple mitigation when the positive-sequence current is injecting Reactive current .....	80
Table 5.1. Performance of the proposed DCC1 at different fault locations with ERCOT-GC.....	98
Table 5.2. Performance of the proposed DCC1 during LL faults with ERCOT-GC.....	101
Table 5.3. Performance of the proposed DCC1 with the NERC guidelines.....	106
Table 5.4. Performance of the proposed DCC1 for faults detected by $R_{38-29}$ .....	109
Table 5.5. Performance of the proposed DCC1 for faults detected by $R_{36-23}$ .....	110
Table 5.6. Performance of the proposed DCC2 during ground faults with ERCOT-GC	119
Table 5.7. Performance of the proposed DCC2 during ground faults with G-GC .....	121
Table 6.1 Performance of the proposed DCC during SLG faults at different fault locations .....	141
Table 6.2. Performance of the proposed DCC during LLG faults at different fault locations .....	144
Table 6.3. Performance of the proposed DCC during LL faults at different fault locations .....	147
Table 6.4. Performance of the proposed DCC during faults at different transmission line's $X/R$ ratio .....	150

## LIST OF FIGURES

Figure 2.1. RES integrated into the grid through a three-phase two-level VSC and an LCL filter.....	6
Figure 2.2. Generic current controlled VSC controller.....	8
Figure 2.3. Space vector transformation into (a) $\alpha\beta$ frame and (b) $dq$ frame.....	10
Figure 2.4. Inner current-control loop in $dq$ reference frame.....	12
Figure 2.5. SRF-PLL schematic diagram. ....	12
Figure 2.6. Inner current-control loop in $d^+q^+$ and $d^-q^-$ reference frames.....	14
Figure 2.7. Inner current-control loop in $\alpha^+\beta^+$ and $\alpha^-\beta^-$ reference frames.....	16
Figure 2.8. Reactive-current generation requirements for the VDE-AR-N 4120-GC.....	16
Figure 2.9. Current-angle-based PSM zones for (a) $\delta_I^0$ , (b) $\delta_I^+$ .....	19
Figure 2.10. Voltage-angle-based PSM $\delta_V^0$ zones.....	20
Figure 2.11. Voltage-angle-based PSM $\delta_V^+$ zones: (a) SLG zones, (b) LL(G) zones. ....	20
Figure 3.1. Sample system for short-circuit analysis: (a) single line diagram, (b) sequence circuits for AG faults, (c) sequence circuits for BCG faults, (d) sequence circuits for BC faults.....	24
Figure 3.2. Sample test system. ....	33
Figure 3.3. Angle measurements of existing PSMs during bolted BCG fault: (a) current PSM, (b) voltage PSM. ....	34
Figure 3.4. Angle measurements of existing PSMs during BCG fault with $R_g = 50 \Omega$ : (a) current PSM, (b) voltage PSM.....	35
Figure 3.5. Angle measurements of existing PSMs during BCG fault with $R_{ph} = 50 \Omega$ : (a) current PSM, (b) voltage PSM.....	35
Figure 3.6. Adaptive $\delta_I^0$ zone for BCG faults.....	38

Figure 3.7. Fault-type adaptive zones: (a) $\delta_I^0$ (b) $\delta_I^+$ .....	39
Figure 3.8. CIGRE MV benchmark system.....	40
Figure 3.9. Angle measurements using the proposed PSM for a BCG fault with $R_g = 50 \Omega$ : (a) IIRES-side, (b) grid-side. ....	42
Figure 3.10. Angle measurements using the proposed PSM for BCG fault with $R_{ph} = 50 \Omega$ : (a) IIRES side, (b) grid side.....	43
Figure 3.11. PSM measurement by R65 for BG fault at bus 5: (a) $\delta_I^0$ , (b) $\delta_I^+$ , (c) $\delta_I^0$ operating time, and (d) $\delta_I^+$ operating time. ....	48
Figure 4.1. Sample power system structure diagram.....	54
Figure 4.2. Sequence circuit at the fault location for an AG fault.....	56
Figure 4.3. Range of $\delta_F^+$ for an AG fault. ....	56
Figure 4.4. Sequence circuit at the fault location for a BCG fault.....	58
Figure 4.5. Relative sequence angles range for a BCG fault: (a) $\delta_F^0$ , (b) $\delta_F^+$ .....	59
Figure 4.6. Sequence circuit at the fault location for a BC fault. ....	60
Figure 4.7. Range of $\delta_F^+$ for a BC fault.....	60
Figure 4.8. Equivalent single-line diagram of the zero-sequence circuit of the system under study.....	61
Figure 4.9. Equivalent single-line diagram of the positive-sequence circuit of the system under study.....	63
Figure 4.10. Equivalent single-line diagram of the negative-sequence circuit of the system under study.....	65
Figure 4.11. Proposed $\delta_V^0$ zones.....	71
Figure 4.12. Proposed $\delta_V^+$ zones: (a) SLG zones, (b) LL(G) zones. ....	72
Figure 4.13. Single-line diagram of the test system.....	73

Figure 4.14. Performance of the proposed PSM during conventional controller: (a) a BCG fault at bus 5, (b) a BG fault at 50% of $L_{25}$ .....	75
Figure 4.15. Performance of the proposed PSM, when the IRES follows the new German GC for a fault at 50% of $L_{25}$ : (a) a CG fault, (b) a CAG fault. ....	78
Figure 4.16. Performance of proposed PSM for a fault at bus 5 during reactive and active power ripples: (a) a BCG fault, (b) an ABG fault.....	81
Figure 5.1. Current-angle-based PSM zones for (a) $\delta^0$ , (b) $\delta^+$ .....	83
Figure 5.2. Sample test system. ....	84
Figure 5.3. Measured $\delta^0$ and $\delta^+$ by $R_{32}$ for a bolted AG fault. ....	85
Figure 5.4. Measured $\delta^0$ and $\delta^+$ by $R_{32}$ for a bolted BCG fault.....	85
Figure 5.5. Measured quantities by $R_{32}$ for a bolted BG fault when the IRES is controlled based on [24]: (a) $\delta^0$ and $\delta^+$ , (b) output power factor. ....	85
Figure 5.6. Structure of the proposed DCC1: (a) Determining $\delta_{F,bis}^0$ and $\delta_{F,bis}^+$ , (b) Determining $\angle I_{t,ref(0)}^-$ , (c) Determining $\angle I_{t,ref(0)}^+$ , (d) Generating $\angle I_{t,ref}^-$ and $\angle I_{t,ref}^+$ , (e) Generating and controlling $I_{ref}^-$ and $I_{ref}^+$ , (f) AC Measurement unit. ....	86
Figure 5.7. The double second-order generalized integrator structure. ....	88
Figure 5.8. Frequency-locked loop. ....	88
Figure 5.9. Determination of $\angle I_{t,ref}^-$ and $\angle I_{t,ref}^+$ . ....	91
Figure 5.10. Loci of sequence currents when $I_{g,ref(0)}^-$ and $I_{g,ref(0)}^+$ satisfy $\delta^0$ 's and $\delta^+$ 's requirements during an AG fault. ....	92
Figure 5.11. Loci of sequence currents when $\angle I_{g,ref(0)}^-$ is below $\delta^+$ minimum limit: (a) $\delta^0$ and $\delta^+$ zones are intersected, (b) $\delta^0$ and $\delta^+$ zones have no intersection. ....	93
Figure 5.12. Loci of sequence currents when $\angle I_{g,ref(0)}^-$ is above $\delta^+$ 's maximum limit: (a) $\delta^0$ and $\delta^+$ zones are intersected, (b) $\delta^0$ and $\delta^+$ zones have no intersection. ..	94
Figure 5.13. PR current controller in the stationary frame. ....	97



Figure 5.14. Single-line diagram of the test system.....	97
Figure 5.15. Measured $\delta^0$ and $\delta^+$ by $R_{25}$ for a bolted BG fault. ....	100
Figure 5.16. POI voltage in the alpha-beta frame for a bolted BG fault: (a) Positive-sequence voltage, (b) Negative-sequence voltage. ....	100
Figure 5.17. IRES output current in the alpha-beta frame for a bolted BG fault. ....	100
Figure 5.18. IRES positive- and negative-sequence current magnitude measured at the inverter's terminals. ....	101
Figure 5.19. Performance of the proposed DCC1 with the German GC: (a) $\delta^0$ measured by $R_{25}$ , (b) $\delta^+$ measured by $R_{25}$ , (c) Relation between output reactive current and voltage drop at the POI. ....	102
Figure 5.20. Performance of the proposed DCC1 with the Spanish GC: (a) $\delta^0$ measured by $R_{25}$ , (b) $\delta^+$ measured by $R_{25}$ , (c) Relation between output reactive current and the voltage magnitude at the POI.....	102
Figure 5.21. Measured $\delta^0$ and $\delta^+$ by $R_{25}$ for a bolted CAG fault. ....	103
Figure 5.22. Performance of the proposed DCC1 during LL faults with the Spanish GC: (a) $\delta^+$ measured by $R_{25}$ , (b) Relation between the reactive output current and the voltage magnitude at the POI.....	104
Figure 5.23. Measured $\delta^0$ and $\delta^+$ by $R_{25}$ for a bolted BCG fault.....	106
Figure 5.24. Active and reactive current magnitude for a bolted BCG fault.....	107
Figure 5.25. Measured quantities by $R_{32}$ for a bolted AG fault when the IRES is controlled using the proposed DCC1: (a) $\delta^0$ and $\delta^+$ , (b) output power factor.....	107
Figure 5.26. Modified IEEE 39-bus test system. ....	108
Figure 5.27. Measured $\delta^0$ and $\delta^+$ by $R_{38\_29}$ for a bolted AG fault.....	109
Figure 5.28. Schematic for the test system executed in real-time. ....	111

Figure 5.29. Measured quantities by $R_{25}$ for a bolted BG fault: (a) $\delta^0$ and $\delta^+$ (time/div.=100 ms and angle/div= 40°), (b) output power factor (time/div.=100 ms and PF/div= 0.1).....	112
Figure 5.30. Measured quantities by $R_{25}$ for an AG fault with $R_{flt} = 50\Omega$ : (a) $\delta^0$ and $\delta^+$ (time/div.=100 ms and angle/div.= 30°), (b) output power factor (time/div.=100 ms and PF/div= 0.2).....	112
Figure 5.31. Measured quantities by $R_{25}$ for a bolted BCG fault: (a) $\delta^0$ and $\delta^+$ (time/div.=100 ms and angle/div= 50°), (b) output power factor (time/div.=100 ms and PF/div= 0.1).....	113
Figure 5.32. Measured quantities by $R_{25}$ for an ABG fault with $R_{flt} = 50\Omega$ : (a) $\delta^0$ and $\delta^+$ (time/div.=200 ms and angle/div.= 50°), (b) output power factor (time/div.=100 ms and PF/div= 0.2).....	113
Figure 5.33. The procedure for determining $\angle I_{t,ref(0)}^+$ .....	114
Figure 5.34. The procedure for determining $\angle I_{t,ref(0)}^-$ .....	115
Figure 5.35. The flow chart of the proposed controller. ....	116
Figure 5.36. The procedure of determining and controlling $i_{ref}^-$ and $i_{ref}^+$ .....	118
Figure 5.37. Dynamic response of the proposed DCC2 for an AG with ERCOT-GC and $R_{flt} = 50\Omega$ : (a) $\delta^0$ and $\delta^+$ , (b) PF. ....	120
Figure 5.38. Dynamic response of the proposed DCC2 for a solid BCG with G-GC: (a) $\delta^0$ and $\delta^+$ , (b) $ I_q^+ $ vs $\Delta V$ .....	122
Figure 6.1. A sample system representing an IRES connected to a power grid.....	124
Figure 6.2. Zero-sequence circuit representation for an IRES connected to the power grid. ....	126
Figure 6.3. Angle measurements during a bolted AG fault at 50% of $L_{25}$ when the IRES's gain constant, i.e., $K$ , equals 2: (a) $\delta^0$ and $\delta^+$ , (b) $\delta_V^+$ , $\phi^+$ , $\delta_V^0$ , and $\phi^-$ .....	131

Figure 6.4. Angle measurements during an AG fault at 50% of $L_{25}$ with $R_g = 20 \Omega$ when $K = 6$ : (a) $\delta^0$ and $\delta^+$ , (b) $\delta_V^+$ , $\phi^+$ , $\delta_V^0$ , and $\phi^-$ .....	132
Figure 6.5. Angle measurements of $\delta^0$ and $\delta^+$ during a BCG fault at 50% of $L_{25}$ when $K = 6$ : (a) $R_g = 50 \Omega$ , (b) $R_{ph} = 60 \Omega$ .....	132
Figure 6.6. Measured $\delta^0$ and $\delta^+$ by $R_{25}$ for an AG fault with $R_g = 30 \Omega$ occurred at 10% of $L_{25}$ .....	142
Figure 6.7. IIREs's phase currents measurements during an AG fault occurred at 10% of $L_{25}$ with $R_g = 30 \Omega$ . .....	142
Figure 6.8. IIREs's Positive- and negative-sequence currents magnitude during an AG fault occurred at 10% of $L_{25}$ with $R_g = 30 \Omega$ . .....	143
Figure 6.9. Measured $\delta^0$ and $\delta^+$ by $R_{25}$ for a CAG fault occurred at 50% of $L_{25}$ with $R_g = R_{ph} = 20 \Omega$ . .....	145
Figure 6.10. IIREs's phase currents measurements during a CAG fault occurred at 50% of $L_{25}$ with $R_g = R_{ph} = 20 \Omega$ .....	146
Figure 6.11. IIREs's Positive- and negative-sequence currents magnitude during a CAG fault occurred at 50% of $L_{25}$ with $R_g = R_{ph} = 20 \Omega$ .....	146
Figure 6.12. Measured $\delta^+$ by $R_{25}$ for a bolted AB fault occurred at 90% of $L_{25}$ . .....	148
Figure 6.13. IIREs's phase currents measurements during a bolted AB fault occurred at 90% of $L_{25}$ . .....	149
Figure 6.14. IIREs's Positive- and negative-sequence currents magnitude during a bolted AB fault occurred at 90% of $L_{25}$ .....	149
Figure 6.15. Measured $\delta^0$ and $\delta^+$ by $R_{25}$ for a bolted CG when the transmission lines' $X/R$ ratios equal to 2 and 10. ....	151

## LIST OF ABBREVIATIONS

DCC	Dual-current controller
DDSRF	Decouple double synchronous reference frame
DSOGI	Dual second-order generalized integrator
EPRI	Electric power research institute
ERCOT	Electric reliability council of Texas
FFT	Fast Fourier transform
FLL	Frequency-locked loop
FRT	Fault ride through
FT	Fourier transform
GCs	Grid codes
G-GC	German GC
GSC	Grid-side converter
HIL	Hardware-in-the-loop
IRES	Inverter-interfaced RES
LL	Line-to-line
LLG	Line-line-to-ground
NA	North American
NERC	North American electric reliability corporation
p.u.	Per unit
PF	Power factor
PI	Proportional-integral
PLL	phase-locked loop

POI	Point of interconnection
PR	Proportional resonance
PSM	Phase selection method
PV	Photovoltaic
RCG	Reactive-current generation
RCP	Rapid control prototyping
RES	Renewable energy source
RTS	Real-time simulator
S-GC	Spanish GC
SGs	Synchronous generators
SLG	Single-line-to-ground
SO-SOGI	Double second-order generalized integrator
SPT	Selective phase tripping
SRF-PLL	Synchronous rotating frame PLL
US	United States

## LIST OF SYMBOLS

### Symbols

$\alpha\beta$	Stationary frame
$C_f$	Capacitance of the IRES's filter
$\delta_{F,bis}$	Fault-type-zone bisector
$\delta_F^+$	Relative angle between the negative- and positive-sequence voltages at the fault location
$\delta_F^0$	Relative angle between the negative- and zero-sequence voltages at the fault location
$\delta_I^+$	Relative angle between the superimposed negative- and positive-sequence currents
$\delta_I^0$	Relative angle between the superimposed negative- and zero-sequence currents
$\delta_R^+$	Relative angle between the negative- and positive-sequence voltages at the relay location
$\delta_R^0$	Relative angle between the negative- and zero-sequence voltages at the relay location
$\Delta\theta_{RF}^-$	Relative angle between the negative-sequence voltage measured at the relay and fault location
$\Delta\theta_{RF}^+$	Relative angle between the positive-sequence voltage measured at the relay and fault location
$\Delta\theta_{RF}^0$	Relative angle between the zero-sequence voltage measured at the relay and fault location
$\delta_V^+$	Relative angle between the negative- and positive-sequence voltages

$\delta_V^0$	Relative angle between the negative- and zero-sequence voltages
$dq$	Synchronous frame
$E$	Inverter's internal voltage
$\varepsilon$	Rotating angle of the $dq$ frame
$f$	Arbitrary electric component, e.g., voltage or current component
$\mathbf{f}$	Arbitrary electric component in state space
$f_s$	Switching frequency
$i$	Inverter's output current
$I_F$	Fault current at the fault location
$I_{F,IRES}$	Fault current measured by the IRES-side relay
$I_{FR}$	Fault current through a relay
$I_{P,ref}$	Reference active current
$I_{Q,ref}$	Reference reactive current
$I_R$	Current measured by a relay
$I_{R,ref}$	Referential angle of a sequence current
$i_t$	IRES's terminal current measured at the POI
$j$	Imaginary axis
$L_f$	Inductance of the IRES's filter
$L_{tr}^0$	Inductance of the transformer zero-sequence impedance
$m$	Modulation index
$\mu$	Margin from the maximum PSM zone boundaries to allow the relay to locate the PSM correctly
$\mathcal{M}_l$	Lower margin

$\mathcal{M}_u$	Upper margin
$\omega$	Angular frequency
$p$	Instantaneous active power
$\tilde{P}_{2\omega}$	Oscillating component of the active power at double the nominal frequency
$\phi$	Phase shift between the IIRES voltage and current
$\varphi$	phase shifts for phases a, b, and c, i.e., $0^\circ$ , $-120^\circ$ , and $120^\circ$
$q$	Instantaneous reactive power
$\tilde{Q}_{2\omega}$	Oscillating component of the reactive power at double the nominal frequency
$R_f$	Resistance of the IIRES's filter
$R_g$	Resistance between the fault and the ground
$R_{\text{Grid}}$	Grid-side relay
$R_{\text{IIRES}}$	IIRES-side relay
$R_{ph}$	Fault arc resistance
$R_{tr}^0$	Resistance of the of the transformer zero-sequence impedance
$S$	A complex frequency domain parameter
$\varepsilon_0$	Initial angle of $dq$ frame at $t = 0$
$t$	Time
$\vartheta$	Space vector angle
$\theta_0$	Initial phase angle measured at $t = 0$
$\theta_{Comp}^+$	Relative angles between the equivalent negative- and positive-sequence impedances



$\theta_{Comp}^0$	Relative angles between the equivalent negative- and zero-sequence impedances
$\Theta_{IIRES,max}$	Reduced value of $\Theta_{max}$ set for the IIRES controller
$\theta_{I_R}$	Sequence current angle measured at the IIRES terminals
$\Theta_{max}^+$	Half the zone boundary relative to the $\delta^+$ 's fault-type-zone bisector
$\Theta_{max}^0$	Half the zone boundary measured relative to the $\delta^0$ 's fault-type-zone bisector
$\theta_{tr}^-$	Negative-sequence current phase shift between the IIRES and grid sides of the transformer
$\theta_{tr}^+$	Positive-sequence current phase shift between the IIRES and grid sides of the transformer
$\theta_{v_F}$	Sequence voltage angle measured at the fault location
$\theta_{v_R}$	Sequence voltage angle measured at the IIRES terminals
$\theta_z$	Sequence impedance angle of the transmission line between the relay and fault locations
$V_F$	Voltage at the fault location
$V_R$	Bus voltage measured by the relay
$v_t$	IIRES's terminal voltage measured at the POI
$V_x$	Nodal voltage
$Z_{eqR}$	Equivalent impedances from the fault location to the ground at the relay side
$Z_{Grid,side}$	Equivalent impedance from the fault location to the grid terminals
$Z_{IIRES,side}$	Equivalent impedances from the fault location to the IIRES terminals
$Z_{RF}$	Line impedance between the relay and the fault location

$Z_{RF}$	Equivalent impedance between the relay and fault locations
$Z_{th}$	Thevenin impedance at the fault location
$Z_{tr}$	Equivalent transformer impedance

### Subscripts

$a, b, c$	Values related to phases $a$ , $b$ , and $c$ , respectively
$\alpha$	Component aligned with phase $a$
$\beta$	Component lagging phase $a$ by $90^\circ$
$d$	Component aligned with $d$ axis
$F$	Component at the fault location
$g$	Grid side quantity
$max$	The maximum value
$peak$	Component's peak value
$\perp$	Phase shift by $90^\circ$
$\Phi$	Phase component
$q$	Component aligned with $q$ axis
$R$	Component measured at the relay location
$ref$	Reference value
$ref(0)$	Initial reference value

### Superscripts

$a, b, c$	Values related to phases $a$ , $b$ , and $c$ , respectively
$+$	Positive-sequence component
$-$	Negative-sequence component
$0$	Zero-sequence component

# Chapter 1

## Introduction

### 1.1 Preface

Significant efforts are underway globally to combat climate changes, with the United States (US) and the European Commission setting ambitious targets to reduce emissions by 2030 by more than 50% compared to their emission levels in 2005 and 1990, respectively [1], [2]. To achieve these goals, there are continuous efforts to promote renewable energy and reduce reliance on fossil fuels. Currently, many countries, such as US and Canada, have policies that require renewable energy sources (RESs) to supply a percentage of the retail loads; this percentage may reach 100% by 2050 in some states, e.g., Arizona and Washington [3]. Accordingly, RESs dependency is expected to grow in both transmission and distribution networks, especially wind and solar energies, which results in increasing the contribution of RESs in total energy production [4].

On the other hand, high penetration levels of RESs increase the complexity and introduce new challenges to modern grids because RESs are mainly connected to the grid through inverters of low inertia and varying control strategies [5]. To overcome these problems, grid codes (GCs) first recommended disconnecting RESs during faults. Nevertheless, these codes have been changed to allow fault ride-through and reactive power support to enhance grid stability and voltage profile during faults and transient conditions [6]. These GCs are designed to ensure RESs' performance during normal and abnormal conditions meets stability criteria and supports the grid voltage, but they do not include guidelines to ensure proper operation of protection relays that are deployed in the power system grid.

Accordingly, the integration of inverter-interfaced RESs (IIRESs) into the grid during fault conditions causes different problems in power system protection [7]. Recently, it has been revealed that IIRESs affect the credibility of the main protection system functions. For instance, it causes malfunctions for distance protection [8], [9], directional elements

[10], and phase selection methods (PSMs) [11], [12]. These problems are raised due to the differences between the fault current signatures of IIRESSs and those of synchronous generators (SGs). Traditional protection is based on the SG model, which is represented as a voltage source behind a constant impedance [13]. However, the IIRESS mainly operates as a current source that varies according to its controller and grid requirements [14]. Thus, it is crucial to have an insightful understanding of the effect of IIRESSs on the protection system operations, which can be the cornerstone for devising new relays and IIRESS controllers that ensure the reliability and resiliency of modern power systems.

## 1.2 Research Motivations

The exotic fault currents of the IIRESSs adversely affect the capability of the protection function to determine faulty phase(s) correctly, which affects the resiliency and reliability of the power system. This improper operation of PSMs could also affect the proper operation of other fundamental protection functions, e.g., distance protection. Consequently, it could add limitations on the capability of the governments to increase RESs integration into the grid. Thus, it is crucial to guarantee a precise operation of PSMs to enhance power grid resiliency and protection reliability and allow IIRESSs to dominate in electricity grids. To guarantee precise PSMs, researchers tried to modify either the relay algorithm or the IIRESS controller. However, each approach faces some challenges that are summarized as follows:

### A. Challenges Facing Devising New PSM Algorithms,

- Fault currents emanating from RESs differ from conventional fault currents due to:  
(i) they have limited short circuit currents leading to a very large magnitude of their equivalent impedances in comparison to conventional impedance values, (ii) they are current-controlled, which differs from the conventional voltage sources, (iii) the IIRESSs have fast controllers leading to the change of the pre-fault voltage values, as soon as the fault occurred, which differ from conventional fault calculations that assume constant internal voltages of the source before and after the fault. Due to these large differences in the fault current signatures between IIRESSs and conventional SGs, a new short circuit analysis should be performed to consider

these differences. Hence, understanding the root causes of the improper operations of conventional and recently developed PSM relays and assisting in developing robust PSMs.

- Fault currents emanating from IIRESSs depend on the supervisor controller objective, which could be eliminating negative-sequence currents, eliminating active power ripples, eliminating reactive-power ripples, or supporting the grid voltages. These various IIRESS controllers introduce challenges in developing a comprehensive PSM that guarantees correct operation with different IIRESS controllers.
- Fault currents emanating from IIRESS have exotic phase angles; thus, the voltage angles between fault and relay locations will be affected according to the IIRESS supervisory controllers, transmission line impedance angles, and the distance between relay and fault locations. Consequently, it is imperative to include the transmission line effect in devising a new PSM algorithm.

#### B. Challenges Facing Devising New Controllers to Guarantee Precise PSM,

- The IIRESS should be controlled to achieve different objectives, e.g., guarantee proper operation of PSMs, follow RCG requirements imposed by different GCs, and inject the maximum current. Thus, it is crucial to design a supervisory control that achieves the best combinations of the aforementioned objectives.
- The IIRESS's controller should have a low computational processing time and possess a rapid inner controller to guarantee rapid relay operation in determining the faulty phase(s) and increasing the speed of clearing faults, thus, enhancing the stability of power systems.

### **1.3 Research Objectives**

The ultimate goal of this dissertation was to enhance the resiliency of the power system grid by guaranteeing precise phase selection, which will minimize the impact of disturbances caused by fault incidences and enable healthy phase(s) to continue to operate properly. This objective is achieved by two approaches.

1. The first approach is to devise protective relaying methods to ensure correct PSM during various IRES controllers and different fault locations and resistances. The specific research objectives related to the first approach are as follows:
  - 1.1. Development of an adaptive current-angle-based PSM, and
  - 1.2. Development of a modified voltage-angle-based PSM.
2. The second approach is to develop IRES controllers that ensure precise operation for the deployed conventional current-angle-based PSM. The specific research objectives of the second approach are as follows:
  - 2.1. Designing a DCC that guarantees precise PSM and follows the positive-sequence reactive current requirements imposed by conventional GCs, and
  - 2.2. Designing a DCC that ensures precise PSM, follows the positive- and negative-sequence reactive-current generation (RCG) requirements by recent GCs, and ensures injecting the allowable maximum positive-sequence active current.

## 1.4 Dissertation Outline

The rest of the dissertation is organized as follows:

Chapter 2 provides a background on the IRES's modeling and the controlling of the positive- and negative-sequence reference currents as well as a survey of the literature related to PSM relays and IRES controllers that are designed to guarantee correct PSM.

Chapter 3 explores the root causes of the failure of the current- and voltage-angle-based PSMs through short circuit analysis. Subsequently, an adaptive current-angle-based PSM is designed based on calculating the equivalent impedance on the relay side.

Chapter 4 explains the effect of the IRESs' controllers on the phase shift between the fault's and relay's voltages. Consequently, a modified voltage-angle-based PSM is designed to guarantee precise PSM regardless of IRESs' controllers and the fault location.

Chapter 5 introduces two DCCs that guarantee precise PSM operation at the relay and follow the positive-sequence reactive current requirements by various GCs.

Chapter 6 investigates the reasons for the failure of the current-angle-based PSMs when IRESs follow recent GC requirements that impose both positive- and negative-sequence

reactive current requirements. Thereafter, a new DCC is proposed to ensure precise PSM without violating the positive- and negative-sequence reactive current requirements by new GCs, e.g., VDE-AR-N 4120.

Chapter 7 provides the dissertation conclusions and contributions and suggests directions for future work.

## Chapter 2

### Background and Literature Review

#### 2.1 Modeling of VSCs

The two-level VSC is one of the most common VSCs utilized in integrating RESs into the grid [15]. Since RESs are power sources that inject power into the grid, VSCs are also called inverters in this dissertation. The RESs basic system, as shown in Figure 2.1, consists of a dc capacitor as a buffer between RESs and the inverter; a two-level VSC consists of three half-bridge legs composed of six electronic switches, in which each switch is built from an IGBT with anti-parallel diode; and an LC(L) filter, which composed of an inductor (L), a capacitor (C), and maybe another inductor (L), to facilitate the integration of the inverter into the grid.

The VSC is controlled by feeding the switches with gate pulses to synthesize the desired inverter's internal voltage ( $E$ ). One of the fundamental techniques to generate the gate pulses is comparing the desired output voltage waveform with fundamental frequency and unity amplitude, i.e., modulation index ( $m$ ), against a carrier, usually a triangle shape with a frequency equal to the switching frequency ( $f_s$ ). By analyzing the output voltage using Fourier transform (FT), it can be observed that the output voltage consists of a fundamental component with a frequency equal to the modulation index frequency and harmonic components with frequencies higher than or equal to the switching frequency [16]. Consequently, the switching frequency is designed much greater than the fundamental

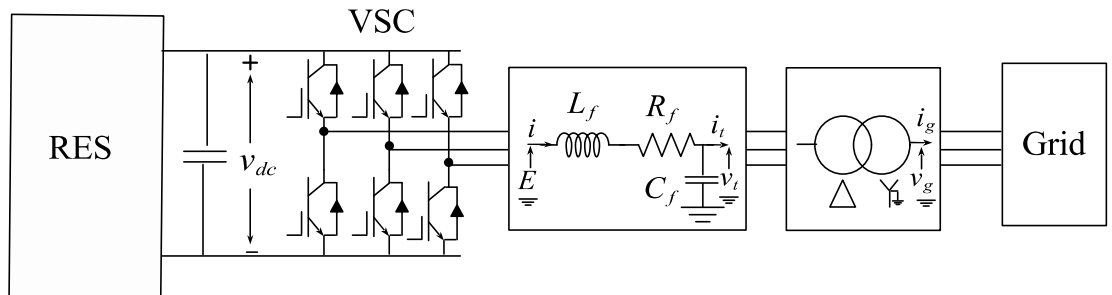


Figure 2.1. RES integrated into the grid through a three-phase two-level VSC and an LCL filter.



frequency, e.g., 51 times the fundamental frequency [17], to enable the LC(L) filter to mitigate these high-frequency harmonics without affecting the low-frequency dynamics.

Accordingly, an average model can be derived to approximate the low-frequency dynamics with a continuous model depending on the average value of the modulation index during each switching periodic time. The average model is used in modeling the VSC to facilitate the control design by developing an average model that relates the VSC's internal voltage with the input signal, i.e., the modulation index. The average model of the VSC is driven in detail in [15], in which the model of the VSC is given by

$$E_{\Phi} = \frac{m_{\Phi}}{2} v_{dc} \quad (2.1)$$

where  $v_{dc}$  is the input dc voltage of the VSC, while the subscript  $\Phi$  represents phase quantity, i.e.,  $a$ ,  $b$ , and  $c$ . It is worth mentioning that this model gives accurate dynamic analysis for frequencies less than  $0.425 \times f_s$ , which is sufficient to represent the VSC controller dynamics efficiently [18].

On the other hand, the LC(L) filter is designed with a cut-off frequency lower than the switching frequency and higher than the controller bandwidth to attenuate switching harmonics without affecting the controller dynamics. In addition, the filter should be accurately designed to have a resonance frequency lower than the switching frequency and higher than the controller bandwidth. It is worth mentioning that the design of current controllers remains almost the same for an  $L$ ,  $LC$  + transformer, or  $LCL$  filter by using appropriate active or passive damping parameters. This is because the capacitance in the  $LC$  and  $LCL$  filters is mainly designed to mitigate harmonics at multiples of the switching frequency. Thus, the capacitor effect can be neglected during the design of current controllers, whereas the total inductance is the main parameter affecting the current controller design.

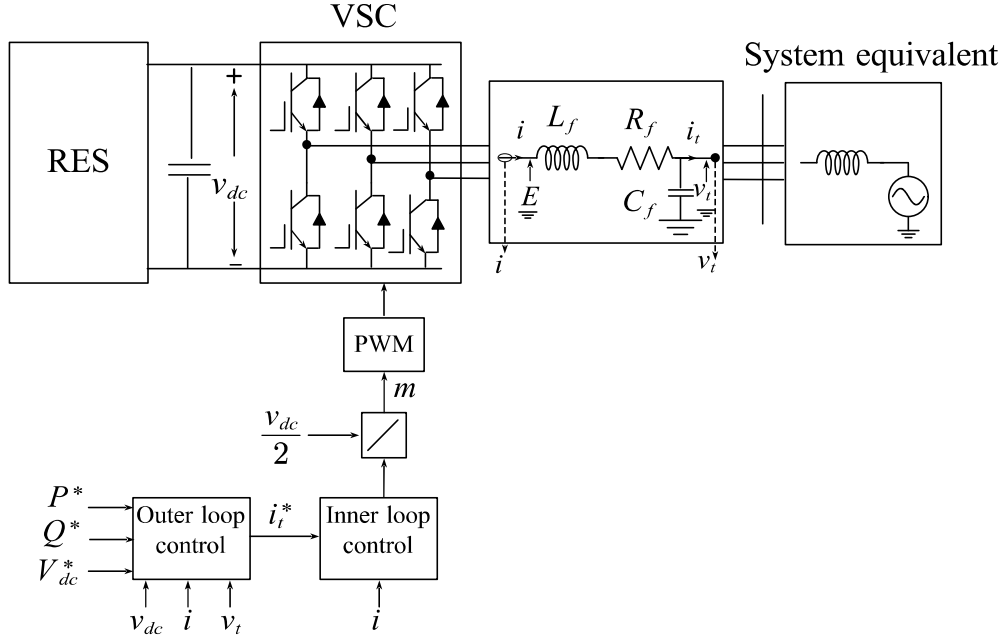


Figure 2.2. Generic current controlled VSC controller.

## 2.2 Inverter Control

The generic current-controlled VSC's controller diagram is shown in Figure 2.2, which is composed of two control loops, i.e., the inner and outer control loops. The inner control loop is responsible for regulating the IRES's reference current with high accuracy and fast dynamics [17]. Its bandwidth is almost chosen to be about one-tenth of the switching frequency to possess high dynamic capability without interfering with the switching frequency and the cut-off frequency of the low-pass filter. On the other hand, the outer control loop is responsible for determining the reference current based on active-power reference, reactive power reference, or regulating the dc-link voltage. The outer loop bandwidth is usually chosen to be smaller than one-tenth of the inner control loop to decouple their control dynamics [19].

### 2.2.1 Inner Control Loop

The inner control loop determines the reference of the inverter's terminal voltages, which forces the inverter to inject the desired reference current. Thus, the first step in designing the current controller is determining the dynamic model that relates the inverter's currents

and voltages. The ac-side dynamics can be written in terms of phase voltages and currents as

$$\begin{cases} E_\phi - v_{t,\phi} = L_f \frac{di_\phi}{dt} + R_f i_\phi \\ i_\phi - i_{t,\phi} = C_f \frac{dv_{t,\phi}}{dt} \end{cases} \quad (2.2)$$

in which  $i$  is the inverter's output current;  $v_t$  and  $i_t$  are the IRES's terminal voltage and current measured at the point of interconnection (POI), respectively;  $R_f$ ,  $L_f$ , and  $C_f$  are the resistance, inductance, and capacitance of the IRES's filter, respectively; and  $t$  indicates the time. Accordingly, each phase can be controlled separately to achieve the required reference current for each phase. To reduce the number of compensators, the references of the three-phase currents are transformed into other frames, e.g., space vector, stationary, and synchronous rotating frames, which require a lower number of compensators.

#### A. Modeling of a System with Balanced Current and Voltage Quantities

The balanced three-phase currents and voltages can be represented by a complex vector, i.e., a space vector. This representation allows analyzing the three-phase system, as a whole, instead of analyzing each phase separately. The space vector is rotating with an angular frequency equal to the three-phase fundamental frequency while it has a constant magnitude that is equal to the phase peak of the electric quantity. The relation between the space vector and phasor representations in a balanced system is given by

$$\mathbf{f} = |f|e^{J\vartheta} = (|f|e^{J\theta_0})e^{J\omega t} \quad (2.3)$$

where  $f$  is an arbitrary electric component, e.g., voltage or current component,  $\mathbf{f}$  is the space vector representation of  $f$ ,  $\vartheta$  is the space vector angle measured at time  $t$ ,  $\theta_0$  is the initial phase angle measured at  $t = 0$ , and  $\omega$  is the angular frequency. Since the space vector is written in complex form, its applications in controlling the reference currents are few, e.g., shifting and scaling the reference currents [15]. Consequently, the space vector is decomposed into a two-dimensional frame, i.e., stationary ( $\alpha\beta$ ) frame, as displayed in

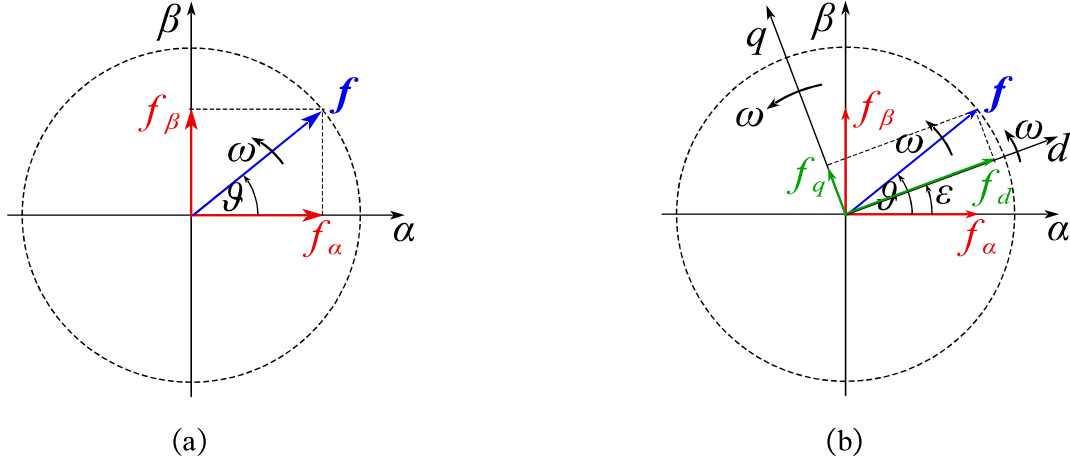


Figure 2.3. Space vector transformation into (a)  $\alpha\beta$  frame and (b)  $dq$  frame.

Figure 2.3(a). The relation between the space vector and stationary frame components is formulated by

$$\mathbf{f} = f_\alpha + jf_\beta \quad (2.4)$$

where  $j$  indicates the imaginary axis, and the subscripts  $\alpha$  and  $\beta$  indicate a component aligned with phase  $a$  and lagging phase  $a$  by  $90^\circ$ , respectively. By substituting (2.4) in (2.3), the phasor quantities can be transferred into stationary quantities using Clarke transformation, as stated in (2.5).

$$\begin{bmatrix} f_\alpha \\ f_\beta \end{bmatrix} = \frac{2}{3} \begin{bmatrix} 1 & -\frac{1}{2} & -\frac{1}{2} \\ 0 & \frac{\sqrt{3}}{2} & -\frac{\sqrt{3}}{2} \end{bmatrix} \begin{bmatrix} f_a \\ f_b \\ f_c \end{bmatrix} \quad (2.5)$$

where the subscripts  $a$ ,  $b$ , and  $c$  indicated values aligned with phase  $a$ ,  $b$ , and  $c$ , respectively. By substituting (2.5) into (2.2), the ac-system dynamics are represented in the  $\alpha\beta$  frame by

$$\begin{cases} E_{\alpha\beta} - v_{t,\alpha\beta} = L_f \frac{di_{\alpha\beta}}{dt} + R_f i_{\alpha\beta} \\ i_{\alpha\beta} - i_{t,\alpha\beta} = C_f \frac{dv_{t,\alpha\beta}}{dt} \end{cases} \quad (2.6)$$

which illustrates that controlling the current references in the  $\alpha\beta$  frame can reduce the number of compensators into two compensators. However, the controlled signals, i.e., the current references, are still sinusoidal, which requires the compensator to possess high bandwidth to reduce the steady-state error. Another frame transformation is formulated by decomposing the  $\alpha\beta$  frame into two rotating axes, i.e., synchronous ( $dq$ ) frame, that rotates with a speed equal to the space vector frequency, as portrayed in Figure 2.3(b). The relation between  $\alpha\beta$  and  $dq$  frames is as follows,

$$f_d + jf_q = (f_\alpha + jf_\beta)e^{-j\varepsilon} = |f|e^{j(\theta_0 - \varepsilon_0)} \quad (2.7)$$

where  $\varepsilon$  is the  $dq$  frame rotating angle and  $\varepsilon_0$  is the initial angle of  $dq$  frame at  $t = 0$ , while the subscripts  $d$  and  $q$  represent the component aligned with  $d$  and  $q$  axis, respectively. It can be observed from (2.7) that the  $dq$  frame quantities are dc-quantities, which simplify the required controller. Moreover, choosing  $\varepsilon_0$  equals  $\theta_0$ , makes the quantity in the  $q$  axis equals zero, which helps in decoupling the outer control loop equations [15]. Thereafter, by substituting (2.7) into (2.5), the electric quantity in the  $abc$  frame can be directly converted to  $dq$  frame using Park transformation, which is written as

$$\begin{bmatrix} f_d \\ f_q \end{bmatrix} = \frac{2}{3} \begin{bmatrix} \cos(\vartheta) & \cos\left(\vartheta - \frac{2\pi}{3}\right) & \cos\left(\vartheta + \frac{2\pi}{3}\right) \\ -\sin(\vartheta) & -\sin\left(\vartheta - \frac{2\pi}{3}\right) & -\sin\left(\vartheta + \frac{2\pi}{3}\right) \end{bmatrix} \begin{bmatrix} f_a \\ f_b \\ f_c \end{bmatrix}. \quad (2.8)$$

Consequently, the inverter ac-side dynamics can be formulated in the  $dq$  frame by

$$\begin{cases} E_{dq} - v_{t,dq} = L_f \frac{di_{dq}}{dt} + R_f i_{dq} \mp \omega L_f i_{qd} \\ i_{dq} - i_{t,dq} = C_f \frac{dv_{t,dq}}{dt} \mp \omega C_f v_{t,qd}. \end{cases} \quad (2.9)$$

It can be observed from (2.9) that the currents in the  $dq$  frame are coupled. The cross-coupling terms in the  $d$  and  $q$  axes and the voltage at the POI can be considered disturbances. Thus, these values are feedforward to the current-control loop to remove the effect of these disturbances. The inner current-control loop in the  $dq$  frame is shown in

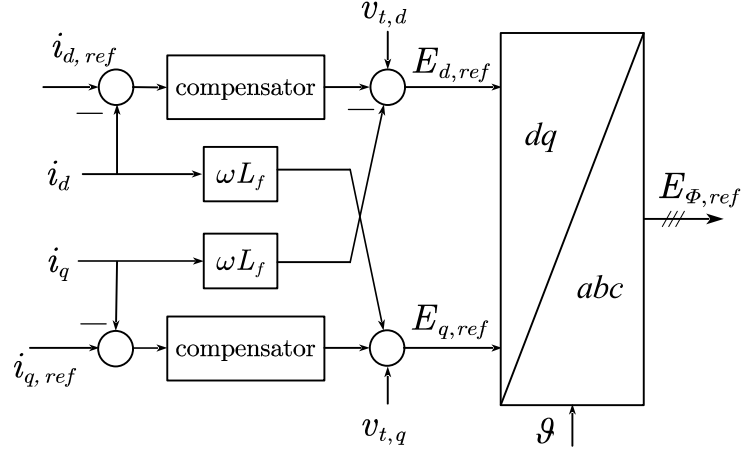


Figure 2.4. Inner current-control loop in  $dq$  reference frame.

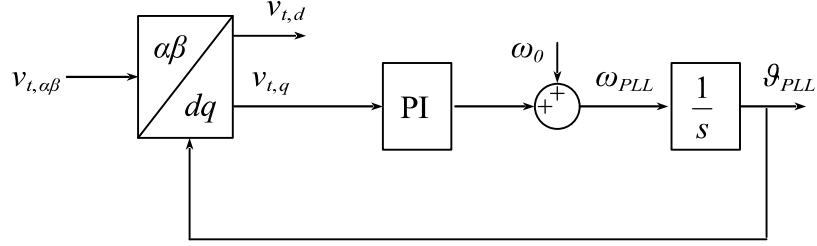


Figure 2.5. SRF-PLL schematic diagram.

Figure 2.4, in which the compensator is usually selected as a proportional-integral (PI) controller, and its parameters are selected based on the ac-side dynamic equation, i.e., (2.9), and the desired dynamic response [15].

Despite the many advantages of designing the controller in the  $dq$  frame, it requires an additional component, called a phase-locked loop (PLL), to determine the space vector rotational angle ( $\vartheta$ ). The basic PLL is called synchronous rotating frame PLL (SRF-PLL), which is shown in Figure 2.5 [20]. It is based on controlling  $\vartheta_{PLL}$  to force the voltage component in the q-axis to be zero, which is achieved when  $\vartheta_{PLL}$  equals to the space vector rotational angle ( $\vartheta$ ).

## B. Modeling of a System with Unbalanced Current or Voltage Quantities

Unbalanced ac systems, e.g., asymmetric faults, are difficult to be analyzed in the  $abc$

frame. Thus, the unbalanced three-phase quantities are transferred to three symmetric balanced components, i.e., the positive-, negative, and zero-sequence components, to facilitate the system study during unbalanced incidences. The transformation from  $abc$  to symmetric components is given by

$$\begin{bmatrix} f^0 \\ f^+ \\ f^- \end{bmatrix} = \frac{1}{3} \begin{bmatrix} 1 & 1 & 1 \\ 1 & 1\angle 120 & 1\angle -120 \\ 1 & 1\angle -120 & 1\angle 120 \end{bmatrix} \begin{bmatrix} f_a \\ f_b \\ f_c \end{bmatrix}. \quad (2.10)$$

where the superscript 0, +, and  $-$  indicates the zero-, positive-, and negative-sequence components, respectively. It is worth mentioning that the driven symmetric components are related to phase  $a$ , while other symmetric phase components can be determined easily by adding the phase shift related to this phase. For RESs controllers, the positive- and negative-sequence components are only controllable because the zero-sequence current that emerged from the IRESs does not affect the grid due to the interfacing transformer between the IRES and grid, which is usually a delta/star-ground transformer.

Consequently, the  $dq$  frame is required to be decomposed into positive and negative sequences, which can be determined by

$$f_\alpha + jf_\beta = (f_d^+ + jf_q^+)e^{j\vartheta} + (f_d^- + jf_q^-)e^{-j\vartheta} \quad (2.11)$$

Thereafter, substituting (2.11) into (2.6) gives the VSC's ac-side dynamics in positive- and negative- sequence  $dq$  frames ( $d^+q^+$  and  $d^-q^-$ , respectively), as stated in (2.12) and (2.13), respectively.

$$\begin{cases} E_d^+ - v_{t,d}^+ = L_f \frac{di_d^+}{dt} + R_f i_d^+ - \omega L_f i_q^+ \\ E_q^+ - v_{t,q}^+ = L_f \frac{di_q^+}{dt} + R_f i_q^+ + \omega L_f i_d^+ \\ i_d^+ - i_{t,d}^+ = C_f \frac{dv_{t,d}^+}{dt} - \omega C_f v_{t,q}^+ \\ i_q^+ - i_{t,q}^+ = C_f \frac{dv_{t,q}^+}{dt} + \omega C_f v_{t,d}^+ \end{cases} \quad (2.12)$$

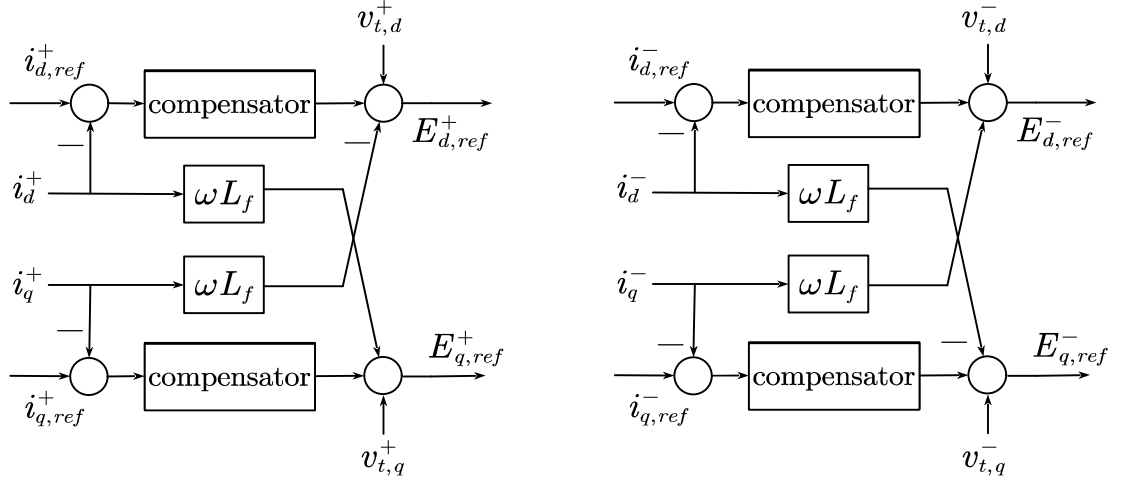


Figure 2.6. Inner current-control loop in  $d^+q^+$  and  $d^-q^-$  reference frames.

$$\begin{cases} E_d^- - v_{t,d}^- = L_f \frac{di_d^-}{dt} + R_f i_d^- + \omega L_f i_q^- \\ E_q^- - v_{t,q}^- = L_f \frac{di_q^-}{dt} + R_f i_q^- - \omega L_f i_d^- \\ i_d^- - i_{t,d}^- = C_f \frac{dv_{t,d}^-}{dt} + \omega C_f v_{oq}^- \\ i_q^- - i_{t,q}^- = C_f \frac{dv_{t,q}^-}{dt} - \omega C_f v_{od}^- \end{cases} \quad (2.13)$$

Accordingly, the inner control loop in the  $dq$  frame is updated by adding a negative-sequence current controller, as depicted in Figure 2.6.

Controlling the IIRES current reference in the  $d^+q^+$  and  $d^-q^-$  frames have some disadvantages, e.g., (i) the conversion from  $abc$  to  $d^+q^+$  contains sinusoidal components related to  $d^-q^-$ , and vice versa, which requires adding a notch filter to eliminate this sinusoidal component; however, it affects the controller's bandwidth, (ii) the PLL requires advanced techniques to determine the state space rotating angle precisely, such as dual second order generalized integrator (DSOGI) PLL [21] and decouple double synchronous reference frame (DDSRF) PLL [22], and (iii) it requires four compensators to control the system in the  $d^+q^+$  and  $d^-q^-$  frames. Thus, many researchers recommend using the  $\alpha\beta$  frame in controlling unbalanced electrical quantities [23]. To separately control the positive and negative sequences for any arbitrary signal  $f$ , the  $\alpha\beta$  quantities are decomposed into positive- and negative-sequence components as given by



$$f_{\alpha\beta} = f_{\alpha\beta}^+ + f_{\alpha\beta}^- = |f^+| \begin{bmatrix} \sin(\omega t + \angle f^+) \\ -\cos(\omega t + \angle f^+) \end{bmatrix} + |f^-| \begin{bmatrix} \sin(\omega t + \angle f^-) \\ \cos(\omega t + \angle f^-) \end{bmatrix}. \quad (2.14)$$

The dynamic model of the VSC in the  $\alpha^+\beta^+$  and  $\alpha^-\beta^-$  is formulated as in (2.15) and (2.16), respectively, by substituting (2.14) into (2.6).

$$\begin{cases} E_{\alpha}^+ - v_{t,\alpha}^+ = -\omega L_f i_{\beta}^+ + R_f i_{\alpha}^+ \\ E_{\beta}^+ - v_{t,\beta}^+ = \omega L_f i_{\alpha}^+ + R_f i_{\beta}^+ \\ i_{\alpha}^+ - i_{t,\alpha}^+ = -\omega C_f v_{t,\beta}^+ \\ i_{\beta}^+ - i_{t,\beta}^+ = \omega C_f v_{t,\alpha}^+ \end{cases} \quad (2.15)$$

$$\begin{cases} E_{\alpha}^- - v_{t,\alpha}^- = \omega L_f i_{\beta}^- + R_f i_{\alpha}^- \\ E_{\beta}^- - v_{t,\beta}^- = -\omega L_f i_{\alpha}^- + R_f i_{\beta}^- \\ i_{\alpha}^- - i_{t,\alpha}^- = \omega C_f v_{t,\beta}^- \\ i_{\beta}^- - i_{t,\beta}^- = -\omega C_f v_{t,\alpha}^- \end{cases} \quad (2.16)$$

Since the  $\alpha^+\beta^+$  and  $\alpha^-\beta^-$  quantities are sinusoidal signals, they can be combined into  $\alpha$  and  $\beta$  references, which reduces the number of compensators into two, as displayed in Figure 2.7.

### C. Inner Control Loop Compensator

The controller's compensators are designed to track the reference current accurately and achieve good dynamic performance, e.g., small rise time, overshoot, and steady-state error. In general, PI controllers are utilized to track the reference currents in the  $dq$  frame, while proportional-resonant (PR) is used in tracking the reference currents in the  $\alpha\beta$  frame. Other researchers investigate the performance of other controllers to enhance the controller's tracking speed, accuracy, and robustness against disturbances, such as deadbeat, fuzzy, and adaptive controllers [24], [25].

## 2.2.2 Outer Control Loop

The outer control loop is responsible for setting the desired reference currents based on power or voltage requirements. These requirements should achieve GCs requirements in normal and abnormal conditions. In abnormal conditions, conventional GCs force the

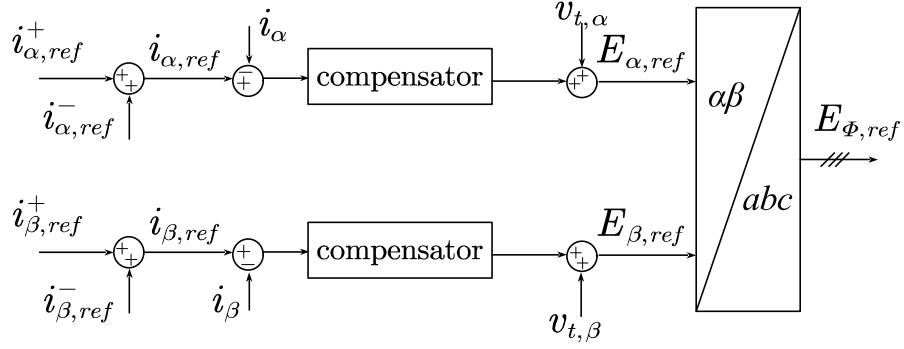


Figure 2.7. Inner current-control loop in  $\alpha^+\beta^+$  and  $\alpha^-\beta^-$  reference frames.

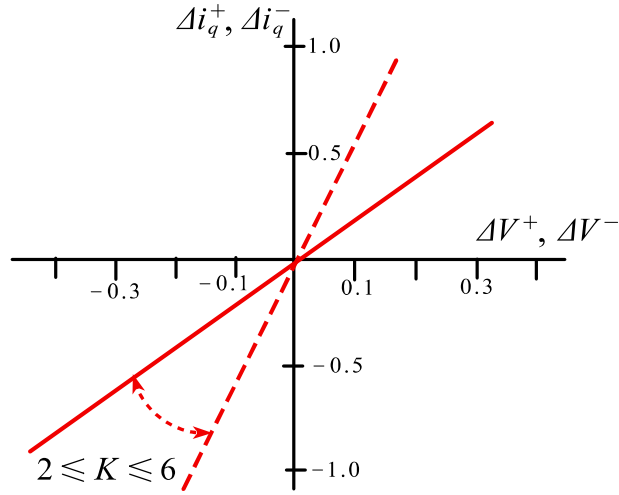


Figure 2.8. Reactive-current generation requirements for the VDE-AR-N 4120-GC.

IRES to support the grid voltage by injecting positive-sequence reactive currents [26]. However, recent GCs, e.g., the first draft of the IEEE P2800 [27], Spanish [28], European guidelines [29], and German GCs [30], set requirements for injecting both positive- and negative-sequence reactive current to support the grid voltage and reduce the voltage unbalance, respectively. Figure 2.8 illustrates the RCG requirements of the German GC, i.e., VDE-AR-N 4120-GC, during abnormal conditions.

#### A. Overview of Various DCCs' Objectives in the Literature

It is worth mentioning that the GC requirements are performance-based guidelines and do not define specific set points for the reference power, voltage, or currents. Thus, many

researchers attempt to determine appropriate current references to enhance power quality, enhance stability, or support the grid voltage without violating GCs requirements, e.g., [31], while others attempt to set current references to enhance the operation of the power system without considering GCs guidelines, which will provide higher flexibility in achieving control objectives hoping the change of the guidelines specified by GCs, e.g., [32].

The authors of [33] propose a DCC, which controls the positive- and negative-sequence current quantities, to mitigate current unbalance, active or reactive-power oscillations. In [34], the DCC references are determined to reduce both active and reactive power ripples based on the instantaneous active-reactive power theory with the assistance of feedforward to eliminate the superimposed third harmonic contents in the output currents. The authors of [35] determine the positive- and negative-sequence currents to reduce the voltage unbalance ratio at the POI, while the authors in [36] minimize the peak current. The aforementioned research was designed to enhance power system operation but does not take into account the behavior of the deployed relays; thus, conventional relays are susceptible to failure when currents are injected from the IIREs during fault conditions, which reduces power system reliability and resiliency. Recently, some researchers have attempted to determine adequate reference currents that enable the proper operation of conventional relays. For instance, [32] proposes a DCC that controls the IIREs current to enable proper operation for the impedance-based directional relay, while [37] controls the IIREs positive sequence current to mimic the SG impedance angle, which secures correct operation for the impedance-based distance relay. Others attempt to solve the problem associated with phase selection, which will be discussed in the following section.

## **2.3 Phase Selection**

Phase selection refers to the ability of relays to determine the faulted phase(s) precisely, which is an essential requirement for other protection functions, such as distance protection and auto-reclosing [38], [39]. Besides, it increases the reliability of distribution systems by allowing single-pole tripping (SPT), which reduces power interruptions and increases RESs utilization [11]. For instance, during a single-line-to-ground (SLG) fault,

disconnecting only the faulty phase can enhance reliability by 67%. The industrial community has proposed solutions to allow phase selection at the distribution level [40]–[42]. Manufacturers of relays and modern reclosers offer commercial products that allow SPT in distribution systems [39], [43]. Some utilities have started implementing phase selection in their distribution systems [40], [44], and others have put plans to implement phase selection [41]. Thus, phase selection is important for distribution and transmission systems, including microgrids.

### 2.3.1 Conventional PSMs

Conventional PSMs can be classified according to the type of the processed electrical quantities into two categories: (i) transient quantities PSMs, which are based on high-frequency components, traveling wave, or wavelet transform [45]–[47], and (ii) steady state quantities' PSMs, which are based on comparing electrical quantities' magnitudes and/or phases [48], [49]. It is worth mentioning that most conventional relays depend on steady-state quantities as they do not require expensive sensors and data analysis [50]. On the other hand, conventional PSMs can be classified based on the compared electrical quantities into (i) current, (ii) voltage, or (iii) both current and voltage quantities [51].

In [52], the faulted phase(s) are determined based on the magnitude comparison of the phase currents, while the authors in [49] rely on comparing the line currents' magnitude to reduce the effect of zero sequence currents. However, these methods are jeopardized during weak grids and high resistive faults. Hence, many deployed relays depend on comparing the current phase angles to determine the fault type accurately during different fault conditions, i.e., current-angle-based PSM [53]–[55]. The principle of operation of the current-angle-based PSM is based on determining the relative angle between the negative- and zero-sequence currents ( $\delta_I^0$ ) and compared with its predefined zone shown in Figure 2.9(a); hence, two types of faults are determined. Thereafter, the relative angle between the negative- and the positive-sequence currents ( $\delta_I^+$ ) are determined and compared to  $\delta_I^+$ 's predefined zones shown in Figure 2.9(b). Consequently, the faulted phase(s) can be determined precisely. Despite the precise operation of the current-angle-based PSMs in conventional grids, they suffer from incorrect operation in the existence of IIREs.

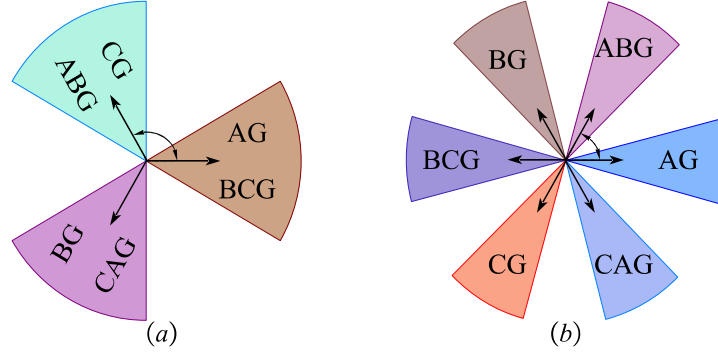


Figure 2.9. Current-angle-based PSM zones for (a)  $\delta_I^0$ , (b)  $\delta_I^+$ .

### 2.3.2 Relay Modifications for Precise PSM

Researchers attempt to solve the problem from the relay side by using data-driven methods, that are based on machine learning and artificial intelligence, or based on circuit analysis. According to the data-driven approach, the authors of [56] classify the fault types based on unsupervised framework using a sparse filter and a capsule network, while probabilistic neural network is utilized in [57] to extract fault features. In [58] a new fault zone has been specified using undecimated discrete wavelet transform and Chebyshev neural network. The authors of [59] determine the fault type using morphology-based approach, while in [60], a decision tree algorithm is utilized for fault classification. These methods are complex in terms of architecture, time, and computational effort making them slow. Besides, they are system dependent, hence, required to be modified for each power system structure. Consequently, other researchers try to solve the phase selection problem based on analytical analysis. In [11], two voltage-angle-based PSMs are proposed for microgrids to determine the faulty phase(s) in the presence of IRESs. The first method is based on the relative angle between negative- and zero-sequence voltages ( $\delta_V^0$ ) and phase voltage magnitudes. The second method is also based on the relative angle between the negative- and zero-sequence voltages, but with the assistance of the relative angle between the negative- and positive-sequence voltages ( $\delta_V^+$ ), i.e., the voltage-angle-based PSM. The principle of operation of the voltage-angle-based PSM is based on comparing  $\delta_V^0$  with predefined zones, as shown in Figure 2.10; hence, two types of faults are determined. Thereafter by comparing  $\delta_V^+$  with the predefined zones, i.e., shown in Figure 2.11, the fault type is pinpointed. The results show high accuracy in ground faults. In [61], line-to-line

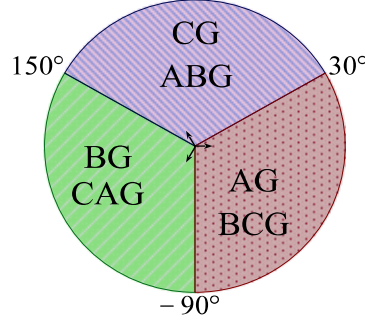


Figure 2.10. Voltage-angle-based PSM  $\delta_V^0$  zones.

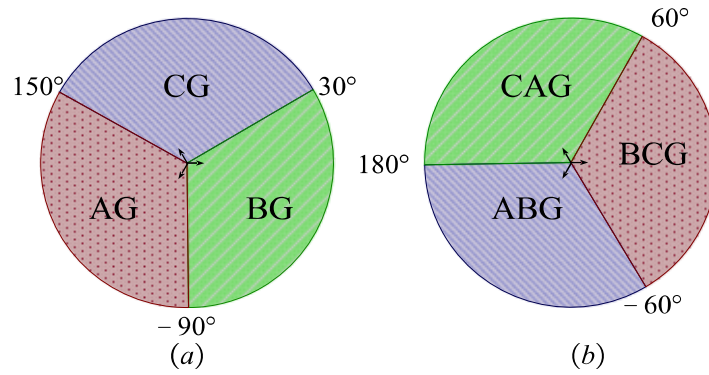


Figure 2.11. Voltage-angle-based PSM  $\delta_V^+$  zones: (a) SLG zones, (b) LL(G) zones.

(LL) and line-to-line-to-ground (LLG) faults are determined using different zones to increase LL fault detection accuracy. However, the effect of fault arc resistance is ignored for LLG faults, which deteriorates the relay accuracy at large arc resistance faults. The authors of [62] suggest using the current-angle-based PSM only for a specific time after fault inception by an adaptive window, which is based on the current transient waveforms. Nevertheless, the performance suffers from maloperation in some tested cases. Hence, there is a requirement to devise a relay that ensures precise phase selection at different fault conditions.

### 2.3.3 DCC Modifications to Guarantee Correct Operation of Conventional PSM

On the other hand, a few IRES controllers are proposed to enable correct operation of the current-angle-based PSM without modifying the currently deployed relays. The authors of [63] suggest controlling the negative-sequence current to mimic the SG negative-sequence

model, which is represented by a constant impedance. In [64], the fault type is identified by the IRES using the voltage-angle-based PSM to specify the reference of the negative-sequence current angle. Then, the negative-sequence current is controlled to enable the accurate placement of either  $\delta^0$  or  $\delta^+$  in their respective fault-type zones. However, the controllers developed in [63] and [64] may not guarantee the simultaneous placement of  $\delta^0$  and  $\delta^+$  under different RCG requirements by GCs. The authors of [65] suggest controlling both positive- and negative-sequence currents by replicating the SG model to enable correct operation for both  $\delta^0$  and  $\delta^+$ . Although the controller of [65] may support the grid with reactive current during faults, it does not comply with the RCG requirements imposed by GCs. Further, the controllers in [63]–[65] are designed in the synchronous frame, which possesses a slower dynamic response during unbalanced faults compared to that implemented in the stationary frame [23]. Thus, it may reduce the relay speed and FRT rapid response requirement. To the best of the author’s knowledge, there is no IRES controller that simultaneously achieves the requirements of the current-angle-based PSM and RCG during unbalanced faults. Thus, it is imperative to develop a new DCC to fulfill this research gap.

## 2.4 Discussion

It has been illustrated in this chapter that ensuring the proper operation of protection functions has attracted increasing interest due to its importance in enhancing power system reliability and resilience. A critical review is conducted to present the recent research in enhancing the operation of PSM when faults are supplied from IRES. This review reveals shortfalls in addressing several challenges. First, there is a lack of studying the root causes of the failure of PSM. Second, the existing relay algorithms in the literature ignore the effect of arc resistance and the shift in the voltage angle due to the transmission line’s impedance and the IRES’s supervisory control, leading to the failure of commercial relays in securing the correct operation of PSMs. Lastly, the proposed DCCs in the literature that attempt to guarantee the correct operation of conventional methods ignore GC requirements, which limits their applicability in most grids that impose GC requirements. Hence, it is essential to develop a PSM that can guarantee precise operation for faulty phase selection, which can be used as a long-term solution due to the expensive cost of rapidly

replacing all the deployed relays in the grid. In addition, the IRES should be controlled precisely to allow accurate operation for conventional PSM without violating RCG requirements, which can be considered a fast solution for enhanced power system reliability and resiliency.



## Chapter 3

# Adaptive Current-Angle-Based Phase Selection for Microgrids with Inverter-Interfaced Renewable Energy Sources

### 3.1 Introduction

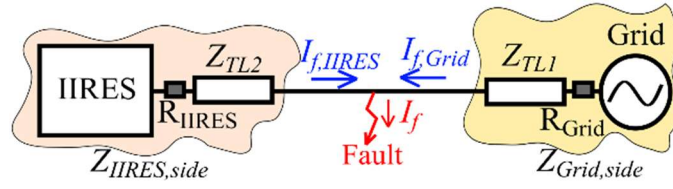
IRESs possess different fault signatures as compared to traditional SGs, thus introducing new challenges for microgrid protection. Among these challenges is phase selection, which is a prerequisite for SPT. This chapter analyzes the root causes behind the failure of current-angle-based PSMs used by commercial relays in microgrids with IRESs. Besides, the operation of the recently developed voltage-angle-based PSM is investigated to unveil its points of strength and weakness. Then, adaptive zoning for the current-angle-based PSM is proposed to cope with the unconventional IRES fault current signatures and enable precise SPT. As a result, microgrid reliability and resiliency during faults are enhanced. Comprehensive time-domain simulations verify the effectiveness of the proposed PSM at various fault resistances, fault locations, and microgrid topologies.

### 3.2 Phase Selection Analysis

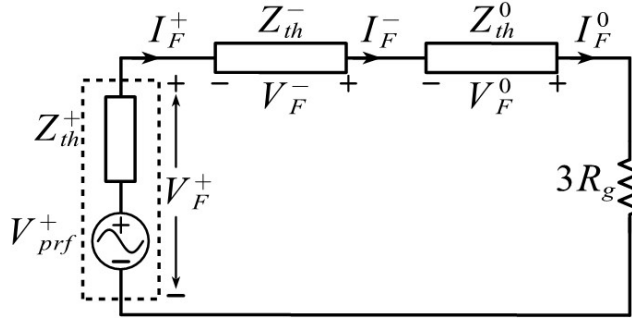
This section elaborates on the root causes behind the failure of PSMs in the presence of IRESs using short-circuit analysis. Two PSMs are analyzed: (i) the current-angle-based PSM used by commercial relays for phase selection [53]; and (ii) the voltage-angle-based PSM [11], which is recently developed to encounter the uncharacteristic nature of IRES fault currents.

#### 3.2.1 Current-Angle-Based PSM

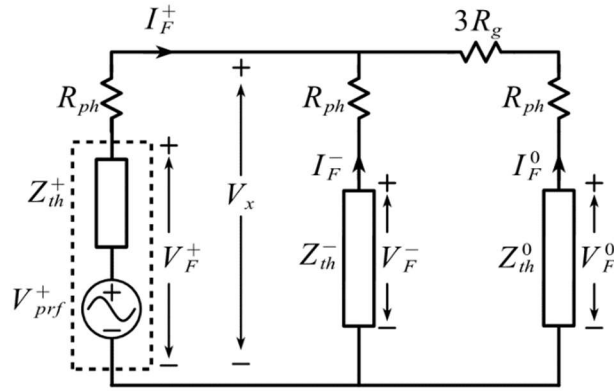
Short circuit analysis is performed to deduce the relative angles between the superimposed negative- and zero-sequence currents, i.e.,  $\delta_I^0 = \angle \Delta I^- - \angle \Delta I^0$ , and the superimposed negative- and positive-sequence currents, i.e.,  $\delta_I^+ = \angle \Delta I^- - \angle \Delta I^+$ . These two angles are



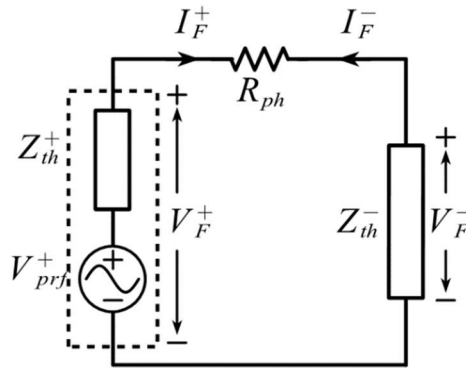
(a)



(b)



(c)



(d)

Figure 3.1. Sample system for short-circuit analysis: (a) single line diagram, (b) sequence circuits for AG faults, (c) sequence circuits for BCG faults, (d) sequence circuits for BC faults.

typically used in commercial relays to identify fault types [66]. The short circuit analysis is executed for a sample system shown in Figure 3.1(a) for single-line-to-ground (SLG), line-line-to-ground (LLG), and line-to-line (LL) faults to pinpoint the defects in the traditional PSMs and reasons for their failure as a consequence of interposing IIRESs into microgrids.

#### A. SLG Faults

An AG fault is investigated as an example of SLG faults. For AG faults, the sequence fault currents at the fault location are equal in both magnitude and angle, as shown in Figure 3.1(b), i.e.,

$$I_F = I_F^+ = I_F^- = I_F^0 \quad (3.1)$$

where  $I_F$  is the fault current at the fault location. In order to determine the fault currents measured by a relay, a relation between the sequence currents at the relay and fault location should be determined. As shown in Figure 3.1(a), the fault current (indicated by red arrow) is divided between the grid and IIRES sides (as displayed by blue arrows). For example, the fault current measured by the IIRES-side relay (i.e.,  $I_{F,IIRES}$ ) is given by

$$I_{F,IIRES} = I_F \times \frac{Z_{Grid,side}}{Z_{IIRES,side} + Z_{Grid,side}} \quad (3.2)$$

where  $Z_{Grid,side}$  and  $Z_{IIRES,side}$  are the equivalent impedances from the fault location to the grid and IIRES terminals, respectively. Multiplying the right-hand side of (3.2) by  $\frac{Z_{IIRES,side}}{Z_{IIRES,side}}$  yields

$$I_{F,IIRES} = I_F \times \frac{Z_{Grid,side} \times Z_{IIRES,side}}{Z_{IIRES,side} + Z_{Grid,side}} \times \frac{1}{Z_{IIRES,side}} = I_F \times \frac{Z_{th}}{Z_{IIRES,side}} \quad (3.3)$$

where  $Z_{th}$  is the Thevenin impedance at the fault location, i.e., given by

$$Z_{th} = \frac{Z_{IIRES,side} \times Z_{Grid,side}}{Z_{IIRES,side} + Z_{Grid,side}}. \quad (3.4)$$

Subsequently, (3.3) can be generalized to be applicable for any relay, whether on the IRES or grid side, by (i) replacing  $I_{F,IRES}$  with  $I_{FR}$ , i.e., the fault current through a relay, and (ii) exchanging  $Z_{IRES,side}$  by  $Z_{eqR}$ , i.e., the equivalent impedance from the fault location to the terminals of a relay branch. Moreover, superscripts  $+$ ,  $-$ , and  $0$  are added to represent sequence quantities. Thus, the sequence fault currents measured by a relay are given by

$$I_{FR}^- = \Delta I_R^- = I_F^- \times \frac{Z_{th}^-}{Z_{eqR}^-} \quad (3.5)$$

$$I_{FR}^0 = \Delta I_R^0 = I_F^0 \times \frac{Z_{th}^0}{Z_{eqR}^0} \quad (3.6)$$

$$I_{FR}^+ = \Delta I_R^+ = I_F^+ \times \frac{Z_{th}^+}{Z_{eqR}^+} \quad (3.7)$$

where  $\Delta$  indicates superimposed quantities and  $I_R$  is the current measured by a relay. The ratios between sequence currents measured by a relay can be determined by substituting (1) into (3.5)–(3.7), as follows:

$$\frac{\Delta I_R^-}{\Delta I_R^0} = \frac{Z_{th}^-}{Z_{th}^0} \times \frac{Z_{eqR}^0}{Z_{eqR}^-}, \quad \frac{\Delta I_R^-}{\Delta I_R^+} = \frac{Z_{th}^-}{Z_{th}^+} \times \frac{Z_{eqR}^+}{Z_{eqR}^-}. \quad (3.8)$$

It is worth mentioning that the sequence currents through lines or relays are not necessarily equal even during SLG faults and depend on the equivalent impedances seen on the relay side.

As the IRES output current is generally limited to 1.5 per unit (p.u.) [67], the equivalent magnitude of its negative- and positive-sequence impedances are much higher than their corresponding grid-side impedances, leading to  $Z_{th} \approx Z_{Grid,side}$ . Since the angles of the positive-, negative-, and zero-sequence impedances on the grid side are nearly equal [68], the measured  $\delta_I^0$  and  $\delta_I^+$  by a relay can be expressed as

$$\delta_I^0 = \angle \Delta I_R^- - \angle \Delta I_R^0 = \angle Z_{eqR}^0 - \angle Z_{eqR}^- \quad (3.9)$$

$$\delta_I^+ = \angle \Delta I_R^+ - \angle \Delta I_R^0 = \angle Z_{eqR}^+ - \angle Z_{eqR}^- \quad (3.10)$$

where  $\angle(\cdot)$  represents the angle of its following variable. From (3.9) and (3.10), it is concluded that  $\delta_I^0$  and  $\delta_I^+$  depend on the angles of  $Z_{eqR}$ . According to the grid-side relay ( $R_{Grid}$ ), the PSM operates correctly because  $\delta_I^0$  and  $\delta_I^+$  are nearly zero, i.e., within the correct AG zones [54], owing to the roughly equal sequence-impedance angles for the traditional SG that may vary within small limits. On the other hand, according to the IRES-side relay ( $R_{IRES}$ ), the phase differences between the superimposed sequence currents depend on  $Z_{IRES,side}$ . Since the IRES negative-sequence impedance varies according to its control strategy and its positive-sequence impedance depends on the GCs' reactive power requirements [63], both  $\delta_I^0$  and  $\delta_I^+$  change unpredictably. From (3.9) and (3.10), it is noted that both  $\delta_I^0$  and  $\delta_I^+$  in SLG faults depend on  $\angle Z_{eqR}$ . However, they are invariant with the change in the fault ground resistance ( $R_g$ ).

## B. LLG Faults

BCG fault is studied as an example of LLG faults. The sequence circuit for a BCG fault at the fault location is shown in Figure 3.1(c). Using this figure, the negative-, zero-, and positive-sequence fault currents are obtained by

$$I_F^- = -\frac{V_x}{Z_{th}^- + R_{ph}} \quad (3.11)$$

$$I_F^0 = -\frac{V_x}{Z_{th}^0 + R_{ph} + 3R_g} \quad (3.12)$$

$$I_F^+ = -(I_F^- + I_F^0) = V_x \left( \frac{1}{Z_{th}^- + R_{ph}} + \frac{1}{Z_{th}^0 + R_{ph} + 3R_g} \right) \quad (3.13)$$

where  $V_x$  is the nodal voltage,  $R_g$  is the resistance between the fault and the ground, and  $R_{ph}$  represents the fault arc resistance. By substituting (3.11)–(3.13) into (3.5)–(3.7), the ratios between the sequence currents measured by the relay can be determined as follows:

$$\frac{\Delta I_R^-}{\Delta I_R^0} = \frac{Z_{th}^-}{Z_{th}^0} \times \frac{Z_{eqR}^0}{Z_{eqR}^-} \times \frac{Z_{th}^0 + R_{ph} + 3R_g}{Z_{th}^- + R_{ph}} \quad (3.14)$$

$$\frac{\Delta I_R^-}{\Delta I_R^+} = -\frac{Z_{th}^-}{Z_{th}^+} \times \frac{Z_{eqR}^+}{Z_{eqR}^-} \times \frac{Z_{th}^0 + R_{ph} + 3R_g}{Z_{th}^- + Z_{th}^0 + 2R_{ph} + 3R_g}. \quad (3.15)$$

Since the angles of  $Z_{th}^-$ ,  $Z_{th}^0$ , and  $Z_{th}^+$  are nearly equal,  $\delta_I^0$  and  $\delta_I^+$  are given by (3.16) and (3.17) when  $R_g$  is neglected

$$\delta_I^0 = \angle Z_{eqR}^0 - \angle Z_{eqR}^- \quad (3.16)$$

$$\delta_I^+ = \angle Z_{eqR}^+ - \angle Z_{eqR}^- - 180^\circ. \quad (3.17)$$

However, if  $R_g$  is large,  $\delta_I^0$  will be formulated as in (3.18), while  $\delta_I^+$  will not be affected.

$$\delta_I^0 = (\angle Z_{eqR}^0 - \angle Z_{eqR}^-) - \angle Z_{th}^0. \quad (3.18)$$

From (3.16)–(3.18), it is inferred that both  $\delta_I^0$  and  $\delta_I^+$  depend on  $\angle Z_{eqR}$ . Thus, when a relay is on the grid side,  $\delta_I^+$  lies in the correct zone independently of the fault resistance. However,  $\delta_I^0$  varies according to the value of  $R_g$  from  $0^\circ$  to  $-\angle Z_{th}^0$  ( $\approx -80^\circ$ ). These deductions reveal the failure of the current-angle-based PSMs for conventional grid protection with large  $R_g$ . Furthermore, both  $\delta_I^0$  and  $\delta_I^+$  measured by R<sub>IRES</sub> could be positioned in the wrong detection zones due to the unconventional IRES impedance angles.

### C. LL Faults

A BC fault is analyzed as a representative case for LL faults. From Figure 3.1(d), it is deduced that  $I_F^-$  and  $I_F^+$  are equal in magnitude but phase shifted by  $180^\circ$ , i.e.,

$$I_F^- = -I_F^+. \quad (3.19)$$

Using (3.5) and (3.7) and replacing  $I_F^-$  by  $-I_F^+$ , the ratio between  $\Delta I_R^-$  and  $\Delta I_R^+$  can be given by

$$\frac{\Delta I_R^-}{\Delta I_R^+} = -\frac{Z_{th}^-}{Z_{th}^+} \times \frac{Z_{eqR}^+}{Z_{eqR}^-}. \quad (3.20)$$

Since  $\angle Z_{th}^-$  and  $\angle Z_{th}^+$  are almost equal,  $\delta_I^+$  can be expressed as

$$\delta_I^+ = \angle Z_{eqR}^+ - \angle Z_{eqR}^- - 180^\circ. \quad (3.21)$$

As can be noted from (3.21),  $\delta_I^+$  depends on the angles of the relay-side equivalent impedances. The uncharacteristic nature of  $\angle Z_{eqR}$  at the IRES side makes the conventional current-angle-based PSM fail to determine the fault type.

### 3.2.2 Voltage-Angle-Based PSM

Short circuit analysis is carried out for SLG and LL(G) faults to pinpoint the operation principles and limitations of the voltage-angle-based PSM, which is proposed in [11] to overcome the shortcomings of the current-angle-based PSM. For that purpose, the angle between the negative- and zero-sequence voltages, i.e.,  $\delta_V^0 = \angle V^- - \angle V^0$ , and that between the negative- and positive-sequence voltages, i.e.,  $\delta_V^+ = \angle V^- - \angle V^+$ , are derived.

#### A. SLG Faults

The sequence voltages at the fault location for an AG fault are deduced from Figure 3.1(b) as follows:

$$V_F^- = -I_F Z_{th}^- \quad (3.22)$$

$$V_F^0 = -I_F Z_{th}^0 \quad (3.23)$$

$$V_F^+ = I_F (Z_{th}^- + Z_{th}^0 + 3R_g) \quad (3.24)$$

where  $V_F$  is the voltage at the fault location. In addition, bus sequence voltages can be determined from Figure 3.1(a) by

$$V_R^- = V_F^- + I_R^- \times Z_{RF}^- \quad (3.25)$$

$$V_R^0 = V_F^0 + I_R^0 \times Z_{RF}^0 \quad (3.26)$$

$$V_R^+ = V_F^+ + I_R^+ \times Z_{RF}^+ \quad (3.27)$$

where  $V_R$  is the bus voltage measured by the relay,  $Z_{RF}$  designates the line impedance between the relay and the fault location. Since the impedance of the line is relatively small in comparison with the IRES impedance, the following assumptions are acceptable

$$V_R^- \approx V_f^-, \quad V_R^0 \approx V_f^0, \quad V_R^+ \approx V_f^+. \quad (3.28)$$

The voltage sequence ratios are obtained from (3.22)–(3.24), and (3.28)

$$\frac{V_R^-}{V_R^0} = \frac{Z_{th}^-}{Z_{th}^0}, \quad \frac{V_R^-}{V_R^+} = -\frac{Z_{th}^-}{(Z_{th}^- + Z_{th}^0 + 3R_g)}. \quad (3.29)$$

Therefore,  $\delta_V^0$  and  $\delta_V^+$  are given by

$$\delta_V^0 = \angle V_R^- - \angle V_R^0 = \angle Z_{th}^- - \angle Z_{th}^0 \quad (3.30)$$

$$\delta_V^+ = \angle V_R^- - \angle V_R^+ = \angle Z_{th}^- - \angle (Z_{th}^- + Z_{th}^0 + 3R_g) - 180^\circ. \quad (3.31)$$

As mentioned in Subsection 3.2.1.A,  $Z_{th}$  is almost equal to  $Z_{Grid,side}$ , which has nearly equal sequence impedance angles. Therefore,  $\delta_V^0$  is ideally equal to zero for AG faults, while  $\delta_V^+$  varies from  $180^\circ$ , when  $R_g$  is small, to  $\left(\tan^{-1} \frac{X_{th}^-}{R_{th}^-} - 180^\circ\right)$ , when  $R_g$  is large. As a result,  $\delta_V^+$  changes from  $100^\circ$  to  $180^\circ$  based on  $R_g$  value. This range is compatible with the proposed SLG fault zones of the voltage-angle-based PSM. The correctness of the voltage-angle-based PSM in SLG faults is achieved because the relative voltage angles lean on the Thevenin impedance angles and do not rely on the impedance angles at the relay side. However, it is affected by the value of  $R_g$ .

## B. LLG Faults

The sequence voltages at the fault location for BCG faults can be determined from Figure 3.1(c) as follows:



$$V_F^- = V_x + I_F^- R_{ph} = V_x \left( \frac{Z_{th}^-}{Z_{th}^- + R_{ph}} \right) \quad (3.32)$$

$$V_F^0 = V_x + I_F^0 (R_{ph} + 3R_g) = V_x \left( \frac{Z_{th}^0}{Z_{th}^0 + R_{ph} + 3R_g} \right) \quad (3.33)$$

$$V_F^+ = V_x + I_F^+ R_{ph} = V_x \left( 1 + \frac{R_{ph}}{Z_{th}^- + R_{ph}} + \frac{R_{ph}}{Z_{th}^0 + R_{ph} + 3R_g} \right) \quad (3.34)$$

The sequence-voltage ratios are calculated by substituting the fault voltages in (3.28) into (3.32)–(3.34), as

$$\frac{V_R^-}{V_R^0} = \frac{Z_{th}^-}{Z_{th}^0} \times \frac{Z_{th}^0 + R_{ph} + 3R_g}{Z_{th}^- + R_{ph}} \quad (3.35)$$

$$\frac{V_R^-}{V_R^+} = \frac{Z_{th}^-}{Z_{th}^- + 2R_{ph} + \frac{R_{ph}(R_{ph} + Z_{th}^-)}{Z_{th}^0 + R_{ph} + 3R_g}}. \quad (3.36)$$

Since the sequence-voltage ratios vary according to  $R_{ph}$  and  $R_g$ ,  $\delta_V^0$  and  $\delta_V^+$  boundaries are determined by investigating extreme values for  $R_{ph}$  and  $R_g$ . If  $R_{ph}$  and  $R_g$  are small, then

$$\delta_V^0 = \angle Z_{th}^- - \angle Z_{th}^0 \quad (3.37)$$

$$\delta_V^+ \approx 0^\circ. \quad (3.38)$$

However, if  $R_g$  is large,  $\delta_V^0$  is affected, as follows:

$$\delta_V^0 \approx -\angle Z_{th}^0. \quad (3.39)$$

On the other hand, if  $R_{ph}$  is large,  $\delta_V^+$  will be given by

$$\delta_V^+ \approx \angle Z_{th}^-. \quad (3.40)$$

It can be inferred from (3.37)–(3.40) that the voltage-angle-based PSM is independent of the IRES equivalent impedance similar to the SLG case. Nonetheless, it is susceptible to  $R_g$

and  $R_{ph}$ .  $\delta_V^0$  is affected by  $R_g$ , while  $\delta_V^+$  is influenced by  $R_{ph}$ . Subsequently, in BCG faults, the value of  $\delta_V^0$  almost changes from  $0^\circ$  to  $-80^\circ$ , whereas  $\delta_V^+$  generally varies from  $0^\circ$  to  $80^\circ$ . It is worth noting that the voltage-angle-based PSM ignores the effect of  $R_{ph}$  in constructing  $\delta_V^+$  zones which can adversely affect the nicety in detecting faults with large  $R_{ph}$ .

### C. LL Faults

The positive- and negative-sequence voltages at the fault location are determined based on Figure 3.1(d) by

$$V_F^- = -I_F^- Z_{th}^- = I_F^+ Z_{th}^- \quad (3.41)$$

$$V_F^+ = I_F^+ (Z_{th}^- + R_{ph}). \quad (3.42)$$

Since  $V_F \approx V_R$ , the ratio between  $V_R^-$  and  $V_R^+$  is calculated by

$$\frac{V_R^-}{V_R^+} = \frac{Z_{th}^-}{Z_{th}^- + R_{ph}}. \quad (3.43)$$

Subsequently,  $\delta_V^+$  is determined by

$$\delta_V^+ = -\angle \left( 1 + \frac{R_{ph}}{Z_{th}^-} \right). \quad (3.44)$$

Hence, it can be illustrated that  $\delta_V^+$  depends on  $R_{ph}$ .  $\delta_V^+$  changes from  $0^\circ$ , when  $R_{ph}$  is negligible, to  $80^\circ$  for large  $R_{ph}$ . These results demonstrate that the voltage-angle-based PSM ignores the effect of  $R_{ph}$  in both LL and LLG faults; thus, it may suffer from erroneous operation at large  $R_{ph}$ .

## 3.3 Assessing Current and Voltage-Angle-Based PSMs

The 34.5-kV, 60-HZ system depicted in Figure 3.2, in which  $R_{ij}$  indicates a relay between buses  $i$  and  $j$ , and next to bus  $i$ , is tested using MATLAB/Simulink to illustrate the impacts

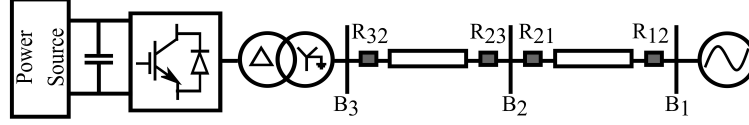


Figure 3.2. Sample test system.

of IIRESSs, fault resistance, and arc resistance on both current- and voltage-angle-based PSMs. The test system parameters are provided in Appendix A.

The relay is augmented with a fast Fourier transform (FFT) to determine the fundamental components of the measured voltage and current quantities. These quantities are then converted to their respective sequence components to calculate the required  $\delta_I$  and  $\delta_V$  for phase selection. The IIRESS is controlled in the synchronous reference ( $dq$ ) frame using the generic positive-sequence controller in [15], where the d-axis current ( $I_d$ ) is determined by a PI controller to regulate the dc-link voltage, while the q-axis current ( $I_q$ ) is set at zero to accommodate the North-American (NA) RCG requirements. The current controller is equipped with voltage feedforward compensation to reduce the effect of transient and starting conditions.

A bolted BCG fault at bus 2 is applied at  $t = 1$  s. The measured values for  $\delta_I^0$  and  $\delta_I^+$  for  $R_{12}$  and  $R_{32}$  are portrayed in Figure 3.3(a).  $\delta_I^0$  and  $\delta_I^+$  for  $R_{12}$  (i.e., grid-side relay) settle around  $0^\circ$  and  $180^\circ$ , respectively. These results comply with the phase selection analysis in Subsection 3.2.1.B and prove the correct operation of the current-angle-based PSM for  $R_{Grid}$ . On the other hand, the measured values for  $R_{32}$  (i.e., IIRESS-side relay) reveal the stumble of the current-angle-based PSM in determining the unhealthy phases. For  $R_{32}$ ,  $\delta_I^0$  indicates an ABG or a CG fault, while  $\delta_I^+$  is  $221.2^\circ$ , which lies outside the customary zones [64] or indicates a CG fault according to the zones in [69]. It is worth mentioning that the positive- and negative-sequence impedances calculated at  $R_{32}$  are found to be  $Z_{IIRESS,side}^+ = 100.1 \angle -28.4^\circ$  and  $Z_{IIRESS,side}^- = 1254 \angle -66.0^\circ$ . Unlike the equivalent impedance angles on the grid side, which are around  $80^\circ$ ,  $\angle Z_{IIRESS,side}^+$  and  $\angle Z_{IIRESS,side}^-$  are arbitrary and should be compensated. This discrepancy in angles clarifies

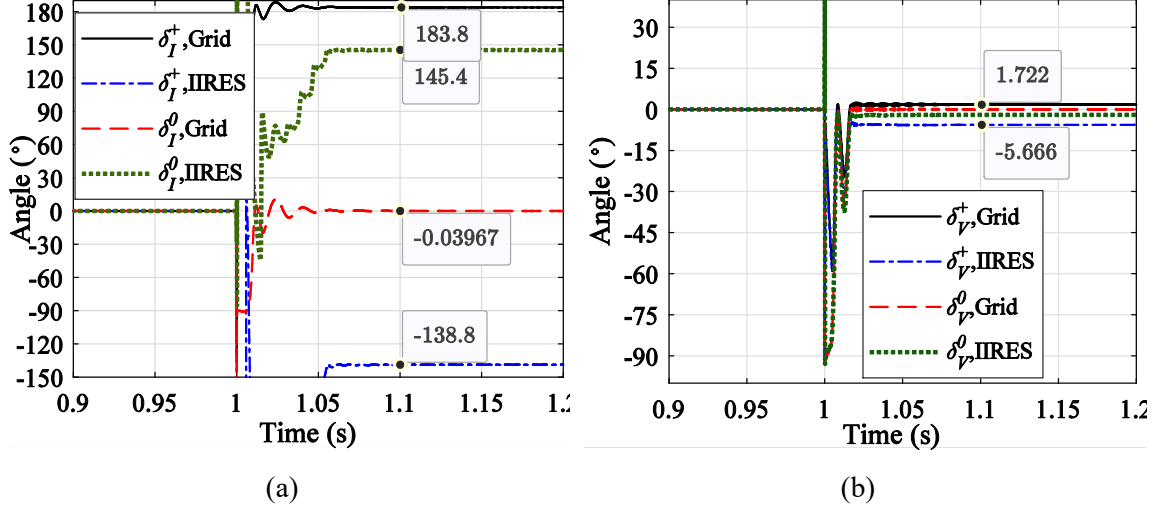


Figure 3.3. Angle measurements of existing PSMs during bolted BCG fault: (a) current PSM, (b) voltage PSM.

the root causes of the conventional current-angle-based PSM failure in the presence of IIRESS. Figure 3.3(b) clarifies the proper phase selection at the two relay locations because  $\delta_V^0$  and  $\delta_V^+$  measured by  $R_{12}$  and  $R_{32}$  are in the vicinity of  $0^\circ$ , as explained analytically.

Another test is performed to determine the effect of  $R_g$  on the current- and voltage-angle-based PSMs. A BCG fault with  $R_g = 50 \Omega$  causes adverse impacts on both PSMs, as shown in Figure 3.4. The measured  $\delta_I^0$  by  $R_{12}$  (grid-side relay), and  $\delta_V^0$  measured by  $R_{12}$  and  $R_{32}$  (IIRES-side relay) decrease to be about  $-75^\circ$ . It is worth noting that the current-angle-based PSM fails to determine the faulted phases even at the grid side according to the classical zones, raising a VOID flag. Whereas the angles measured by the IIRES-side relay are greatly altered according to the new IIRES impedance angles. However, the voltage-angle-based PSM is capable of determining the faulted phases correctly.

Lastly, the effect of  $R_{ph}$  is examined in case of a BCG fault with  $R_{ph} = 50 \Omega$ . The results in Figure 3.5(a) verify that the current-angle-based PSM in the grid side is insusceptible to arc resistance values as  $\delta_I^0$  and  $\delta_I^+$  are in the proximity of  $0^\circ$  and  $180^\circ$ , respectively. While  $\delta_I^0$  and  $\delta_I^+$  measured by  $R_{32}$  are affected by the changes in the IIRES controller reaction against different faults. According to the voltage-angle-based PSM

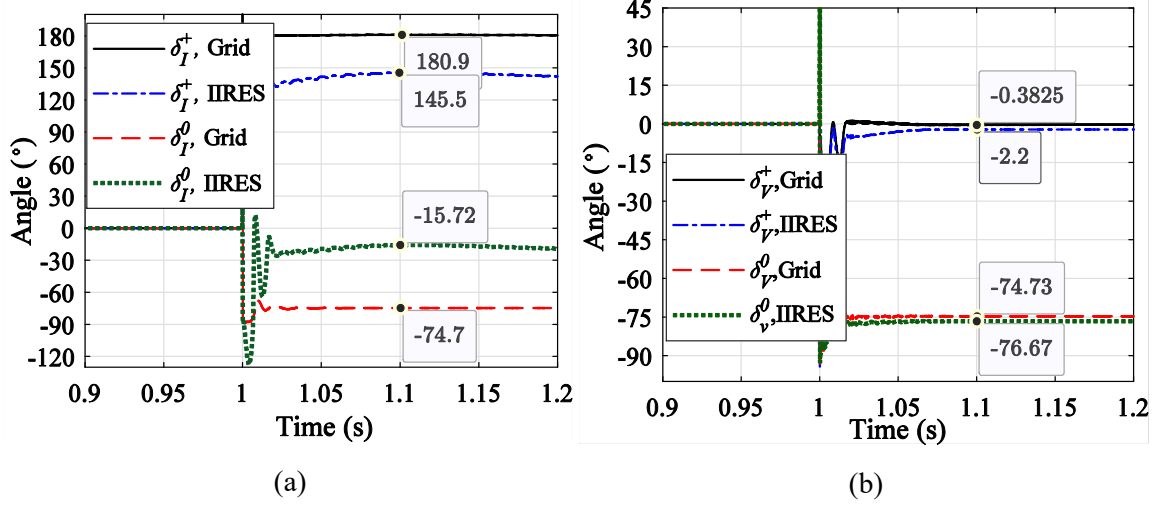


Figure 3.4. Angle measurements of existing PSMs during BCG fault with  $R_g = 50 \Omega$ : (a) current PSM, (b) voltage PSM.

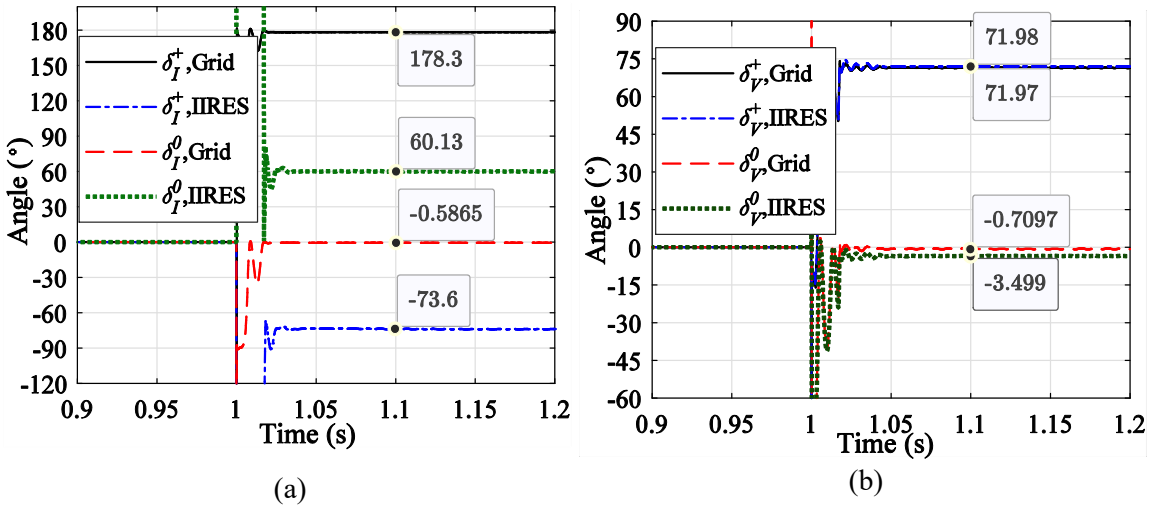


Figure 3.5. Angle measurements of existing PSMs during BCG fault with  $R_{ph} = 50 \Omega$ : (a) current PSM, (b) voltage PSM.

displayed in Figure 3.5(b),  $\delta_V^+$  measured by  $R_{12}$  and  $R_{32}$  is about  $72^\circ$ , which represents  $\angle Z_{th}^-$ , leading to erroneous phase selection based on the existing voltage-angle-based zones. These results clarify the imperfection of the current- and voltage-angle-based PSMs in determining the faulty phase(s) accurately. Thus, there is a need to devise a new PSM to overcome the traditional PSM shortcomings.

### 3.4 Adaptive Current-Angle-Based PSM

As analyzed in Section 3.2, the main problem associated with the current-angle-based PSM at the IRES-side relay is the variation of the IRES impedance based on the inverter's control scheme and RCG requirements. This creates challenges in tackling the problem with fixed zones. Nevertheless, if local relay measurements determine the IRES-side equivalent impedance, the traditional PSM zones can be modified to explore faulty phases correctly.

From Figure 3.1(b) or (c), the relations between the sequence currents and voltages at the fault location are formulated as

$$I_F^- = -\frac{V_F^-}{Z_{th}^-}, \quad I_f^0 = -\frac{V_F^0}{Z_{th}^0}, \quad I_f^+ = -\frac{\Delta V_F^+}{Z_{th}^+}. \quad (3.45)$$

It is to be noted that  $I_F^-$  and  $I_f^+$  in (3.45) are also applicable for LL faults based on Figure 3.1(d). By substituting (3.45) into (3.5)–(3.7) and using  $\Delta V_R^-$  and  $\Delta V_R^0$  instead of  $V_R^-$  and  $V_R^0$ , respectively, to compensate for the effect of pre-fault imbalance; the relations between the relay measured currents and voltages can be derived as

$$\Delta I_R^- = -\frac{\Delta V_R^-}{Z_{eqR}^-}, \quad \Delta I_R^0 = -\frac{\Delta V_R^0}{Z_{eqR}^0}, \quad \Delta I_R^+ = -\frac{\Delta V_R^+}{Z_{eqR}^+}. \quad (3.46)$$

Then, the ratios between the equivalent sequence impedances at the relay side are given by

$$\frac{Z_{eqR}^-}{Z_{eqR}^0} = \frac{\Delta V_R^- / \Delta V_R^0}{\Delta I_R^- / \Delta I_R^0}, \quad \frac{Z_{eqR}^-}{Z_{eqR}^+} = \frac{\Delta V_R^- / \Delta V_R^+}{\Delta I_R^- / \Delta I_R^+}. \quad (3.47)$$

Using (3.47), relative angles between the equivalent negative- and zero-sequence impedances (i.e.,  $\theta_{Comp}^0 = \angle Z_{eqR}^- - \angle Z_{eqR}^0$ ), and those between the negative- and positive-sequence impedances (i.e.,  $\theta_{Comp}^+ = \angle Z_{eqR}^- - \angle Z_{eqR}^+$ ) can be calculated by the relay. These angles are used to adapt PSM zones for  $\delta_I^0$  and  $\delta_I^+$  to enable precise phase selection regardless of the IRES controller because  $\theta_{Comp}^0$  and  $\theta_{Comp}^+$  compensate for any

discrepancies in IIRES sequence impedances. Subsequently, the proposed PSM solves the erroneous operation of the conventional current-angle-based PSM by only updating the relay software without the need for a hardware upgrade or communication. It is worth mentioning that the proposed PSM can operate in both distribution and transmission systems because (3.47) is not affected by the voltage level as it relies on voltage ratios.

It is noteworthy that the sequence currents measured by the relay are not equal; thus, the denominator of (3.47) should be regarded even during SLG faults. Further, (3.47) is based on the superimposed sequence currents and voltages, which makes it different from the voltage-angle-based PSM in [11] that employs only the measured sequence voltages. In SLG and LLG faults, the updated zones are formulated by subtracting  $\theta_{Comp}^0$  and  $\theta_{Comp}^+$  from the traditionally measured  $\delta_I^0$  and  $\delta_I^+$  with added margins to make the traditional current-angle-based PSM operate successfully at different faults. Since the zero-sequence current is nil in LL faults, only  $\delta_I^+$  zones are updated using  $\theta_{Comp}^+$ . The formation of the proposed adaptive zones is explained for BC(G) and AG faults. Then, this formation can be generalized for other LLG and SLG faults by shifting their respective zones with either  $\pm 120^\circ$ .

### 3.4.1 Adaptive Zones of $\delta_I^0$

The adaptive zones of  $\delta_I^0$  are formulated by subtracting  $\theta_{Comp}^0$  from the traditional zone-centric angle, i.e., the angle at zero fault resistances, e.g., zero for BCG faults. Besides, an extra upper margin ( $\mathcal{M}_u^0$ ) and lower margin ( $\mathcal{M}_l^0$ ) are considered to extend the width of  $\delta_I^0$  zone to secure proper operation of phase selection during measurement uncertainties and assumptions. The conventional  $\delta_I^0$  value in LLG faults is affected by ground fault resistances, as illustrated in Subsection 3.2.1. Thus, for BCG faults, the conventional  $\delta_I^0$  zone should be extended from  $0^\circ$  to  $-80^\circ$  to secure the correct operation of  $\delta_I^0$  for different fault resistances. As a result, the range of the adaptive  $\delta_I^0$  zone should be from  $0^\circ - \theta_{Comp}^0$  to  $-80^\circ - \theta_{Comp}^0$ . This makes the zone width  $80^\circ$ . However, it is suggested to extend the width of  $\delta_I^0$  zone to  $120^\circ$  in order to enhance the detection speed [69]. Therefore,  $\mu_u^0$  and  $\mu_l^0$  are added to extend  $\delta_I^0$ -zone width; where  $\mu_u^0 + \mu_l^0 = 40^\circ$ .

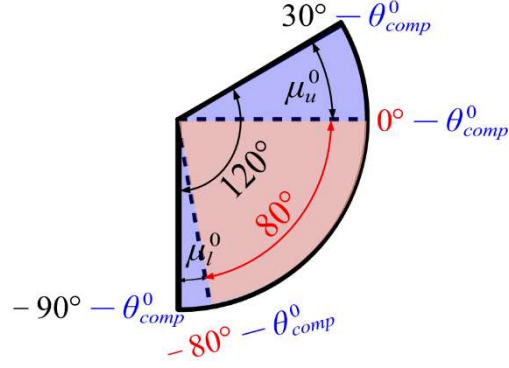


Figure 3.6. Adaptive  $\delta_I^0$  zone for BCG faults.

Since a lower extension of  $80^\circ$  is added to the center of the conventional zone, i.e., zero for BCG faults, a  $10^\circ$  margin is found to be reasonable for  $\mu_l^0$ , and thus,  $\mu_u^0$  is selected to be  $30^\circ$ , as shown in Figure 3.6. Thus, the adaptive BCG zone is between  $-\theta_{Comp}^0 + 30^\circ$  and  $-\theta_{Comp}^0 - 90^\circ$ .

On the other hand, for AG faults, the fault resistance does not affect  $\delta_I^0$ , as clarified in Subsection 3.2.1. As a result, the adaptive AG zone can start from  $-\theta_{Comp}^0 + \mathcal{M}_u^0$  to  $-\theta_{Comp}^0 - \mathcal{M}_l^0$ . Nonetheless, BCG and AG faults typically share the same zone limits. Thus, the adaptive AG zone is also located between  $-\theta_{Comp}^0 + 30^\circ$  and  $-\theta_{Comp}^0 - 90^\circ$ . The proposed adaptive zones for  $\delta_I^0$  are shown in Figure 3.7(a), where BG and CG zones are designed by shifting the AG zone by  $-120^\circ$  and  $120^\circ$ , respectively. Similarly, ABG and CAG zones are shifted from the BCG zone by  $120^\circ$  and  $-120^\circ$ , respectively.

### 3.4.2 Adaptive Zones of $\delta_I^+$

For BC(G) faults, the traditional BC(G) zone-centric angle (i.e.,  $180^\circ$ ) is subtracted by  $\theta_{Comp}^+$ . Then, adequate margins are considered, i.e.,  $\mathcal{M}_u^+$  and  $\mathcal{M}_l^+$ , to increase the PSM detection speed and secure precise faulty phase(s) detections during measurement uncertainties. such that each zone sector is  $60^\circ$  wide. Thus, the adaptive BC(G) fault zone has an upper limit of  $(-\theta_{Comp}^+ + 180^\circ) + \mathcal{M}_u^+$  and a lower limit of  $(-\theta_{Comp}^+ + 180^\circ) - \mathcal{M}_l^+$ . Since  $\delta_I^+$  in LL(G) faults are not affected by fault resistances,  $\mathcal{M}_u^+$  and  $\mathcal{M}_l^+$  are selected equal to half  $\delta_I^+$ -zone width, i.e.,  $60/2 = 30^\circ$ . Subsequently, the modified BCG zone is limited by  $-\theta_{Comp}^+ + 150^\circ$  and  $-\theta_{Comp}^+ + 210^\circ$ .



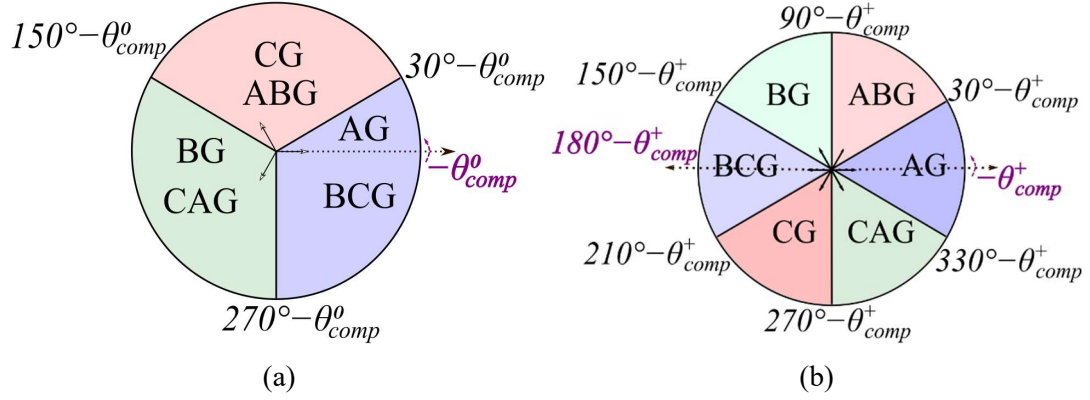


Figure 3.7. Fault-type adaptive zones: (a)  $\delta_I^0$ , (b)  $\delta_I^+$ .

For AG faults,  $-\theta_{Comp}^+$  represents the zone-centric angle (i.e., the ideal position) of the  $\delta_I^+$ 's adaptive zone. Because  $\delta_I^+$  in SLG faults are not affected by fault resistances, the adaptive AG upper- and lower-zone limits are selected as  $-\theta_{Comp}^0 + 30^\circ$  and  $-\theta_{Comp}^0 - 30^\circ$ , respectively. The proposed  $\delta_I^+$ 's adaptive zones are depicted in Figure 3.7(b), in which ABG and CBG zones are shifted by  $120^\circ$  and  $-120^\circ$ , respectively, from the BCG zone. On the other hand, BG and CG zones are shifted with respect to the AG zone by  $-120^\circ$  and  $120^\circ$ , respectively.

### 3.5 Performance Evaluation

Extensive simulations are performed to substantiate the accuracy of the proposed adaptive current-angle-based PSM. First, the system depicted in Figure 3.2 is tested in MATLAB/SIMULINK environment to validate the precision of the proposed PSM against different fault resistances. Moreover, PSCAD/EMTDC simulations are used to validate the method reliability at different fault locations, grid topologies, and IRES types using the North-American CIGRE benchmark system [70]. As represented in Figure 3.8, the CIGRE benchmark system contains a 2-MW IRES connected to bus 8 through a 3-MVA, 4.16/12.47 kV, dYg transformer with  $x = 0.1$  p.u, 2.5-MW type-I wind turbine linked to bus 6, and an 8-MW SG at bus 4, which operates in an islanded mode. The type-I wind turbine is fixed speed and equipped with an induction generator (IG).

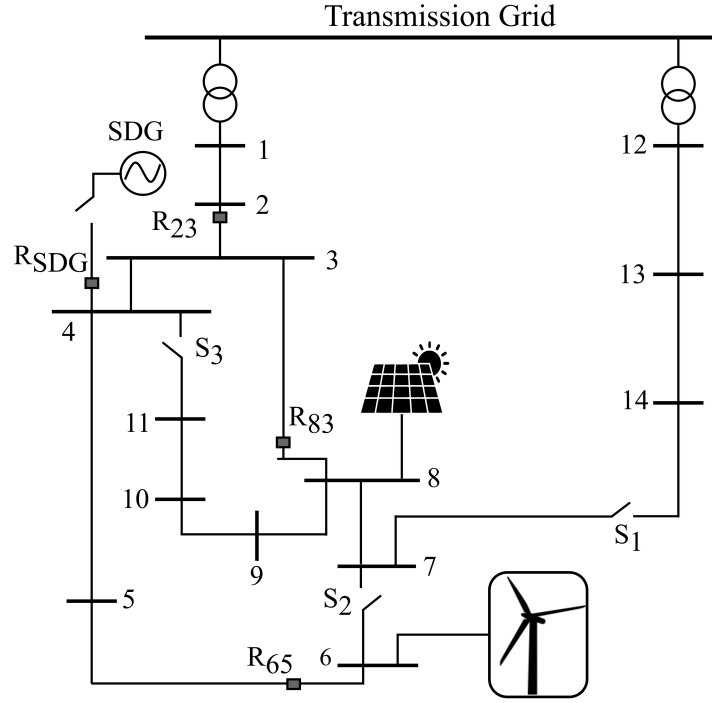


Figure 3.8. CIGRE MV benchmark system.

### 3.5.1 Effect of Fault Resistances

Table 3.1 reports the values of  $\delta_I^0$ ,  $\delta_I^+$ ,  $\theta_{comp}^0$ ,  $\theta_{comp}^+$ , and the deviations in  $\delta_I^0$  and  $\delta_I^+$  from their ideal positions within their adaptive zones as measured by  $R_{IIRES}$  and  $R_{Grid}$ . According to  $R_{32}$  (i.e.,  $R_{IIRES}$ ),  $\delta_I^0$  and  $\delta_I^+$  have exotic angles, which result in erroneous phase selection for the conventional PSM.  $\theta_{comp}^0$  precisely estimates the difference between  $\angle Z_{th}^-$  and  $\angle Z_{th}^0$ , while  $\theta_{comp}^+$  correctly estimates the difference between  $\angle Z_{th}^-$  and  $\angle Z_{th}^+$ ; thus, the zones are adjusted to identify the fault type correctly. In light of the results for SLG faults, the adaptive zones precisely make all measured  $\delta_I^0$  and  $\delta_I^+$  settle in the vicinity of their ideal positions with slight variations from  $-3.7^\circ$  to  $-3.1^\circ$  and  $-2.9^\circ$  to  $2.6^\circ$ , respectively. These results verify the harmony of the adaptive zones with the mathematical exegesis and the robustness of SLG phase selection against different fault resistances. Considering LLG fault results,  $\theta_{comp}^0$  and  $\theta_{comp}^+$  rotate the zones to place  $\delta_I^0$  and  $\delta_I^+$  correctly in their faulted zones. Table 3.1 also demonstrates that  $R_{ph}$  does not affect the correct placement of  $\delta_I^0$  and  $\delta_I^+$  in their respective adaptive zones. However, the loci

Table 3.1. Sample system measurements at different fault resistances

Fault Type	$R_{ph}$	$R_g$	IIRES Side ( $R_{32}$ )						Grid Side ( $R_{12}$ )					
			$\delta_I^0$	$\theta_{comp}^0$	Shift from ideal position	$\delta_I^+$	$\theta_{comp}^+$	Shift from ideal position	$\delta_I^0$	$\theta_{comp}^0$	Shift from ideal position	$\delta_I^+$	$\theta_{comp}^+$	Shift from ideal position
AG	-	0	43.6	-47.3	-3.7	-46.8	49.3	2.6	-1.3	0.02	-1.3	1.8	0.02	1.8
		50	62.2	-65.4	-3.1	127.0	-129.7	-2.7	-0.9	0.07	-0.9	-1.9	0.07	-1.8
BG	-	0	-76.3	-47.5	-3.7	73.4	49.2	2.6	-121.3	-0.07	-1.4	121.8	-0.02	1.8
		50	-57.3	-65.9	-3.2	247.1	-130.0	-2.9	-120.9	-0.2	-1.1	118.1	-0.2	-2.1
CG	-	0	163.9	-47.6	-3.7	-166.5	49.05	2.6	118.7	0.05	-1.3	-118.2	-0.01	1.8
		50	182.4	-65.5	-3.1	7.0	-129.7	-2.7	119.1	0.1	-0.8	-121.9	0.1	-1.8
ABG	0	0	265.2	-147.2	-2.0	103.1	-37.3	5.8	120	-0.004	-0.004	64.1	-0.01	4.1
		50	104.1	-61.0	-76.9	25.3	37.1	2.4	45.3	-0.03	-74.7	60.9	0.01	0.9
	25	0	180.9	-63.4	-2.5	177.5	-119.9	-2.4	119.7	-0.02	-0.28	58.5	-0.02	-1.5
		50	168.6	-63.8	-15.2	174.5	-118.9	-4.4	107.0	-0.008	-13.0	56.5	-0.02	-3.5
	50	0	182.5	-65.4	-2.9	190.2	-132.8	-2.6	119.4	-0.09	-0.7	58.3	-0.1	-1.8
		50	176.8	-65.5	-8.7	188.8	-132.8	-4.0	113.6	-0.06	-6.5	56.9	-0.1	-3.1
CG	0	0	145.4	-147.4	-2.0	223.3	-37.5	5.8	-0.04	0.03	-0.005	184.1	0.01	4.1
		50	-15.7	-61.2	-76.9	145.5	36.9	2.4	-74.7	-0.01	-74.7	180.9	-0.01	0.9
	25	0	61.1	-63.6	-2.5	-62.2	-120.2	-2.4	-0.2	-0.04	-0.24	178.5	-0.04	-1.5
		50	48.7	-63.9	-15.2	-65.3	-119.0	-4.3	-12.9	-0.03	-12.9	176.5	-0.02	-3.5
	50	0	62.7	-65.5	-2.8	-49.9	-132.7	-2.6	-0.6	-0.09	-0.6	178.3	-0.1	-1.8
		50	56.9	-65.6	-8.7	-51.5	-132.5	-3.9	-6.4	-0.07	-6.5	176.9	-0.1	-3.2
CAG	0	0	25.2	-147.2	-2.0	-16.9	-37.3	5.8	-120.0	-0.02	-0.02	-55.9	0.01	4.1
		50	-135.9	-61.0	-76.9	-94.7	37.1	2.4	-194.7	0.02	-74.7	-59.1	0.01	0.9
	25	0	-59.2	-63.2	-2.4	57.5	-119.9	-2.4	-120.3	0.06	-0.2	-61.5	0.06	-1.4
		50	-71.5	-63.7	-15.2	54.6	-118.0	-3.4	-133.0	0.0	-13	-63.5	0.0	-3.5
	50	0	-57.8	-64.9	-2.7	69.9	-132.5	-2.5	-120.6	0.2	-0.4	-61.7	0.2	-1.6
		50	-63.5	-65.1	-8.6	68.7	-132.5	-3.8	-126.4	0.1	-6.3	-63.1	0.1	-2.9

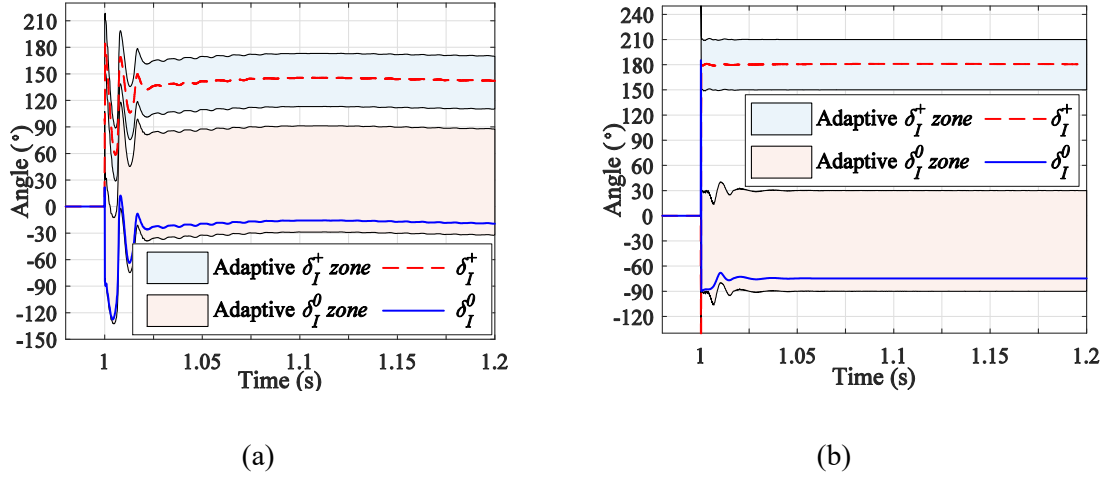


Figure 3.9. Angle measurements using the proposed PSM for a BCG fault with  $R_g = 50 \Omega$ : (a) IIRES-side, (b) grid-side.

of  $\delta_I^0$  in its zones is affected when  $R_g = 50 \Omega$ . In that case,  $\delta_I^0$  is shifted from its ideal position by  $-77^\circ$ . This verifies the importance of shifting the lower limit of the LLG fault zones by  $-80^\circ$  to cope with large values of  $R_g$  as demonstrated in Section 3.4. Besides,  $\delta_I^+$  adaptive zones verify their robustness against different fault types as all the measured  $\delta_I^+$ 's are placed in the vicinity of the correct zones' ideal position. For instance, in a bolted BCG fault, the measured value of  $\delta_I^0$  is  $145.5^\circ$  demonstrates the failure of the conventional PSM because it incorrectly determines a CG or ABG fault. However,  $\theta_{comp}^0$  precisely shifts the conventional zone by  $-(-147.4^\circ)$ , which accurately return  $\delta_I^0$  to be placed in its exemplary position within the adaptive BCG fault zone. Besides,  $\delta_I^+$  equals  $223.3^\circ$ , i.e., closer to the limit of the non-adaptive CG zone according to the traditional PSM. On the contrary, by shifting the traditional  $\delta_I^+$  zones by  $-\theta_{comp}^+$ ,  $\delta_I^+$  is suited in BCG adaptive zone with only a  $5.8^\circ$  shift from its ideal position.

Figures 3.9(a) and 3.10(a) represent the highlighted case studies in Table 3.1 for BCG faults with  $R_g = 50 \Omega$  and  $R_{ph} = 50 \Omega$ , respectively. These figures prove that  $\theta_{comp}^0$  mitigates the impact of the IIRES fault currents and make  $\delta_I^0$  at the IIRES-side relay match that of the grid-side relay. Further,  $\theta_{comp}^+$  accurately modifies  $\delta_I^+$ 's fault-type zone such that  $\delta_I^+$  is placed near the zone ideal position. These results also demonstrate the success of the proposed PSM in handling the angle deviations displayed in Figures 3.4 and 3.5.

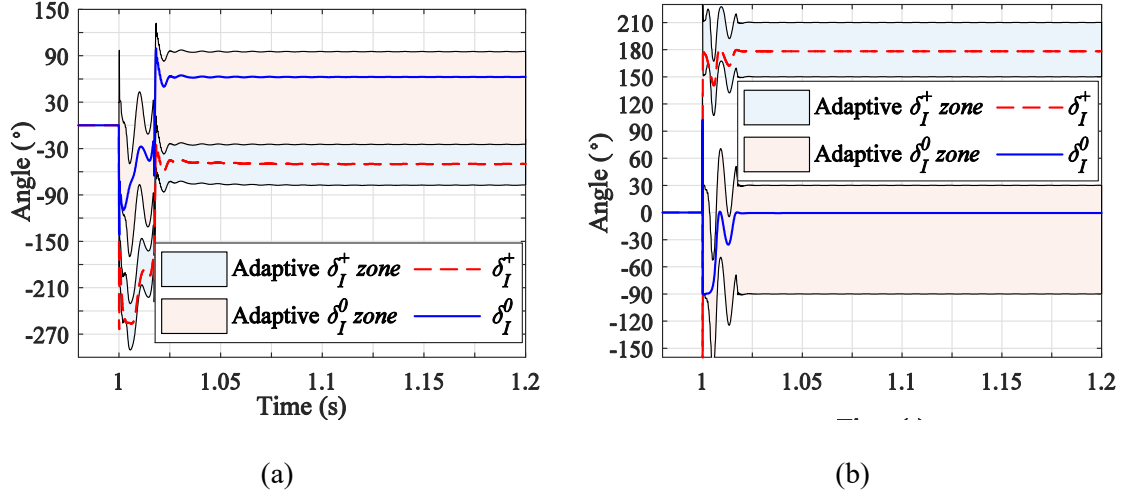


Figure 3.10. Angle measurements using the proposed PSM for BCG fault with  $R_{ph} = 50 \Omega$ : (a) IIRES side, (b) grid side.

The proposed PSM only adds the calculation of  $\theta_{comp}^0$  and  $\theta_{comp}^+$  to the computational burden of the conventional current-angle-based PSM. The execution time of the conventional PSM is compared to that of the proposed PSM using MATLAB. It is found that the proposed PSM increases the computational burden by 0.72% using a desktop computer with the following specifications: Intel Core i7-6700 CPU @ 3.4 GHz, 64-bit, and 16-GB RAM. Therefore, the proposed PSM is computationally efficient.

On the grid side, the measurements of  $R_{12}$  (i.e.,  $R_{Grid}$ ) demonstrate the correct estimation for  $\theta_{comp}^0$  and  $\theta_{comp}^+$  because they are around zeros for different fault resistances. This happens because the angles of the equivalent grid-side sequence impedances are equal. Thus, the adaptive zones share the same zone-centric angle as the conventional zones but with larger margins to accurately determine the fault type at different fault resistances. For instance, in a BCG fault with  $R_g = 50 \Omega$ , as shown in Figure 3.9(b),  $\delta_I^0$  equals  $-74.7^\circ$ , i.e., equivalent to  $-\angle Z_{th}^-$ , whereas  $\delta_I^+$  is equal to  $180.9^\circ$ , which is correctly placed at the BCG ideal position. In such a case,  $\theta_{comp}^0$  and  $\theta_{comp}^+$  are  $-0.01^\circ$ , leading to accurate identification of a BCG fault. Figure 3.10(b) emphasizes the applicability of the proposed PSM on the grid side, where the compensation angles do not change the fault type zones. Thus, the proposed PSM does not weaken the operation of the conventional PSM on the grid side.

Table 3.2. Sample system measurements for LL faults

Fault Type	$R_{ph}$	IIRES Side ( $R_{32}$ )			Grid Side ( $R_{12}$ )		
		$\delta_I^+$	$\theta_{comp}^+$	Shift from ideal position	$\delta_I^+$	$\theta_{comp}^+$	Shift from ideal position
AB	0	24.1	40.9	5.3	63.4	0.0	3.4
	25	173.4	-116.0	-2.6	58.2	-0.02	-1.8
	50	188.0	-130.8	-2.8	58.1	-0.05	-2.0
BC	0	144.3	40.7	5.0	183.4	0.0	3.4
	25	-66.5	-116.1	-2.6	178.2	-0.02	-1.8
	50	-52.4	-130.4	-2.8	178.1	-0.03	-1.9
CA	0	-95.9	40.8	4.9	-56.6	0.006	3.4
	25	53.4	-116.0	-2.6	-61.8	0.04	-1.8
	50	67.9	-130.6	-2.7	-61.9	0.08	-1.8

It is noteworthy that  $\theta_{comp}^0$  and  $\theta_{comp}^+$  calculated at the grid-side relay are approximately zero, i.e., between  $\pm 0.25^\circ$ , as shown in Table 3.1. On the other hand,  $\theta_{comp}^0$  and  $\theta_{comp}^+$  determined at the IIRES-side relay are away from zero. Therefore,  $\theta_{comp}^0$  and  $\theta_{comp}^+$  can be used as an index for the fault current direction. The absolute values of  $\theta_{comp}^0$  and  $\theta_{comp}^+$  can be compared to a threshold (e.g.,  $5^\circ$ ). If both  $|\theta_{comp}^0|$  and  $|\theta_{comp}^+|$  are below  $5^\circ$ ; then the fault current is from the grid. Otherwise, the fault current is supplied from the IIRES. Therefore, the proposed PSM can contribute to identifying fault current directions in the presence of IIRESSs. For instance, during a bolted BG ground fault,  $\theta_{comp}^0$  and  $\theta_{comp}^+$  measured by the grid-side relay are  $-0.07^\circ$  and  $-0.02^\circ$ , respectively, which confirms that the fault is supplied from the grid. In contrast,  $\theta_{comp}^0$  and  $\theta_{comp}^+$  measured by the IIRES-side relay are  $-65.9^\circ$  and  $-130.0^\circ$ , respectively, which assures that the fault current is from the IIRES.

Furthermore, Table 3.2 verifies the applicability of the proposed PSM for LL faults at both IIRES- and grid-side relays. On the IIRES side, the measured  $\delta_I^+$  demonstrates erroneous operation of the conventional current-angle-based PSM. However, by adjusting the conventional PSM zones with  $\theta_{comp}^+$ ,  $\delta_I^+$  is located correctly near the center of the fault-type zone. For instance, the measured  $\delta_I^+$  is  $-66.5^\circ$  for a BC fault with  $R_{ph} = 25 \Omega$ , which

Table 3.3. IIRES-side relay ( $R_{83}$ ) measurements in the grid-connected CIGRE benchmark system

Fault Type	Grid Topology	Grid Code	Fault at bus 3						Fault at bus 5					
			$\delta_I^0$	$\theta_{comp}^0$	Shift from ideal position	$\delta_I^+$	$\theta_{comp}^+$	Shift from ideal position	$\delta_I^0$	$\theta_{comp}^0$	Shift from ideal position	$\delta_I^+$	$\theta_{comp}^+$	Shift from ideal position
AG	Radial	NA	57.1	-64.7	-7.6	-16.4	19.1	2.7	56.7	-65.0	-8.3	-13.7	17.3	3.7
		Spanish	56.9	-64.5	-7.5	44.8	-44.0	0.8	56.5	-64.8	-8.3	50.8	-49.7	1.1
		German	56.9	-64.4	-7.5	37.7	-36.4	1.3	56.5	-64.7	-8.2	43.7	-42.0	1.7
	Mesh	NA	6.0	-13.6	-7.6	-5.1	7.7	2.5	173.6	-182.6	-9.0	6.6	-3.6	2.9
		Spanish	6.1	-13.6	-7.6	-1.0	2.2	1.1	173.6	-182.6	-9.0	2.4	-1.1	1.3
		German	6.0	-13.6	-7.6	-1.9	3.4	1.5	173.6	-182.6	-9.0	4.1	-2.4	1.7
BCG	Radial	NA	60.5	-63.3	-2.8	162.6	20.7	3.3	61.4	-63.0	-1.6	171.1	13.4	4.6
		Spanish	60.7	-63.6	-2.8	219.9	-38.4	1.5	61.8	-63.5	-1.7	231.8	-49.5	2.3
		German	60.7	-64.4	-3.7	227.7	-46.4	1.3	61.8	-63.5	-1.7	239.6	-58.0	1.6
	Mesh	NA	11.7	-13.7	-1.9	179.3	4.5	3.8	-181.2	179.6	-1.6	-175.6	0.5	4.9
		Spanish	11.7	-13.7	-1.9	182.4	0.4	2.7	-181.2	179.5	-1.7	179.8	3.7	3.5
		German	11.7	-13.7	-2.0	183.1	0.8	3.9	-181.1	179.5	-1.6	177.8	5.2	3.0

incorrectly indicates a CA fault for conventional PSM. However, shifting the zones by  $116.1^\circ$  (i.e.,  $-\theta_{comp}^+$ ) leads to identifying a BC fault precisely. On the other hand,  $\theta_{comp}^+$  measured at the grid-side relay is negligible because the sequence-impedance angles at the grid side are nearly equal. As a result,  $\delta_I^+$  is kept in its correct fault type zone, which confirms the applicability of the proposed PSM for grid-side relays.

### 3.5.2 Grid-Connected Mode of CIGRE Benchmark System

The grid-connected CIGRE benchmark system is used to validate the robustness of the proposed method at different microgrid topologies, fault locations, and IIRES types. Table 3.3 shows the angles measured by  $R_{83}$  (i.e.,  $R_{IIRES}$ ) for bolted faults for both mesh and radial grids at different RCG requirements by (i) the North-American (NA)-GCs, and (ii) the Spanish and German GCs, as representative cases for the European GCs [26]. The results clarify the ability of the proposed method to place both  $\delta_I^0$  and  $\delta_I^+$  at their respective adaptive zones with large margin clearance, which reflects the robustness of the proposed

method. For instance, during a bolted AG fault at bus 3, the proposed adaptive zoning makes both  $\delta_I^0$  and  $\delta_I^+$  settle with maximum angle shifts of  $-7.6^\circ$  and  $2.7^\circ$  from their ideal positions, respectively. It is worth noting that the deviation from the ideal position of  $\delta_I^0$  is larger than  $\delta_I^+$  because the line impedance angle for the negative- and zero-sequence equals  $68.2^\circ$  and  $79^\circ$ , respectively. The results also demonstrate that RCG requirements have a minor effect on  $\delta_I^0$  for both radial and meshed grid topologies. However, RCG requirements have a noticeable effect on  $\delta_I^+$  because  $\angle Z_{IRES,side}^+$  is varying according to the RCG requirements. Thus,  $\theta_{comp}^+$  should compensate for the variation in  $\angle Z_{IRES,side}^+$  to cope up with  $\delta_I^+$  changes. For instance,  $\theta_{comp}^+$  measured in the radial topology during a bolted AG faults changes to be  $19.1^\circ$ ,  $-44.8^\circ$ , and  $37.7^\circ$  for the NA-, Spanish-, and German-GCs, respectively, to accurately place  $\delta_I^+$  in its adaptive zone.

On the other hand, changing the grid topology varies the angles of the equivalent sequence impedances. Thus,  $\theta_{comp}^0$  and  $\theta_{comp}^+$  are altered to compensate for these variations. For example, the values of  $\theta_{comp}^0$  in the NA-GC changes from  $-64.7^\circ$  to  $-13.6^\circ$ , while  $\theta_{comp}^+$  varies from  $19.1^\circ$  to  $7.7^\circ$  for radial and mesh grids, respectively. The reason behind the changes in the compensation angles is the effect of adding impedance in parallel with the IRES equivalent impedance. Thus, the resultant impedance is closer to the grid impedance, in which all sequence-impedance angles are nearly the same. Changing the fault location from bus 3 to bus 5 also affects the relative impedance angles as reported in Table 3.3. Nevertheless, the compensation angles correctly adapt the zones to maintain the measured values for both  $\delta_I^0$  and  $\delta_I^+$  in their adaptive zones.

Table 3.4 displays the angles measured by  $R_{65}$  on the IG side (i.e., the type-I wind turbine) for bolted unbalanced faults when the IRES operates at a unity power factor. The results support the compatibility of the proposed method for the IG side, where the tested fault types are determined fussily with large tolerance from their zone limits. Table 3.4 demonstrates that changing the grid topology or the fault location affect  $\delta_I^0$  and  $\delta_I^+$  due to their impact on the relay-side equivalent impedances. To cope with these variations,  $\theta_{comp}^0$  and  $\theta_{comp}^+$  precisely update the traditional zones leading to settling the measured values for both  $\delta_I^0$  and  $\delta_I^+$  in their respective adaptive zones. For instance, Figure 3.11 displays the



Table 3.4. IG-side relay (R<sub>65</sub>) measurement in grid-connected CIGRE benchmark system

Fault Type	Grid Topology	Fault at bus 3					
		$\delta_I^0$	$\theta_{comp}^0$	Shift from ideal position	$\delta_I^+$	$\theta_{comp}^+$	Shift from ideal position
AG	Radial	-6.4	-4.2	-10.6	-154.9	159.1	4.2
	Mesh	-0.8	-10.6	-11.4	-26.3	29.4	3.1
BG	Radial	-124.8	-5.7	-10.5	-31.8	155.9	4.0
	Mesh	-119.4	-11.7	-11.2	94.3	28.7	3.0
CG	Radial	115.8	-5.9	-10.1	97.2	147.3	4.5
	Mesh	121.1	-12.1	-11.0	-148.6	31.9	3.3
ABG	Radial	116.1	-3.9	-7.8	221.3	-157.9	3.4
	Mesh	123.8	-11.2	-7.4	53.0	10.4	3.4
BCG	Radial	2.8	-8.4	-5.5	-7.1	-168.7	4.2
	Mesh	8.5	-13.9	-5.4	173.3	10.9	4.2
CAG	Radial	-122.5	-3.6	-6.2	109.7	-165.5	4.2
	Mesh	-116.	-9.4	-6.1	-70.2	14.3	4.0
		Fault at bus 5					
AG	Radial	-7.144	-4.0	-11.179	-156.3	160.5	4.2
	Mesh	0.556	-12.1	-11.532	-4.6	7.857	3.2
BG	Radial	-125.8	-5.6	-11.4	-33.2	157.1	3.9
	Mesh	-119.0	-12.5	-11.6	115.4	7.64	3.1
CG	Radial	115.5	-6.3	-10.8	96.7	147.7	4.4
	Mesh	120.9	-12.2	-11.2	-124.9	8.32	3.3
ABG	Radial	117.2	-4.092	-6.9	-138.7	-157.2	4.1
	Mesh	126.9	-12.8	-5.9	60.7	3.53	4.3
BCG	Radial	3.1	-8.3	-5.2	-6.9	-168.2	4.8
	Mesh	8.6	-12.8	-4.2	181.3	3.72	5.0
CAG	Radial	-121.9	-3.7	-5.6	108.9	-164.2	4.8
	Mesh	-113.7	-11.2	-4.9	-60.0	4.7	4.8

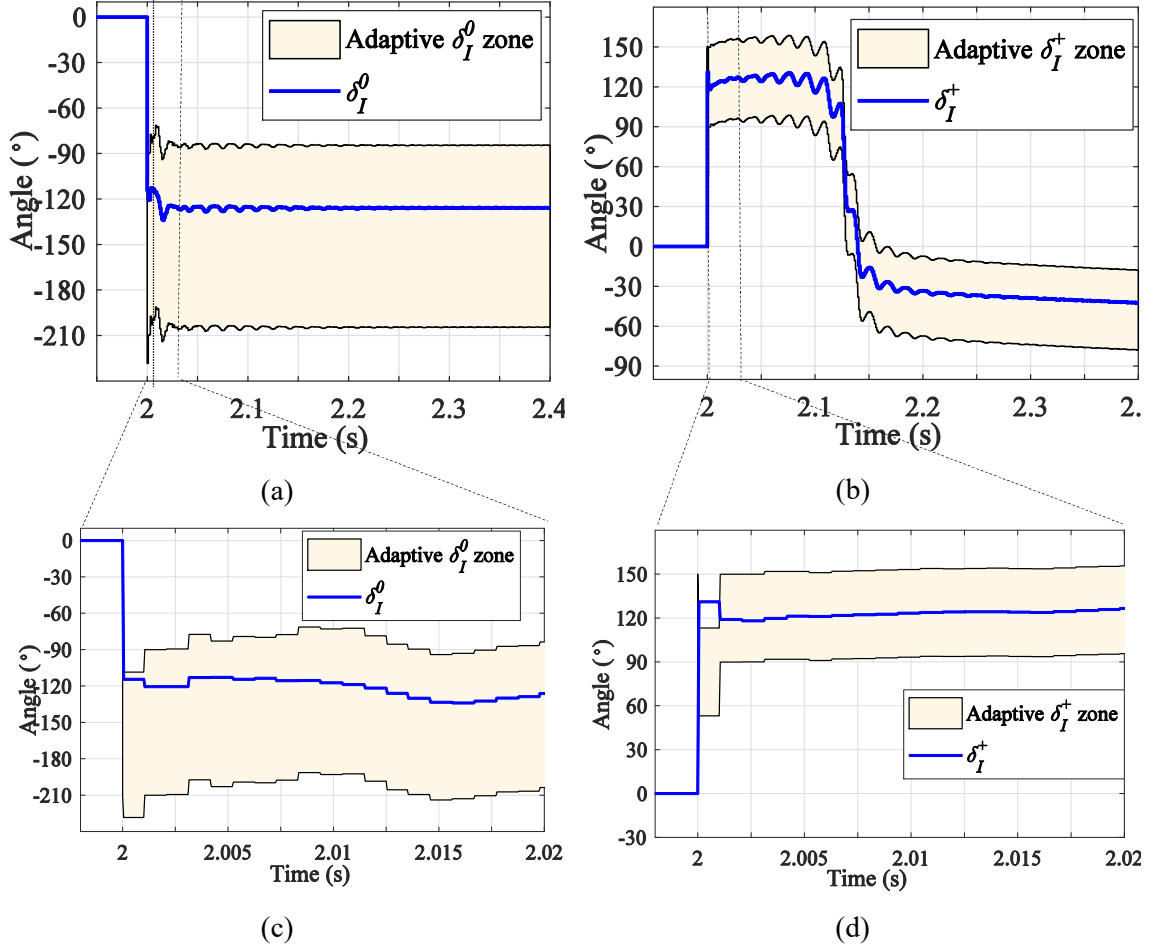


Figure 3.11. PSM measurement by  $R_{65}$  for BG fault at bus 5: (a)  $\delta_I^0$ , (b)  $\delta_I^+$ , (c)  $\delta_I^0$  operating time, and (d)  $\delta_I^+$  operating time.

measured angles during a BG bolted fault at bus 5 in the radial grid as a representative case from Table 3.4. Figure 3.11(a) demonstrates that the measured  $\delta_I^0$ , i.e.  $-125.8^\circ$ , correctly settles within the BG zone using the conventional PSM because the IG negative-sequence impedance is similar to the SG impedance [71]. There is a small difference between  $\angle Z_{eq}^-$  and  $\angle Z_{eq}^0$  that results in a small  $\theta_{comp}^0$ , ( $-5.6^\circ$ ), which shifts  $\delta_I^0$  to the zone's ideal position. On the other hand, Figure 3.11(b) illustrates that  $\delta_I^+$  is correctly placed in the traditional BG zone immediately after fault inception because the IG operates like an SG according to the constant flux theorem [71]. However, after a few cycles, the IG is demagnetized due to the voltage drop caused by the fault that reduces the generator's active and reactive power injections [71]. Consequently,  $\delta_I^+$  varies leading to bizarre measured angles as

displayed in Figure 3.11(b). Despite these significant variations,  $\theta_{comp}^+$  varied correctly to maintain  $\delta_l^+$  in the correct zone regardless of the value of  $\angle Z_{eq}^+$ , which demonstrates the robustness of the proposed adaptive PSM. Further, Figures 11(c) and (d) clarify the quick operation of the proposed PSM as it can determine the faulted phase in less than half a cycle. Thus, the proposed PSM can be utilized even for instantaneous protective relaying.

### 3.5.3 Islanded Mode of CIGRE Benchmark System

The proposed method is also tested during the islanded mode of operation to prove the thoroughness of the proposed adaptive zoning. Bolted faults are tested for different microgrid topologies and different relay locations. Table 3.5 reports the measured angles by  $R_{83}$  due to faults at bus 3. As exhibited, all fault types are accurately determined by the adaptive zones, in which  $\delta_l^0$  and  $\delta_l^+$  are precisely situated in the proximity of their adaptive zones with a maximum shift of  $5.3^\circ$  from their ideal positions. Although the microgrid topology affects the values of  $\delta_l^0$  and  $\delta_l^+$ , as observed in the grid-connected mode, the values of  $\theta_{comp}^0$  and  $\theta_{comp}^+$  accurately adapt the zones to determine the fault type correctly.

In addition, the IG-side relay ( $R_{65}$ ) is tested in the islanded mode, and its measured angles are revealed in Table 3.6. The results further emphasize the validity of the adaptive PSM at different relay locations and microgrid topologies. A bolted CAG fault at bus 5 in a meshed microgrid is considered a representative case to compare Table 3.4 and 3.6 results. For the grid-connected mode of operation,  $\delta_l^0$  and  $\theta_{comp}^0$  are equal to  $-113.7^\circ$  and  $-11.2^\circ$ , respectively, which slightly change to  $-118.1^\circ$  and  $-6.8^\circ$  in the islanded mode of operation due to equivalent impedances variation. These results illustrate the necessity for adaptive zones that can determine the fault type correctly at different operational conditions.

Table 3.5. IRES-side relay ( $R_{83}$ ) measurement in islanded CIGRE benchmark system

Fault Type	Grid Topology	$\delta_I^0$	$\theta_{comp}^0$	Shift from ideal position	$\delta_I^+$	$\theta_{comp}^+$	Shift from ideal position
AG	Radial	59.8	-65.1	-5.3	-14.7	15.9	1.3
	Mesh	2.1	-6.9	-4.8	-2.4	3.8	1.4
BG	Radial	-58.4	-66.3	-4.7	109.4	11.8	1.2
	Mesh	-117.7	-6.4	-4.2	117.1	4.6	1.7
CG	Radial	176.1	-60.7	-4.7	-137.2	18.7	1.5
	Mesh	121.7	-5.6	-4.0	-122.8	4.6	1.8
ABG	Radial	194.0	-78.6	-4.6	52.7	7.8	0.5
	Mesh	123.6	-8.3	-4.7	60.0	0.01	0.04
BCG	Radial	60.1	-63.3	-3.1	159.9	21.2	1.1
	Mesh	3.3	-5.5	-2.2	179.5	2.2	1.8
CAG	Radial	-72.5	-50.2	-2.8	-93.2	34.8	1.6
	Mesh	-117.1	-5.5	-2.6	-60.6	2.0	1.5

Table 3.6. IG-side relay ( $R_{65}$ ) measurement in islanded CIGRE benchmark system

Fault Type	Grid Topology	$\delta_I^0$	$\theta_{comp}^0$	Shift from ideal position	$\delta_I^+$	$\theta_{comp}^+$	Shift from ideal position
AG	Radial	-2.6	-4.1	-6.7	-157.2	159.7	2.5
	Mesh	1.4	-8.2	-6.8	-7.6	9.6	2.0
BG	Radial	-121.0	-5.6	-6.6	-34.0	156.3	2.3
	Mesh	-117.8	-8.3	-6.2	112.4	9.7	2.2
CG	Radial	120.2	-6.1	-5.9	-263.8	146.4	2.6
	Mesh	121.9	-7.6	-5.8	-127.7	10.1	2.3
ABG	Radial	116.6	-3.4	-6.8	-147.0	207.6	0.6
	Mesh	122.1	-9.1	-6.9	58.8	1.5	0.3
BCG	Radial	3.4	-9.1	-5.7	-16.9	197.9	1
	Mesh	4.3	-8.7	-4.4	180.2	1.5	1.7
CAG	Radial	-121.3	-3.9	-5.2	-261.3	202.6	1.3
	Mesh	-118.1	-6.8	-4.9	-61.5	2.9	1.4

Table 3.7. IIRES-side relay ( $R_{83}$ ) measurement when the IIRES is controlled to mitigate active power ripples

Fault Type	Grid Topology	Grid-connected mode of operation					
		$\delta_I^0$	$\theta_{comp}^0$	Shift from ideal position	$\delta_I^+$	$\theta_{comp}^+$	Shift from ideal position
AG	Radial	53.7	-67.8	-14.1	-22.8	20.5	-2.3
	Mesh	12.1	-23.6	-11.5	-1.9	1.9	0.0
BCG	Radial	77.5	-84.4	-6.9	173.5	2	-4.5
	Mesh	29.1	-33.6	-4.5	192.1	-13.3	-1.2
		Islanded mode of operation					
BG	Radial	291.7	-63.9	-12.2	96.9	18.5	-4.6
	Mesh	250.1	-20.5	-10.4	122.6	-5.9	-3.3
CAG	Radial	-68.5	-58.7	-7.2	-94.5	29.5	-5.0
	Mesh	-102.4	-23.3	-5.7	-49.5	-13.8	-3.3

### 3.5.4 Performance Against Different IIRES Controllers

The performance of the proposed PSM is tested against various IIRES control strategies. The IIRES is controlled to either mitigate active or reactive power ripples by following the controllers in [72]. Table 3.7 presents the angles measured by  $R_{83}$  (i.e.,  $R_{IIRES}$ ) for bolted faults at bus 3 for different microgrid topologies and modes of operation. In this scenario, the IIRES is controlled to mitigate active power ripples and follows the RCG requirements of the NA-GCs. The results show the capability of the proposed PSM to place  $\delta_I^0$  and  $\delta_I^+$  in their correct zones when the active power ripples are canceled. For instance, the results during a BG fault in the islanded mode of operation clarifies that  $\theta_{comp}^+$  accurately places  $\delta_I^+$  around its ideal position. Moreover,  $\theta_{comp}^0$  shifts the conventional fault-type zones by  $63.9^\circ$  and  $20.5^\circ$  for radial and mesh grids.

On the other hand, Table 3.8 displays  $R_{83}$ 's measured angles during bolted faults at bus 3 when the IIRES is controlled to mitigate reactive power ripples. The measured values for  $\delta_I^0$ ,  $\delta_I^+$ ,  $\theta_{comp}^0$ , and  $\theta_{comp}^+$  illustrate the precise operation of the proposed PSM when the IIRES complies with the NA-GC. A bolted ABG fault in the meshed grid-connected mode of operation is selected as a representative case from Table 3.8. This case clarifies that

Table 3.8. IIRES-side relay ( $R_{83}$ ) measurement when the IIRES is controlled to mitigate reactive power ripples

Fault Type	Grid Topology	Grid-connected mode of operation					
		$\delta_I^0$	$\theta_{comp}^0$	Shift from ideal position	$\delta_I^+$	$\theta_{comp}^+$	Shift from ideal position
AG	Radial	-67.3	63.6	-3.7	-144.8	152	7.2
	Mesh	1.5	-6.2	-4.7	-10.4	15.6	5.2
BCG	Radial	-83.5	81.6	-1.9	10.5	-179.7	10.8
	Mesh	-2.2	0.3	-1.9	166.2	20.8	7.6
		Islanded mode of operation					
CG	Radial	58.5	60.4	-1.1	102.5	143.2	5.7
	Mesh	116.8	2.3	-0.9	-128.4	13.7	5.3
ABG	Radial	58.8	59.1	-2.1	-91	159.8	8.8
	Mesh	97.8	18.2	-4	37.3	28.4	5.7

$\theta_{comp}^0$  and  $\theta_{comp}^+$  accurately place  $\delta_I^0$  and  $\delta_I^+$  in their correct fault-type zones with a small shift from their ideal positions, i.e.,  $-4^\circ$  and  $5.7^\circ$ , respectively. These results demonstrate that the proposed PSM can determine the fault type successfully with different IIRES controllers.

### 3.6 Conclusions

Accurate PSM is crucial for the correct operation of different protection elements. However, the exotic fault characteristics of IIRESSs adversely affect the relay's credibility in determining the fault type. In this chapter, the current- and voltage-angle-based PSMs in the presence of IIRESSs are mathematically analyzed to highlight the leading causes of their failure. Consequently, the classical current-angle-based PSM is modified using adaptive zones capable of operating with different fault current signatures. The adaptive zones are based on rotating the classic PSM zones online by a compensation angle, which provides the required information about the relative angles of the relay-side sequence impedances. Simulation studies reveal the proposed method's accuracy in adjusting the PSM zones such that the measured phase selection signatures (i.e.,  $\delta_I^0$  and  $\delta_I^+$ ) correctly determine the faulted phase(s). The results also validate the efficiency of the proposed PSM

in determining the fault type for different microgrid topologies, fault resistance, RCG requirements, and IRES controllers.

## Chapter 4

# Reliable Phase Selection for Transmission Networks

## Considering Arc Resistances and Various Control Functions of Renewable Energy Sources

## 4.1 Introduction

In Chapter 3, an analytical analysis of the voltage-angle-based PSM is performed at the fault location to determine the reasons for its failure. Then, it was assumed that the voltage's angle measured by the relay is equivalent to the voltage's angle at the fault location, which is an acceptable assumption for short transmission lines and conventional grids. However, it is not precise for fault currents emanating from IIRESSs long transmission lines. Consequently, in this chapter, the relative angles between sequence voltages measured at the relay location are determined analytically in two stages: (i) a short-circuit analysis is performed at the fault location to determine the relative angles between sequence voltages, (ii) an analysis of the transmission line impact on the phase difference between the relay's and fault's sequence voltages is conducted for different IIRESS' controllers. Consequently, new PSM zones that are based on relative angles between sequence voltages are designed to allow accurate PSM regardless of the IIRESS fault currents, fault resistances, or fault locations. Comprehensive time-domain simulations confirm the accuracy of the proposed PSM at different fault locations, resistances, types, and fault currents.

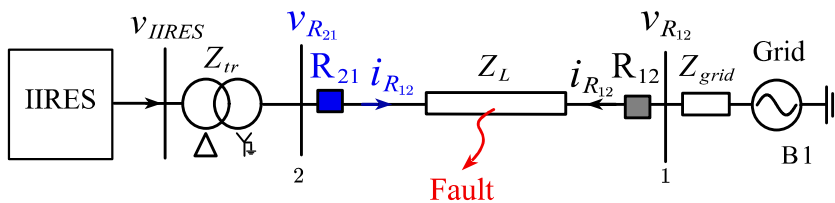


Figure 4.1. Sample power system structure diagram.



## 4.2 Analysis of Relative Angles between Sequence Fault Voltages

In this section, the short circuit analysis performed in Subsection 3.2.2 is revisited to add information about  $\delta_V^0$  and  $\delta_V^+$  range in practical power systems. The short circuit analysis is performed on a sample power system, as shown in Figure 4.1, for SLG, LLG, and LL faults to determine the relative angle between the negative- and zero-sequence voltages measured at the fault location, i.e.,  $\delta_F^0 = \angle V_F^- - \angle V_F^0$ , and that between the negative- and positive-sequence voltages, i.e.,  $\delta_F^+ = \angle V_F^- - \angle V_F^+$ , as follows:

### 4.2.1 SLG Fault Analysis

In this subsection, the sequence network for an AG fault is analyzed, as a representative for SLG faults, to determine the relation between the sequence fault voltages, i.e.,  $V_F^+$ ,  $V_F^-$ , and  $V_F^0$ , and their relative angles. The sequence fault currents, i.e.,  $I_F^+$ ,  $I_F^-$ , and  $I_F^0$ , are equal, as shown in Figure 4.2, which is a duplication of Figure 3.1(b) for ease of referencing. On the other hand, the sequence fault voltages are formulated by

$$V_F^- = -I_F Z_{th}^- \quad (4.1.a)$$

$$V_F^0 = -I_F Z_{th}^0 \quad (4.1.b)$$

$$V_F^+ = I_F (Z_{th}^- + Z_{th}^0 + 3R_g) \quad (4.1.c)$$

By dividing (4.1.a) by (4.1.b) and (4.1.c), the relation between the negative- and zero-sequence voltages and that between the negative- and positive-sequence voltages are determined as follows:

$$\frac{V_F^-}{V_F^0} = \frac{Z_{th}^-}{Z_{th}^0} \quad (4.2.a)$$

$$\frac{V_F^-}{V_F^+} = \frac{-Z_{th}^-}{(Z_{th}^- + Z_{th}^0 + 3R_g)}. \quad (4.2.b)$$

Hence,  $\delta_F^0$  and  $\delta_F^+$  are given by

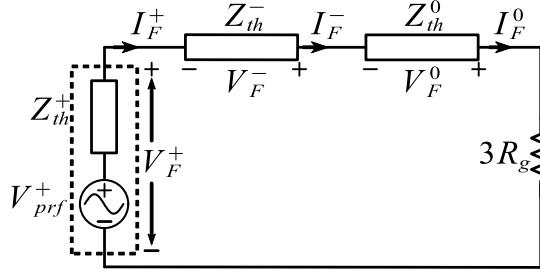


Figure 4.2. Sequence circuit at the fault location for an AG fault.

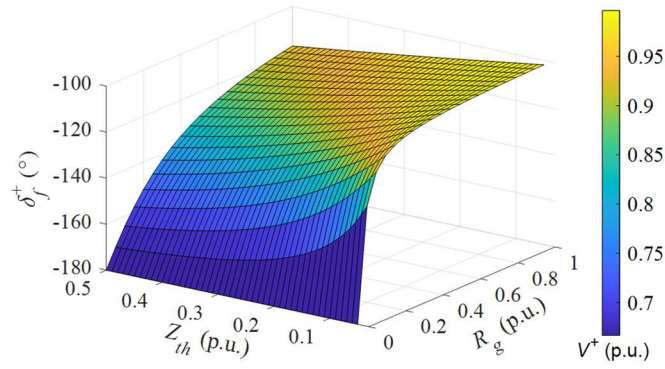


Figure 4.3. Range of  $\delta_F^+$  for an AG fault.

$$\delta_F^0 = \angle Z_{th}^- - \angle Z_{th}^0 \quad (4.3.a)$$

$$\delta_F^+ = \angle Z_{th}^- - \angle(Z_{th}^- + Z_{th}^0 + 3R_g) - 180^\circ \quad (4.3.b)$$

In a typical power system, the positive-, negative-, and zero-sequence equivalent impedance angles are almost equal, and they are around  $80^\circ$  [68]. Since the IRES equivalent impedance is much greater than the grid side impedance, the Thevenin impedance is roughly equal to the grid side impedance [68], i.e.,  $\angle Z_{th}^+ \approx \angle Z_{th}^- \approx \angle Z_{th}^0 \approx 80^\circ$ . Hence, it can be deduced that  $\delta_F^0 \approx 0$ , while  $\delta_F^+$  varies according to the magnitude of  $R_g$ , as shown in Figure 4.3.

It can be observed from Figure 4.3 that  $\delta_F^+ = -180^\circ$  for solid faults, and it increases as  $R_g$  increases. It is also deduced that the effect of  $R_g$  on  $\delta_F^+$  increases when the magnitude of  $Z_{th}$ , i.e.,  $|Z_{th}|$ , decreases. Thus, to determine  $\delta_F^+$ 's maximum variation from the solid fault condition, the minimum value of  $|Z_{th}|$  should be utilized. It is worth mentioning that

the fault current in three-phase faults can reach 4 to 20 times its rated value [73], [74]. Thus, the minimum value of  $|Z_{th}^+| \approx 0.05$  p.u. Since,  $|Z_{th}^-|$  is almost equivalent to  $|Z_{th}^+|$  [27], the minimum value of  $|Z_{th}^-| \approx 0.05$  p.u. On the other hand,  $|Z_{th}^0|$  is usually higher than  $|Z_{th}^+|$ , i.e.,  $|Z_{th}^0| = k^0|Z_{th}^+|$ , where  $k^0$  is a constant that depends on the neutral conductor size and varies from 1 to 5 [75]. In order to get the minimum value of  $|Z_{th}^0|$ ,  $k^0$  is selected at 1, and the minimum value of  $|Z_{th}^+|$  in Figure 4.3 is selected, such that,  $|Z_{th}^+| = |Z_{th}^-| = |Z_{th}^0| = |Z_{th}| = 0.05$  p.u. It can be observed from Figure 4.3 that  $\delta_F^+$  varies from  $-180^\circ$  for solid faults to  $-100^\circ$  at high-resistance faults. However, increasing the fault resistance reduces the positive-sequence voltage drop. The practical range for  $\delta_F^+$  for AG faults is limited by  $V_F^+ = 0.9$  p.u., and thus,  $\delta_F^+$  ranges from  $-180^\circ$  to  $-110^\circ$ .

#### 4.2.2 LLG Fault Analysis

As a representative of LLG faults, the sequence network for a BCG fault shown in Figure 4.4, which is a duplication of Figure 3.1(c) for ease of referencing, is analyzed. Consequently, the sequence voltages are inferred as

$$V_F^- = V_x + I_F^- R_{ph} \quad (4.4.a)$$

$$V_F^0 = V_x + I_F^0 (R_{ph} + 3R_g) \quad (4.4.b)$$

$$V_F^+ = V_x + I_F^+ R_{ph} \quad (4.4.c)$$

On the other hand, the relation between sequence currents and their corresponding voltages is given by

$$I_F^- = -\frac{V_F^-}{Z_{th}^-} \quad (4.5.a)$$

$$I_F^0 = -\frac{V_F^0}{Z_{th}^0} \quad (4.5.b)$$

$$I_F^+ = -(I_F^- + I_F^0) = \frac{V_F^-}{Z_{th}^-} + \frac{V_F^0}{Z_{th}^0}. \quad (4.5.c)$$

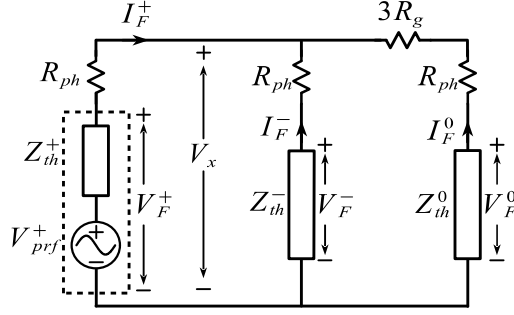


Figure 4.4. Sequence circuit at the fault location for a BCG fault.

Thus, using (4.5) and (4.4),  $V_F^-$ ,  $V_F^0$ , and  $V_F^+$  can be given by

$$V_F^- = V_x \left( \frac{Z_{th}^-}{Z_{th}^- + R_{ph}} \right) \quad (4.6.a)$$

$$V_F^0 = V_x \left( \frac{Z_{th}^0}{Z_{th}^0 + R_{ph} + 3R_g} \right) \quad (4.6.b)$$

$$V_F^+ = V_x \left( 1 + \frac{R_{ph}}{Z_{th}^- + R_{ph}} + \frac{R_{ph}}{Z_{th}^0 + R_{ph} + 3R_g} \right). \quad (4.6.c)$$

Subsequently,  $V_F^-/V_F^0$  and  $V_F^-/V_F^+$  are determined by

$$\frac{V_F^-}{V_F^0} = \frac{Z_{th}^-}{Z_{th}^0} \times \frac{Z_{th}^0 + R_{ph} + 3R_g}{Z_{th}^- + R_{ph}} \quad (4.7.a)$$

$$\frac{V_F^-}{V_F^+} = \frac{Z_{th}^-}{Z_{th}^- + 2R_{ph} + \frac{R_{ph}(R_{ph} + Z_{th}^-)}{Z_{th}^0 + R_{ph} + 3R_g}}. \quad (4.7.b)$$

Hence, for solid faults,  $\delta_F^0$  and  $\delta_F^+$  are given by

$$\delta_F^0 = 0 \quad (4.8.a)$$

$$\delta_F^+ = \frac{Z_{th}^-}{Z_{th}^- + \frac{Z_{th}^-}{Z_{th}^0}} \approx 0. \quad (4.8.a)$$

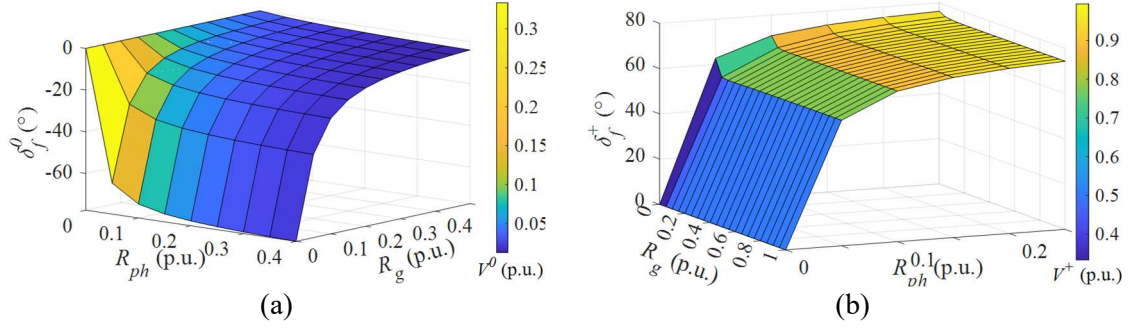


Figure 4.5. Relative sequence angles range for a BCG fault: (a)  $\delta_F^0$ , (b)  $\delta_F^+$ .

However, the values of  $\delta_F^0$  and  $\delta_F^+$  varies according to the value of  $R_{ph}$  and  $R_g$ , as demonstrated in Figure 4.5. It is worth noting that Figure 4.5 is determined by varying  $R_{ph}$  and  $R_g$ , while  $|Z_{th}^-|$  and  $|Z_{th}^0|$  are selected at their minimum value, which is 0.05 p. u., to get the maximum range for both  $\delta_F^0$  and  $\delta_F^+$ . It can be deduced from Figure 4.5(a) that  $R_{ph}$  has a neglectable effect on  $\delta_F^0$ , while increasing  $R_g$  directly affect the value of  $\delta_F^0$ . At large  $R_g$ ,  $\delta_F^0 \approx -\angle Z_{th}^0$ ; thus,  $\delta_F^0$  can vary from  $0^\circ$  to  $-80^\circ$  in a BCG fault. However, the practical range of  $\delta_F^0$  is from  $0^\circ$  to  $-73^\circ$ , as illustrated in Figure 4.5(a). On the other hand,  $\delta_F^+$  negligibly affected by  $R_g$ , but substantially impacted by the value of  $R_{ph}$ , as shown in Figure 4.5(b). For considerable  $R_{ph}$ ,  $\delta_F^+ \approx \angle Z_{th}^-$ ; hence,  $\delta_F^+$  can vary in a BCG fault from  $0^\circ$  to  $80^\circ$ . This range matches the total range determined in Figure 4.5(b). However, the effective range of  $\delta_F^+$  is from  $0^\circ$  to  $68^\circ$ .

### 4.2.3 LL Fault Analysis

In this subsection, the sequence network for a BC fault is analyzed. The relation between  $V_F^+$  and  $V_F^-$  is derived from Figure 4.6, , which is a duplication of Figure 3.1(d) for ease of referencing, as follows:

$$V_F^+ = V_F^- + I_F^+ R_{ph} = V_F^- \left( \frac{Z_{th}^- + R_{ph}}{Z_{th}^-} \right). \quad (4.9)$$

Thereafter, the ratio between  $V_F^-$  and  $V_F^+$  is determined by

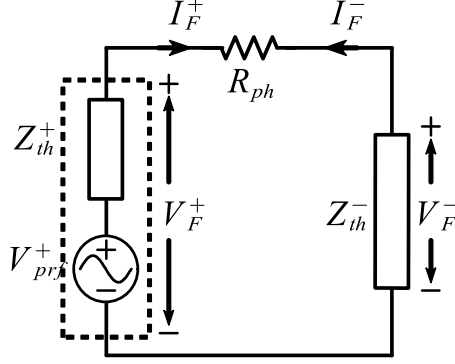


Figure 4.6. Sequence circuit at the fault location for a BC fault.

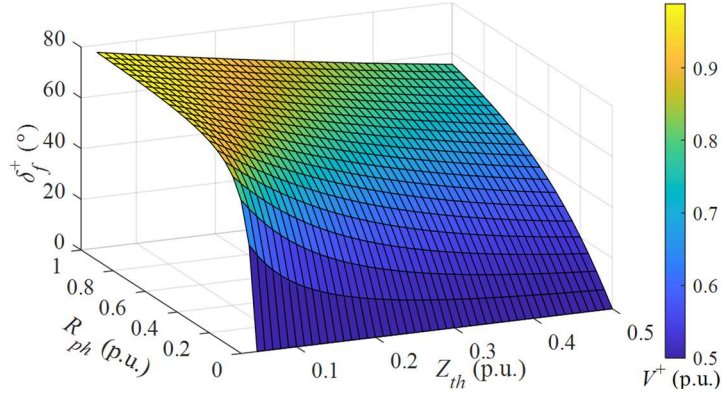


Figure 4.7. Range of  $\delta_F^+$  for a BC fault.

$$\frac{V_F^-}{V_F^+} = \frac{Z_{th}^-}{Z_{th}^- + R_{ph}}. \quad (4.10)$$

Consequently, it can be inferred that  $\delta_F^+$  is susceptible to  $R_{ph}$ . If  $R_{ph} = 0$ ,  $\delta_F^+ = 0$ . On the other hand, if  $R_{ph}$  is noticeable,  $\delta_F^+ \approx \angle Z_{th}^- \approx 80^\circ$ . Figure 4.7 depicts the value of  $\delta_F^+$  against wide range of  $|Z_{th}^-|$  and  $R_{ph}$ . The figure manifest that the theoretical range of  $\delta_F^+$  can vary from  $0^\circ$  to  $80^\circ$  for a BC fault. Whereas the practical range is between  $0^\circ$  to  $68^\circ$ .

### 4.3 Analysis of Phase Shifts between Sequence Voltages

The transmission line introduces a voltage phase shift between sequence voltages measured at the relay and fault location. This phase shift is negligible in a traditional grid, where the source is modeled as a voltage source behind a constant impedance. However, for IIRESSs,

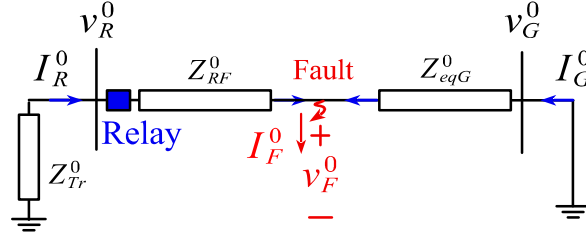


Figure 4.8. Equivalent single-line diagram of the zero-sequence circuit of the system under study.

the current angle and magnitude differ from those of traditional sources. The transmission line could considerably affect the sequence-voltage relative angles measured at the relay or IRES location. Thus, the transmission line effect on the angles of the sequence voltages should be analyzed to determine the relative angle between the negative- and zero-sequence voltages measured at the relay location, i.e.,  $\delta_R^0 = \angle V_R^- - \angle V_R^0$ , and that between the negative- and positive-sequence voltages, i.e.,  $\delta_R^+ = \angle V_R^- - \angle V_R^+$ . To the authors' knowledge, this analysis is missing in the literature; however, it is essential for accurate protective relaying.

#### 4.3.1 Zero-sequence Voltage

The IRES is usually integrated into the grid through a delta/star-ground transformer. Thus, the IRES controller does not affect the zero-sequence current. The single-line diagram for the zero-sequence circuit is illustrated in Figure 4.8, where the zero-sequence voltage measured at the relay side, i.e.,  $V_R^0$ , can be determined by

$$V_R^0 = V_F^0 \times \frac{Z_{Tr}^0}{Z_{RF}^0 + Z_{Tr}^0} \quad (4.11)$$

in which,  $Z_{Tr}^0$  is the zero-sequence equivalent transformer impedance, and  $Z_{RF}$  is the equivalent impedance between the relay and a fault location. Since  $\angle Z_{Tr}^0 \approx \angle Z_{RF}^0$ , the relative angle between the zero-sequence voltage measured at the relay and fault location, i.e.,  $\Delta\theta_{RF}^0 = \angle V_R^0 - \angle V_F^0$ , is approximately equal to zero. This angle can be theoretically neglected, but its effect is considered as a margin when setting the proposed PSM zones.

### 4.3.2 Negative- and Positive-sequence Voltages

In this subsection, the range of the phase shift between the relay's and fault's negative-sequence voltages, i.e.,  $\Delta\theta_{RF}^- = \angle V_R^- - \angle V_F^-$ , and that between the relay's and fault's positive-sequence voltages, i.e.,  $\Delta\theta_{RF}^+ = \angle V_R^+ - \angle V_F^+$ , are analyzed for different IRES controllers.

#### A. Conventional Controller

The controller is designed to inject only positive-sequence current, where a PI controller is used to track the reference current, and a feed-forward voltage is utilized to enhance the controller's dynamic response, but it diminishes the negative-sequence current and makes it similar to the balanced-current control strategy, i.e.,  $|I_{IRES}^-| \approx 0$ . Hence, the effect of  $\Delta\theta_{RF}^-$  is abandoned in both balanced and conventional controllers.

On the other hand, the full range of the positive-sequence voltage phase shift between the fault and relay location is required to be analyzed. To determine the maximum angle of  $\Delta\theta_{RF}^+$ , the system is studied at the furthest point from the fault, which is the IRES location, because increasing the impedance between the relay and fault location increases the phase shift. Figure 4.9 represents an equivalent positive-sequence single-line diagram of Figure 4.1, where  $Z_{RF}^+$  is the maximum positive-sequence equivalent impedance between the relay (IRES) and fault location, while the IRES is represented by a current source of magnitude  $|I_{IRES}^+|$  and phase  $\theta_{v_R^+} - \phi^+$ . The angle  $\theta_{v_R^+}$  is the positive-sequence voltage angle measured at the IRES terminals, i.e., the relay location of the maximum phase shift, and  $\phi^+$  is the phase shift between the IRES positive-sequence voltage and current.

Using Figure 4.9, the relation between the voltage at the IRES, i.e., farthest relay location, and fault location can be determined by

$$|V_R^+| \angle \theta_{v_R^+} = |Z_{RF}^+| |I_{IRES}^+| \angle (\theta_{v_R^+} - \phi^+ + \theta_{Z^+}) + |V_F^+| \angle \theta_{v_F^+} \quad (4.12)$$

where  $\theta_{v_R^+}$  and  $\theta_{v_F^+}$  are the positive-sequence voltage angles measured at the relay and fault locations, respectively, while  $\theta_{Z^+}$  is the positive-sequence impedance angle. By decomposing (4.12) into real and imaginary parts and applying trigonometric function



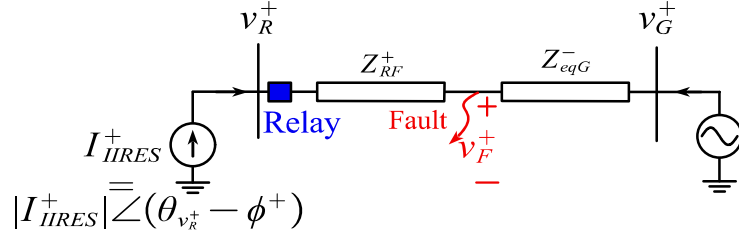


Figure 4.9. Equivalent single-line diagram of the positive-sequence circuit of the system under study.

properties,  $\Delta\theta_{RF}^+$  can be calculated as in (4.13).

$$\Delta\theta_{RF}^+ = \sin^{-1} \left( \frac{|Z_{RF}^+| |I_{IRES}^+|}{|V_F^+|} \sin(-\phi^+ + \theta_{Z^+}) \right). \quad (4.13)$$

To determine the maximum range of  $\Delta\theta_{RF}^+$ ,  $|I_{IBR}^+|$  is selected equal to the IRES's maximum current limit, i.e., 1.5 p.u. [67], while the maximum value of  $|Z_{RF}^+|$  is determined from the transmission-line design limitations, which should be designed to allow a maximum of 5% voltage regulation at the rated load [73], [74]. Thus,  $|Z_{RF}^+| \approx 0.1$  p.u., while  $\theta_Z^+ \approx 80^\circ$ ; since the IRES injects positive-sequence active and reactive currents during faults,  $\phi^+$  can vary between  $0^\circ$  and  $90^\circ$ . To obtain  $\Delta\theta_{RF}^+$ 's maximum range,  $\phi^+$  is set at its limits, i.e.,  $0^\circ$  and  $90^\circ$ . On the other hand,  $|V_F^+|$  varies according to the value of the fault resistance. Thus,  $\Delta\theta_{RF}^+$  is determined at the minimum and maximum value of  $|V_F^+|$  to get the maximum range of  $\Delta\theta_{RF}^+$  for different fault resistances.

The minimum value of  $|V_F^+|$  occurs during bolted faults, and it differs according to the fault type, as follows:

- For SLG fault, the minimum value of  $|V_F^+|$  is equal to  $2/3$  p.u.; thus, for bolted fault, the maximum value of  $\Delta\theta_{RF}^+$  during SLG faults changes from  $-2.3^\circ$  to  $12.5^\circ$ .
- For LLG faults, the minimum value of  $|V_F^+| = 1/3$  p.u. Thus, for a negligible value of  $R_{ph}$ , the maximum variation of  $\Delta\theta_{RF}^+$  for LLG faults is varied from  $-4.5^\circ$  to  $26^\circ$ .
- For LL faults, the minimum value of  $|V_F^+|$  is 0.5 p.u.; hence, for bolted LL faults,  $\Delta\theta_{RF}^+$  range is  $[-3^\circ, 17.2^\circ]$ .

Table 4.1. Range of  $\Delta\delta_{RF}^+$  and  $\Delta\delta_{RF}^0$  in conventional control

Fault type	Fault resistance	$\Delta\theta_{RF}^-$	$\Delta\theta_{RF}^+$	$\Delta\delta_{RF}^+$	$\Delta\delta_{RF}^0$
<b>AG</b>	bolted	0	[-2.3,12.8]	[-12.8,2.3]	0
	High $R_g$	0	[-1.7,9.5]	[-9.5,1.7]	0
<b>BCG</b>	bolted	0	[-4.5,26.3]	[-26.3,4.5]	0
	High $R_g$	0	[-4.5,26.3]	[-26.3,4.5]	0
	High $R_{ph}$	0	[-1.7,9.5]	[-9.5,1.7]	0
<b>BC</b>	bolted	0	[-3,17.2]	[-17.2,3]	0
	High $R_{ph}$	0	[-1.7,9.5]	[-9.5,1.7]	0

On the other hand, the maximum value of  $|V_F^+|$ , i.e., at high resistive faults, is selected at 0.9 p.u., which is the threshold for a positive-sequence relay to operate. Thus, for high-resistive faults, i.e., high  $R_g$  in SLG and high  $R_{ph}$  in LL(G) faults, the range of  $\Delta\theta_{RF}^+$  is  $[-1.7^\circ, 9.5^\circ]$ . Consequently, the difference between  $\delta_R^+$  and  $\delta_F^+$ , i.e.,  $\Delta\delta_{RF}^+$ , and the difference between  $\delta_R^0$  and  $\delta_F^0$ , i.e.,  $\Delta\delta_{RF}^0$ , due to the transmission line effect, when the IIRES injects a balanced current, is concluded in Table 4.1.

#### B. Following New Grid Codes

The IIRES's controller is designed to inject both positive- and negative-sequence currents according to recent GC specifications. Thus,  $\Delta\theta_{RF}^-$  and  $\Delta\theta_{RF}^+$  is determined by studying the negative- and positive-circuit, respectively.

In the negative-sequence circuit, the IIRES is controlled to inject negative-sequence current at the IIRES terminals, while the conventional grid can be represented by a constant impedance. Thus, the reduced single-line diagram in the negative sequence can be depicted, as shown in Figure 4.10. Hence, the relation between  $V_R^-$  and  $V_F^-$  resembles (4.13) determined for the positive-sequence circuit, as follows:

$$|V_R^-| \angle \theta_{v_R^-} = |Z_{RF}^-| |I_{IIRES}^-| \angle (\theta_{v_R^-} - \phi^- + \theta_{Z^-}) + |V_F^-| \angle \theta_{v_F^-}. \quad (4.14)$$

Consequently, the value of  $\Delta\theta_{RF}^-$  can be inferred by

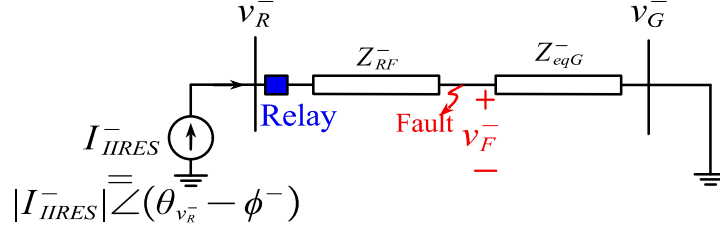


Figure 4.10. Equivalent single-line diagram of the negative-sequence circuit of the system under study.

$$\Delta\theta_{RF}^- = \sin^{-1} \left( \frac{|Z_{RF}^-| |I_{IRES}^-|}{|V_F^-|} \sin(-\phi^- + \theta_{Z^-}) \right). \quad (4.15)$$

Recent GCs impose the injection of negative-sequence current to reduce unbalanced voltage during asymmetric faults. For instance, the German GC, i.e., VDE-AR-N 4120-GC [30], enforces the IIRES to inject negative-sequence current according to

$$I_q^- = K |V_R^-| \quad (4.16)$$

where  $I_q^-$  is an inductive negative-sequence reactive current, and  $K$  is a constant that can be selected from the following range: [2, 6]. Thus, the maximum negative-sequence current is equal to  $6|V_R^-|$ , while  $\phi^- = -90^\circ$ . By substituting  $|I_{IRES}^-| = 6|V_R^-|$ ,  $\phi^- = -90^\circ$  and assume  $|V_R^-| = |V_F^-|$  in (4.15), the maximum value of  $\Delta\theta_{RF}^-$  is  $5.98^\circ$ . It is worth mentioning that  $|V_R^-| < |V_F^-|$ . Thus, the actual maximum value of  $\Delta\theta_{RF}^-$  is less than  $5.98^\circ$ . The actual maximum value of  $\Delta\theta_{RF}^-$  can be determined by substituting  $|I_{IRES}^-| = 6|V_R^-|$ ,  $\phi^- = -90^\circ$  and  $Z_R^- = 0.1 \angle 80^\circ$  in (4.14), as follows:

$$|V_R^-| \angle \theta_{v_R^-} = 0.6 |V_R^-| \angle (\theta_{v_R^-} + 170^\circ) + |V_F^-| \angle \theta_{v_F^-}. \quad (4.17)$$

By solving (4.17),  $\Delta\theta_{RF}^-$ 's actual maximum value is  $3.75^\circ$ , which could be lower at bolted faults because the current is limited to avoid exceeding the maximum current limit. However, this reduction is small; thus, the maximum value of  $\Delta\theta_{RF}^-$  is considered equal to  $3.75^\circ$  for both bolted and high resistive faults. On the other hand, the minimum value is  $0^\circ$  at faults close to the relay location.

Table 4.2. Range of  $\Delta\delta_{RF}^+$  and  $\Delta\delta_{RF}^0$  when IRES follows the new grid codes

Fault type	Fault resistance	$\Delta\theta_{RF}^-$	$\Delta\theta_{RF}^+$	$\Delta\delta_{RF}^+$	$\Delta\delta_{RF}^0$
AG	bolted	[0,3.8]	[1.7,-2.3]	[-1.7,6.1]	[0,3.8]
	High $R_g$	[0,3.8]	[0,8.6]	[0,-5.1]	[0,3.8]
BCG	bolted	[0,3.8]	[0,-4.5]	[0,8.3]	[0,3.8]
	High $R_g$	[0,3.8]	[0,-4.5]	[0,8.3]	[0,3.8]
	High $R_{ph}$	[0,3.8]	[0,8.6]	[0,-5.1]	[0,3.8]
BC	bolted	[0,3.8]	[0,-3]	[0,6.8]	-
	High $R_{ph}$	[0,3.8]	[0,8.6]	[0,-5.1]	-

On the other hand, the positive-sequence circuit can be similarly analyzed as in subsection 4.3.2.A, where the positive sequence current magnitude and power factor are determined from GC requirements. In the German GC, the IRES should inject positive-reactive power according to

$$I_q^+ = K|\Delta V_R^+| \quad (4.18)$$

where  $I_q^+$  is a capacitive positive-sequence reactive current. In addition, the IRES should inject positive-sequence active current to achieve the maximum current limit. Thus, for bolted faults,  $\phi^+$  is equal to  $90^\circ$  for  $K = 6$ , but it could be reduced to  $70^\circ$  in SLG faults for  $K = 2$ , while at high resistive faults, i.e.,  $\Delta V_R^+ = 0.1$  p.u.,  $\phi^+$  is equal to  $8.8^\circ$  and  $42^\circ$  when  $K$  equals 2 and 6, respectively. Moreover,  $|I_{IRES}^+|$  is set at its maximum value, i.e., 1.5 p.u. Consequently, for bolted faults,  $\Delta\delta_{RF}^+$  approaches its maximum value when  $\phi^+$  is equal to  $90^\circ$ , while the minimum value occurs when  $\phi^+$  is equal to  $70^\circ$ . On the other hand, during high resistive faults,  $|\Delta\delta_{RF}^+|$  reaches its maximum value, when  $\phi^+$  equals  $8.8^\circ$ .

The transmission line effect on  $\Delta\delta_{RF}^+$  and  $\Delta\delta_{RF}^0$ , when the IRES is controlled according to new GCs, is shown in Table 4.2.

### C. Eliminating Active and Reactive Power Ripples

Active- and reactive-power ripples introduce challenges in the IRES control and generate double oscillation in the dc link voltage, which could reduce the lifetime of the dc link

capacitor. Thus, some scholars suggest injecting negative-sequence current with specific magnitude and angle to eliminate either active- or reactive-power ripples. However, they do not consider the reliable operation of protection functions in their controllers. The instantaneous active and reactive power can be deduced from the instantaneous positive- and negative-sequence currents and voltages as follows:

$$p = v_R^+ \cdot i_R^+ + v_R^- \cdot i_R^- + \underbrace{v_R^- \cdot i_R^+ + v_R^+ \cdot i_R^-}_{\tilde{P}_{2\omega}} \quad (4.19.a)$$

$$q = v_{\perp R}^+ \cdot i_R^+ + v_{\perp R}^- \cdot i_R^- + \underbrace{v_{\perp R}^- \cdot i_R^+ + v_{\perp R}^+ \cdot i_R^-}_{\tilde{Q}_{2\omega}} \quad (4.19.b)$$

where  $p$  and  $q$  are the instantaneous active and reactive power, respectively;  $\tilde{P}_{2\omega}$  and  $\tilde{Q}_{2\omega}$  are the oscillating components of active and reactive power at twice the nominal frequency, respectively;  $v_{\perp R}^+$  is lagging the positive-sequence voltage measured at the relay, i.e.,  $v_R^+$ , by  $90^\circ$ ; and  $v_{\perp R}^-$  is leading  $v_R^-$  by  $90^\circ$ . One of the methods to eliminate active power oscillation is obtained by setting  $|I_{IIRES}^-|$  and  $\angle I_{IIRES}^-$ , as follows:

$$|I_{IIRES}^-| = \frac{|V_R^-|}{|V_R^+|} |I_{IIRES}^+| \quad (4.20.a)$$

$$\angle I_{IIRES}^- = \theta_{v_R^-} - \phi^+ + 180^\circ. \quad (4.20.b)$$

Consequently,  $\phi^-$  is inferred by

$$\phi^- = \phi^+ + 180^\circ. \quad (4.21)$$

On the other hand, a method to eliminate reactive power ripples is inferred by calculating  $|I_{IIRES}^-|$  and  $\angle I_{IIRES}^-$  using

$$|I_{IIRES}^-| = \frac{|V_R^-|}{|V_R^+|} |I_{IIRES}^+| \quad (4.22.a)$$

$$\angle I_{IIRES}^- = \theta_{v_R^-} - \theta_{v_R^+} + (\theta_{v_R^+} - \phi^+) = \theta_{v_R^-} - \phi^+. \quad (4.22.b)$$

Hence,  $\phi^-$  should be given by

$$\phi^- = \phi^+. \quad (4.23)$$

It can be observed that  $|I_{IRES}^-|$  is the same for active- and reactive-power ripple elimination; thus,  $\Delta\theta_{RF}^-$  for these two control strategies has the same expression. By substituting (4.20.a) in (4.15),  $\Delta\theta_{RF}^-$  is formulated by

$$\Delta\theta_{RF}^- = \sin^{-1} \left( \frac{|Z_{RF}^-| \frac{|V_R^-|}{|V_R^+|} |I_{IRES}^+|}{|V_F^-|} \sin(-\phi^- + \theta_{Z^-}) \right). \quad (4.24)$$

Since the IRES fault current is limited, it is assumed that  $|V_R^-| \approx |V_F^-|$ . Then, by comparing the result with (4.13),  $\Delta\theta_{RF}^-$  and  $\Delta\theta_{RF}^+$  are deduced by

$$\Delta\theta_{RF}^\pm = \sin^{-1} \left( \frac{|Z_{RF}^\pm| |I_{IRES}^+|}{|V_R^+|} \sin(-\phi^\pm + \theta_{Z^\pm}) \right). \quad (4.25)$$

It is worth mentioning that IRESs inject positive- and negative-sequence currents simultaneously; thus,  $|I_{IRES}^+|$  is limited to avoid exceeding IRES's current limit. The maximum phase current magnitude of each phase, i.e.,  $I_{peak\phi}$ , can be represented in terms of positive- and negative-sequence currents, as follows:

$$I_{peak\phi} = \sqrt{\frac{|I_{IRES}^+|^2 + |I_{IRES}^-|^2 + 2|I_{IRES}^+||I_{IRES}^-|\cos(\varphi_{a,b,c} + \angle I_{IRES}^+ - \angle I_{IRES}^-)}{}} \quad (4.26)$$

where  $\varphi_{a,b,c}$  represents a phase shift of  $0^\circ$ ,  $-120^\circ$ , and  $120^\circ$  for phases a, b, and c, respectively. To avoid any phase current from exceeding its maximum limit, the limit current, i.e.,  $I_{limit}$ , is equivalent to the maximum phase, which is calculated by

$$I_{peak} = \sqrt{\frac{|I_{IRES}^+|^2 + |I_{IRES}^-|^2 + 2|I_{IRES}^+||I_{IRES}^-|\max\{\cos(\varphi_{a,b,c} + \angle I_{IRES}^+ - \angle I_{IRES}^-)\}}{}}. \quad (4.27)$$

According to (4.27), the maximum  $|I_{IRES}^+|$  is determined when the value of  $\max\{\cos(\varphi_{a,b,c} + \angle I_{IRES}^+ - \angle I_{IRES}^-)\}$  is minimum, which is equal to 0.5 when  $\angle I_{IRES}^+ - \angle I_{IRES}^- = 0^\circ, 180^\circ$ , or  $300^\circ$ . Thus, the maximum value of  $|I_{IRES}^+|$  is derived from

$$I_{peak} = \sqrt{|I_{IRES}^+|^2 + |I_{IRES}^-|^2 + |I_{IRES}^+||I_{IRES}^-|} = I_{limit}. \quad (4.28)$$

By substituting (4.20.a) into (4.28),  $|I_{IRES}^+|$  is obtained by

$$|I_{IRES}^+| = I_{limit} \frac{|V_R^+|^2}{\sqrt{|V_R^+|^2 + |V_R^-|^2 + |V_R^+||V_R^-|}}. \quad (4.29)$$

By substituting (4.29) into (4.25) and keeping  $I_{limit} = 1.5$  p. u.,

$$\Delta\theta_{RF}^\pm = \sin^{-1} \left( \frac{1.5|Z_{RF}^\pm|}{\sqrt{|V_R^+|^2 + |V_R^-|^2 + |V_R^+||V_R^-|}} \sin(-\phi^\pm + \theta_{Z^\pm}) \right). \quad (4.30)$$

Since  $\phi^+$  ranges between  $0^\circ$  and  $90^\circ$ ,  $\phi^-$  varies from  $180^\circ$  to  $-90^\circ$  when the system is controlled to eliminate active power ripples. Thus, for bolted faults  $\Delta\theta_{RF}^+$  and  $\Delta\theta_{RF}^-$  is as follows:

- For SLG,  $|V_F^+| = 2/3$  p.u., while  $|V_F^-| = 1/3$  p.u.; thus,  $\Delta\theta_{RF}^\pm$  range is  $[\mp 1.7^\circ, \pm 9.7^\circ]$ .
- For LLG faults,  $|V_F^\pm| = 1/3$  p.u.; thus,  $\Delta\theta_{RF}^\pm$  ranges from  $\mp 2.6^\circ$  to  $\pm 14.9^\circ$ .
- For LL faults,  $|V_F^\pm| = 1/2$  p.u.; thus,  $\Delta\theta_{RF}^\pm$  range is  $[\mp 1.8^\circ, \pm 9.9^\circ]$ .
- During high resistive faults, i.e.,  $|V_F^+| = 0.9$  p.u.,  $\Delta\theta_{RF}^\pm$  varies from  $\mp 1.6^\circ$  to  $\pm 9.1^\circ$ .

On the other hand,  $\phi^-$  for reactive-power ripple elimination varies from  $0^\circ$  to  $90^\circ$ ; thus,  $\Delta\theta_{RF}^-$  equals  $\Delta\theta_{RF}^+$  and the effect of the transmission line on  $\Delta\delta_{RF}^+$  can be neglected.

Table 4.3 and Table 4.4 summarize the effect of the transmission line on  $\Delta\delta_{RF}^+$  and  $\Delta\delta_{RF}^0$ , respectively when the IRES is controlled to eliminate active- and reactive-power ripples. It can be inferred that active power ripple elimination can affect  $\Delta\delta_{RF}^+$  significantly, e.g.,  $-30^\circ$  in LLG faults with high  $R_g$ . On the hand,  $\Delta\delta_{RF}^0$  can vary from  $-15^\circ$  to  $15^\circ$

Table 4.3. Range of  $\Delta\delta_{RF}^+$  and  $\Delta\delta_{RF}^0$  when the IRES is controlled to eliminate active-power ripples

Fault type	Fault resistance	$\Delta\theta_{RF}^-$	$\Delta\theta_{RF}^+$	$\Delta\delta_{RF}^+$	$\Delta\delta_{RF}^0$
AG	bolted	[-9.7,-1.7]	[9.7,1.7]	[-19.4,3.4]	[-9.7,1.7]
	High $R_g$	[-9.1,-1.6]	[9.1,1.6]	[-18.2,3.2]	[-9.1,1.6]
BCG	bolted	[-14.9,-2.6]	[14.9,2.6]	[-29.8,5.2]	[-14.9,2.6]
	High $R_g$	[-14.9,-2.6]	[14.9,2.6]	[-29.8,5.2]	[-14.9,2.6]
	High $R_{ph}$	[-9.1,-1.6]	[9.1,1.6]	[-18.2,3.2]	[-9.1,1.6]
BC	bolted	[-9.9,-1.8]	[9.9,1.8]	[-19.8,3.6]	-
	High $R_{ph}$	[-9.1,-1.6]	[9.1,1.6]	[-18.2,3.2]	-

Table 4.4. Range of  $\Delta\delta_{RF}^+$  and  $\Delta\delta_{RF}^0$  when the IRES is controlled to eliminate reactive-power ripples

Fault type	Fault resistance	$\Delta\theta_{RF}^-$	$\Delta\theta_{RF}^+$	$\Delta\delta_{RF}^+$	$\Delta\delta_{RF}^0$
AG	bolted	[-1.7,9.7]	[-1.7,9.7]	[0,0]	[-1.7,9.7]
	High $R_g$	[-1.6,9.1]	[-1.6,9.1]	[0,0]	[-1.6,9.1]
BCG	bolted	[-2.6,14.9]	[-2.6,14.9]	[0,0]	[-2.6,14.9]
	High $R_g$	[-2.6,14.9]	[-2.6,14.9]	[0,0]	[-2.6,14.9]
	High $R_{ph}$	[-1.6,9.1]	[-1.6,9.1]	[0,0]	[-1.6,9.1]
BC	bolted	[-1.8,9.9]	[-1.8,9.9]	[0,0]	-
	High $R_{ph}$	[-1.6,9.1]	[-1.6,9.1]	[0,0]	-

according to the type of controller. These significant phase shifts can affect the performance of PSM and should be taken into consideration while designing the PSM's zones.

#### 4.4 Proposed Voltage-Angle-Based PSM

According to the analysis conducted in Sections 4.2 and 4.3, the range for  $\delta_R^+$  and  $\delta_R^0$  is determined to allow accurate PSM for different fault resistances, IRES controllers, and fault locations. First,  $\delta_F^+$  and  $\delta_F^0$  are determined for bolted and high resistive faults, as illustrated in Section 4.2. Then,  $\Delta\delta_{RF}^+$  and  $\Delta\delta_{RF}^0$  full ranges are determined for bolted and high resistive faults, separately, by selecting the maximum and minimum shifts deduced



Table 4.5. Range of  $\delta_R^+$  and  $\delta_R^0$  for faults fed by IIRES.

Fault type	Fault resistance	$\Delta\delta_{RF}^+$	$\Delta\delta_{RF}^0$	$\delta_F^+$	$\delta_F^0$	$\delta_R^+$	$\delta_R^0$	$\delta_R^+$	$\delta_R^0$
<b>AG</b>	bolted	[-20,6]	[-10,10]	-180	0	[-200, -174]	[-10,10]	[-200,-96]	[-10,10]
	high	[-19,4]	[-10,10]	-100	0	[-119, -96]	[-10,10]		
<b>BCG</b>	bolted	[-30,9]	[-15,15]	0	0	[-30,9]	[-15,15]	[-30,72]	[-88,10]
	High Rg	[-30,9]	[-15,15]	0	-73	[-30,9]	[-88, -65]		
	High Rph	[-19,4]	[-10,10]	68	0	[49,72]	[-10,10]		
<b>BC</b>	bolted	[-20,7]	-	0	-	[-20,7]	-	[-20,72]	-
	high	[-19,4]	-	68	-	[49,76]	-		

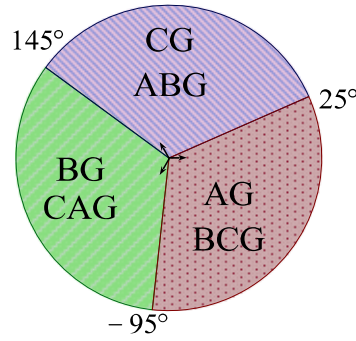


Figure 4.11. Proposed  $\delta_V^0$  zones.

from Section 4.3 for different IIRES's controllers. Hence, the full range of  $\delta_R^+$  and  $\delta_R^0$  for bolted and high resistive faults are determined individually, as shown in Table 4.5. Lastly, the range of  $\delta_R^+$  and  $\delta_R^0$  are deduced by combining the results from bolted and high resistive faults, as presented in Table 4.5. It is worth noting that this method will not add extra computational burden compared with conventional methods because it determines the fault type directly by comparing the voltage angle with predefined zones.

#### 4.4.1 Modified Zones of $\delta_V^0$

It can be deduced that  $\delta_R^0$  for AG and BCG faults can vary from  $-10^\circ$  to  $10^\circ$  and from  $-88^\circ$  to  $10^\circ$ , respectively. Thus, these zones can be combined; then, by extending the zone width to  $120^\circ$ ,  $\delta_V^0$ 's zone for AG and BCG faults ranges from  $-95^\circ$  to  $25^\circ$ . Subsequently, BG and CAG faults can be determined by shifting the BG/CAG zone by  $-120^\circ$ , while CG

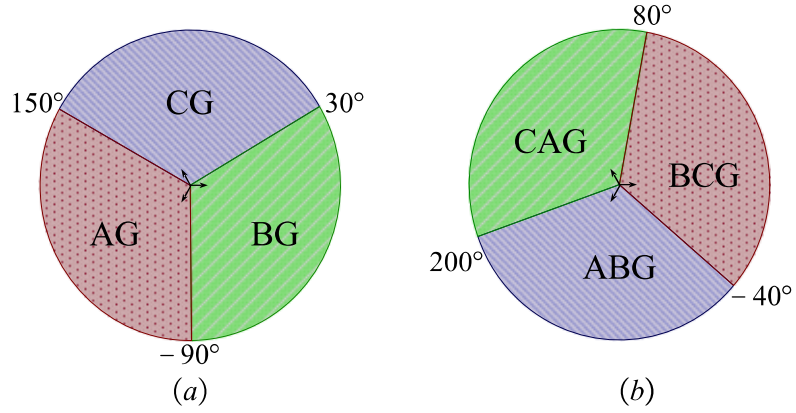


Figure 4.12. Proposed  $\delta_V^+$  zones: (a) SLG zones, (b) LL(G) zones.

and ABG are deduced by shifting the BG/CAG zones by  $120^\circ$ . The proposed zones for  $\delta_V^0$  are depicted in Figure 4.11.

#### 4.4.2 Modified Zones of $\delta_V^+$

It can be observed from Table 4.5 that  $\delta_R^+$  for AG and BC(G) faults are different and cannot be combined. Thus, the zones for AG and BC(G) faults are constructed separately. For an AG fault,  $\delta_R^+$  zone ranges between  $-200^\circ$  and  $-96^\circ$ . Thus, by extending the zone to  $120^\circ$ ,  $\delta_V^+$  zone's range is from  $-210^\circ$  to  $-90^\circ$ . Hence,  $\delta_V^+$  zones for SLG faults are determined, as shown in Figure 4.12(a), by shifting the AG zone by  $120^\circ$  and  $-120^\circ$  for CG and BG faults, respectively. On the other hand,  $\delta_V^+$  zones for BC and BCG faults can be united and their range is from  $-40^\circ$  to  $80^\circ$ . Lastly, LL(G) zones for  $\delta_V^+$  is inferred as depicted in Figure 4.12(b), where AB(G) and CA(G) are determined by shifting BC(G) zone by  $-120^\circ$  and  $120^\circ$ , respectively.

#### 4.4.3 Pinpoint the Fault Type

First,  $\delta_V^0$  is compared with its proposed zones; thus, two types of faults, e.g., AG and BCG faults, can be determined. Thereafter,  $\delta_V^+$  is used to differentiate between SLG and LLG faults. Consequently, the fault type is pinpointed, e.g., if  $\delta_V^+$  is within the AG zone, an AG fault is identified, but if it is located in the BCG zone, a BCG fault is determined. The two types of faults determined by  $\delta_V^0$  zones have different zones when using  $\delta_V^+$ . Thus, the fault type can be determined effectively.

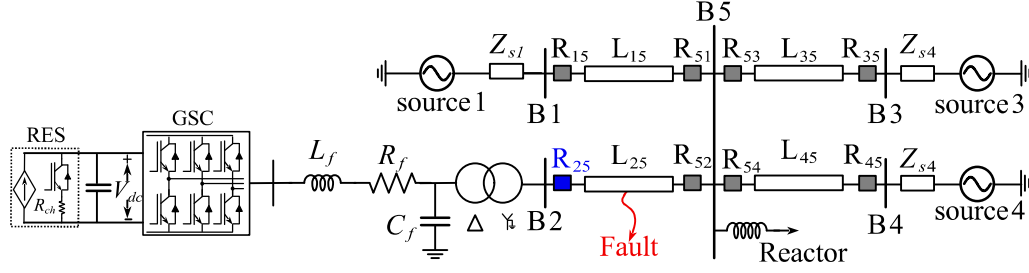


Figure 4.13. Single-line diagram of the test system.

## 4.5 Performance Evaluation

The accuracy of the fault analysis and the effectiveness of the proposed PSM are verified using PSCAD/EMTDC simulations, which are carried out for several fault locations, resistances, types, and IRES controllers. Figure 4.13 represents a 230-kV, 60-Hz transmission system under study, where the subscripts 1, 3, and 4 represent the number of buses connected to a source. Other details and system parameters are provided in Appendix A.

### 4.5.1 Compatibility with Conventional Controllers

Table 4.6 reports the values of  $\delta^+$  and  $\delta^0$  measured at the relay and fault locations and illustrates the transmission line effect on the phase shift between  $\delta_R^+$ ,  $\delta_R^0$  and  $\delta_F^+$ ,  $\delta_F^0$ , respectively, when the IRES is controlled to inject positive-sequence current. The results of Table 4.6 verify the accuracy of the mathematical analysis where the transmission line has a negligible effect on  $\Delta\delta_{RF}^0$  during conventional controllers because  $I_{IBR}^- \approx 0$  and the zero-sequence impedance angle are almost equal for the transmission and interfacing transformer. Furthermore, injecting positive-sequence active current produces a negative value of  $\Delta\delta_{RF}^+$ , whose magnitude depends on fault location, type, and resistance. Increasing the distance between the fault and relay locations increases the value of  $|\Delta\delta_{RF}^+|$ . For instance, during a bolted BC fault,  $\Delta\delta_{RF}^+$  equals  $-8.4^\circ$  and  $-5.2^\circ$  for faults at bus 5 and in the middle of  $L_{25}$ , respectively. Moreover, the value of  $|\Delta\delta_{RF}^+|$  is inversely proportional to  $|V_F^+|$ , e.g.,  $\Delta\delta_{RF}^+$  equals  $-12.5^\circ$  and  $-24.9^\circ$  for bolted AG and BCG faults at bus 5, respectively, where  $|V_F^+|$  approximately equals 0.67 p.u. and 0.33 p.u., respectively.

Table 4.6. Active power generation during conventional controller

	$R_g$	$R_{ph}$	Fault at 50% of $L_{25}$						Fault at bus 5					
			$\delta_F^+$	$\delta_R^+$	$\Delta\delta_{RF}^+$	$\delta_F^0$	$\delta_R^0$	$\Delta\delta_{RF}^0$	$\delta_F^+$	$\delta_R^+$	$\Delta\delta_{RF}^+$	$\delta_F^0$	$\delta_R^0$	$\Delta\delta_{RF}^0$
AG	0	-	180	173.3	-6.7	0	0	0	180.3	167.8	-12.5	0	0	0
	50	-	-127.6	-130.9	-3.3	0.3	0.4	0.1	-118.7	-126.3	-7.6	0.2	0.5	0.3
BCG	0	0	0	-14.7	-14.7	0	0	0	0	-24.9	-24.9	0	-0.1	-0.1
	0	50	61.1	55.5	-5.6	-6.5	-6.5	0	73.1	64.3	-8.8	5.6	6.2	0.6
	50	0	0	-9	-9	-66.3	-66	0	0	-17.9	-17.9	-68.9	-69	-0.1
BC	-	0	0	-8.6	-8.6	-	-	-	0	-17.4	-17.4	-	-	-
	-	50	55.3	50.1	-5.2	-	-	-	67	58.6	-8.4	-	-	-

Further,  $\Delta\delta_{RF}^+$  is equal to  $-12.5^\circ$  and  $-9.2^\circ$  for bolted and high resistive AG faults, respectively, where  $|V_F^+|$  is almost equal to 0.33 p.u. and 0.9 p.u., respectively. On the other hand, Table 4.6 confirms the correctness of the proposed zones in determining the fault type accurately, where  $\delta_R^+$  and  $\delta_R^0$  are settled in their corresponding fault-type zones. For example,  $\delta_R^+$  and  $\delta_R^0$  are equal to  $64.3^\circ$  and  $6.2^\circ$ , respectively, for a BCG fault with  $R_{ph} = 50 \Omega$  that occurred at bus 5, it is worth mentioning that the zones proposed in [11] fail to determine the correct fault type because the maximum limit for  $\delta_R^+$  was set at  $60^\circ$ .

Table 4.7 demonstrates the effect of the conventional IRES's controller, when it injects reactive-positive-sequence current, on the values of  $\Delta\delta_{RF}^+$  and  $\Delta\delta_{RF}^0$  and verifies the accuracy of the proposed PSM zones. In light of the results, the accuracy of the proposed short-circuit analysis is assured.  $\Delta\delta_{RF}^0$  is  $0^\circ$  similar to Table 4.6, while  $\Delta\delta_{RF}^+$  has a positive value. The values of  $\Delta\delta_{RF}^+$  increases for far faults, e.g.,  $\Delta\delta_{RF}^+$  is  $0.8^\circ$  and  $2.3^\circ$  for faults at 10% and 50% from  $L_{25}$ , respectively. However, increasing  $|V_F^+|$  decreases  $\Delta\delta_{RF}^+$ . For illustration,  $\Delta\delta_{RF}^+$  is equal to  $0.2^\circ$ ,  $1^\circ$ ,  $1.4^\circ$ , and  $2.3^\circ$  when  $|V_F^+|$  approximately equals 0.9, 0.67, 0.5, and 0.3 p.u., respectively, for faults at 50% of  $L_{25}$ . Further, it can be deduced that  $\delta_R^+$ ,  $\delta_R^0$ ,  $\delta_F^+$ , and  $\delta_F^0$  falls correctly in their respective fault type zones. For instance, for a BG fault at 50% of  $L_{25}$  and  $R_g = 50 \Omega$ ,  $\delta_R^+ = -8.5^\circ$  and  $\delta_R^0 = -120^\circ$ , which settles in their correct zones, respectively. It is worth mentioning that at a high value of  $R_g$ ,  $\delta_F^0$  is almost similar to a bolted fault condition, while  $\delta_F^+$  is shifted by about  $60^\circ$ , as explained in the short circuit analysis.

Table 4.7. Reactive power generation during conventional controller

	$R_g$	$R_{ph}$	Fault at 10% of $L_{25}$						Fault at 50% of $L_{25}$					
			$\delta_F^+$	$\delta_R^+$	$\Delta\delta_{RF}^+$	$\delta_F^0$	$\delta_R^0$	$\Delta\delta_{RF}^0$	$\delta_F^+$	$\delta_R^+$	$\Delta\delta_{RF}^+$	$\delta_F^0$	$\delta_R^0$	$\Delta\delta_{RF}^0$
BG	0	-	-60	-59.8	0.2	-120	-120	0	-60	-59	1	-120	-120	0
	50	-	-8.6	-8.5	0.1	-120	-120	0	-8.6	-8.5	0.1	-120	-120	-0.1
CAG	0	0	120	120.8	0.8	-120	-120	0	120	122.3	2.3	-120	-120	0
	0	50	169	169.6	0.2	-148	-148	0	-178.9	-178	0.9	-127	-127	0
	50	0	120	120.3	0.3	167	167	0	120	121.5	1.5	173.7	174	0
CA	-	0	120	120.3	0.3	-	-	-	120	121.4	1.4	-	-	-
	-	50	168	168.1	0.2	-	-	-	175.3	176.1	0.8	-	-	-

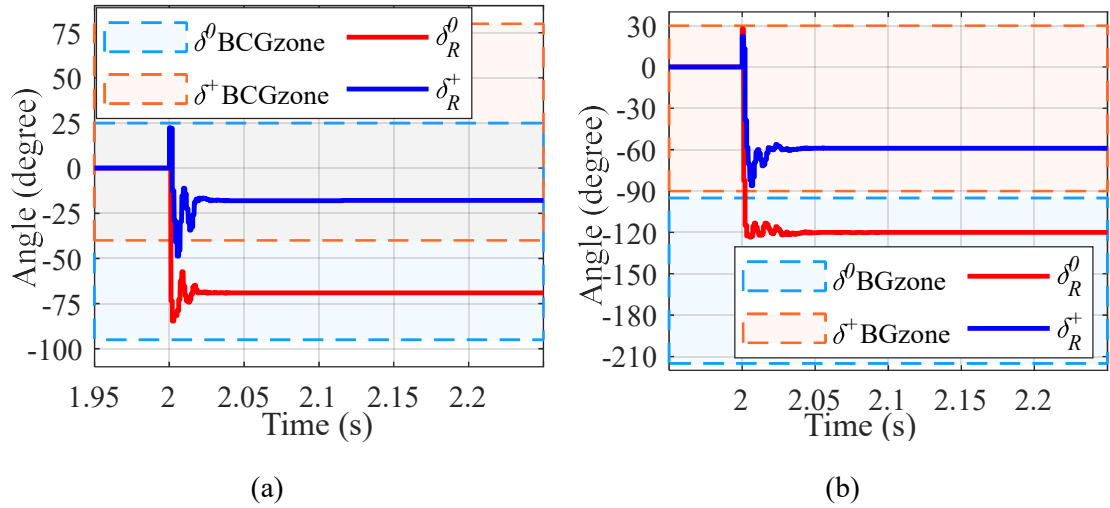


Figure 4.14. Performance of the proposed PSM during conventional controller: (a) a BCG fault at bus 5, (b) a BG fault at 50% of  $L_{25}$ .

Figure 4.14 demonstrates a case study from Tables 4.6 and 4.7 to ensure the accuracy of the proposed method. Figure 4.14(a) represents a BCG fault at bus 5, when the IRES injects a unity power factor current. The results show that both  $\delta_R^+$  and  $\delta_R^0$  settle correctly within the proposed zones in less than half a cycle. In addition,  $\delta_R^+$  and  $\delta_R^0$  are placed in their zones with adequate margins from their zone limits, i.e., about  $25^\circ$ . On the other hand, Figure 4.14(b) exhibits the results for a bolted BG fault at 50% of  $L_{25}$  when the IRES is injecting reactive current. The results show that  $\delta_R^+$  and  $\delta_R^0$  are placed in their correct zones

Table 4.8. IIRES's controller following the German grid code, when  $K = 6$

	$R_g$	$R_{ph}$	Fault at 50% of $L_{25}$						Fault at bus 5					
			$\delta_F^+$	$\delta_R^+$	$\Delta\delta_{RF}^+$	$\delta_F^0$	$\delta_R^0$	$\Delta\delta_{RF}^0$	$\delta_F^+$	$\delta_R^+$	$\Delta\delta_{RF}^+$	$\delta_F^0$	$\delta_R^0$	$\Delta\delta_{RF}^0$
CG	0	-	61	63.5	2.5	122	123.7	1.7	60.5	64.8	4.3	121	124	3
	50	-	117.4	116.6	-0.8	122	123.7	1.7	123.2	120.7	-2.5	121	125	3.6
ABG	0	0	-120	-116	3.7	120	121.7	1.7	-120	-113.8	6.2	120	123	2.8
	0	20	-67.5	-64.6	2.9	122	123.5	1.7	-56.4	-51.9	4.5	130	133	3
	50	0	-120	-117	2.9	53.7	55.4	1.7	-120	-115.1	4.9	51.1	53.9	2.8
AB	-	0	-120	-117	2.8	-	-	-	-120	-115.2	4.8	-	-	-
	-	20	-76.7	-74.2	2.5	-	-	-	-64.7	-60.6	4.1	-	-	-

for both transient and steady-state conditions. In which,  $\delta_R^+$  settled at  $-59^\circ$ , while  $\delta_R^0$  settled at  $-120^\circ$ , which is almost equal to the mathematical results for a bolted BG fault.

#### 4.5.2 Compatibility with Recent Grid Codes

In this section, the precision of the proposed PSM zones when the IIRES is controlled to follow the new German GC is validated. Moreover, the correctness of the mathematical analysis, which studies the effect of the transmission line on  $\Delta\delta_{RF}^+$  and  $\Delta\delta_{RF}^0$  is confirmed. Table 4.8 displays the values of  $\delta_R^+$ ,  $\delta_R^0$ ,  $\delta_F^+$ ,  $\delta_F^0$ ,  $\Delta\delta_{RF}^+$  and  $\Delta\delta_{RF}^0$ , when  $K = 6$ , for faults at 50% of  $L_{25}$  and bus 5. All the values of  $\delta_R^+$  and  $\delta_R^0$  demonstrated in Table 4.8 lay in the proposed zones correctly with minimum margins of  $10^\circ$  and  $25^\circ$  for  $\delta_R^+$  and  $\delta_R^0$ , respectively. For instance, when an ABG fault occurs at bus 5 with  $R_{ph} = 20 \Omega$ ,  $\delta_R^+$  is  $-51.9^\circ$  and  $\delta_R^0$  is  $133^\circ$ , which are placed in their correct fault type zones. On the other hand, the zones proposed in [11] fail to determine the fault type properly. In addition, the results show that the value of  $\Delta\delta_{RF}^0$  is positive and varies between  $1.7^\circ$  to  $3.6^\circ$  which coincides with the analysis in Subsection 4.3.2.B. Moreover,  $\Delta\delta_{RF}^+$  has positive values for bolted faults and range from  $4.2^\circ$  to  $6.2^\circ$  for faults at bus 5. On the other hand,  $\Delta\delta_{RF}^+$  is negative for SLG faults when  $R_g = 50 \Omega$ . For instance,  $\Delta\delta_{RF}^+ = -0.8^\circ$  and  $-2.5^\circ$  for a CG fault at 50% of  $L_{25}$  and bus 5, respectively. However,  $\Delta\delta_{RF}^+$  is positive for high resistive LLG faults because the fault resistance is not sufficient to enforce the IIRES to inject active-positive-sequence current.

Table 4.9 IIRES's controller following the German grid code, when  $K = 2$ 

	$R_g$	$R_{ph}$	Fault at 10% of $L_{25}$						Fault at 50% of $L_{25}$					
			$\delta_F^+$	$\delta_R^+$	$\Delta\delta_{RF}^+$	$\delta_F^0$	$\delta_R^0$	$\Delta\delta_{RF}^0$	$\delta_F^+$	$\delta_R^+$	$\Delta\delta_{RF}^+$	$\delta_F^0$	$\delta_R^0$	$\Delta\delta_{RF}^0$
BG	0	-	-59.5	-59.4	0.1	-118	-118	0.2	-59.4	-61.1	-1.7	-119	-118	0.8
	50	-	-3.5	-4	-0.5	-118	-118	0.1	-5.2	-8.2	-3	-119	-118	0.8
CAG	0	0	120	120.8	0.8	-120	-120	0.2	120	122.3	2.3	-120	-119	0.8
	0	20	161.5	161.1	-0.4	-142	-141	0.2	168.2	166	-2.2	-122	-121	0.7
	50	0	120	120.4	0.4	167	168	0.2	120	121.5	1.5	174	174.5	0.8
CA	-	0	120	120.3	0.3	-	-	-	120	121.4	1.4	-	-	-
	-	20	152.2	152	-0.2	-	-	-	158.5	157.3	-1.2	-	-	-

Table 4.9 displays the measured values of  $\delta^+$  and  $\delta^0$  at the relay and fault locations and their variations when  $K = 2$ . It can be deduced that  $\Delta\delta_{RF}^0$  has a positive value, and it is affected by the fault location. For instance,  $\Delta\delta_{RF}^0$  equals 0.3 and 0.8 p. u. for bolted CAG faults at 10% and 50% of  $L_{25}$ , respectively. In addition,  $\Delta\delta_{RF}^0$  is almost constant, i.e.,  $\Delta\delta_{RF}^0 \approx 0.8^\circ$ , in different fault types and fault resistance, because the IIRES's current does not exceed its maximum thermal limit. On the other hand, the value of  $\Delta\delta_{RF}^+$  is affected by fault location and resistance. At high resistive faults, i.e.,  $R_g = 50\Omega$  and  $R_{ph} = 20\Omega$ , for SLG and LL(G) faults, respectively,  $\Delta\delta_{RF}^+$  is negative because the IIRES's current is mainly composed of active current components. On the other hand, for bolted faults at 50% of  $L_{25}$ , it can be observed that  $\Delta\delta_{RF}^+$  equals  $-1.7^\circ$  for SLG faults and equals  $2.3^\circ$  and  $1.4^\circ$  for LLG and LL faults, respectively, which agrees with the theoretical analysis. The difference in  $\Delta\delta_{RF}^+$  signs for SLG and LL(G) bolted faults when  $K = 2$  occurs because  $\Delta V^+$  is small during SLG faults, thus,  $I_q^+$  is small and the IIRES can inject an active-positive sequence current that is responsible for the negative sign. However, for LL and LLG bolted faults,  $\Delta V^+$  is sufficient to enforce the IIRES to inject only positive-sequence reactive current, which leads to a positive value of  $\Delta\delta_{RF}^+$  like the values determined from the mathematical analysis. The results also assert the accuracy of the chosen fault type zones as all angles lay in their respective zones.

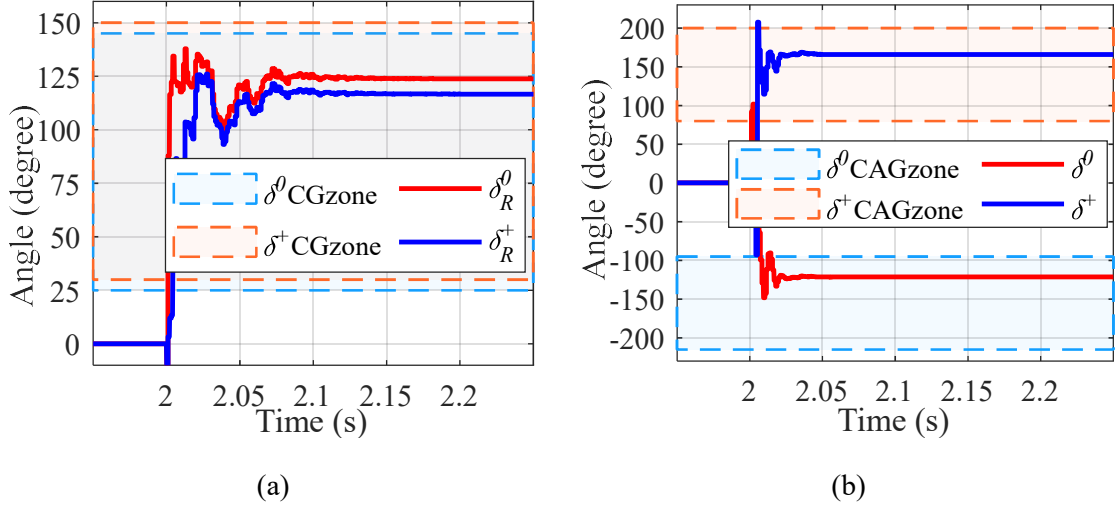


Figure 4.15. Performance of the proposed PSM, when the IRES follows the new German GC for a fault at 50% of  $L_{25}$ : (a) a CG fault, (b) a CAG fault.

Figures 4.15(a) and (b) exhibit a case study from Table 4.8 and Table 4.9, respectively, for faults at 50% of  $L_{25}$ , when the IRES is controlled to follow the new German GC. Figure 4.15 (a) presents the results for a CG fault when  $K = 6$ . The measured  $\delta_R^+$  and  $\delta_R^0$  are equal to  $116.6^\circ$  and  $123.7^\circ$ , which are located in their corresponding fault-type zones. In addition, it can be observed that the PSM can determine the fault type in less than half a cycle from fault inception. On the other hand, Figure 4.15(b) displays the results when  $K = 2$ .  $\delta_R^+$  and  $\delta_R^0$  are placed inside their correct zone with and away from the maximum limit by about  $30^\circ$  and  $20^\circ$ , respectively.

#### 4.5.3 Compatibility with Active and Reactive Power Ripple Mitigation

In this subsection, the mathematical analysis and the proposed PSM accuracy are verified, when the IRES is controlled to eliminate either active- or reactive-power ripples. Table 4.10 displays the measured angles for faults that take place on bus 5, when the IRES is injecting positive-sequence active current and eliminating either active- or reactive-power ripples. It can be observed from Table 4.10 that  $|\Delta\delta_{RF}^0|$  has almost the same value in both the active- and reactive-power ripple elimination cases, but they have opposite signs for  $\Delta\delta_{RF}^0$ . For example,  $\Delta\delta_{RF}^0$  equals  $-8.3^\circ$  and  $8.5^\circ$ , when the IRES is controlled to



Table 4.10. Active and reactive-power ripple mitigation when the positive-sequence current is injecting active current

	$R_g$	$R_{ph}$	Active-power ripple elimination						Reactive-power ripple elimination					
			$\delta_F^+$	$\delta_R^+$	$\Delta\delta_{RF}^+$	$\delta_F^0$	$\delta_R^0$	$\Delta\delta_{RF}^0$	$\delta_F^+$	$\delta_R^+$	$\Delta\delta_{RF}^+$	$\delta_F^0$	$\delta_R^0$	$\Delta\delta_{RF}^0$
AG	0	-	177.9	160.9	-17	-3.7	-11.9	-8.2	182.4	182.4	0	4.2	12.6	8.4
	50	-	-123	-132.5	-9.8	-3.8	-10.5	-6.7	-116	-116	-0.2	3.6	10.7	7.1
BCG	0	0	0	-24.6	-24.6	0	-11.7	-11.7	0	0	0	0	13.7	13.7
	0	40	68.3	53	-15.3	4	-3.5	-7.5	74	73.9	-0.1	8.8	17	8.2
	50	0	0	-18.5	-18.5	-68.9	-77.8	-8.9	0	0	0	-68.9	-58.9	10
BC	-	0	0	-18.2	-18.2	.	.	.	0	0	0	.	.	.
	-	40	61.7	47	-14.7	.	.	.	67.5	67.4	-0.1	.	.	.

eliminate active- and reactive-power ripples for a bolted AG fault, respectively. This is because  $\phi^-$  is equal to  $\phi^+ + 180^\circ$  and  $\phi^+$  for active- and reactive-power ripple mitigations, respectively. In addition, the measured values match theoretical calculations results, e.g., the maximum calculated value of  $|\Delta\delta_{RF}^0|$  in LLG is equal to  $14.9^\circ$ , which is slightly higher than the measured value, i.e.,  $13.7^\circ$ . This small difference is expected because the mathematical calculations are determined when the angle difference between  $\theta_V^+$  and  $\theta_V^-$  produce maximum  $|I_{IBR}^+|$ . In addition, the results verify the accuracy of the calculated values of  $\Delta\delta_{RF}^+$  in both active- and reactive-power ripple mitigations. For instance,  $\Delta\delta_{RF}^+$  is almost equal to  $0^\circ$  for reactive-power ripple mitigation and equals a negative value that varies according to the fault type and resistance when the IRES is controlled to eliminate active power ripples. For example, for a BCG fault when the IRES is injecting active current and eliminating active-power ripples,  $\Delta\delta_{RF}^+$  equals to  $-24.6^\circ$ ,  $-15.3^\circ$ , and  $-18.5^\circ$  for bolted,  $R_{ph} = 40 \Omega$ , and  $R_g = 50 \Omega$ , respectively. Furthermore, the measured values of  $\delta_R^+$  and  $\delta_R^0$  are placed correctly in their correct fault-type zones. For example,  $\delta_R^+$  and  $\delta_R^0$  are equal to  $-18.5^\circ$  and  $-77.8^\circ$ , respectively, for an BCG fault with  $R_g = 50 \Omega$ .

Table 4.11 demonstrates the results when the IRES injects reactive current and eliminates active or reactive power ripples. It can be observed that  $\Delta\delta_{RF}^0$  and  $\Delta\delta_{RF}^+$  shown in Table 4.11 are opposite in sign compared to results in Table 4.10, which agrees with the

Table 4.11. Active and reactive-power ripple mitigation when the positive-sequence current is injecting Reactive current

	$R_g$	$R_{ph}$	Active-power ripple elimination						Reactive-power ripple elimination					
			$\delta_F^+$	$\delta_R^+$	$\Delta\delta_{RF}^+$	$\delta_F^0$	$\delta_R^0$	$\Delta\delta_{RF}^0$	$\delta_F^+$	$\delta_R^+$	$\Delta\delta_{RF}^+$	$\delta_F^0$	$\delta_R^0$	$\Delta\delta_{RF}^0$
CG	0	-	60.4	63.7	3.3	120.6	121.9	1.3	59.6	59.6	0	119.3	117.8	-1.5
	50	-	102.4	104.9	2.5	120.5	121.5	1	100.3	100.3	0	119.3	117.8	-1.5
ABG	0	0	-120	-115.6	4.4	120	121.5	1.5	-120	-119.9	0.1	120	117.7	-2.3
	0	40	-48.1	-45.3	2.8	127.3	128.4	1.1	-51	-51	0	123.8	122.3	-1.5
	50	0	-120	-116.4	3.6	51.1	52.3	1.2	-120	-119.9	0.1	65.3	63.5	-1.8
AB	-	0	-120	-116.7	3.3	..	.	.	-120	-120	0	..	.	.
	-	40	-55	-52.8	2.2	.	.	.	-57.3	-57.3	0	.	.	.

mathematical analysis. In light of the results of a bolted AG fault,  $\Delta\delta_{RF}^0$  equals  $1.3^\circ$  and  $-1.5^\circ$  for active and reactive power elimination, respectively, which is slightly smaller than the maximum value determined from mathematical analysis, i.e.,  $1.7^\circ$  and  $-1.7^\circ$ , respectively. Further,  $\Delta\delta_{RF}^+ = 0$  in reactive-power ripple elimination, which coincides with the mathematical analysis. Moreover,  $\Delta\delta_{RF}^+ = 2.6^\circ$ , which is slightly lower than the maximum shift calculated analytically, i.e.,  $3.4^\circ$ . Furthermore, the results verify the accuracy of the proposed zones in determining the fault type accurately.

Figure 4.16(a) displays a sample result from Table 4.10 for a BCG fault at  $R_{ph} = 40 \Omega$ , when the IRES injects active current and eliminates reactive-power ripples.  $\delta_R^0$  settled at  $17^\circ$  because  $\Delta\delta_{RF}^0 = 9^\circ$ , as shown in Table 4.10. This verifies the accuracy of both mathematical analysis and fault-type zones. As shown in Figure 4.16(a),  $\delta_R^+$  settles at  $73.9^\circ$  its correct zone with a  $6^\circ$  margin from its limit. It is worth noting that zones in [11] fail to determine this type of fault properly. On the other hand, Figure 4.16(b) reveals the dynamics of a sample case study from Table 4.11 for an ABG fault with  $R_g = 50 \Omega$ , when the IRES injects reactive current and eliminates active-power ripples. The results verify the accuracy of the proposed zones in determining the fault type while eliminating the active and reactive power ripples. For instance,  $\delta_R^+ = -116.4^\circ$  and  $\delta_R^0 = 52.3^\circ$ , respectively, lays in their correct fault-type zones. In addition, the PSM determines the fault type in less than half a cycle.

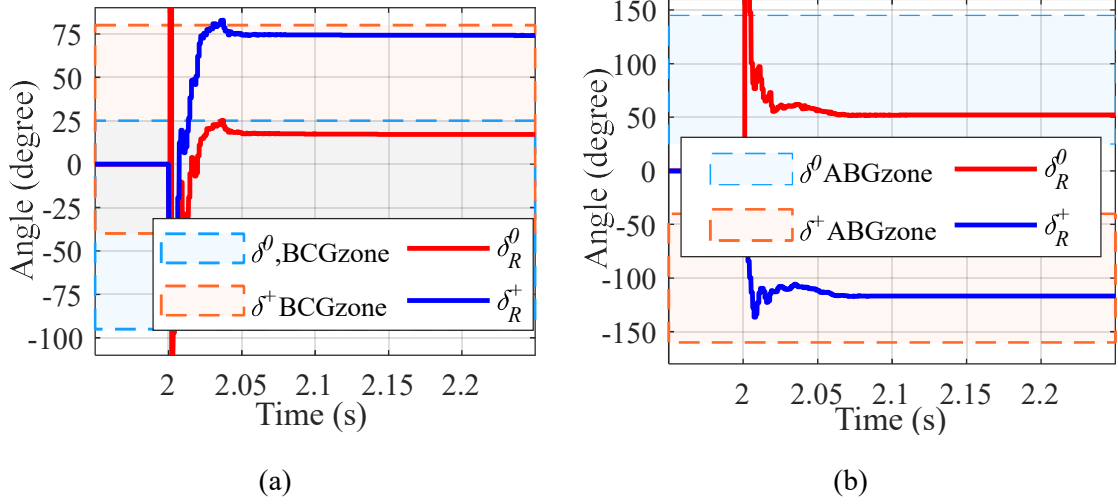


Figure 4.16. Performance of proposed PSM for a fault at bus 5 during reactive and active power ripples: (a) a BCG fault, (b) an ABG fault.

## 4.6 Conclusions

The exotic fault currents from the IIREs could introduce a phase shift between the voltage angle measured at the relay and fault locations, which introduces challenges to the voltage-angle-based PSM. In this chapter, the root causes for the failure of the voltage-angle-based PSM, which is based on the relative angles between sequence voltage measured at relay locations, i.e.,  $\delta_R^0$  and  $\delta_R^+$ , are elaborated. First, short circuit analysis at the fault location is investigated to determine the relative angles between sequence voltage measured at fault locations, i.e.,  $\delta_F^0$  and  $\delta_F^+$ . Then,  $\delta_R^0$  and  $\delta_R^+$  are determined by analyzing the transmission line effect on the angle difference between sequence voltages measured at the relay and fault locations. Further, new PSMs' zones are designed to guarantee precise fault type identification for different fault resistances. Simulation studies substantiate the effectiveness of the proposed method with various IIREs controllers and fault conditions, i.e., ground and arc resistances, fault types, and fault locations.

## Chapter 5

# Fault Ride Through of Inverter-Interfaced Renewable Energy Sources for Enhanced Resiliency and Grid Code Compliance

### 5.1 Introduction

In Chapters 3 and 4, the relay algorithm has been modified to tackle the erroneous operation of PSMs during fault currents supplied by IIRESSs. Replacing the current traditional relays with these solutions is necessary, but it can be a time-consuming process and may result in a significant expense due to the need to replace the currently deployed relays. On the other hand, modifying the IIRESS to enable the correct operation of conventional PSM can be considered a faster solution with lower cost. This chapter develops two DCCs that regulate the inverter's negative- and positive-sequence currents to simultaneously meet phase selection and RCG requirements. First, the negative-sequence-current angle is obtained based on the angles of both zero- and positive-sequence currents to enable a correct operation for phase selection. Then, the positive-sequence current angle is adjusted to reach a trade-off between RCG requirements and phase selection achieved by the negative-sequence current. Lastly, the reference currents of the IIRESS are generated in the stationary frame without violating the inverter's current limits. The proposed DCCs support the grid voltage by meeting the RCG requirements and enhancing the grid's reliability and resilience by enabling correct phase selection. Comprehensive time-domain simulations verify the precise operation of the proposed DCCs under various fault conditions and GCs. In addition, real-time simulations are performed to validate the proposed approach.

### 5.2 Problem Statement

The most common PSM depends on comparing the angles between the measured sequence currents as follows: (i) the relative angle between the negative- and zero-sequence current, i.e.,  $\delta^0 = \angle I^- - \angle I^0$ , is determined and compared with zones depicted in Figure 5.1(a),

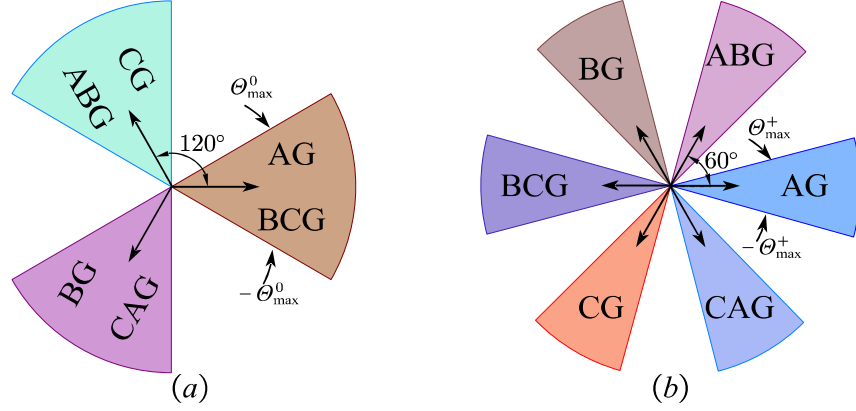
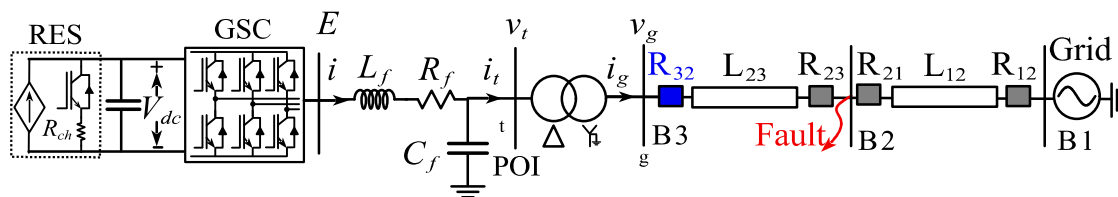


Figure 5.1. Current-angle-based PSM zones for (a)  $\delta^0$ , (b)  $\delta^+$ .

which identify two types of faults, (ii) the relative angle between the negative- and positive-sequence currents, i.e.,  $\delta^+ = \angle I^- - \angle I^+$ , is determined and compared with the positive-sequence zones shown in Figure 5.1(b) [48], [69]. For illustration, if  $\delta^0$  falls between  $\theta_{max}^0$  and  $-\theta_{max}^0$ , where  $\theta_{max}^0$  is half the zone boundary measured relative to the  $\delta^0$ 's fault-type-zone bisector, i.e.,  $\delta_{F,bis}^0$ , then it is either an AG or BCG fault. Then, by measuring  $\delta^+$ , an AG fault can be determined if  $\theta_{max}^+ \leq \delta^+ \leq -\theta_{max}^+$ , where  $\theta_{max}^+$  is half the zone boundary relative to the  $\delta^+$ 's fault-type-zone bisector, i.e.,  $\delta_{F,bis}^+$ . However, a BCG fault is determined if  $180^\circ + \theta_{max}^+ \leq \delta^+ \leq 180^\circ - \theta_{max}^+$ . It is worth mentioning that increasing the boundary width of  $\theta_{max}^0$  or/and  $\theta_{max}^+$  increases the speed of fault detection and its reliability. The most common values for  $\theta_{max}^0$  and  $\theta_{max}^+$  are  $60^\circ$  and  $30^\circ$ , respectively [9]. Although the commercial current-angle-based PSM is an accurate method for determining the faulty phase(s) in conventional grids, the peculiar IRES fault current signatures can lead to incorrect operation. The maloperation of commercial PSMs was first reported in [11]. Thereafter, a few IRES control methods are proposed to assist commercial relays with the main focus on protection objectives.

A 34.5-kV, 60-Hz test system modeled in MATLAB/Simulink environment is used to clarify that relevant controllers in the literature do not simultaneously achieve the current-angle-based PSM and RCG requirements by GCs. The test system displayed in Figure 5.2 includes a 9.2-MW IRES. The RES block in Figure 5.2 represents an energy source, e.g., a photovoltaic (PV) array or wind turbine, along with a source-side converter. The time



span associated with renewable energy variations is significantly longer than the short fault period. Further, the dc-link capacitor decouples the fast dynamics of the RES block from those of the grid and eliminates current ripples. Therefore, the RES block is modeled by a controllable current source behind a chopper circuit, which limits the dc-link voltage during faults [34]. The grid-side converter (GSC) block is modeled as a three-phase two-level inverter, which is controlled to inject current at 0.95 lagging power factor (PF) to follow the Electric Reliability Council of Texas (ERCOT) GCs (ERCOT-GCs), as an example of the North American GCs [76], [77]. The IRES is connected to a 14-MW, 4.16/34.5 kV dYG transformer with an impedance of 0.1 p.u. It is worth mentioning that the dYG connection is considered a recommended connection for the interconnection of IRESs by many utilities, e.g., Xcel Energy [78], as reported by the Electric power research institute (EPRI) [79]. This connection is recommended because it facilitates rapid detection of ground faults on the utility side, blocks third harmonic current flowing from the IRES to the grid, and hinders overvoltage and resonance issues.

Figure 5.3 demonstrates the angle measurements by relay  $R_{32}$  during a solid AG fault at bus 2, where the inverter controls the negative-sequence current angle to achieve an adequate  $\delta^0$ , as suggested in [63]. The results exhibit that  $\delta^0$  is correctly located near the center of its respective AG zone. However,  $\delta^+$  is laid outside the maximum limits of the  $\delta^+$  AG zone. This occurs as the authors maintained the output PF equals 0.95 lagging at the expense of precise phase selection. On the other hand, the response to a bolted BCG fault is depicted in Figure 5.4, when the controller is designed to regulate the negative-sequence current angle to achieve a specific  $\delta^+$  following [63]. It is clear that the controller

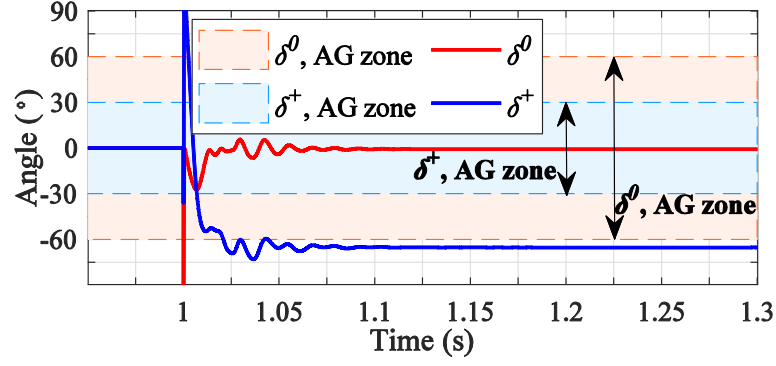


Figure 5.3. Measured  $\delta^0$  and  $\delta^+$  by  $R_{32}$  for a bolted AG fault.

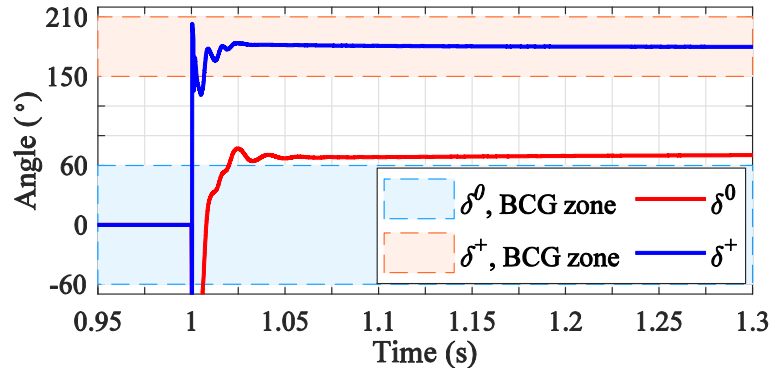


Figure 5.4. Measured  $\delta^0$  and  $\delta^+$  by  $R_{32}$  for a bolted BCG fault.

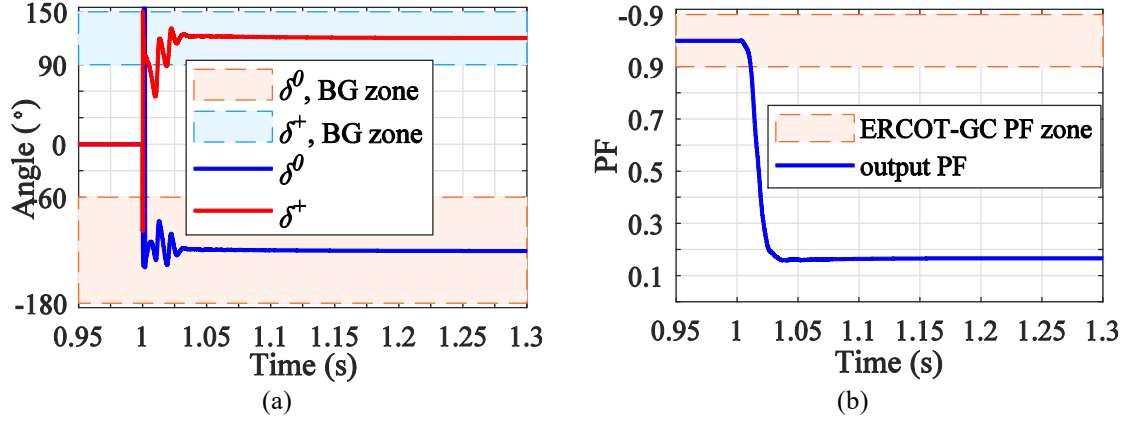


Figure 5.5. Measured quantities by  $R_{32}$  for a bolted BG fault when the IRES is controlled based on [24]: (a)  $\delta^0$  and  $\delta^+$ , (b) output power factor.

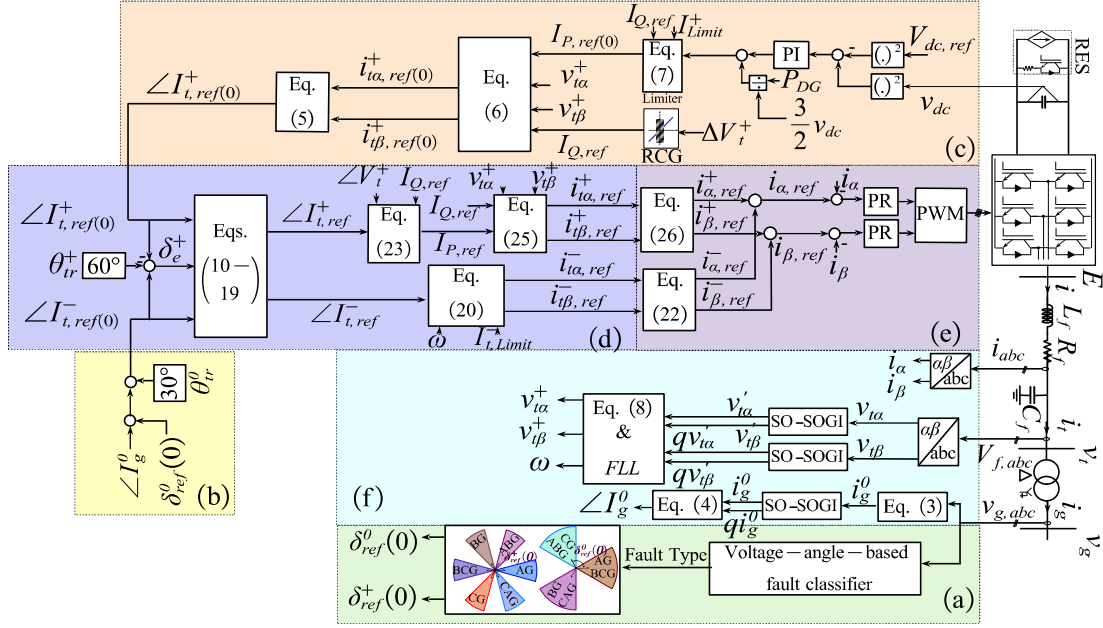


Figure 5.6. Structure of the proposed DCC1: (a) Determining  $\delta_{F,bis}^0$  and  $\delta_{F,bis}^+$ , (b) Determining  $\angle I_{t,ref}^+(0)$ , (c) Determining  $\angle I_{t,ref}^-(0)$ , (d) Generating  $\angle I_{t,ref}^-$  and  $\angle I_{t,ref}^+$ , (e) Generating and controlling  $I_{ref}^-$  and  $I_{ref}^+$ , (f) AC Measurement unit.

accurately places  $\delta^+$  near the middle of the  $\delta^+$  BCG zone. Nevertheless, the measured  $\delta^0$  exceeds  $\delta^0$ 's BCG upper-zone limit. Moreover, testing the controller in [65] for a bolted BG fault demonstrates its ability to settle  $\delta^0$  and  $\delta^+$  in their correct zones, as portrayed in Figure 5.5(a). However, Figure 5.5(b) illustrates that the IRES's PF exceeds the permissible limits imposed by ERCOT. For instance, the IRES output PF is 0.16 lagging, while the accepted PF should lay between  $\pm 0.9$ . Thus, it violates the ERCOT-GCs requirements. These results highlight the need for an enhanced controller to precisely set both  $\delta^0$  and  $\delta^+$  in their proper zones, while complying with RCG requirements.

### 5.3 Proposed Dual Current Controller for PSM and GC Compliance

The proposed DCC1, depicted in Figure 5.6, aims to regulate the IRES negative- and positive-sequence current angles to ensure accurate operation of the current-angle-based PSM and comply RCG requirements imposed by various GCs. The commercial current-angle-based PSM identifies the fault type by comparing the measured values of  $\delta^0$  and  $\delta^+$  with the zones displayed in Figure 5.1. Thus, the IRES should be controlled to reach a



trade-off between tracking appropriate reference values of  $\delta^0$  and  $\delta^+$  (i.e.,  $\delta_{ref}^0$  and  $\delta_{ref}^+$ ) and injecting adequate reactive currents as per the GC requirements. The proposed DCC1 is designed in five stages as follows:

### 5.3.1 Stage I. Initial Values of $\delta_{ref}^0$ and $\delta_{ref}^+$

The first step is determining the fault type at the inverter side using the voltage-angle-based PSM proposed in Chapter 4, which relies on the relative angles between sequence voltages. Consequently,  $\delta_{F,bis}^0$  and  $\delta_{F,bis}^+$  are determined by comparing the fault type with the current-angle-based PSM's zones shown in Figure 5.1. These angles, i.e.,  $\delta_{F,bis}^0$  and  $\delta_{F,bis}^+$ , are selected as the initial reference for  $\delta_{ref}^0$  and  $\delta_{ref}^+$ , respectively. The steps of Stage I are displayed in Figure 5.6(a). For example, for an AG fault, both  $\delta_{F,bis}^0$  and  $\delta_{F,bis}^+$  should be set at zero. However, for an ABG fault,  $\delta_{F,bis}^0$  and  $\delta_{F,bis}^+$  should be  $120^\circ$  and  $60^\circ$ , respectively.

### 5.3.2 Stage II. Initial Reference Angle of the Negative-Sequence Current

The initial reference angle of the negative-sequence current at the POI  $\angle I_{t,ref(0)}^-$ , which makes  $\delta^0$  follow  $\delta_{F,bis}^0$  at the transformer's grid side is calculated by

$$\angle I_{t,ref(0)}^- = \delta_{F,bis}^0 + \angle I_g^0 + \theta_{tr}^- \quad (5.1)$$

where  $\angle I_g^0$  is the zero-sequence current angle measured at the transformer grid-side and  $\theta_{tr}^-$  is the negative-sequence current phase shift between the IRES and grid sides of the transformer, where  $\angle I_t^- = \angle I_g^- + \theta_{tr}^-$ . For instance, if the transformer's IRES side is connected in delta, while the grid side is connected in star,  $\angle I_t^-$  leads  $\angle I_g^-$  by  $30^\circ$ ; thus,  $\theta_{tr}^- = 30^\circ$ .  $\angle I_g^0$  in (5.1) is calculated from the instantaneous value of the zero-sequence current ( $i_g^0$ ), which is determined using the measured phase currents on the transformer's grid side, i.e.,

$$i_g^0 = \frac{1}{3} (i_g^a + i_g^b + i_g^c) = |I_g^0| \sin(\omega t + \angle I_g^0) \quad (5.2)$$

where  $|I_g^0|$  denotes the magnitude of the zero-sequence current on the transformer's grid

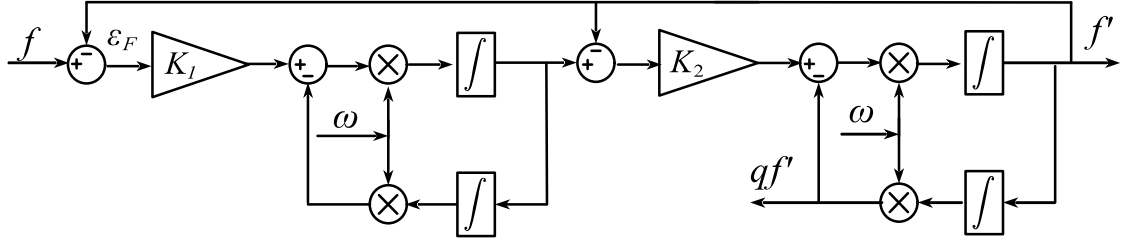


Figure 5.7. The double second-order generalized integrator structure.

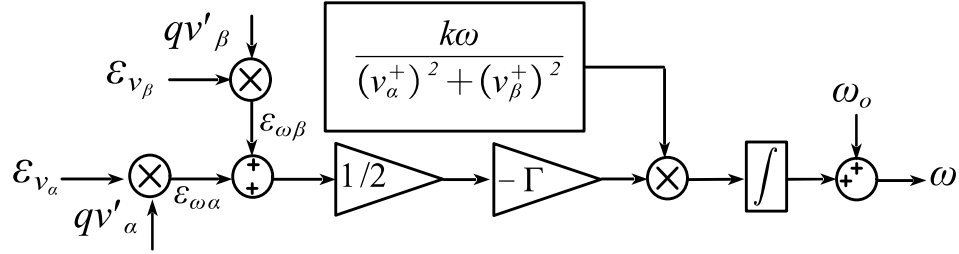


Figure 5.8. Frequency-locked loop.

side, and the superscripts  $a$ ,  $b$ , and  $c$  represent the quantities aligned with phases  $a$ ,  $b$ , and  $c$ , respectively. The zero-sequence current can be calculated from the measured phase voltages on the grid side ( $v_g$ ) to eliminate the requirement for a current sensor on the grid side using (5.3), as clarified in [64].

$$i_g^0 = \frac{-1}{SL_{tr}^0 + R_{tr}^0} \times \frac{1}{3} (v_g^a + v_g^b + v_g^c). \quad (5.3)$$

in which  $S$  is a complex frequency domain parameter, while  $L_{tr}^0$  and  $R_{tr}^0$  are the inductance and the resistance of the transformer zero-sequence impedance, respectively. Thereafter, the zero-sequence current is converted into two orthogonal components (i.e.,  $i_g^0$  and  $i_{g\perp}^0$ , which lags  $i_g^0$  by  $90^\circ$ ) using the double second-order generalized integrator (SO-SOGI). The SOGI is shown in Figure 5.7 [80], in which  $f'$  is the fundamental component of  $f$  (i.e., a voltage or current signal), which is determined by filtering the input signal's harmonic contents. Accordingly, the zero-sequence current angle in (5.1) can be calculated using

$$\angle I_g^0 = \tan^{-1} \left( \frac{-I_{g\perp}^0}{I_g^0} \right) - \omega t \quad (5.4)$$

where  $\omega$  is determined by augmenting the SO-SOGI with a frequency-locked loop (FLL), as shown in Figure 5.8, in which,  $\varepsilon_{v_{M\alpha}}, qv'_{t,\alpha}, \varepsilon_{v_{f,\beta}}, qv'_{t,\beta}$  are determined by the SO-SOGI shown in Figure 5.7 when its inputs are  $v_{t,\alpha}$  and  $v_{t,\beta}$ , respectively[81], while  $\Gamma$  is the frequency locked-loop gain. It is to be noted that the second stage is performed only for ground faults.

### 5.3.3 Stage III. Initial Reference Angle of the Positive-Sequence Current

The initial positive-sequence current angle ( $\angle I_{t,ref(0)}^+$ ), which is compatible with RCG requirements at the POI, is calculated using the  $\alpha\beta$  positive-sequence currents, as follows:

$$\angle I_{t,ref(0)}^+ = \tan^{-1} \left( \frac{-i_{t,\beta,ref(0)}^+}{i_{t,\alpha,ref(0)}^+} \right) - \omega t \quad (5.5)$$

in which,  $i_{t,\alpha,ref(0)}^+$  and  $i_{t,\beta,ref(0)}^+$  are obtained from the active- and reactive-current references as follows:

$$\begin{bmatrix} i_{t,\alpha,ref(0)}^+ \\ i_{t,\beta,ref(0)}^+ \end{bmatrix} = \frac{2}{3} \begin{bmatrix} \frac{v_{t,\alpha}^+}{\sqrt{(v_{t,\alpha}^+)^2 + (v_{t,\beta}^+)^2}} & \frac{v_{t,\beta}^+}{\sqrt{(v_{t,\alpha}^+)^2 + (v_{t,\beta}^+)^2}} \\ \frac{v_{t,\beta}^+}{\sqrt{(v_{t,\alpha}^+)^2 + (v_{t,\beta}^+)^2}} & \frac{-v_{t,\alpha}^+}{\sqrt{(v_{t,\alpha}^+)^2 + (v_{t,\beta}^+)^2}} \end{bmatrix} \begin{bmatrix} I_{P,ref(0)} \\ I_{Q,ref} \end{bmatrix} \quad (5.6)$$

where the reference reactive current  $I_{Q,ref}$  is set based on the RCG requirements, while the initial active current reference  $I_{P,ref(0)}$  is specified using a PI controller that keeps the dc-link voltage at its reference value. During faults, the positive-sequence current injected by the inverter may exceed the inverter current limits. Thus, the positive-sequence current should be limited to  $I_{limit}^+$ , which is set at 1.2 p. u. It is worth noting that the reactive current is more significant than the active current during voltage dips to meet RCG requirements

and support the grid voltage, while the chopper circuit limits the dc-link voltage. Thus, the active current maximum limit, i.e.,  $I_{P,max}^+$  is determined by

$$I_{P,max}^+ = \sqrt{(I_{limit}^+)^2 - (I_{Q,ref})^2}. \quad (5.7)$$

In (5.6),  $v_{t,\alpha}^+$  and  $v_{t,\beta}^+$  are acquired from the stationary frame voltages by first using the SO-SOGI to determine the fundamental and quadrature components of the instantaneous voltages. Then, the positive- and negative-sequence voltages can be obtained by

$$\begin{cases} \begin{bmatrix} v_{t,\alpha}^+ \\ v_{t,\beta}^+ \end{bmatrix} = \begin{bmatrix} 1 & -q \\ q & 1 \end{bmatrix} \begin{bmatrix} v_{t,\alpha} \\ v_{t,\beta} \end{bmatrix} \\ \begin{bmatrix} v_{t,\alpha}^- \\ v_{t,\beta}^- \end{bmatrix} = \begin{bmatrix} 1 & q \\ -q & 1 \end{bmatrix} \begin{bmatrix} v_{t,\alpha} \\ v_{t,\beta} \end{bmatrix}. \end{cases} \quad (5.8)$$

#### 5.3.4 Stage IV. Reference Angles of the Negative- and Positive-Sequence Currents

The reference angles of the negative- and positive-sequence currents at the POI, i.e.,  $\angle I_{t,ref}^-$  and  $\angle I_{t,ref}^+$ , are determined to reach a trade-off between the phase selection and RCG requirements. Consequently, these angles should provide RCG without violating the limits of  $\delta^0$ 's and  $\delta^+$ 's zones. The load and controller disturbances can slightly shift  $\delta^0$  and  $\delta^+$  from their reference values. Therefore, a margin from the fault-type zone limits should be considered to prevent  $\delta^0$  and  $\delta^+$  measured by the relay from exceeding their zone limits. It is worth noting that increasing the margin enhances the robustness of the PSM. However, it reduces the flexibility in reaching the required GC requirements. Thus, a  $5^\circ$  margin is selected to secure the PSM operation and provide highly flexible control. Consequently, the relative angles between  $\angle I_{t,ref}^-$  and  $\angle I_{t,ref}^+$  are controlled to be within the reduced  $\delta^0$ 's and  $\delta^+$ 's zone limits (i.e.,  $\delta_{F,bis}^0 \pm \Theta_{IRES,max}^0$  and  $\delta_{F,bis}^+ \pm \Theta_{IRES,max}^+$ ), where  $\Theta_{IRES,max}$  is  $\Theta_{max}$  set for the IRES controller.  $\Theta_{IRES,max}$  is equal to  $\Theta_{max} - \mu$ , where  $\mu$  is a margin from the maximum PSM zone boundaries to allow the relay to locate the PSM correctly and it is set to  $5^\circ$ . Thus,  $\Theta_{IRES,max}^0$  and  $\Theta_{IRES,max}^+$  are set at  $55^\circ$  and  $25^\circ$ , respectively, measured from  $\delta^0$ 's and  $\delta^+$ 's zone bisectors, i.e.,  $\delta_{F,bis}^0$  and  $\delta_{F,bis}^+$ . For instance, in a BCG fault,  $\delta^0$ 's and  $\delta^+$ 's reduced zones are bounded by  $\pm 55^\circ$  and  $180^\circ \pm 25^\circ$ , respectively.

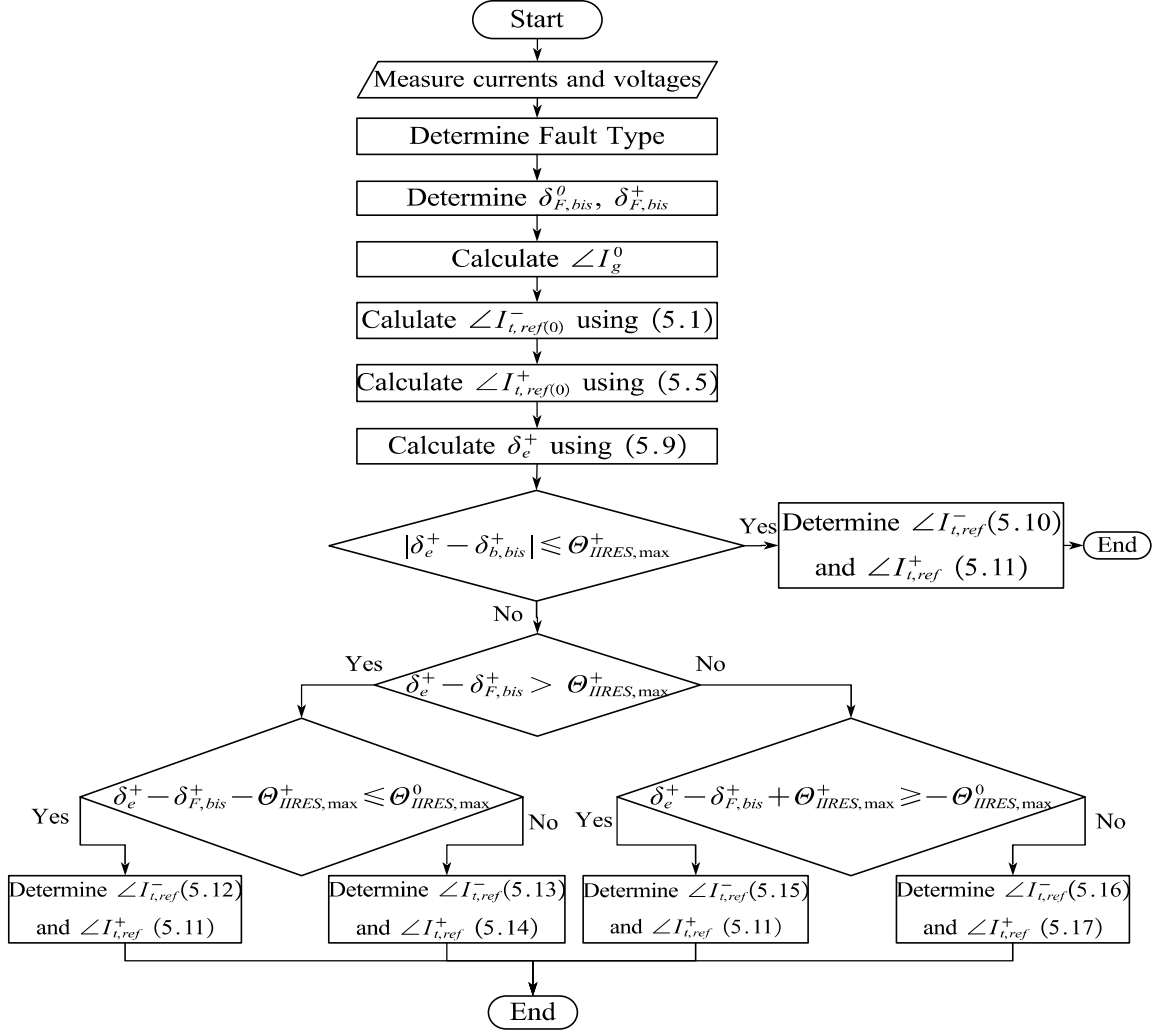


Figure 5.9. Determination of  $\angle I_{t,ref}^-$  and  $\angle I_{t,ref}^+$ .

#### A. Unbalanced Ground Faults

In unbalanced ground faults (i.e., SLG and LLG faults), the fault type is detected according to the location of both  $\delta^0$  and  $\delta^+$ . Thus,  $\angle I_{t,ref}^-$  should be selected precisely to guarantee the correct placement of  $\delta^0$  and  $\delta^+$  without enforcing  $\angle I_{t,ref}^+$  to violate RCG requirements. This is achieved by shifting  $\angle I_{t,ref}^-$  within the accepted  $\delta^0$  zone limits. The flow chart for determining  $\angle I_{t,ref}^-$  and  $\angle I_{t,ref}^+$  during ground faults is illustrated in Figure 5.9.

First, the expected  $\delta^+$  on the transformer's grid side (i.e.,  $\delta_e^+$ ), which occurs when  $\angle I_{t,ref}^-$  and  $\angle I_{t,ref}^+$  are equal to  $\angle I_{t,ref(0)}^-$  and  $\angle I_{t,ref(0)}^+$ , respectively, is calculated by

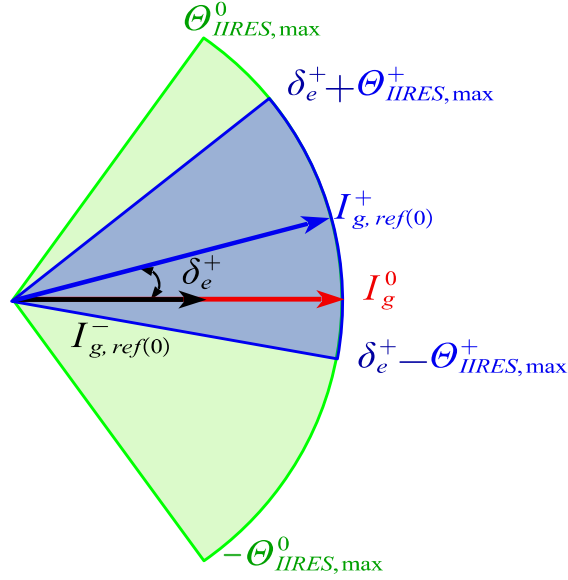


Figure 5.10. Loci of sequence currents when  $I_{g,ref(0)}^-$  and  $I_{g,ref(0)}^+$  satisfy  $\delta^0$ 's and  $\delta^+$ 's requirements during an AG fault.

$$\delta_e^+ = \angle I_{f,ref(0)}^- - \angle I_{f,ref(0)}^+ - \theta_{tr}^- + \theta_{tr}^+ \quad (5.9)$$

where  $\theta_{tr}^+$  is the phase shift between the positive-sequence currents at the transformer's low- and high-voltage sides. For instance, a delta-star-ground makes  $\angle I_t^+$  lags  $\angle I_g^+$  by  $30^\circ$ ; thus,  $\theta_{tr}^+$  is equal  $-30^\circ$ , while  $\angle I_t^-$  leads  $\angle I_g^-$  by  $30^\circ$ ; thus,  $\theta_{tr}^-$  is equal to  $30^\circ$ .

Subsequently, the difference between  $\delta_e^+$  and  $\delta_{F,bis}^+$  is checked. If this difference is between  $\pm\Theta_{IIRES,max}^+$ ,  $\angle I_{t,ref(0)}^-$  and  $\angle I_{t,ref(0)}^+$  are maintained as the final values of the reference angles as given by (5.10) and (5.11). This condition is illustrated by Figure 5.10 for an AG fault, where  $\angle I_{g,ref(0)}^-$  and  $\angle I_{g,ref(0)}^+$  are the referred  $\angle I_{t,ref(0)}^-$  and  $\angle I_{f,ref(0)}^+$  to the transformer grid side, respectively. Figure 5.10 demonstrates that the phasor of  $I_{g,ref(0)}^-$  is placed within  $\delta^0$ 's and  $\delta^+$ 's zone limits (i.e., the zones with green and blue backgrounds, respectively). Thus, both  $\delta^0$  and  $\delta^+$  operate correctly without the need to tune either  $\angle I_{t,ref(0)}^-$  or  $\angle I_{t,ref(0)}^+$ .

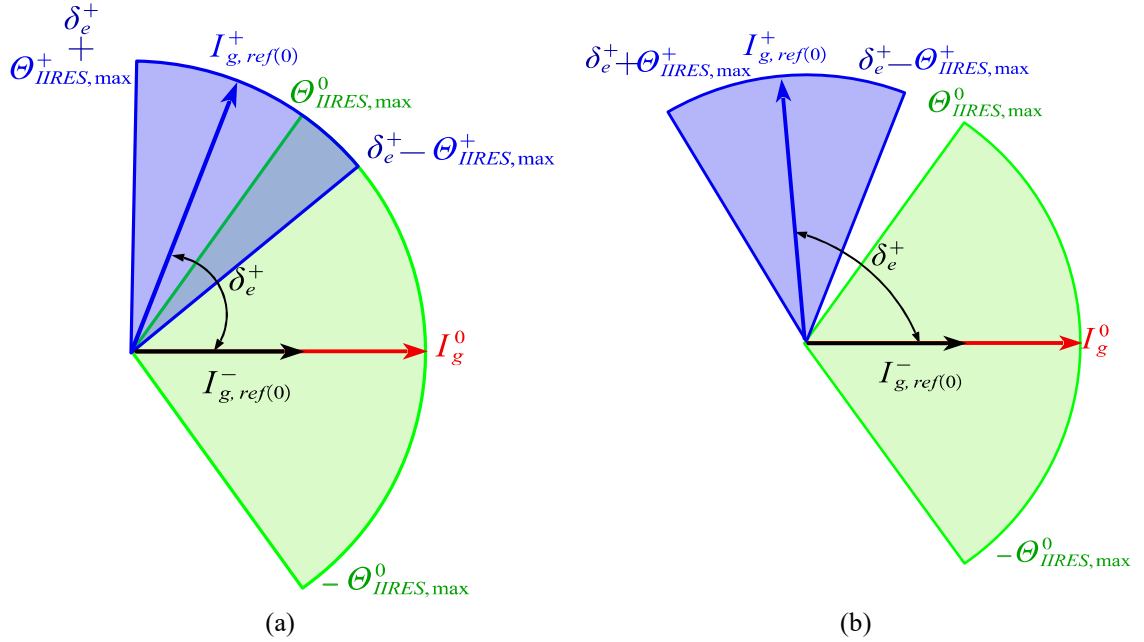


Figure 5.11. Loci of sequence currents when  $\angle I_{g,ref(0)}^-$  is below  $\delta^+$  minimum limit: (a)  $\delta^0$  and  $\delta^+$  zones are intersected, (b)  $\delta^0$  and  $\delta^+$  zones have no intersection.

$$\angle I_{t,ref}^- = \angle I_{t,ref(0)}^- \quad (5.10)$$

$$\angle I_{t,ref}^+ = \angle I_{t,ref(0)}^+. \quad (5.11)$$

Otherwise, if  $\delta_e^+ - \delta_{F,bis}^+$  is greater than  $\Theta_{IIRES,max}^+$ , as shown in Figure 5.11(a), where the phasor of  $I_{g,ref(0)}^-$  is below  $\delta^+$  minimum limit,  $\angle I_{t,ref}^-$  should be adjusted to force  $\delta^+$  into its correct fault-type zone without violating  $\delta^0$ 's zone limits. Thus,  $\angle I_{t,ref}^-$  should be given by

$$\angle I_{t,ref}^- = \angle I_{t,ref(0)}^- - (\delta_e^+ - \delta_{F,bis}^+ - \Theta_{IIRES,max}^+). \quad (5.12)$$

However, (5.12) may cause  $\delta^0$  to settle outside its correct zone boundaries if the required shift for  $\angle I_{t,ref(0)}^-$ , i.e.,  $\angle I_{t,ref}^- - \angle I_{t,ref(0)}^-$ , is greater than  $\Theta_{IIRES,max}^0$ . In other words,  $\angle I_{t,ref(0)}^-$  is below  $\delta^+$ 's minimum zone limit and there is no intersection between  $\delta^0$ 's and  $\delta^+$ 's zones, as depicted in Figure 5.11(b). In this case, the current-angle-based PSM operation could be adversely affected. Thus, both  $\angle I_{t,ref}^-$  and  $\angle I_{t,ref}^+$  should be altered

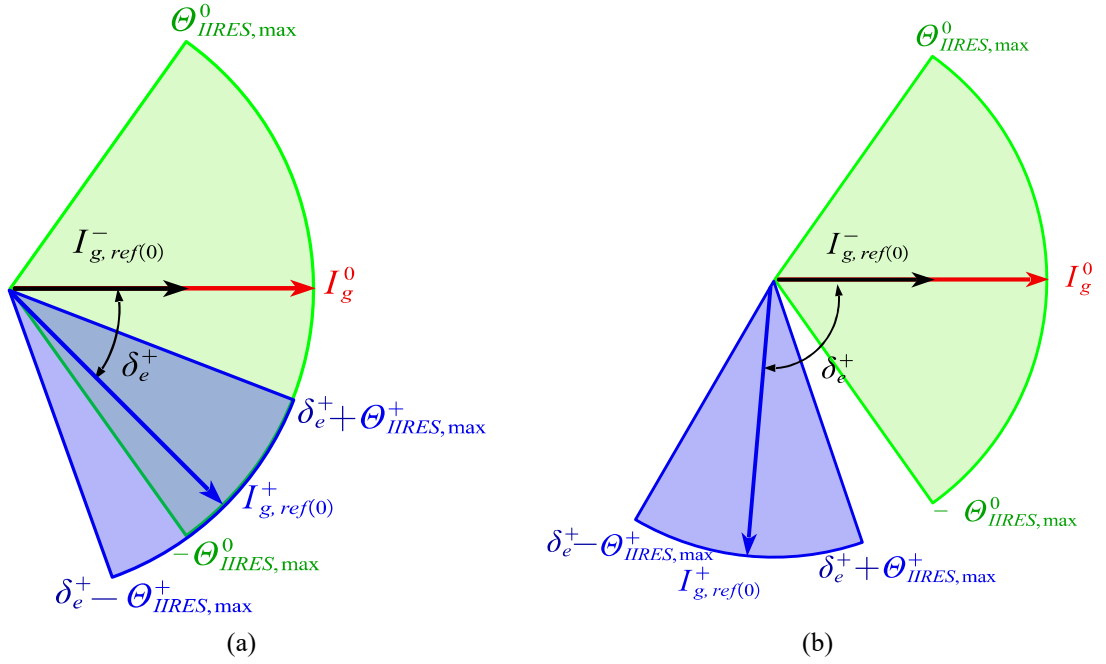


Figure 5.12. Loci of sequence currents when  $\angle I_{g,ref(0)}^-$  is above  $\delta^+$ 's maximum limit: (a)  $\delta^0$  and  $\delta^+$  zones are intersected, (b)  $\delta^0$  and  $\delta^+$  zones have no intersection.

simultaneously as follows:

$$\angle I_{t,ref}^- = \angle I_{t,ref(0)}^- - \Theta_{IIRES,max}^0 \quad (5.13)$$

$$\angle I_{t,ref}^+ = \angle I_{t,ref(0)}^+ + (\delta_e^+ - \delta_{F,bis}^+ - \Theta_{IIRES,max}^+). \quad (5.14)$$

Otherwise, if  $\delta_e^+ - \delta_{F,bis}^+$  is less than  $-\Theta_{IIRES,max}^+$ ,  $\angle I_{t,ref}^-$  should be adjusted to guarantee that both  $\delta^+$  and  $\delta^0$  are placed correctly in their fault-type zones, as given by (5.14). An illustration of this condition is depicted in Figure 5.12(a), where  $I_{t,ref(0)}^-$  is located above  $\delta^+$ 's maximum limit and there is an intersection between  $\delta^0$ 's and  $\delta^+$ 's zones.

$$\angle I_{t,ref}^- = \angle I_{t,ref(0)}^- - (\delta_e^+ - \delta_{F,bis}^+ + \Theta_{IIRES,max}^+). \quad (5.15)$$

Lastly, (5.15) could cause erroneous phase selection, if the required shift of  $\angle I_{t,ref(0)}^-$  is less than  $-\Theta_{IIRES,max}^0$ ; this scenario happens when  $\angle I_{t,ref(0)}^-$  is above  $\delta^+$ 's maximum



limit and there is no intersection between  $\delta^{0's}$  and  $\delta^{+'s}$  zones, as depicted in Figure 5.12(b). Therefore, both  $\angle I_{t,ref}^-$  and  $\angle I_{t,ref}^+$  should be formulated as follows:

$$\angle I_{t,ref}^- = \angle I_{t,ref(0)}^- + \theta_{IRES,max}^0 \quad (5.16)$$

$$\angle I_{t,ref}^+ = \angle I_{t,ref(0)}^+ + (\delta_e^+ - \delta_{F,bis}^+ + \theta_{IRES,max}^0). \quad (5.17)$$

### B. Unbalanced Ungrounded Faults

In unbalanced ungrounded faults (i.e., LL faults),  $\angle I_{t,ref}^-$  and  $\angle I_{t,ref}^+$  are designed to force the relative angle between the negative- and positive-sequence currents to be in the correct  $\delta^{+'s}$  fault-type zone and concurrently comply with RCG requirements. Thus,  $\angle I_{t,ref}^+$  is selected as follows:

$$\angle I_{t,ref}^+ = \angle I_{t,ref(0)}^+. \quad (5.18)$$

Thereafter,  $\angle I_{t,ref}^-$  is selected to ensure that  $\delta^+$  is located in the center of its fault-type zone; thus,  $\angle I_{t,ref}^-$  is given by

$$\angle I_{t,ref}^- = \angle I_{t,ref(0)}^+ + \delta_{F,bis}^+ + \theta_{tr}^- - \theta_{tr}^+. \quad (5.19)$$

### 5.3.5 Stage V. Inverter's $\alpha\beta$ Reference Currents:

The negative-sequence current reference at the inverter's terminals  $I_{ref}^-$  is designed to satisfy  $\angle I_{t,ref}^-$ , which is determined in Stage IV, and the IRES negative-sequence current limit ( $I_{limit}^-$ ), which is selected to be 0.3 p.u.  $I_{t,ref}^-$  is computed in the negative-sequence stationary frame using  $\angle I_{f,ref}^-$  as follows:

$$\begin{cases} i_{t,\alpha,ref}^- = I_{t,limit}^- \sin(\omega t + \angle I_{t,ref}^-) \\ i_{t,\beta,ref}^- = I_{t,limit}^- \cos(\omega t + \angle I_{t,ref}^-) \end{cases} \quad (5.20)$$

where  $I_{t,limit}^-$  is the negative-sequence current limit at the POI.  $I_{t,limit}^-$  can be determined, as illustrated in Appendix B, by

$$I_{t,limit}^- = \sqrt{\frac{(I_{limit}^-)^2 + \omega^2 C_f^2 (V_t^-)^2}{+2\omega C_f I_{limit}^- V_t^- \sin(\angle V_t^- - \angle I_{ref}^-)}}. \quad (5.21)$$

To compensate for the capacitor current,  $i_{ref}^-$  is formulated in the negative-sequence stationary frame by

$$\begin{cases} i_{\alpha,ref}^- = i_{t,\alpha,ref}^- + \omega C_f v_{t,\beta}^- \\ i_{\beta,ref}^- = i_{t,\beta,ref}^- - \omega C_f v_{t,\alpha}^- \end{cases} \quad (5.22)$$

On the other hand, the positive-sequence current reference at the inverter terminals  $I_{ref}^+$  is determined to generate the correct  $\angle I_{t,ref}^+$  obtained in Stage IV. Thus, the final active-current reference ( $I_{p,ref}$ ) is calculated using (5.23) based on  $I_{Q,ref}$  and the angle between  $I_{t,ref}^+$  and  $V_t^+$ , i.e.,  $\angle I_{t,ref}^+ - \angle V_t^+$ .

$$I_{p,ref} = \frac{I_{Q,ref}}{\tan(\angle I_{t,ref}^+ - \angle V_t^+)} \quad (5.23)$$

where  $I_{Q,ref}$  and  $I_{p,ref}$  should be bounded by current limits to avoid exceeding the IRES thermal limit while keeping  $\angle I_{ref}^+$  intact. If the magnitude of  $I_{t,ref}^+$ , i.e.,  $\sqrt{(I_{p,ref})^2 + (I_{Q,ref})^2}$ , exceeds  $I_{t,limit}^+$ , then  $I_{p,ref}$  and  $I_{Q,ref}$  should be limited at

$$\begin{bmatrix} I_{Q,limit}^* \\ I_{p,limit}^* \end{bmatrix} = \begin{bmatrix} I_{p,ref} \\ I_{Q,ref} \end{bmatrix} \times \frac{I_{t,limit}^+}{\sqrt{(I_{p,ref})^2 + (I_{Q,ref})^2}}. \quad (5.24)$$

Subsequently, the positive-sequence current references in the  $\alpha\beta$  frame at the POI (i.e.,  $i_{t,\alpha,ref}^+$  and  $i_{t,\beta,ref}^+$ ) are obtained by

$$\begin{bmatrix} i_{t,\alpha,ref}^+ \\ i_{t,\beta,ref}^+ \end{bmatrix} = \frac{2}{3} \begin{bmatrix} \frac{v_{t,\alpha}^+}{\sqrt{(v_{t,\alpha}^+)^2 + (v_{t,\beta}^+)^2}} & \frac{v_{t,\beta}^+}{\sqrt{(v_{t,\alpha}^+)^2 + (v_{t,\beta}^+)^2}} \\ \frac{v_{f\beta}^+}{\sqrt{(v_{t,\alpha}^+)^2 + (v_{t,\beta}^+)^2}} & \frac{-v_{f\alpha}^+}{\sqrt{(v_{t,\alpha}^+)^2 + (v_{t,\beta}^+)^2}} \end{bmatrix} \begin{bmatrix} I_{p,ref} \\ I_{Q,ref} \end{bmatrix}. \quad (5.25)$$

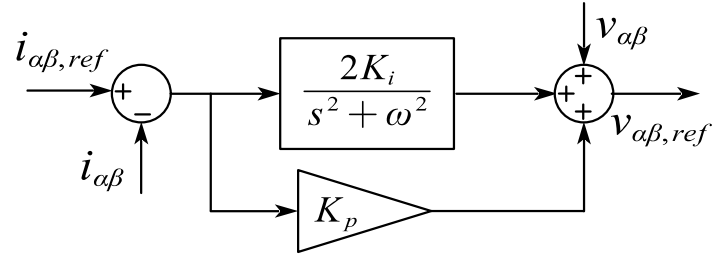


Figure 5.13. PR current controller in the stationary frame.

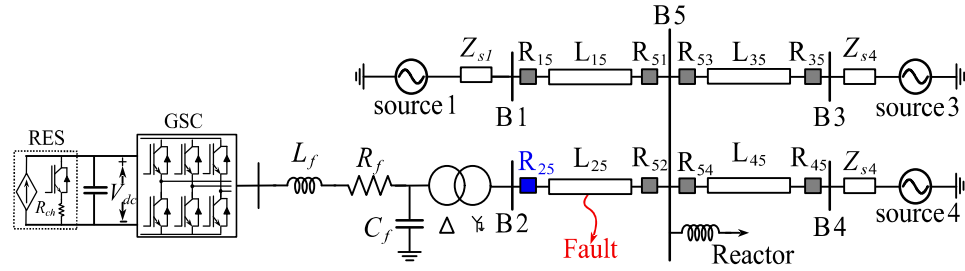


Figure 5.14. Single-line diagram of the test system.

After that, the inverter's positive-sequence current references ( $i_{\alpha,ref}^+$  and  $i_{\beta,ref}^+$ ) are determined by compensating the capacitor current, as follows:

$$\begin{cases} i_{\alpha,ref}^+ = i_{t,\alpha,ref}^+ - \omega C_f v_{t,\beta}^+ \\ i_{\beta,ref}^+ = i_{t,\beta,ref}^+ + \omega C_f v_{t,\alpha}^+ \end{cases} \quad (5.26)$$

Lastly,  $i_{\alpha,ref}$  and  $i_{\beta,ref}$  are calculated using

$$\begin{cases} i_{\alpha,ref} = i_{\alpha,ref}^+ + i_{\alpha,ref}^- \\ i_{\beta,ref} = i_{\beta,ref}^+ + i_{\beta,ref}^- \end{cases} \quad (5.27)$$

These  $\alpha\beta$  reference currents are tracked using a PR controller, as shown in Figure 5.13, while its parameters are identified based on the procedures in [15], [82].

## 5.4 Performance Evaluation of DCC1

Extensive simulations are executed to assess the effectiveness of the proposed DCC1 in achieving accurate phase selection and meeting RCG requirements by GCs. The test system shown in Figure 5.14, similar to Figure 4.13, is simulated using PSCAD/EMTDC at

Table 5.1. Performance of the proposed DCC1 at different fault locations with ERCOT-GC

Fault Type	$R_{ft}$	Fault at 10% of $L_{25}$			Fault at 50% of $L_{25}$			Fault at 90% of $L_{25}$		
		$\delta^0$	$\delta^+$	PF	$\delta^0$	$\delta^+$	PF	$\delta^0$	$\delta^+$	PF
AG	0	50.2	-24.2	0.9505	47.7	-24.7	0.9505	46.9	-25.0	0.9508
	50	0.0	-25.1	0.9504	0.0	-23.5	0.9503	-0.4	-16.3	0.9509
BG	0	-69.8	95.8	0.9508	-71.85	95.03	0.9507	-73.1	94.9	0.9508
	50	240.0	94.9	0.9505	240.0	96.5	0.9504	239.6	103.7	0.9510
CG	0	-189.8	-144.2	0.9512	-192.3	-144.8	0.9509	-193.1	-145.1	0.9510
	50	-240.0	-145.1	0.9507	-240.0	-143.5	0.9507	-240.4	-136.4	0.9512
ABG	0	176.9	35.9	0.9501	173.0	36.3	0.9513	173.3	36.5	0.9513
	50	123.3	52.8	0.9507	123.3	47.4	0.9508	123.5	49.2	0.9508
BCG	0	56.8	155.9	0.9507	53.0	156.2	0.9522	53.2	156.5	0.9523
	50	3.3	172.8	0.9514	3.3	167.3	0.9515	3.4	169.2	0.9514
ACG	0	-63.2	-84.1	0.9503	-67.0	-83.7	0.9518	-66.8	-83.5	0.9517
	50	-116.7	-67.2	0.9514	-116.7	-72.7	0.9512	-116.5	-70.8	0.9511

different GCs, fault locations, and fault resistances to verify the accuracy of DCC1 in achieving PSM requirements without impeding the fulfillment of RCG requirements.

#### 5.4.1 Response at Different Fault Locations

Table 5.1 displays  $\delta^0$  and  $\delta^+$  measured by  $R_{25}$  as well as the PF measured at the inverter terminals. These results are determined for various unbalanced faults when the IRES is controlled to comply with the ERCOT-GC, which requires the IRES's PF to be higher than or equal to 0.95 lag [77]. During the examined tests, the IRES's PF reference is set initially at 0.95 to meet the ERCOT-GC requirements.

The results of Table 5.1 unveil the correct operation of the proposed DCC1 as both  $\delta^0$  and  $\delta^+$  settle in their correct zones without changing  $\angle I_{ref}^+$ , which is illustrated by maintaining the PF at 0.95 lagging. For various fault resistances and locations,  $\delta^0$  varies within its correct zone from  $0^\circ$  to  $55^\circ$  with respect to the zone bisector to prevent  $\delta^+$  from violating its zone limits. The results also demonstrate the controller's effectiveness because it maintains the  $5^\circ$  margin from the zone limits of  $\delta^0$  and  $\delta^+$ . For instance, during bolted AG faults,  $\delta^+$  is almost kept at  $-25^\circ$ , while  $\delta^0$  is slightly changed from  $50.2^\circ$  to  $46.9^\circ$  for

faults at 10% and 90% of  $L_{25}$ , respectively. The successful operation of the proposed DCC1 is attained by initially adjusting  $\angle I_o^-$  to place  $\delta^0$  at its correct zone bisector ( $\delta_{F,bis}^+$ ), then, this current angle is adjusted to prevent  $\delta^+$  from violating its zone limits, i.e.,  $\delta_{F,bis}^+ \pm 25^\circ$ . On the other hand, during highly resistive faults,  $\delta^0$  is almost maintained at  $0^\circ$ , while  $\delta^+$  changes from  $-25.1^\circ$  to  $-16.3^\circ$  during near-end and far-end faults, respectively. At high PFs and during highly resistive faults,  $\delta^0$  is preserved near the AG zone bisector, i.e.,  $0^\circ$ , which unveils that the proposed DCC1 at these conditions can enable precise phase selection without further adjustment for the RCG requirements. In addition, the difference between  $\delta^+$  and the zone bisector is reduced, when the distance between the fault location and IRES increases because the impedance between the fault and the IRES increases.

Figures 5.15–5.18 manifest the dynamic response of the proposed DCC1 during a bolted BG fault, i.e., the highlighted sample case in Table 5.1. Figure 5.15 depicts that  $\delta^0$  and  $\delta^+$  measured by  $R_{25}$ , successfully settle in the correct BG zones after 25 ms from the fault inception. This dynamic response indicates that the relay can operate appropriately in less than two cycles after fault occurrence. In addition, both angles are stabilized near the zone limits to make the proposed DCC1 meet the RCG requirements without compromising the relay's ability to determine the faulty phase(s). Figure 5.16 clarifies the efficacy of the utilized positive and negative-sequence extractor in the  $\alpha\beta$  frame. Before the fault inception, the extracted positive-sequence voltages and the measured voltages in the  $\alpha\beta$  frame are identical, while the extracted  $\alpha\beta$  negative-sequence voltages are maintained at zero because the measured phase voltages are balanced. In addition, it clarifies the proper extractor operation in an unbalanced system, where  $V_\alpha^+$  leads  $V_\beta^+$  by  $90^\circ$  but with equal voltage magnitudes. On the other hand,  $V_\alpha^-$  lags  $V_\beta^-$  by  $90^\circ$ , while sharing the same magnitude, i.e., 0.3 pu, as anticipated for a bolted SLG fault. The responsiveness and adequacy of the PR controller in tracking a sinusoidal signal are shown in Figure 5.17. The figure exposes that  $I_\alpha$  and  $I_\beta$  promptly track their reference values in both steady-state and transient conditions. In addition, Figure 5.18 demonstrates that the controller succeeds to limit  $I^+$  and  $I^-$  at 1.2 and 0.3 p.u., respectively.

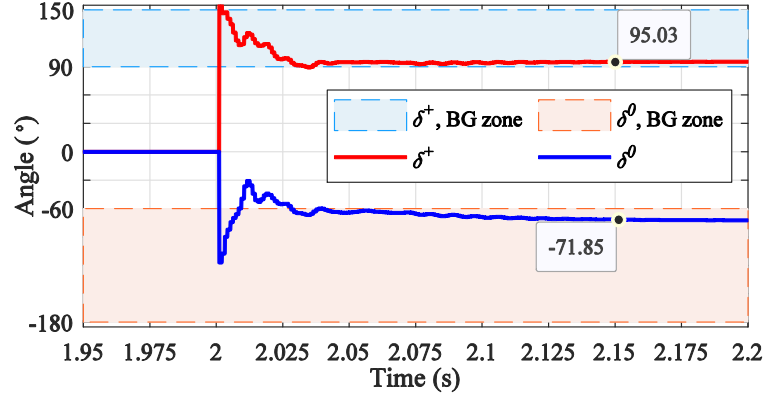


Figure 5.15. Measured  $\delta^0$  and  $\delta^+$  by  $R_{25}$  for a bolted BG fault.

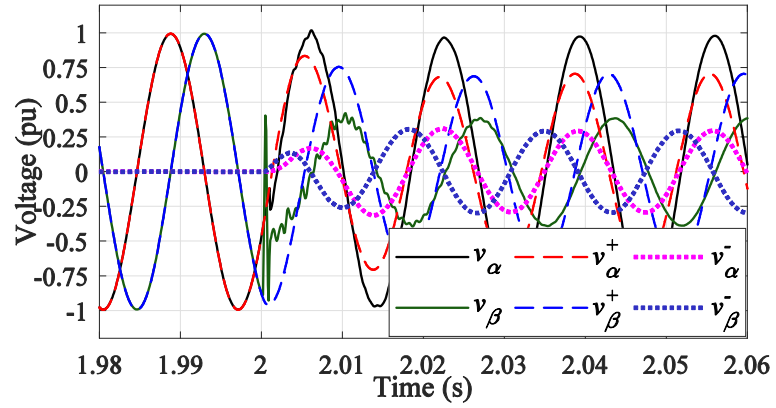


Figure 5.16. POI voltage in the alpha-beta frame for a bolted BG fault: (a) Positive-sequence voltage, (b) Negative-sequence voltage.

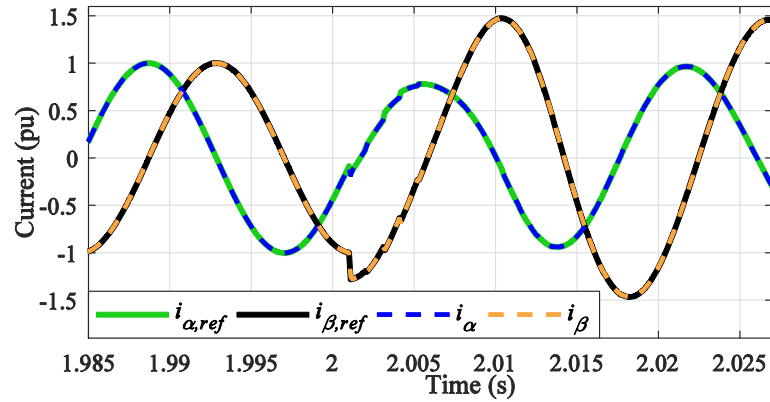


Figure 5.17. IRES output current in the alpha-beta frame for a bolted BG fault.

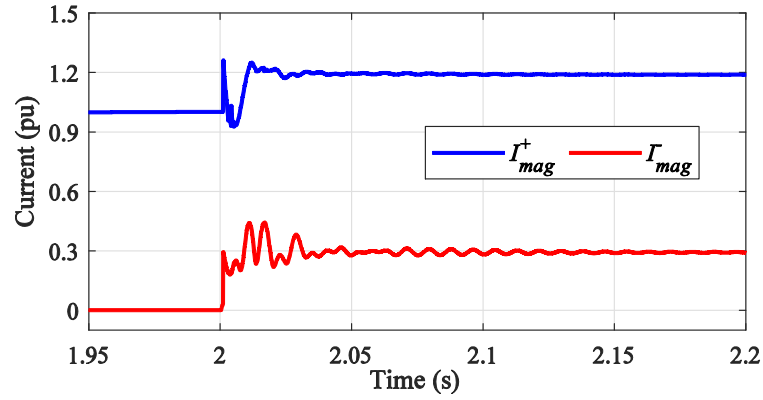


Figure 5.18. IRES positive- and negative-sequence current magnitude measured at the inverter's terminals.

Table 5.2. Performance of the proposed DCC1 during LL faults with ERCOT-GC

Fault Type	$R_{flt}$	Fault at 10% of $L_{25}$		Fault at 90% of $L_{25}$	
		$\delta^+$	PF	$\delta^+$	PF
AB	0	62.7	0.9493	62.7	0.9493
	50	59.2	0.9493	59.2	0.9494
BC	0	182.7	0.9501	182.7	0.9501
	50	179.2	0.9498	179.2	0.9498
AC	0	-57.3	0.9497	-57.3	0.9497
	50	-60.8	0.9496	-60.8	0.9496

In addition, Table 5.2 confirms the applicability of the proposed DCC1 to meet RCG and phase selection requirements during ungrounded faults. Table 5.2 shows that  $\delta^+$  measured by the relay is settled accurately in its fault-type zone with a maximum of  $3^\circ$  shift from the zone center. This is essential for LL faults as  $\delta^+$  is solely used for fault type discrimination. Moreover, the IRES output PF is maintained at the GC desired value, which is 0.95 lagging. For instance, during an AB fault with  $50 \Omega$  fault resistance, the measured  $\delta^+$  and the output PF are  $59.2^\circ$  and 0.9493 lagging, respectively. Furthermore, the results show that the variation in fault resistance or fault location has a negligible effect on the DCC1 response.

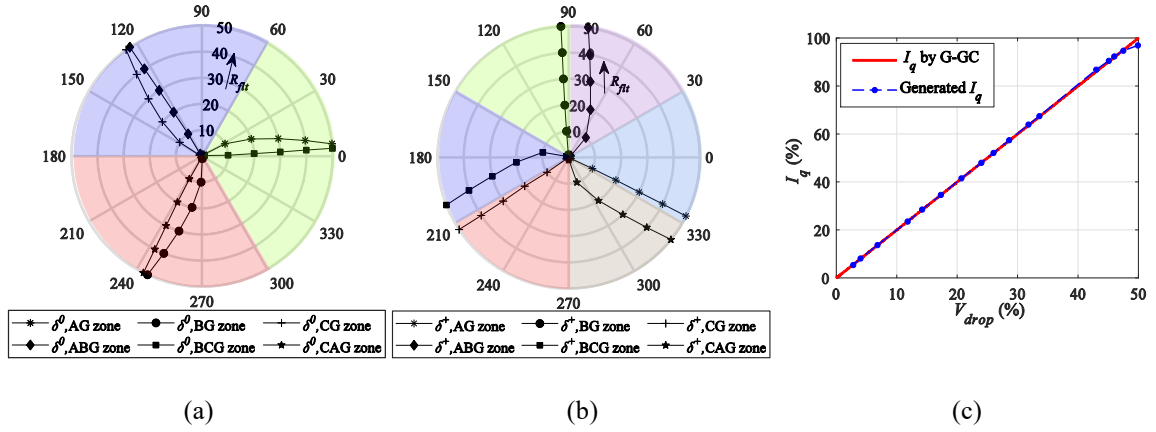


Figure 5.19. Performance of the proposed DCC1 with the German GC: (a)  $\delta^0$  measured by  $R_{25}$ , (b)  $\delta^+$  measured by  $R_{25}$ , (c) Relation between output reactive current and voltage drop at the POI.

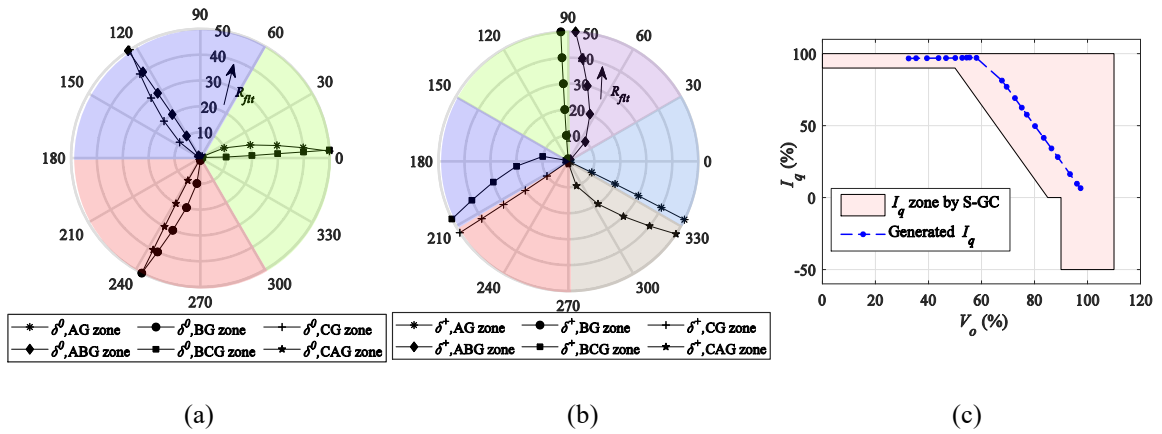


Figure 5.20. Performance of the proposed DCC1 with the Spanish GC: (a)  $\delta^0$  measured by  $R_{25}$ , (b)  $\delta^+$  measured by  $R_{25}$ , (c) Relation between output reactive current and the voltage magnitude at the POI.

#### 5.4.2 Compatibility with Various GCs

This section investigates the compatibility of the proposed DCC1 with various RCG requirements imposed by two European GCs, i.e., the German GC (G-GC) that requires the injected  $I_q$  to be twice the POI voltage-drop percentage and the Spanish GC (S-GC) that defines a range for  $I_q$  based on the POI voltage. The controller is examined for various unbalanced faults at a wide range of fault resistances, taking place at the mid-point of  $L_{25}$ . The system response is portrayed in Figure 5.19 when the proposed controller follows the



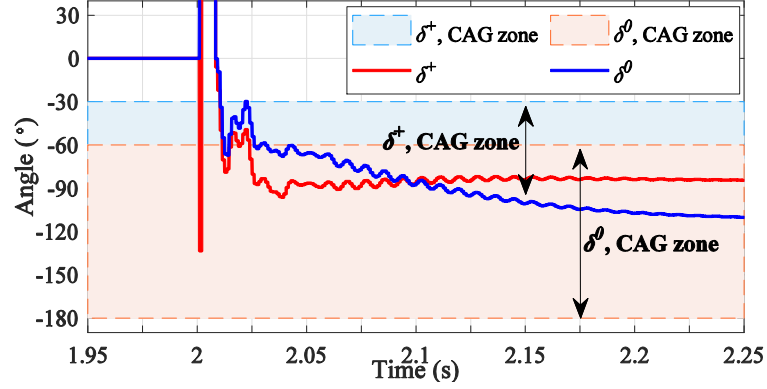


Figure 5.21. Measured  $\delta^0$  and  $\delta^+$  by  $R_{25}$  for a bolted CAG fault.

RCG requirements by the G-GCs. This figure substantiates the correct operation of the controller in enabling both the current-angle-based PSM and meeting the RCG requirements of the G-GC. It is worth noting that  $\delta^0$  settles around its zone bisector for different fault resistances, and thus, the G-GC requires less angle compensation for  $\angle I^-$  to achieve correct phase selection as compared with the ERCOT-GC. However, the placement of  $\delta^+$  in its fault-type zone changes based on the fault resistance. Figure 5.19(c) demonstrates the ability of the proposed DCC1 to inject  $I_q$  required by the G-GC at different voltage drop percentages. Figure 5.20 shows similar results to the case of the S-GC because the proposed DCC1 achieves its two objectives by making the relay determine the faulty phase(s) and fulfilling the RCG requirements. Figure 5.20(c) demonstrates that the S-GC provides more flexibility with respect to the RCG requirements. Thus, the reactive power could be varied to keep both  $\delta^0$  and  $\delta^+$  around their zone bisectors. This figure further illustrates the success of the proposed DCC1 in achieving the RCG requirements by the S-GC. Figure 5.21 demonstrates a sample dynamic response of  $\delta^0$  and  $\delta^+$  for a bolted CAG fault when complying with the G-GC. This figure reveals that both  $\delta^0$  and  $\delta^+$  are placed correctly in their respective zones after modifying  $\angle I^-$  without the necessity to modify  $\angle I^+$ . The results affirm the accuracy of the proposed DCC1 and its ability to control the current angles to achieve phase selection without disregarding the RCG requirements.

Furthermore, Figure 5.22 unveils the proper operation of the proposed DCC1 during LL faults. Figure 5.22(a) shows that the negative-sequence current angle is regulated precisely

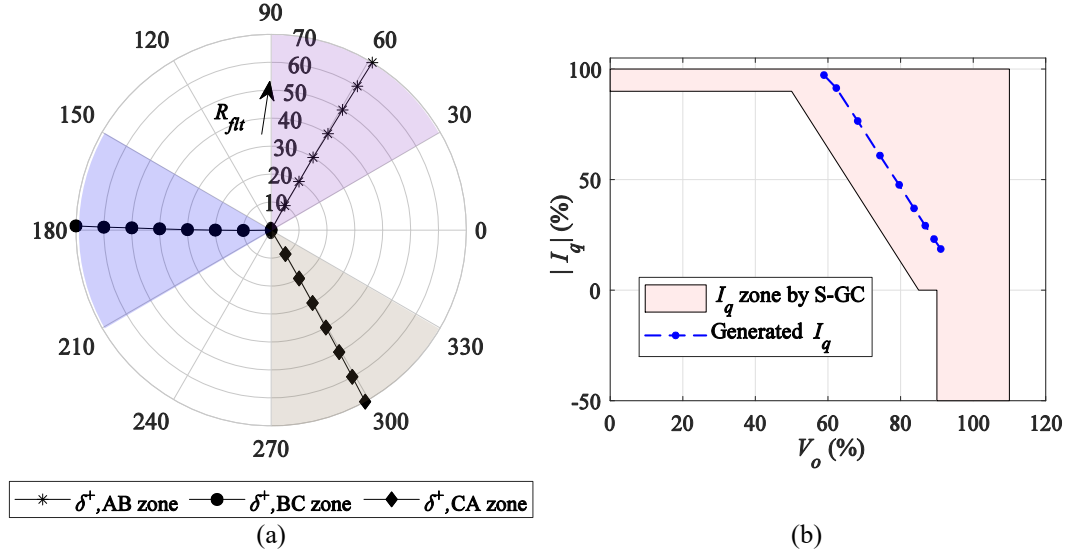


Figure 5.22. Performance of the proposed DCC1 during LL faults with the Spanish GC: (a)  $\delta^+$  measured by  $R_{25}$ , (b) Relation between the reactive output current and the voltage magnitude at the POI.

to place  $\delta^+$  at the center of its fault-type zone. Further, this figure verifies the effectiveness of the proposed DCC1 as it is not affected by fault resistance variations. - On the other hand, Figure 5.22(b) substantiates the DCC's ability to inject the required positive sequence reactive current during different voltage sags.

### 5.4.3 Compatibility with the NERC Reliability guidelines

The North American Electric Reliability Corporation (NERC) continuously updates its guidelines to support the reliability of IIRESSs. These guidelines are the basis for developing new reliability standards by different North-American entities, considering their business practices, system design, and configuration [83].

The 2020 NERC guidelines state that an IIRESS should inject an active current of at least 80% of the IIRESS pre-fault active current [84]. In this case, the power factor is not a decisive factor as it depends on the pre-fault active current. In this case, minor modifications are made to the proposed method by modifying the active and reactive current references to (i) prevent the active current during faults from being lower than 80% of its pre-fault value and (ii) inject the maximum available reactive current to enhance the voltage profile. First, the initial active and reactive current references are determined by

$$I_{P,ref(0)} = 0.8 \times I_{P,ref}^{pre} \quad (5.28)$$

$$I_{Q,ref(0)} = \sqrt{(I_{limit}^+)^2 - (I_{P,ref(0)})^2} \quad (5.29)$$

where  $I_{P,ref}^{pre}$  is the pre-fault active current reference. Then, the proposed procedure explained in Section 5.3 should be followed, except for  $I_{P,ref}$  and  $I_{Q,ref}$ , which are calculated as follows. If  $(\angle I_{t,ref}^+ - \angle V_t^+)$  is greater than  $(\angle I_{t,ref(0)}^+ - \angle V_t^+)$ , the active and reactive current references are adjusted as

$$I_{P,ref} = I_{P,ref(0)} \quad (5.30)$$

$$I_{Q,ref} = I_{P,ref} \times \tan(\angle I_{t,ref}^+ - \angle V_t^+) \quad (5.31)$$

Otherwise, the active and reactive references are amended as

$$I_{Q,ref} = I_{Q,ref(0)} \quad (5.32)$$

$$I_{P,ref} = \frac{I_{Q,ref}}{\tan(\angle I_{t,ref}^+ - \angle V_t^+)} \quad (5.33)$$

It is worth noting that the new NERC guidelines are employed when the POI voltage is lower than 0.9 p. u.; otherwise, the controller should inject reactive current such that the PF is above 0.95, as explained in Subsection 5.4.1.

Table 5.3 demonstrates the effectiveness of the proposed method in following the NERC guidelines at different loading and fault resistances. The results unveil that the new guidelines could achieve PSM requirements by adjusting the negative sequence angle with an acceptable shift from  $\delta^0$ 's zone bisector. Further, the proposed method succeeds in injecting the maximum positive-sequence current magnitude, i.e., 1.2 p. u., during different fault conditions. In addition, the proposed DCC1 sufficiently controls the positive-sequence active current to be higher than 80% of the pre-fault active current. For instance, for a solid BCG fault when the pre-fault active current equals 1.0 p. u., the proposed DCC1 maintains  $\delta^0$  and  $\delta^+$  within their zone limits by setting them at  $18.2^\circ$  and  $155.5^\circ$ .

Table 5.3. Performance of the proposed DCC1 with the NERC guidelines

Loading ( $I_{P,ref}^{pre}$ )	Fault Type	$R_{flt}$	$\delta^0$	$\delta^+$	$I_P^+$	$I_Q^+$
1	AG	0	16.4	-25.4	0.802	-0.888
		25	0.07	-10.1	0.801	-0.888
	BCG	0	18.2	155.5	0.803	-0.882
		25	2.8	184.8	0.802	-0.884
	CA	0	-	-57.7	0.803	-0.890
		25	-	-60.72	0.801	-0.891
0.8	CG	0	125.6	-145.6	0.642	-1.008
		25	120.1	-119.5	0.641	-1.009
	ABG	0	126.2	35.1	0.644	-1.004
		25	122.8	76.1	0.643	-1.006
	BC	0	-	181.9	0.642	-1.011
		25	-	178.8	0.641	-1.012
0.6	BG	0	-119.9	98.7	0.481	-1.094
		25	-119.9	130.4	0.481	-1.095
	CAG	0	-119.5	-79.8	0.483	-1.087
		25	-117.2	-33.4	0.483	-1.089
	AB	0	-	61.5	0.481	-1.098
		25	-	58.4	0.481	-1.098

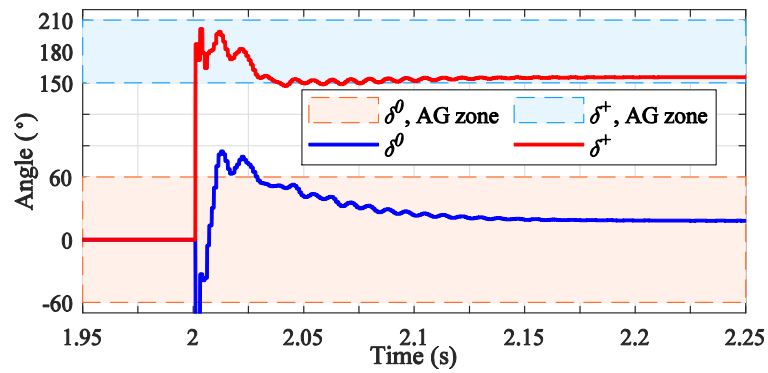


Figure 5.23. Measured  $\delta^0$  and  $\delta^+$  by  $R_{25}$  for a bolted BCG fault.

Further, the dynamic response of the proposed DCC1 illustrated in Figure 5.23 unveils the rapid response of the proposed controller, which reaches correct phase selection in about one cycle. Lastly, Figure 5.24 manifests the achievement of the NERC requirements by

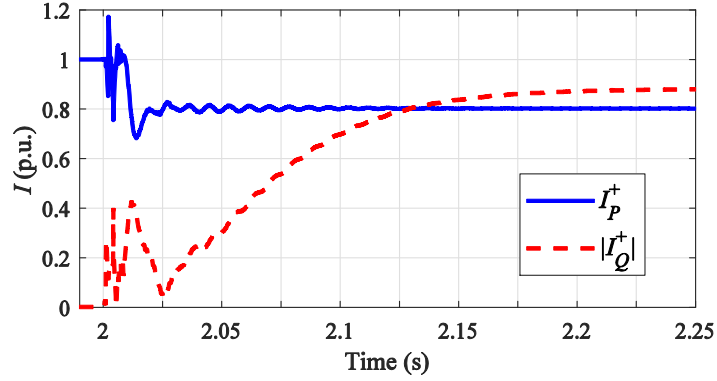


Figure 5.24. Active and reactive current magnitude for a bolted BCG fault.

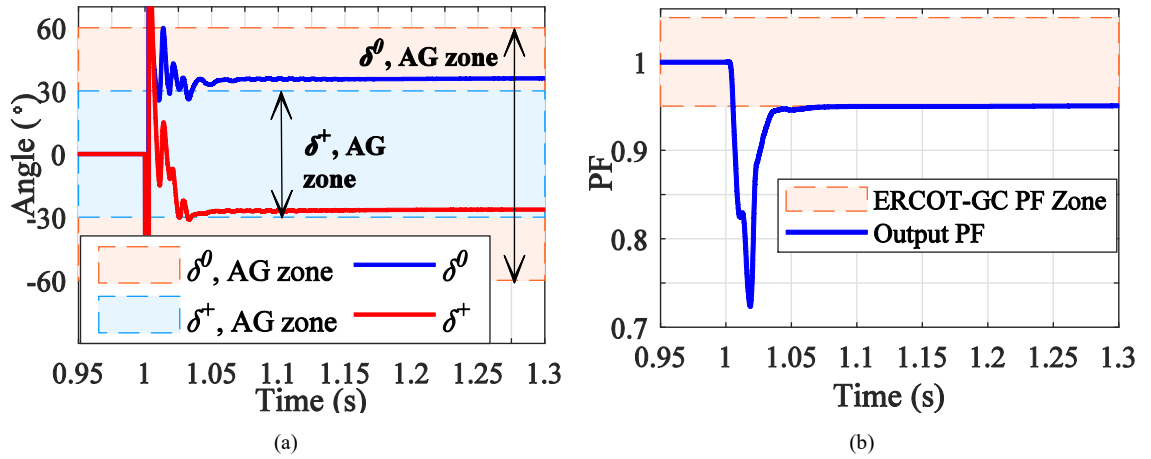


Figure 5.25. Measured quantities by  $R_{32}$  for a bolted AG fault when the IRES is controlled using the proposed DCC1: (a)  $\delta^0$  and  $\delta^+$ , (b) output power factor.

retaining the active current above 80% of its pre-fault value and injecting the maximum available reactive current to support the POI voltage.

#### 5.4.4 Comparison with Other DCCs

In this case study, the system in Figure 5.2 is simulated using MATLAB/Simulink, and the performance of the proposed controller is compared with other DCCs. Figure 5.25 displays  $R_{32}$  measurements during a bolted AG fault when the IRES is controlled by the proposed DCC1 following the ERCOT-GC. The results demonstrate the success of the proposed method in placing  $\delta^0$  and  $\delta^+$  in their correct zones, which shows its advantage against the DCC in [63] that only succeeds to locate  $\delta^0$  correctly. Besides, the proposed DCC1

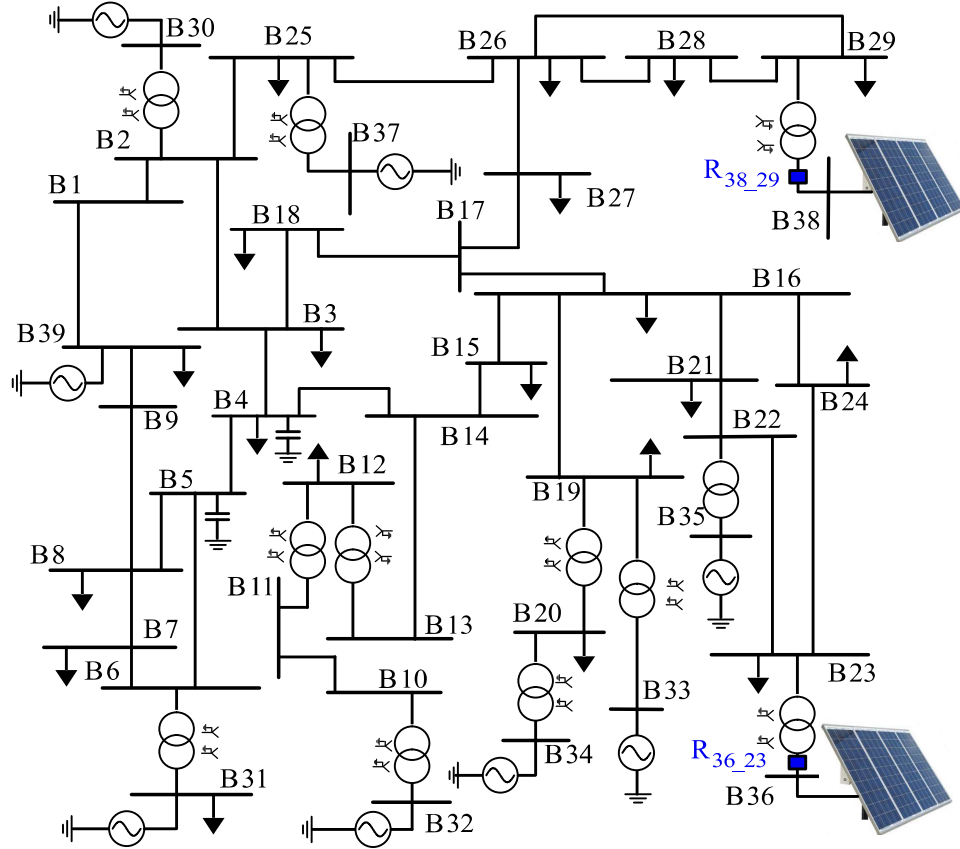


Figure 5.26. Modified IEEE 39-bus test system.

accurately maintains the PF at 0.95 lagging, as shown in Figure 5.25(b). These results demonstrate that the proposed DCC1 has better performance with respect to GC requirements as opposed to the DCC of [65], in which the PF settles at 0.16 lagging PF. In addition, Figure 5.25(a) unveils a faster response compared to that in Figure 5.3 because the proposed DCC1 is implemented in the stationary frame, making it reach a steady state in less than 0.05 s.

#### 5.4.5 Further Results

In this subsection, the proposed DCC1 is examined with the IEEE 39-bus system [85]. The IEEE test system is modified by replacing the sources at buses 36 and 38 with two 50-MW IRESs, as shown in Figure 5.26. The IRESs are controlled to follow the G-GC requirements and are integrated into the grid through 100-MW, 22/230 kV dYG transformers with an equivalent impedance of 0.1 p.u. Table 5.4 displays  $\delta^0$  and  $\delta^+$

Table 5.4. Performance of the proposed DCC1 for faults detected by  $R_{38-29}$

Fault type	Fault bus	$R_{flt}$	$\delta^0$	$\delta^+$	$\Delta V$	$ I_q $
AG	29	0	35.3	-26.3	0.375	0.744
		50	14.4	-27.6	0.171	0.313
	28	0	33.4	-26.1	0.361	0.727
		50	10.0	-26.7	0.146	0.307
	29	0	35.3	-26.3	0.375	0.744
		50	14.4	-27.6	0.171	0.313
BCG	29	0	14.1	152.7	0.644	1
		50	2.4	-169.4	0.53	1
	28	0	15.0	152.7	0.645	1
		50	2.4	-169.8	0.53	1
	29	0	14.1	152.7	0.644	1
		50	2.4	-169.4	0.53	1

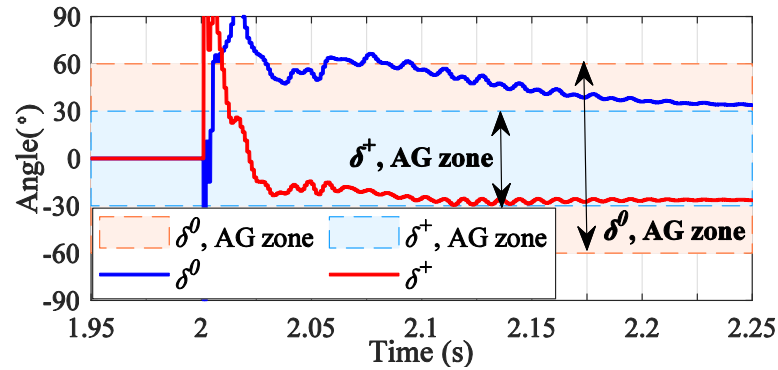


Figure 5.27. Measured  $\delta^0$  and  $\delta^+$  by  $R_{38-29}$  for a bolted AG fault.

measured by  $R_{38-29}$ , and  $\Delta V$  and  $I_q$  measured at the IRES terminals during different fault locations and fault resistances. The results validate the ability of the proposed controller to achieve the PSM requirements and inject  $I_q$ , i.e., double  $\Delta V$ . For instance, the highlighted case study during a bolted AG fault shows that  $\delta^0$  and  $\delta^+$  are within their accepted zone boundaries, as shown in Figure 5.27. In addition, the DCC1 successfully complies with the G-GCs by making  $I_q$  twice  $\Delta V$ , i.e., 0.727 p.u. and 0.361 p.u., respectively.

Table 5.5. Performance of the proposed DCC1 for faults detected by  $R_{36-23}$ 

Fault type	$R_{flt}$	$\delta^0$	$\delta^+$	$\Delta V$	$ I_q $
CG	0	152.5	-144.9	0.379	0.757
	50	119.6	-136.8	0.122	0.244
CAG	0	-102.1	-84.8	0.674	1
	50	-128.1	-32.5	0.507	1
AB	0	-	57.4	0.495	1
	50	-	58.1	0.101	0.254

Table 5.5 demonstrates the successful operation of PSM measured by  $R_{36-23}$  during faults at bus 23 when the IIREs are controlled by the proposed DCC1. The results show the accurate operation of the proposed DCC1 at different fault types, i.e., SLG, LLG, and LL faults, where  $\delta^0$  and  $\delta^+$  are located within their zone limits with acceptable margins. In addition, the proposed DCC1 achieved G-GC requirements by making the injected reactive current equal to twice the voltage drop. For instance, during a bolted AB fault,  $\delta^+$  is  $58.1^\circ$ , thus achieving the PSM requirements. Further,  $\Delta V$  and  $I_q$  are 0.101 p.u. and 0.254 p.u., respectively, i.e., complying with the G-CG requirements.

#### 5.4.6 Real-time Simulations

The case study in Subsection 5.4.1 is conducted experimentally using a Speedgoat real-time simulator (RTS) to verify the accuracy of the proposed method in real time. The Speedgoat RTS is a 2.0 GHz quad-core processor with parallel computation capability used to simulate complex models with high accuracy [86]. In the experiment, the simulation is reorganized to allow the RTS to perform two functions on two separate cores, i.e., CPU1 and CPU2, as shown in Figure 5.28. The first function is rapid control prototyping (RCP), in which the proposed controller is implemented using CPU1. RCP controllers are utilized because they are easier to implement and debug and more flexible than actual controllers. The second function performed by the RTS is a hardware-in-the-loop (HIL) simulation, which is used to realize a virtual grid in real-time using CPU2. The data exchange between CPU1 and CPU2 is done externally using two terminal boards, namely, 17-Pin M12. The communication between the terminal boards is done through hardwires, like in real-world



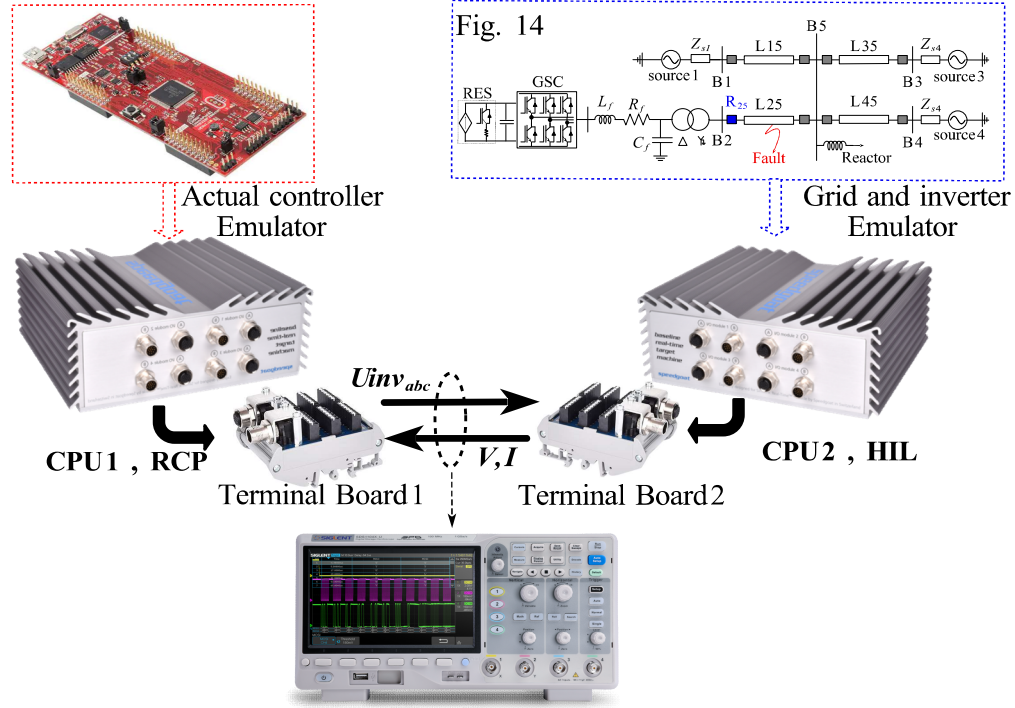


Figure 5.28. Schematic for the test system executed in real-time.

scenarios. Also, the measured signals are filtered using an  $RC$  low-pass filter with a cut-off frequency of 20 kHz to eliminate high-frequency noise.

Figure 5.29 shows the results of the RTS during a bolted BG, where  $\delta^0$  and  $\delta^+$  settle accurately inside their correct zones and maintain a  $4^\circ$  margin from their zone limits. In addition, the proposed controller keeps the desired PF at 0.95 lagging, which validates the accuracy of the proposed method in real-time. Figure 5.30 asserts the capability of the proposed DCC1 to achieve the RCG and PSM requirements simultaneously during a high resistive fault, i.e.,  $R_{flt} = 50 \Omega$ . The measured data exhibit  $\delta^0$  and  $\delta^+$  during an AG fault, where they almost lie at the centers of their respective zones; besides, the PF is maintained at 0.95 lagging.

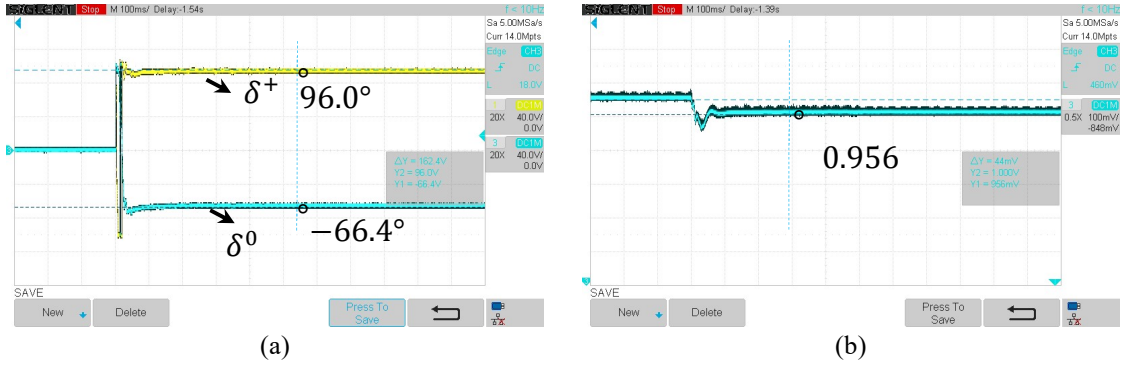


Figure 5.29. Measured quantities by  $R_{25}$  for a bolted BG fault: (a)  $\delta^0$  and  $\delta^+$  (time/div.=100 ms and angle/div= $40^\circ$ ), (b) output power factor (time/div.=100 ms and PF/div=0.1).

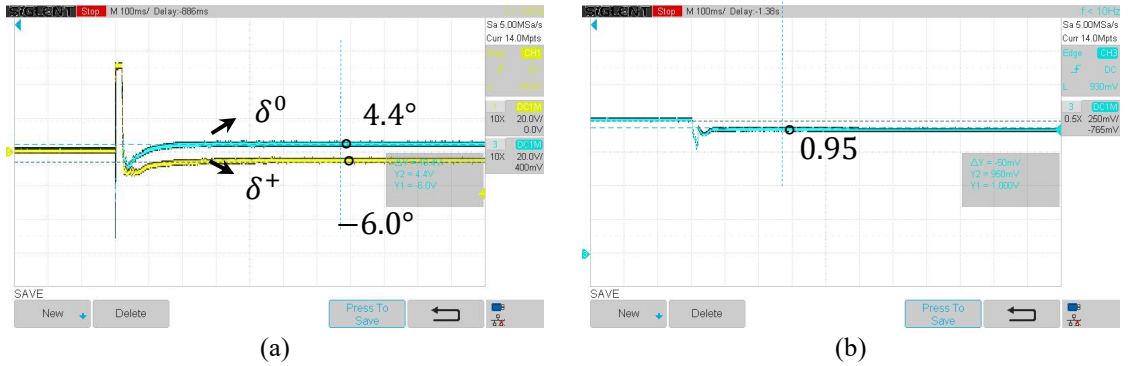


Figure 5.30. Measured quantities by  $R_{25}$  for an AG fault with  $R_{flt} = 50\Omega$ : (a)  $\delta^0$  and  $\delta^+$  (time/div.=100 ms and angle/div= $30^\circ$ ), (b) output power factor (time/div.=100 ms and PF/div=0.2).

On the other hand, Figures 31 and 32 display the measured signals during BCG and ABG faults, respectively. Figure 5.31 reveals the effectiveness of the proposed method during a bolted BCG fault, where  $\delta^0$ ,  $\delta^+$ , and the PF are regulated successfully. Likewise, Figure 5.32 confirms that maintaining a high PF during a high resistive fault, i.e.,  $R_{flt} = 50\Omega$ , is achieved by slightly shifting  $\delta^0$  and  $\delta^+$  from their zone bisectors without jeopardizing phase selection.

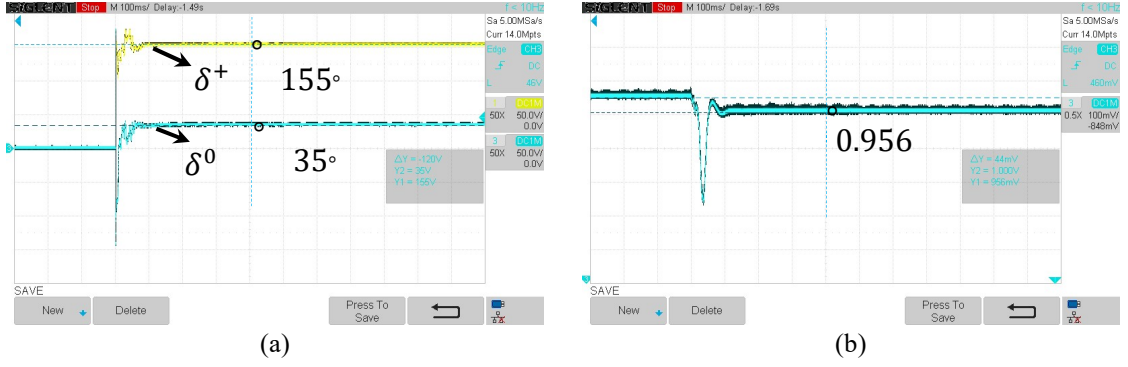


Figure 5.31. Measured quantities by  $R_{25}$  for a bolted BCG fault: (a)  $\delta^0$  and  $\delta^+$  (time/div.=100 ms and angle/div= 50°), (b) output power factor (time/div.=100 ms and PF/div= 0.1).

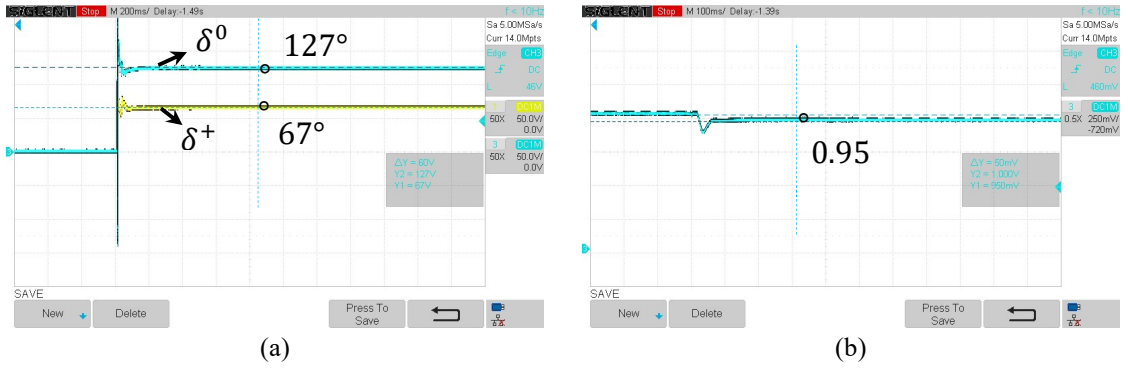


Figure 5.32. Measured quantities by  $R_{25}$  for an ABG fault with  $R_{flt} = 50\Omega$ : (a)  $\delta^0$  and  $\delta^+$  (time/div.=200 ms and angle/div.= 50°), (b) output power factor (time/div.=100 ms and PF/div=0.2).

## 5.5 Proposed Dual Current Controller for Enhanced PSM Security and Compliance with RCG Requirements

In DCC1, the reference currents are determined to allow proper operation for PSM and comply with RCG requirements simultaneously. DCC1 was controlled to maintain  $\delta^0$  with high security as DCC1 attempts to settle  $\delta^0$  to be equal to  $\delta_{F,bis}^0$ , if  $\delta^+$  is still within the acceptable range. However, this methodology allows the measured value of  $\delta^+$  to reach its marginal limit before changing the negative-sequence current angle, which reduces the security for  $\delta^+$ , leading to lowering the PSM security. Thus, in this section, another DCC is designed to equalize the difference between  $\delta^0$  and  $\delta_{F,bis}^0$  with that between  $\delta^+$  and

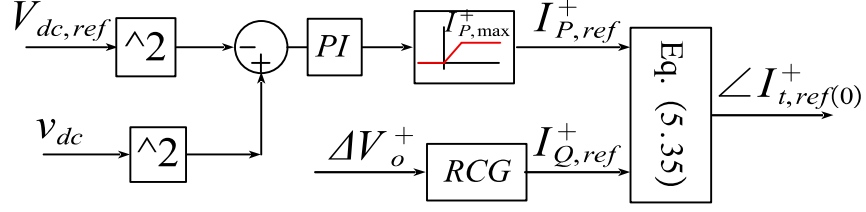


Figure 5.33. The procedure for determining  $\angle I_{t,ref(0)}^+$ .

$\delta_{F,bis}^+$  to increase the overall security of the PSM. Another difference is that this DCC is designed to allow an extended  $\Theta_{max}^+$ , i.e., equal to  $60^\circ$ , compared to  $\Theta_{max}^+$  selected in DCC1, which is set at  $30^\circ$ . Thus, in this controller,  $\Theta_{max}^+$  is set equal to  $\Theta_{max}^0 = 60^\circ$  and they both are designated by  $\Theta_{max}$ . It is worth mentioning that increasing the boundary width of  $\Theta_{max}^0$  or/and  $\Theta_{max}^+$  increases the speed of fault detection and its reliability. Thus, conventional PSM was initially set  $\Theta_{max}^0$  and  $\Theta_{max}^+$  to be set to  $60^\circ$  and  $30^\circ$ , respectively [9]. Lately,  $\delta^+$  zones are suggested to be expanded to have  $\Theta_{max}^+$  equal to  $60^\circ$  to enhance the PSM reliability [69]. The proposed DCC2 is designed in four stages as follows.

### 5.5.1 Determining the Initial Positive-Sequence Current Angle at POI

The positive-sequence current should be controlled to generate an adequate positive-reactive current based on RCG requirements and inject the maximum available active current to enhance the system stability. Figure 5.33 illustrates the procedure for determining  $\angle I_{t,ref(0)}^+$ . The positive-sequence reactive current component, i.e.,  $I_{Q,ref}^+$ , is determined based on the RCG requirements. On the other hand, the positive-sequence active current component, i.e.,  $I_{P,ref}^+$ , is obtained using a PI controller that is used to regulate the dc-link voltage; then, this current is limited to avoid IRES's current from exceeding positive-sequence current limits, i.e.,  $I_{limit}^+$  usually set at 1.2 p.u. [64]. Most GCs give priority to the positive-sequence reactive current generation; thus, the maximum positive-sequence active current component, i.e.,  $I_{P,max}^+$ , is determined by (5.34).

$$I_{P,max}^+ = \sqrt{(I_{limit}^+)^2 - (I_{Q,ref}^+)^2}. \quad (5.34)$$

Subsequently,  $\angle I_{t,ref(0)}^+$  is determined according to

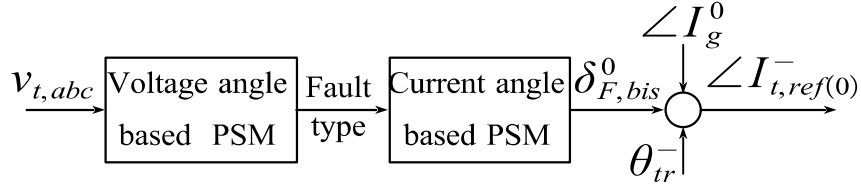


Figure 5.34. The procedure for determining  $\angle I_{t,ref(0)}^-$ .

$$I_{t,ref(0)}^+ = \tan^{-1} \left( \frac{-I_{Q,ref}^+}{I_{P,ref}^+} \right). \quad (5.35)$$

### 5.5.2 Determining the Initial Negative-Sequence Current Angle at POI

The initial negative-sequence current angle at POI, i.e.,  $\angle I_{t,ref(0)}^-$ , is designed, as depicted in Figure 5.34, to impose  $\delta^0$  measured by the grid-side relay to be equal  $\delta^0$ 's correct fault-type-zone bisector. Thus,  $\angle I_{t,ref(0)}^-$  is calculated by

$$\angle I_{t,ref(0)}^- = \delta_{F,bis}^0 + \angle I_g^0 + \theta_{tr}^- \quad (5.36)$$

in which  $\delta_{F,bis}^0$  is determined by applying a voltage-angle-based classifier at the IRES terminals.

### 5.5.3 Determining the Negative- and Positive-Sequence Current Angles at POI

In this stage, the initial negative- and positive-sequence current angles, i.e.,  $\angle I_{t,ref(0)}^-$  and  $\angle I_{o,ref(0)}^+$ , are updated to allow  $\delta^0$  and  $\delta^+$  calculated on the relay side to be within the correct current-angle-based PSM zones without violating RCG requirements. The procedure for updating  $\angle I_{t,ref(0)}^-$  and  $\angle I_{t,ref(0)}^+$  during ground faults, i.e., SLG (AG, BG, and CG) and LLG (ABG, BCG, and CAG), is illustrated in Figure 5.35. In stage B,  $\angle I_{t,ref(0)}^-$  is determined by forcing  $\delta^0$  to align with  $\delta_{F,bis}^0$ ; thus,  $\delta^0$  measured by the relay refers to its correct fault-type zone. However, there is no guarantee that  $\delta^+$  calculated at the relay side refers to its correct fault-type zone. Consequently,  $\angle I_{t,ref(0)}^-$  should be updated by allowing  $\delta^0$  and  $\delta^+$  to be within their correct fault-type zone and be minimum shifted from their correct zone bisectors, i.e.,  $\delta_{F,bis}^0$  and  $\delta_{F,bis}^+$ . First, the expected  $\delta^+$

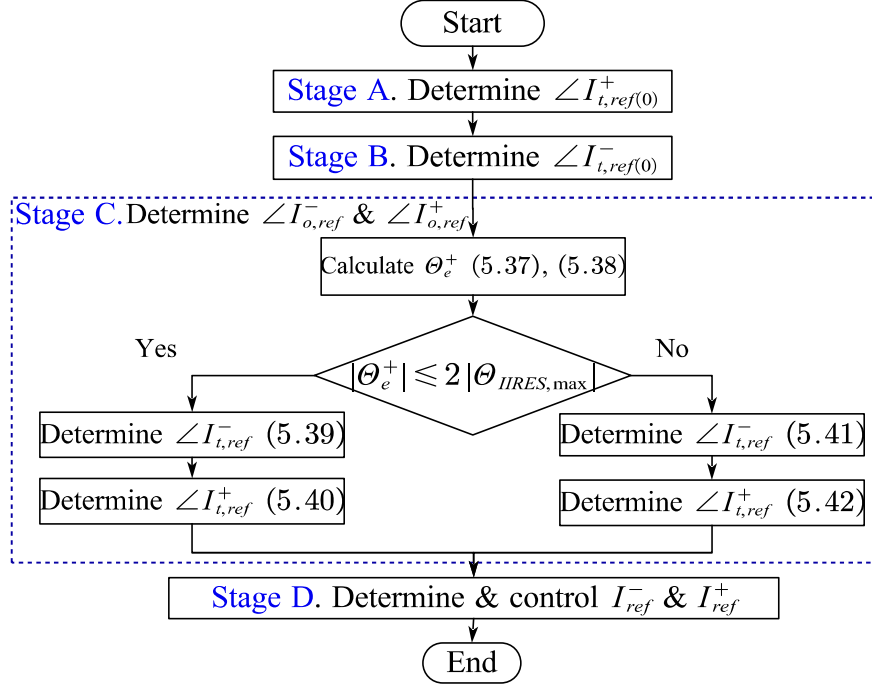


Figure 5.35. The flow chart of the proposed controller.

measured by the relay when the IIRES is controlled to inject current with angles set to  $\angle I_{t,ref}^-$  and  $\angle I_{t,ref}^+$ , i.e.,  $\delta_e^+$ , is determined by

$$\delta_e^+ = \angle I_{t,ref}^- - \angle I_{t,ref}^+ - \theta_{tr}^- + \theta_{tr}^+ \quad (5.37)$$

Then,  $\Theta_e^+$  (the expected phase shift of  $\delta_e^+$  from the correct fault-type zone bisector) is determined by

$$\Theta_e^+ = \delta_e^+ - \delta_{f,bis}^+ \quad (5.38)$$

Consequently,  $\angle I_{t,ref}^-$  and  $\angle I_{t,ref}^+$  are updated by (5.39) and (5.40), respectively, if  $|\Theta_e^+|$  is smaller than  $2|\Theta_{IRES,max}|$ , where  $\Theta_{IBR,max}$  is equal to  $\Theta_{max} - \mu$ , where  $\mu$  is set in this DCC to  $10^\circ$  to have higher security. In addition, by applying (5.37) and (5.38), both  $\delta^0$  and  $\delta^+$  are shifted with the same angle from  $\delta_{f,bis}^0$  and  $\delta_{f,bis}^+$ , respectively, which results in higher security of the proposed method compared to DCC1 which does not update  $\angle I_{t,ref}^-$  until  $\delta_e^+$  exceeds its zone boundaries.

$$\angle I_{t,ref}^- = \angle I_{t,ref(0)}^- - \frac{\theta_e^+}{2} \quad (5.39)$$

$$\angle I_{t,ref}^+ = \angle I_{t,ref(0)}^+. \quad (5.40)$$

On the other hand, if  $|\theta_e^+|$  is greater than  $2|\Theta_{IIRES,max}|$ , both  $\angle I_{t,ref(0)}^-$  and  $\angle I_{t,ref(0)}^+$  should be updated.  $\angle I_{t,ref(0)}^-$  is updated with the maximum allowable shift without exceeding  $\Theta_{IIRES,max}$ . Thereafter,  $\angle I_{t,ref(0)}^+$  is minimally updated to allow  $\delta^+$  to be within  $\pm\Theta_{IIRES,max}$ , as shown in (5.46) and (5.47).

$$\angle I_{o,ref}^- = \angle I_{o,ref(0)}^- - \Theta_{IIRES,max} \times \text{sgn}(\theta_e^+) \quad (5.41)$$

$$\angle I_{o,ref}^+ = \angle I_{o,ref(0)}^+ + \theta_e^+ - \Theta_{IIRES,max} \times \text{sgn}(\theta_e^+) \quad (5.42)$$

where  $\text{sgn}$  is the signum function, which determines the sign of the function.

#### 5.5.4 Determining and Controlling the Negative- and Positive-Sequence Current References at the IIRES

The negative- and positive-sequence current references are determined based on their pre-defined reference angles and the inverter's maximum current limit to achieve PSM requirements and inject maximum current during fault. The procedure of determining and controlling  $i_{ref}^-$  and  $i_{ref}^+$  in the  $\alpha\beta$  frame is depicted in Figure 5.36. The  $\alpha\beta$  reference positive- and negative-sequence currents at POI, i.e.,  $i_{t,\alpha,ref}^\pm$  and  $i_{t,\beta,ref}^\pm$ , are determined by

$$\begin{cases} i_{t,\alpha,ref}^\pm = I_{limit}^\pm \sin(\pm\omega t + \angle I_{t,ref}^\pm) \\ i_{t,\beta,ref}^\pm = \pm I_{limit}^\pm \cos(\pm\omega t + \angle I_{t,ref}^\pm) \end{cases} \quad (5.43)$$

where  $I_{limit}^\pm$  are the inverter's maximum current in the positive- and negative-sequence frame, which are set as 1.2 and 0.3 p.u., respectively. Subsequently, the  $\alpha\beta$  positive- and negative-sequence current references at the IIRES's terminals, i.e.,  $i_{\alpha,ref}^\pm$  and  $i_{\beta,ref}^\pm$ , are calculated based on  $i_{t,\alpha,ref}^\pm$  and  $i_{t,\beta,ref}^\pm$  after compensating for the phase shift introduced by the filter's capacitor. The positive- and negative-sequence currents are formulated by

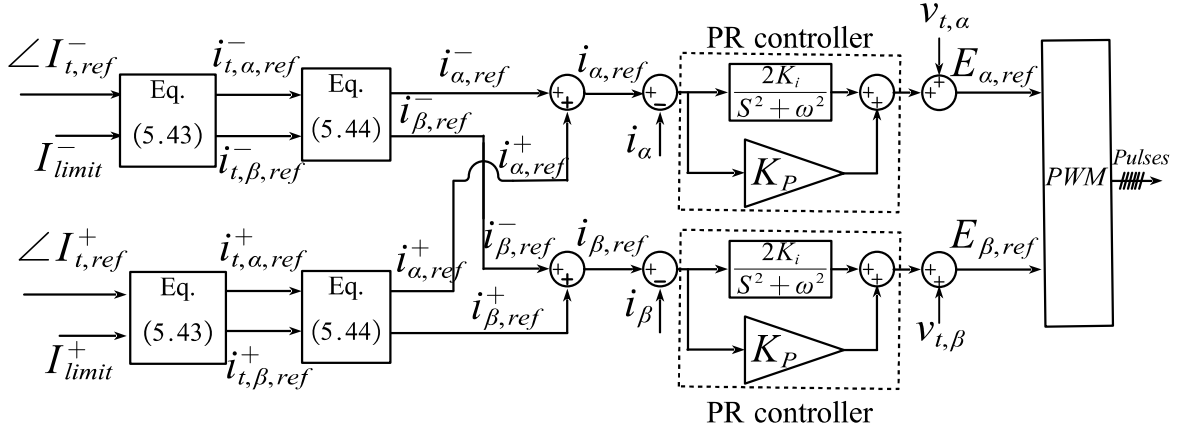


Figure 5.36. The procedure of determining and controlling  $i_{ref}^-$  and  $i_{ref}^+$ .

$$\begin{cases} i_{a,ref}^\pm = i_{t,a,ref}^\pm \mp \omega C_f v_{t,\beta}^\pm \\ i_{\beta,ref}^\pm = i_{t,\beta,ref}^\pm \pm \omega C_f v_{t,\alpha}^\pm \end{cases} \quad (5.44)$$

Thereafter, the reference positive- and negative-sequence currents are added together to reduce the number of controllers. Thus,  $i_{a,ref}$  and  $i_{\beta,ref}$  are determined by

$$\begin{cases} i_{a,ref} = i_{a,ref}^+ + i_{a,ref}^- \\ i_{\beta,ref} = i_{\beta,ref}^+ + i_{\beta,ref}^- \end{cases} \quad (5.45)$$

Finally, a PR compensator is utilized to track the reference currents in the  $\alpha\beta$  frame.

## 5.6 Performance Evaluation of DCC2

The accuracy of the proposed DCC2 in achieving PSM and RCG requirements simultaneously is validated by testing a 230-kV, 60 Hz transmission system, which is illustrated in Figure 5.14, using PSCAD/EMTDC simulations for various fault types, locations, and resistances with different RCG requirements.

### 5.6.1 Compatibility with GCs Imposing Constant Power Factor

The proposed DCC2 is examined when the positive-sequence current is controlled to maintain a constant PF, i.e., 0.95 lagging, as stated by the ERCOT, which is considered an example of North American GCs. Table 5.6 reports the results of  $\delta^0$  and  $\delta^+$  measured by



Table 5.6. Performance of the proposed DCC2 during ground faults with ERCOT-GC

Fault Type	$R_{flt}$	Fault at 5% of $L_{25}$			Fault at 50% of $L_{25}$			Fault at 95% of $L_{25}$		
		$\delta^0$	$\delta^+$	PF	$\delta^0$	$\delta^+$	PF	$\delta^0$	$\delta^+$	PF
AG	0	38.7	-36.3	0.9502	36.9	-35.5	0.9505	36.4	-35.5	0.9504
	50	12.0	-12.7	0.9500	11.1	-12.2	0.9501	5.8	-8.4	0.9500
BG	0	-81.3	83.7	0.9504	-83.0	84.5	0.9506	-83.6	84.5	0.9503
	50	-108.0	107.3	0.9502	-108.9	107.8	0.9501	-114.1	111.6	0.9501
CG	0	158.7	-156.3	0.9509	157.0	-155.5	0.9508	156.4	204.5	0.9506
	50	132.0	-132.7	0.9504	131.1	-132.2	0.9503	125.8	-128.4	0.9503
ABG	0	162.3	19.5	0.9514	159.8	23.2	0.9508	160.1	23.4	0.9507
	50	127.4	58.3	0.9503	130.8	54.9	0.9503	129.7	56.3	0.9503
BCG	0	42.3	139.5	0.9519	39.9	143.2	0.9515	40.1	143.4	0.9517
	50	7.4	178.2	0.9510	10.7	175.0	0.9511	9.7	176.3	0.9511
CAG	0	-77.7	-100.5	0.9517	-80.2	-95.8	0.9512	-79.9	-96.6	0.9512
	50	-112.6	-61.7	0.9510	-109.2	-65.0	0.9509	-110.3	-63.7	0.9508

the relay  $R_{25}$  and the PF measured at the inverter terminals for various fault types, resistances, and locations. Table 5.6 verifies the accuracy of the proposed DCC2 in maintaining  $\delta^0$  and  $\delta^+$  in their correct fault-type zones without violating GC requirements by controlling the PF at 0.95 lagging. In addition, the proposed DCC2 successfully divides the phase shift of  $\delta^0$  and  $\delta^+$  from their bisector equally. As a result, the proposed DCC2 offers greater security than DCC1 by ensuring that  $\delta^0$  is shifted from its bisector before  $\delta^+$  reaches its limit. For instant,  $\delta^0$  is shifted from  $\delta_{F,bis}^0$  by  $38.7^\circ$  and  $12.0^\circ$ , while  $\delta^+$  is shifted from  $\delta_{F,bis}^+$  by  $36.3^\circ$  and  $12.7^\circ$  in SLG faults for fault resistance ( $R_{flt}$ ) equals 0 and  $50 \Omega$ , respectively.

The PF of fault current that is resulted from SGs is affected by the fault resistance and location. For instance, as the fault resistance increases, the fault current's PF is near unity, while the PF slightly decreases as the distance of the fault location increases far from the source location. Thus, to keep the PF constant, the proposed DCC2 changes the phase shift of  $\delta^0$  and  $\delta^+$  from their bisectors. For example, in a BCG fault,  $\delta^0$  is shifted from  $\delta_{F,bis}^0$  by  $42.3^\circ$  and  $7.4^\circ$ , while  $\delta^+$  is shifted from its bisector by  $40.5^\circ$  and  $1.8^\circ$  for solid and

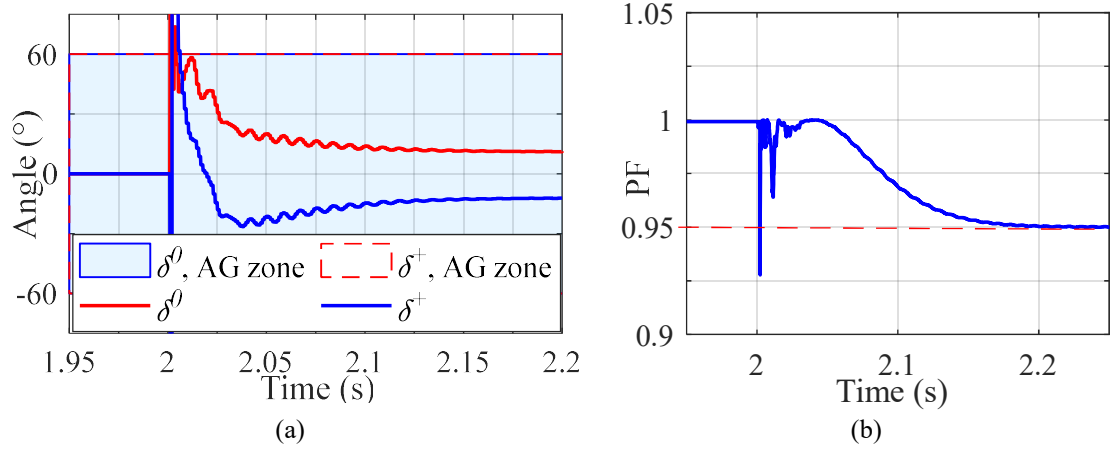


Figure 5.37. Dynamic response of the proposed DCC2 for an AG with ERCOT-GC and  $R_{flt} = 50\Omega$ : (a)  $\delta^0$  and  $\delta^+$ , (b) PF.

high resistive faults, respectively. On the other hand,  $\delta^0$  and  $\delta^+$  are slightly changed by varying fault locations, e.g., the maximum change of  $\delta^0$  and  $\delta^+$  when the fault location changed from 5% to 95% of  $L_{25}$  is  $6.2^\circ$  and  $3.9^\circ$ , respectively.

For illustration, the response of an AG fault, at 50% of  $L_{25}$  with  $R_{flt} = 50\Omega$ , is portrayed in Figure 5.37 to represent the highlighted case study of Table 5.6. Figure 5.37(a) shows that the proposed DCC2 controlled  $\angle I^-$  to maintain  $\delta^0$  and  $\delta^+$  in their correct fault type zones, i.e.,  $11.1^\circ$  and  $-12.1^\circ$ , respectively. In addition, the figure verifies the rapid dynamic response of the proposed controller as  $\delta^0$  and  $\delta^+$  are settled in their appropriate zones in less than 0.5 cycles. On the other hand, Figure 5.37(b) demonstrates the capability of the proposed method to maintain a constant PF, i.e., 0.95 lagging, without violating phase selection requirements.

### 5.6.2 Compatibility with GCs Imposing Reactive Current Relative to Voltage Drop

The applicability of the proposed DCC2 under GCs requires a variation of the reactive-current magnitude according to the value of the voltage drop is verified in this subsection. Table 5.7 displays  $\delta^0$  and  $\delta^+$  determined by the relay as well as the positive-sequence reactive current magnitude ( $|I_q^+|$ ) and the voltage drop measured at the inverter's terminals ( $\Delta V$ ), where  $|I_q^+| = 2\Delta V$ , following the G-GC. Table 5.7 manifests the capability of the

Table 5.7. Performance of the proposed DCC2 during ground faults with G-GC

Fault Type	$R_{flt}$	Fault at 50% of $L_{25}$				Fault at bus5			
		$\delta^0$	$\delta^+$	$ I_q^+ $	$\Delta V$	$\delta^0$	$\delta^+$	$ I_q^+ $	$\Delta V$
AG	0	33.6	-32.27	0.521	0.262	35.4	-34.5	0.438	0.220
	20	22.6	-22.5	0.412	0.207	20.3	-20.9	0.267	0.135
BG	0	-86.4	87.7	0.521	0.262	-84.6	85.5	0.438	0.221
	20	-97.3	97.5	0.412	0.207	-99.7	99.1	0.267	0.135
CG	0	153.5	207.7	0.521	0.262	155.4	205.5	0.439	0.220
	20	142.6	217.5	0.412	0.207	140.3	219.1	0.267	0.135
ABG	0	137.5	44.3	0.99	0.561	137.2	45.0	0.992	0.508
	20	119.4	64.7	0.985	0.497	120.1	64.9	0.897	0.452
BCG	0	17.6	164.3	0.992	0.560	17.2	165.0	0.993	0.508
	20	-0.6	-175.3	0.986	0.497	0.1	-175.1	0.897	0.452
ACG	0	-102.4	-75.7	0.991	0.560	-102.7	-75.0	0.992	0.508
	20	-120.6	-55.33	0.986	0.496	-120.1	-55.1	0.897	0.451

proposed method to achieve PSM requirements and RCG requirements by GCs, simultaneously. From Table 5.7, it can be verified that the proposed DCC2 controlled  $\angle I^-$  properly by keeping roughly equal phase shift between  $\delta^0$  and  $\delta_{F,bis}^0$  and that between  $\delta^+$  and  $\delta_{bis}^+$ . For instance,  $\delta^0$  and  $\delta^+$  are almost shifted by  $17^\circ$  and  $1^\circ$  in LLG faults for  $R_{flt} = 0$  and  $20 \Omega$ , respectively. In addition, the proposed controller accurately tracks  $|I_q^+|$  to have a magnitude double  $\Delta V$ , e.g., for solid SLG faults,  $|I_q^+| = 0.412$  when  $\Delta V = 0.207$ , while  $|I_q^+| = 0.99$  when  $\Delta V = 0.56$  for solid LLG faults. It is worth mentioning that  $|I_q^+|$  is limited at 1 p.u. to allow the IRES to inject adequate active current during faults. Figure 5.38 illustrates the highlighted case study in Table 5.7 for a solid BCG fault that occurs on bus 5. Figure 5.38(a) substantiates the thoroughness of the proposed DCC2 in tracking  $\angle I^-$  to maintain accurate PSM, i.e.,  $\delta^0 = 17.2^\circ$  and  $\delta^+ = 165.0^\circ$ . Moreover, it verifies the rapid ability of the proposed DCC2 to achieve PSM requirements, such that  $\delta^0$  and  $\delta^+$  are settled in their correct fault-type zones in less than 1.5 cycles. In addition,  $|I_q^+|$  is precisely controlled to equal double the voltage drop, i.e., 0.993 and 0.508, respectively, as displayed in Figure 5.38(b).

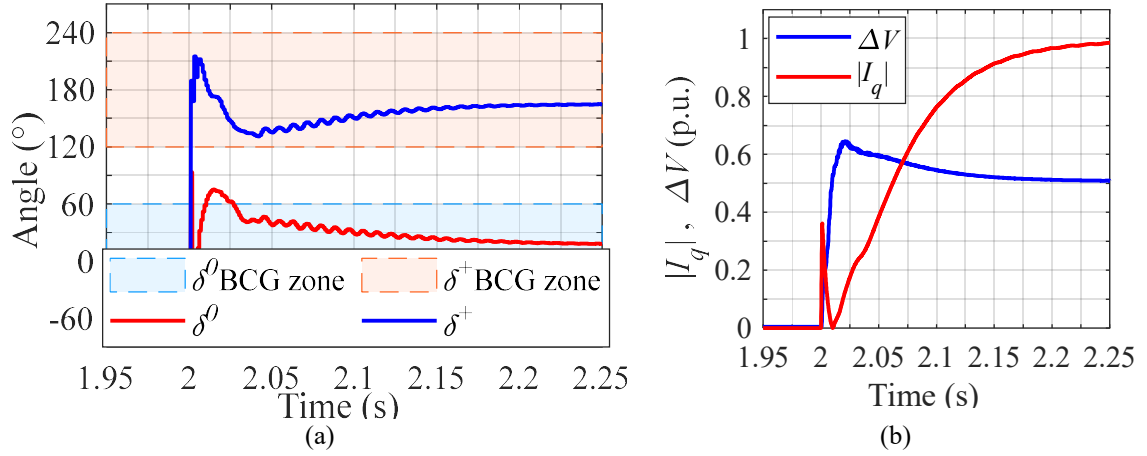


Figure 5.38. Dynamic response of the proposed DCC2 for a solid BCG with G-GC: (a)  $\delta^0$  and  $\delta^+$ , (b)  $|I_q^+|$  vs  $\Delta V$ .

## 5.7 Conclusions

Commercial PSM reliability is imperiled when faults are emanating from IIRESSs. In this chapter, two DCCs are proposed to allow conventional phase selection elements to operate precisely without violating RCG requirements. The proposed DCCs are based on selecting an adequate negative-sequence current angle to allow current-angle PSM to operate precisely. On the other hand, the positive-sequence current is determined based on RCG requirements. However, this angle is permitted to be slightly varied if the negative-sequence current angle is not capable, alone, to force both terms of PSM to be placed correctly in their respective zones. Subsequently, the current references are determined to possess the reference positive- and negative-sequence current angles without violating the maximum current limit of the IIRESS. Simulation studies were conducted for different RCG requirements, fault locations, fault resistance, and fault type to manifest the accuracy of the proposed DCC in achieving the requirements for both RCG and PSM, simultaneously.

## Chapter 6

# Dual Current Control of IIRESSs for Phase Selection and Compliance with Recent Negative-Sequence RCG

### 6.1 Introduction

In Chapter 5, the IIRESS was controlled to allow proper operation of PSMs and ensure that the emanating currents following the positive-sequence RCG requirements by different GCs. Recently, GCs, such as VDE-AR-N 4120-GC and the first draft of IEEE P2800, impose requirements for both positive- and negative-sequence RCG. Thus, in this chapter, the IIRESS's DCC is designed to allow the precise operation of PSMs while following the positive- and negative-sequence RCG requirements imposed by recent GCs. First, the negative-sequence current reference is designed to comply with the GC requirements and inject the minimum value of active-negative-sequence current that secures correct operation of PSMs. Subsequently, the positive-sequence-reactive current is designed to allow injecting the maximum available positive-sequence active current that allows proper operation of PSM without hindering the RCG requirements. Comprehensive time-domain simulations verify the effectiveness of the proposed DCC in achieving both PSM and recent RCG requirements during different fault type, resistances, and locations.

### 6.2 Problem Statement

In this section, the root causes of the current-angle-based PSM maloperation are elaborated by investigating a sample power system shown in Figure 6.1, when the IIRESS follows the recent German GC, i.e., VDE-AR-N 4120-GC [30]. The VDE-GC forces the IIRESS to inject positive- and negative-sequence currents to enhance the grid voltage during unbalanced faults. The IIRESS should be controlled to inject an inductive-negative-sequence current, i.e.,  $I_q^-$ , to reduce the voltage imbalance, and its magnitude is given by

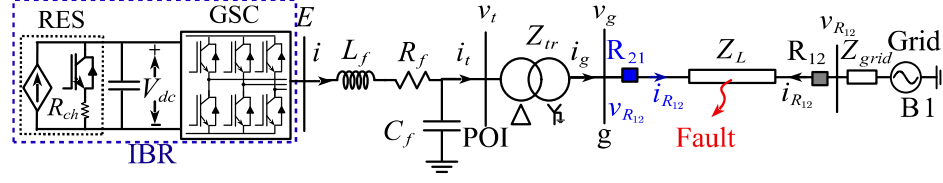


Figure 6.1. A sample system representing an IRES connected to a power grid.

$$I_q^- = K^- |V_t^-| \quad (6.1)$$

where  $K^-$  is a constant ranging from 2 to 6. Consequently, the negative-sequence current, i.e.,  $I^-$ , can be formulated by

$$I^- = K^- |V_t^-| \angle(\theta_{V_t^-} + 90^\circ) \quad (6.2)$$

where  $\theta_{V_t^-}$  is the phase angle of  $V_t^-$ . Subsequently, the relation between the current and voltage angles measured at the relay can be determined by

$$\theta_{I_R^-} = \angle(\theta_{V_R^-} + 90^\circ) \quad (6.3)$$

where  $\theta_{V_R^-}$  and  $\theta_{I_R^-}$  are the phase angles of  $V_R^-$  and  $I_R^-$ , respectively. In addition, the IRES should be controlled to inject a capacitive-reactive current to support the positive-sequence voltage such that the positive-sequence reactive current,  $I_q^+$ , is obtained as

$$I_q^+ = K^+ |\Delta V_t^+| \quad (6.4)$$

where  $K^+$  is a constant ranging from 2 to 6, and  $\Delta V_t^+$  represents the positive-sequence voltage drop measured at the IRES terminals. It is worth noting that most researchers set  $K^- = K^+ = K$ ; thus, in the problem statement section,  $K$  is used to represent the value for both  $K^-$  and  $K^+$ . Furthermore, the IRES should generate a positive-sequence active current, i.e.,  $I_p^+$ , to inject the maximum current limit and enhance the system stability, where  $I_p^+$  is given by

$$I_p^+ = \sqrt{(I_{limit}^+)^2 - (I_q^+)^2} \quad (6.5)$$

where  $I_{limit}^+$  is the maximum positive-sequence current injected by the IRES, whereas the vector summation of  $I_{limit}^+$  and  $I^-$  should not exceed the inverter's maximum current limit, i.e.,  $I_{limit} = I_{limit}^+ + I^-$ . The positive-sequence current can be represented according to its magnitude, i.e.,  $I_{limit}^+$ , and its phase angle by

$$I^+ = I_{limit}^+ \angle (\theta_{V_t^+} - \phi^+) \quad (6.6)$$

where  $\theta_{V_t^+}$  is the phase angle of  $V_t^+$  and  $\phi^+$  is the phase angle between  $I^+$  and  $V_t^+$ , which can be calculated by

$$\phi^+ = -\tan^{-1} \left( \frac{I_q^+}{I_p^+} \right) = -\tan^{-1} \left( \frac{K^+ |\Delta V_t^+|}{\sqrt{(I_{limit} - K^- |V_t^-|)^2 - (K^+ |\Delta V_t^+|)^2}} \right). \quad (6.7)$$

According to (6.7),  $\phi^+$  varies based on  $I_{limit}$  and the magnitude of  $\Delta V_t^+$  and  $V_t^-$ , which are affected by the fault resistance, type, location, and the constants  $K$ . To interpret the problem, the applicable values of  $\phi^+$  should be known for different values of  $K$  and  $\Delta V_t^+$ . As an illustrative case study, if  $I_{limit}$  is set at 1.5 p.u. and  $K = 2$ ,  $\phi^+$  will be approximately equal to  $9^\circ$ ,  $40^\circ$ , and  $90^\circ$ , when  $\Delta V_t^+$  equals 0.1,  $1/3$ , and  $1/2$  p.u., i.e., representative values for high resistive faults, bolted SLG faults, and bolted LL(G) faults, respectively. On the other hand, if  $K = 6$ ,  $\phi^+$  will be almost equal to  $42^\circ$  when  $\Delta V_t^+ = 0.1$  p.u., which represents a very high resistive fault. However, the value of  $\phi^+$  will increase as  $|\Delta V_t^+|$  increases and will reach the saturation value, i.e.,  $90^\circ$ , when  $|\Delta V_t^+|$  is greater than 0.2 p.u., which represents a wide range of resistive faults, including bolted SLG and LL(G) faults. It can be concluded that  $\phi^+$  depends on the VDE-GC constant, i.e.,  $K$ , at different  $|\Delta V_t^+|$ . For instance, if  $|\Delta V_t^+| = 0.1$  p.u., i.e., a high resistive fault,  $\phi^+$  increases from  $9^\circ$  to  $42^\circ$  when  $K$  increases from 2 to 6, but if  $|\Delta V_t^+| = 1/3$  p.u., i.e., bolted SLG fault,  $\phi^+$  changes from  $40^\circ$  to  $90^\circ$  by increasing  $K$  from 2 to 6. However, the value of  $K$  does not affect bolted LL(G) faults because  $|\Delta V_t^+|$  is enough to saturate  $\phi^+$  at  $90^\circ$ . The relation between the voltage and current angles on the grid side is given by (6.8), which is deduced by shifting both sides of (6.6) with the same shift angle.

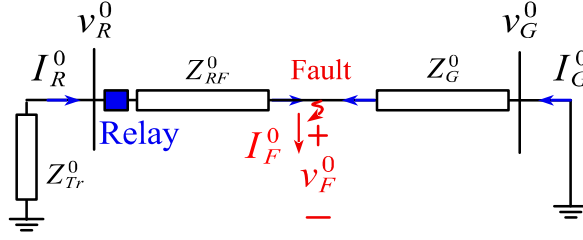


Figure 6.2. Zero-sequence circuit representation for an IRES connected to the power grid.

$$\theta_{I_R}^+ = \angle(\theta_{V_R}^+ - \phi^+) \quad (6.8)$$

where  $\theta_{V_R}^+$  and  $\theta_{I_R}^+$  are the phase angle of  $V_R^+$  and  $I_R^+$ .

On the other hand, the zero-sequence current is independent of the IRES controller because IRESs are connected to the grid through delta/star-ground transformers. Thus, the zero-sequence current, i.e.,  $I^0$ , can be determined by analyzing the circuit shown in Figure 6.2, as follows:

$$I_R^0 = \frac{-V_F^0}{Z_{RF}^0 + Z_{tr}^0} = \frac{|V_F^0|}{|Z_{RF}^0 + Z_{tr}^0|} \angle(\theta_{V_F}^0 - \theta_Z^0 + 180^\circ). \quad (6.9)$$

Since the angles of the transformer's and transmission line's impedances are approximately equal, according to the voltage division principle,  $\theta_{V_R}^0$  is almost equal to  $\theta_{V_F}^0$ . On the other hand, the impedance angles of TLs in conventional grids are close to  $80^\circ$  [68]; hence,  $I^0$  can be approximated, as follows:

$$I_R^0 = \frac{|V_F^0|}{|Z_{RF}^0 + Z_{tr}^0|} \angle(\theta_{V_R}^0 + 100^\circ). \quad (6.10)$$

It can be inferred from (6.2) and (6.10) that the relative angles between the negative- and zero-sequence currents, i.e.,  $\delta^0$ , can be determined by

$$\delta^0 = (\theta_{V_R}^- - \theta_{V_R}^0) - 10^\circ. \quad (6.11)$$



On the other hand, the relative angles between the negative- and positive-sequence currents, i.e.,  $\delta^+$ , can be determined by subtracting  $\angle I_R^-$  in (6.2) from  $\angle I_R^+$  in (6.5), as follows:

$$\delta^+ = (\theta_{V_R}^- - \theta_{V_R}^+) + (90^\circ + \phi^+). \quad (6.12)$$

When the IIRES is controlled according to VDE-GC, the relative angles between its sequence currents depend on the sequence-voltage angles. Thus, to elaborate on the problems associated with the current-angle-based PSM, the relative angles between sequence voltages should be determined for different fault types as follows.

### 6.2.1 SLG Faults

It is concluded in Chapter 3 that the relative angle between the negative- and positive-sequence voltages depends on the magnitude of the fault resistance. At bolted fault,  $\theta_{V_R}^- - \theta_{V_R}^+ \approx -180^\circ$ , but at high resistive faults,  $\theta_{V_R}^- - \theta_{V_R}^+ \approx -100^\circ$ . Subsequently, by substituting for the sequence voltage angles in (6.11) and (6.12),  $\delta^0$  and  $\delta^+$  for AG faults can be approximated by

$$\delta^0 \approx -10^\circ \quad (6.13)$$

$$\delta^+ \approx \begin{cases} -90^\circ + \phi^+ & \text{at bolted faults} \\ -10^\circ + \phi^+ & \text{at high resistive faults} \end{cases} \quad (6.14)$$

It can be deduced from (6.13) that  $\delta^0$  measured for an AG fault will be located in its correct fault-type zone, i.e., from  $-60^\circ$  to  $60^\circ$ , as shown in Figure 2.9(a). On the other hand, it can be inferred from (6.14) that  $\delta^+$  will vary according to the value of  $\phi^+$  and based on the fault resistance and  $K$ . For instance, for bolted AG faults,  $\delta^+$  changes from  $-50^\circ$  to  $0^\circ$  when  $K$  changes from 2 to 6. However, for high resistive faults,  $\delta^+$  varies from  $-1^\circ$  to  $32^\circ$  when  $K$  changes from 2 to 6. Since  $\delta^+$ 's zone for an AG fault is from  $-30^\circ$  to  $30^\circ$ , the current-angle-based PSM may fail to determine the fault type correctly for some values of  $K$ .

### 6.2.2 LLG Faults

It is deduced in Chapter 3 that the relative angles between sequence voltages depend on the fault resistance. Thus, these relative angles are separately analyzed for bolted, high- $R_g$ , and high- $R_{ph}$  faults.

#### A. Bolted Faults

For bolted faults,  $R_{ph} = R_g = 0$ , thus,  $V_R^-/V_R^0$  and  $V_R^-/V_R^+$  are reduced to

$$\frac{V_R^-}{V_R^0} = \frac{Z_{th}^-}{Z_{th}^0} \times \frac{Z_{th}^0}{Z_{th}^-} = 1, \quad \frac{V_R^-}{V_R^+} = \frac{Z_{th}^-}{Z_{th}^+} = 1. \quad (6.15)$$

Hence,  $\theta_{V_R}^- - \theta_{V_R}^0$  and  $\theta_{V_R}^- - \theta_{V_R}^+$  for bolted faults are equal to zero as stated in (6.16).

$$\theta_{V_R}^- - \theta_{V_R}^0 = 0, \quad \theta_{V_R}^- - \theta_{V_R}^+ = 0. \quad (6.16)$$

By substituting (6.16) into (6.11) and (6.12),  $\delta^0$  and  $\delta^+$  for bolted LLG faults are equal to

$$\delta^0 \approx -10^\circ \quad (6.17)$$

$$\delta^+ \approx 90^\circ + \phi^+ \approx 180^\circ. \quad (6.18)$$

#### B. High $R_g$

If  $R_g$  is large compared to the magnitude of the Thevenin impedance,  $V_R^-/V_R^0$  and  $V_R^-/V_R^+$  can be simplified to

$$\frac{V_R^-}{V_R^0} = \frac{3R_g}{Z_{th}^0}; \quad \frac{V_R^-}{V_R^+} = \frac{Z_{th}^-}{Z_{th}^+} = 1. \quad (6.19)$$

Consequently, the relative angle between the negative- and zero-sequence voltages and that between the negative- and positive-sequence voltages are given by

$$\theta_{V_R}^- - \theta_{V_R}^0 = -\angle Z_{th}^0 \approx -80^\circ; \quad \theta_{V_R}^- - \theta_{V_R}^+ = 0. \quad (6.20)$$

Thereafter,  $\delta^0$  and  $\delta^+$  for LLG faults with large  $R_g$  are determined by substituting (6.20) into (6.11) and (6.12), as follows:

$$\delta^0 \approx -80^\circ - 10^\circ \approx -90^\circ \quad (6.21)$$

$$\delta^+ \approx 90^\circ + \phi^+ \approx 180^\circ. \quad (6.22)$$

It is worth noting that increasing  $R_g$  has an ignorable effect on the positive-sequence voltage drop; thus,  $\phi^+ \approx 90^\circ$ .

### C. High $R_{ph}$

With large arc resistances, the ratio between the negative- and zero-sequence voltages and that between the zero- and positive-sequence voltages can be approximated by

$$\frac{V_R^-}{V_R^0} = \frac{Z_{th}^-}{Z_{th}^0}; \quad \frac{V_R^-}{V_R^+} = \frac{Z_{th}^-}{3R_{ph}}. \quad (6.23)$$

Thus,  $\theta_{V_R}^- - \theta_{V_R}^0$  and  $\theta_{V_R}^- - \theta_{V_R}^+$  are determined by (6.24) during high values of  $R_{ph}$ .

$$\theta_{V_R}^- - \theta_{V_R}^0 \approx 0^\circ, \quad \theta_{V_R}^- - \theta_{V_R}^+ = \angle Z_{th}^- \approx 80^\circ. \quad (6.24)$$

Accordingly, by using (6.24), (6.11), and (6.12),  $\delta^0$  and  $\delta^+$  for LLG faults at high values of  $R_{ph}$  are determined, as follows:

$$\delta^0 \approx -10^\circ \quad (6.25)$$

$$\delta^+ \approx 80^\circ + 90^\circ + \phi^+ \approx \begin{cases} 80^\circ + 90^\circ + 9^\circ = 179^\circ; & K = 2 \\ 80^\circ + 90^\circ + 42^\circ = 212^\circ; & K = 6 \end{cases} \quad (6.26)$$

Thus, for BCG faults, it can be concluded that  $\delta^0$  can vary from  $-10^\circ$  to  $-90^\circ$ , depending on the value of  $R_g$ . This range exceeds the conventional current-angle-based PSM range, which is from  $-60^\circ$  to  $60^\circ$ . Moreover,  $\delta^+$  varies from  $179^\circ$  to  $212^\circ$ , depending on the value of  $R_{ph}$  and the IRES control strategy. This range also violates the conventional BCG zone limits, i.e.,  $[150^\circ, 210^\circ]$ .

### 6.2.3 LL Faults

According to Chapter 3's analysis, it is inferred that the relative angle between the negative- and positive-sequence voltage angles relies on the arc resistance value, as follows:

$$\theta_{V_R}^- - \theta_{V_R}^+ = \angle Z_{th}^- - \angle (Z_{th}^- + R_{ph}). \quad (6.27)$$

Accordingly,  $\theta_{V_R}^- - \theta_{V_R}^0$  changes from  $0^\circ$  to  $\angle Z_{th}^- \approx 80^\circ$  as the value of  $R_{ph}$  increases. Hence, by substituting (6.27) into (6.12),  $\delta^+$  for BC faults can be approximated by

$$\delta^+ \approx \begin{cases} 90^\circ + \phi^+ = 180^\circ & \text{at bolted faults} \\ 170^\circ + \phi^+ & \text{at high resistive faults} \end{cases} \quad (6.28)$$

By analyzing (6.28), it can be deduced that the current-angle-based PSM is reliable during bolted BC faults, when the IRES obeys the VDE-GC. However, the PSM may operate improperly at high resistive faults because  $\delta^+$  can vary from  $179^\circ$  to  $212^\circ$  according to the selected value of  $K$ , which exceeds the standard zone limits for the BC fault.

## 6.3 Assessing Current-Angle-Based PSM when IRES Follows VDE-GC

A 230-kV, 60-Hz transmission system, which is illustrated in Figure 4.13, represents the test system under study. A PSCAD/EMTDC simulation is utilized to affirm the improper operation of the current-angle-based PSM when the IRES controller complies with VDE-AR-N 4120-GC requirements.

A bolted AG fault is applied at the middle of  $L_{25}$  at  $t = 2$  s, when the IRES's controller gain is set to 2. Figure 6.3(a) exhibits the values of  $\delta^0$  and  $\delta^+$  measured by the relay R<sub>25</sub>, whereas  $\delta^0$  settled within the correct PSM zone at  $-7.5^\circ$ . On the other hand,  $\delta^+$  settled outside the correct AG zone at  $-51.7^\circ$ , which matches the theoretical results. Figure 6.3(b) displays  $\delta_V^+$ , i.e.,  $\theta_{V_R}^- - \theta_{V_R}^+$ ,  $\delta_V^0$ , i.e.,  $\theta_{V_R}^- - \theta_{V_R}^0$ ,  $\phi^+$ , and  $\phi^-$  measured at the IRES.  $\delta_V^+$  and  $\delta_V^0$  are equal to  $178.8^\circ$  and  $2^\circ$ , which slightly deviate from their ideal values during

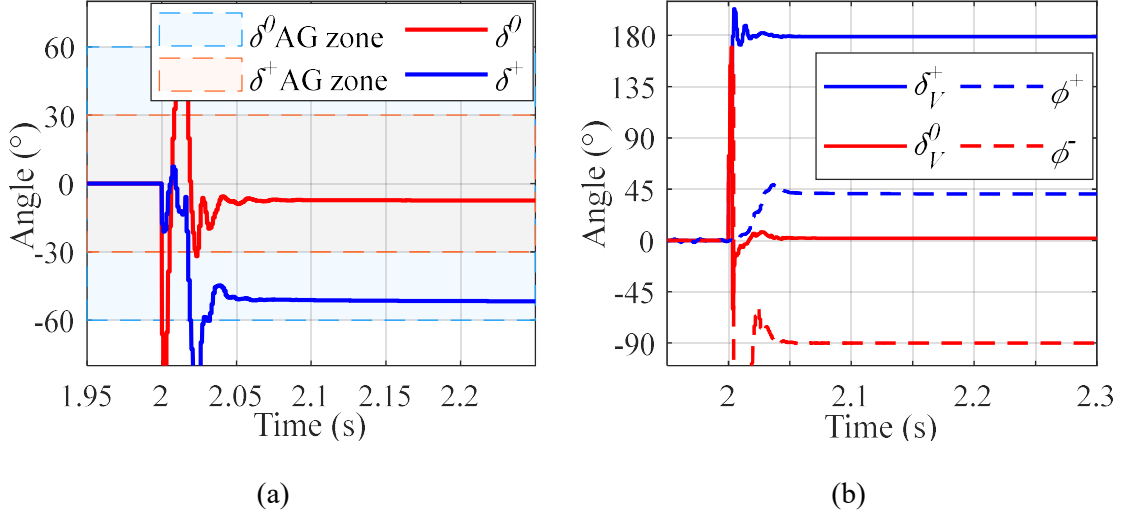


Figure 6.3. Angle measurements during a bolted AG fault at 50% of  $L_{25}$  when the IRES's gain constant, i.e.,  $K$ , equals 2: (a)  $\delta^0$  and  $\delta^+$ , (b)  $\delta_V^+$ ,  $\phi^+$ ,  $\delta_V^0$ , and  $\phi^-$ .

bolted AG fault, i.e.,  $180^\circ$  and  $0^\circ$ , respectively. In addition, Figure 6.3(b) manifests that the IRES is controlled to follow the new VDE-GC correctly, where  $\phi^-$  is controlled correctly at  $-90^\circ$  to reduce the voltage imbalance while  $\phi^+$  is equal to  $40^\circ$  to reach the IRES's maximum current limit, i.e., 1.5 p. u. Further,  $\delta_V^0 - \phi^- + \phi^+$  is equal to  $-51.2^\circ$ , which is approximately equal to the measured  $\delta_V^+$  at  $R_{25}$ . These results coincide with the theoretical analysis in Section 6.2.

Another test is performed to test the reliability of PSM when the IRES follows the new VDE-GC, as shown in Figure 6.4, where an AG fault with  $R_g = 20 \Omega$  is applied at 50% of  $L_{25}$  when  $K = 6$ . Figure 6.4(a) verifies that  $\delta^0$  is placed precisely in its correct PSM zone because  $\delta_V^0$  and  $\phi^-$  are around  $0^\circ$  and  $-90^\circ$ , respectively, as exhibits in Figure 6.4(b). On the other hand,  $\delta^+$  displayed in Figure 6.4(a) settles at  $40^\circ$ , which is outside the correct AG zone limits, leading to improper identification of the faulted phase. It is worth noting that  $\delta^+$  measured by the relay agrees with the mathematical calculation of  $\delta_V^0 - \phi^- + \phi^+$ , where  $\delta_V^+$ ,  $\phi^-$ , and  $\phi^+$  are  $218^\circ$ ,  $-90^\circ$ ,  $90^\circ$ , respectively, as shown in Figure 6.4(b). These results demonstrate the unreliable operation of the current-angle-based PSM during low-resistance faults when the IRES complies with the new VDE-GC requirements.

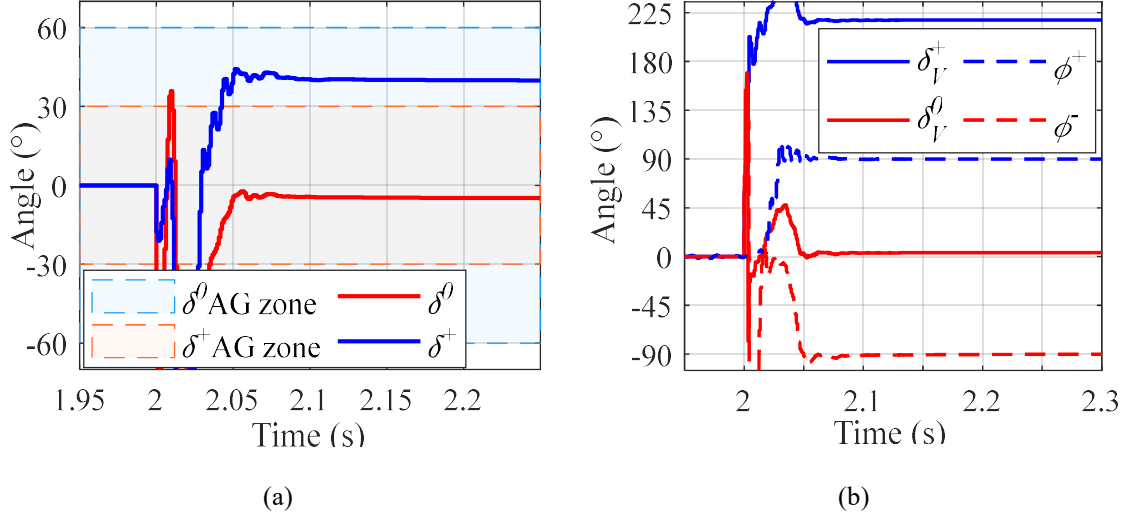


Figure 6.4. Angle measurements during an AG fault at 50% of  $L_{25}$  with  $R_g = 20 \Omega$  when  $K = 6$ : (a)  $\delta^0$  and  $\delta^+$ , (b)  $\delta_V^+$ ,  $\phi^+$ ,  $\delta_V^0$ , and  $\phi^-$ .

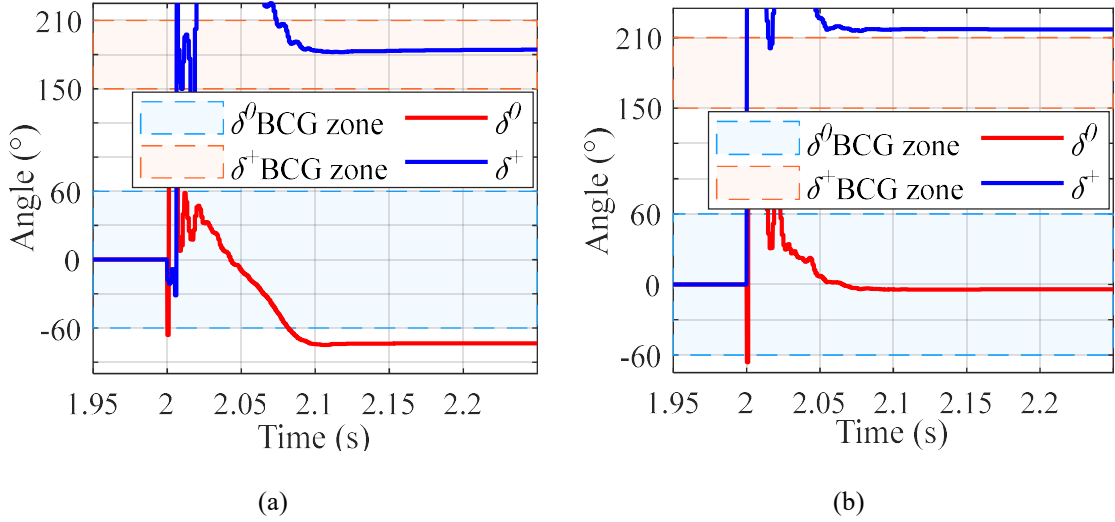


Figure 6.5. Angle measurements of  $\delta^0$  and  $\delta^+$  during a BCG fault at 50% of  $L_{25}$  when  $K = 6$ : (a)  $R_g = 50 \Omega$ , (b)  $R_{ph} = 60 \Omega$ .

Furthermore, the reliability of the current-angle-based PSM is tested during a BCG fault at 50% of  $L_{25}$  when the IIREs follows the VDE-GC. Figure 6.5(a) displays the values of  $\delta^0$  and  $\delta^+$  during a BCG fault with  $R_g = 50 \Omega$ . The results illustrate that  $\delta^+$  is placed precisely in the middle of the BCG zone while  $\delta^0$  is outside its fault-type zone and is equal to  $-75.5^\circ$ , i.e., deviating from  $\delta^0$ 's BCG-zone limit by  $15.5^\circ$ . Lastly, Figure 6.5(b)

exhibits the values of  $\delta^0$  and  $\delta^+$  during a BCG fault with  $R_{ph} = 60 \Omega$ . The results manifest the inability of the current-angle-based to determine faulted phase(s) precisely, as  $\delta^+ = 217^\circ$ , which exceeds the maximum  $\delta^+$ 's BCG zone limit, i.e.,  $210^\circ$ . These results verify that the current-angle-based PSM may operate improperly if the IRES is controlled to follow the new VDE-GC. Thus, the controller constant, i.e.,  $K$ , should adaptably vary to allow a proper operation of the commercial PSM without violating the new GC requirements.

## 6.4 The Proposed Dual Current Controller

The proposed DCC aims to regulate the negative- and positive-sequence current references to satisfy PSM requirements and fault-ride through imposed by new VDE-CG, which can be divided into (i) meeting positive- and negative-sequence RCG requirements, and (ii) injecting the maximum available positive-sequence active current. The proposed DCC is designed in six stages as follows.

### 6.4.1 Stage I. The Referential Angle of the Negative-Sequence Current

The referential angle of the IRES's negative-sequence current, i.e.,  $\angle I_{R,ref}^-$ , guarantees that  $\delta^0$  measured by the grid-side relay is equal to  $\delta_{F,bis}^0$ , i.e., the bisector of  $\delta^0$ 's fault-type zone. This can be achieved by making the negative-sequence current angle measured on the grid side, i.e.,  $\angle I_g^-$ , equal to  $\delta_{F,bis}^0 + \angle I_g^0$ , where  $\angle I_g^0$  is the zero-sequence current angle measured on the IRES grid side. Since the transformer introduces a phase shift between the negative-sequence current angles measured on the POI and the grid side ( $\theta_{tr}^-$ ),  $\angle I_{R,ref}^-$  should be determined by

$$\angle I_{R,ref}^- = \angle I_g^- + \theta_{tr}^- = \delta_{F,bis}^0 + \angle I_g^0 + \theta_{tr}^- \quad (6.29)$$

in which  $\delta_{F,bis}^0$  can be obtained, as follows: (i) identifying the fault type at the IRES terminals using the voltage-angle-based classifier explained in Chapter 4, (ii) determining  $\delta_{F,bis}^0$  using a look-up table that links between the fault type and  $\delta_{F,bis}^0$ , which is generated from Figure 2.9(a). For instance, if the fault type is distinguished as a BG or CAG fault,  $\delta_{F,bis}^0 = -120^\circ$ .

### 6.4.2 Stage II. The Reference of the Negative-Sequence Current

The reference of the negative-sequence current, i.e.,  $I_{ref}^-$ , is determined to force  $I^-$  injected by the IRES to follow the VDE-GC requirements and impose  $\delta^0$  measured by the relay to lay in the correct fault-type zone. Thus, the negative-sequence reactive current reference should be determined according to (6.1), i.e.,  $I_{q,ref}^- = K|V_t^-|$ , while the negative-sequence active current reference, i.e.,  $I_{p,ref}^-$ , should be minimized without violating the PSM requirements. First, an initial negative-sequence current angle, i.e.,  $\angle I_{ref(0)}^-$ , is determined, which forces  $I_p^-$  to zero. Consequently,  $\angle I_{ref(0)}^-$  is calculated by

$$\angle I_{ref(0)}^- = \angle V_t^- + 90^\circ \quad (6.30)$$

where  $90^\circ$  is selected as the initial phase difference between the negative-sequence voltage and current. Subsequently,  $\angle I_{ref(0)}^-$  is compared with  $\angle I_{R,ref}^-$ ; if  $|\angle I_{ref(0)}^- - \angle I_{R,ref}^-|$  is greater than  $\theta_{IRES,max}^0$ , i.e., a reduced value of  $\theta_{max}^0$  and set equal to  $55^\circ$ ,  $\angle I_{ref}^-$  is determined by

$$\angle I_{ref}^- = \angle I_{ref(0)}^- - (|\angle I_{ref(0)}^- - \angle I_{R,ref}^-| - \theta_{IRES,max}^0) \times \text{sgn}(\angle I_{ref(0)}^- - \angle I_{R,ref}^-). \quad (6.31)$$

Otherwise,  $\angle I_{ref}^-$  is obtained by

$$\angle I_{ref}^- = \angle I_{ref(0)}^-. \quad (6.32)$$

For LL faults,  $\angle I_{ref}^-$  is always equal to  $\angle I_{ref(0)}^-$ . Thus,  $|I_{ref}^-|$  is derived as follows:

$$|I_{ref}^-| = \frac{I_{q,ref}^-}{\sin \phi^-} = \frac{K|V_t^-|}{\sin(\angle V_t^- - \angle I_{ref}^-)} \quad (6.33)$$

where  $\phi^-$  is the phase shift between the negative-sequence voltage and current angles. Consequently,  $I_{ref}^-$  is determined by

$$I_{ref}^- = |I_{ref}^-| \angle(-\omega t + \angle I_{ref}^-). \quad (6.34)$$



### 6.4.3 Stage III. The Referential Angle of the Positive-Sequence Current

The referential angle  $\angle I_{R,ref}^+$  is the IRES's positive-sequence current angle that makes  $\delta^+$  measured by the relay to be settled at  $\delta_{F,bis}^+$ , i.e., the bisector of  $\delta^+$ 's fault-type zone. This can be fulfilled if  $\angle I_g^+$ , i.e., the positive-sequence current angle measured on the IRES grid side, is equal to  $-\delta_{F,bis}^+ + \angle I_g^-$ , i.e.,  $-\delta_{F,bis}^+ + \angle I_{ref}^- - \theta_{tr}^-$ . Consequently,  $\angle I_{R,ref}^+$  is calculated by

$$\angle I_{R,ref}^+ = \angle I_g^- + \theta_{tr}^+ = -\delta_{F,bis}^+ + \angle I_{ref}^- - \theta_{tr}^- + \theta_{tr}^+ \quad (6.35)$$

in which  $\delta_{F,bis}^+$  can be determined by first determining the fault type using the voltage-angle-based classifier, which utilizes the voltage measurements at the IRES terminals; then, a look-up table that relies on Figure 2.9(b) is used to select the value of  $\delta_{F,bis}^+$ , e.g., in a BG fault,  $\delta_{F,bis}^+$  is set at  $180^\circ$ . From (6.35) and Figure 2.9(b),  $\angle I_{R,ref}^+ - \angle I_{ref}^-$  can be obtained for different fault types as follows:

$$\angle I_{R,ref}^+ - \angle I_{ref}^- = -\delta_{F,bis}^+ - 60^\circ = \begin{cases} 300^\circ, & AG \text{ Fault} \\ 240^\circ, & AB(G) \text{ Fault} \\ 180^\circ, & BG \text{ Fault} \\ 120^\circ, & BC(G) \text{ Fault} \\ 60^\circ, & CG \text{ Fault} \\ 0^\circ, & CA(G) \text{ Fault} \end{cases} \quad (6.36)$$

### 6.4.4 Stage IV. The Initial Reference of the Positive-Sequence Current Angle

The initial reference of the positive-sequence current angle, i.e.,  $\angle I_{ref(0)}^+$ , satisfies PSM requirements and maximizes  $|I^+|$  and  $|I^-|$ . The IRES must limit its output current to avoid its phase current from exceeding its maximum allowable current, i.e.,  $I_{Limit}$ . The peak current for each phase, i.e.,  $I_{peak\phi}$ , can be determined by

$$I_{peak\phi} = \sqrt{\frac{|I^+|^2 + |I^-|^2 + 2|I^+||I^-|\cos(\varphi + \angle I^+ - \angle I^-)}{2}} \quad (6.37)$$

where  $\varphi$  represent phase shifts of  $0^\circ$ ,  $-120^\circ$ , and  $120^\circ$  for phases  $a$ ,  $b$ , and  $c$ , respectively. To avoid any phase from exceeding the maximum limit, i.e.,  $I_{Limit}$ , the

maximum phase current for all phases i.e.,  $I_{peak} = \max\{I_{peak_\Phi}\}$ ,  $\forall \Phi \in \{a, b, c\}$ , is set equal to  $I_{Limit}$ .  $I_{peak}$  is derived by obtaining the maximum value of  $I_{peak_\Phi}$  as follows:

$$I_{peak} = \sqrt{2|I^+||I^-|\max\{\cos(\varphi + \angle I_{IRES}^+ - \angle I^-)\}}, \quad \forall \varphi \in \{a, b, c\} \quad (6.38)$$

It can be inferred from (6.38) that the maximum value of  $|I^+|$  and  $|I^-|$  can be achieved if the value of  $\max\{\cos(\varphi + \angle I^+ - \angle I^-)\}$  is minimum. This condition can be achieved if  $\angle I^+ - \angle I^-$  equals  $60^\circ$ ,  $180^\circ$ , or  $300^\circ$ . Consequently, it is preferable to have  $\angle I_{ref(0)}^+ - \angle I_{ref}^-$  as close as possible to  $60^\circ$ ,  $180^\circ$ , or  $300^\circ$  to maximize the positive- and negative-sequence current magnitudes. By comparing the preferred values of  $\angle I_{ref(0)}^+ - \angle I_{ref}^-$  with  $\angle I_{R,ref}^+ - \angle I_{ref}^-$ , i.e., determined from Stage III for precise phase selection,  $\angle I_{ref(0)}^+ - \angle I_{ref}^-$  can be deduced for each fault type as given by

$$\angle I_{ref(0)}^+ - \angle I_{ref}^- = \begin{cases} 300^\circ, & AG \text{ Fault} \\ 240^\circ \pm \theta_{IRES,max}^+, & AB(G) \text{ Fault} \\ 180^\circ, & BG \text{ Fault} \\ 120^\circ \pm \theta_{IRES,max}^+, & BC(G) \text{ Fault} \\ 60^\circ, & CG \text{ Fault} \\ 0^\circ \pm \theta_{IRES,max}^+, & CA(G) \text{ Fault} \end{cases} \quad (6.39)$$

where,  $\theta_{IBR,max}^+$ , i.e., equal to  $25^\circ$ , is a reduced value of  $\theta_{max}^+$  to guarantee that  $\delta^+$  measured at the relay does not violate the  $\pm\theta_{max}^0$  limits. It can be observed from (6.39) that during SLG faults,  $\angle I_{ref(0)}^+ - \angle I_{ref}^-$  can achieve the maximum value of  $|I^\pm|$  and guarantee precise phase selection, simultaneously. On the other hand, during LL(G) faults, a compromised solution is achieved by determining the maximum permissible value of  $|I^\pm|$  without violating phase selection requirements. Consequently, there are two potential solutions, which involve placing  $\delta^+$  inside its respective zone near to the upper or lower zone boundaries with a suitable margin, i.e.,  $5^\circ$ . For instance, during CAG faults,  $\angle I_{ref(0)}^+$  can be selected as  $\angle I_{ref}^- + \theta_{IRES,max}^+$ , i.e., solution 1, or  $\angle I_{ref}^- - \theta_{IRES,max}^+$ , i.e., solution 2. Accordingly,  $\phi_{(0)}^+$ , i.e., the phase shift between the PS voltage and initial reference

current angle, is calculated using (38) for the two acceptable solutions of  $\angle I_{ref(0)}^+$ . Then,  $\angle I_{ref(0)}^+$  that leads to  $\phi_{(0)}^+$  approaching its upper limit, i.e., solution 1, is selected to support the grid during fault conditions.

$$\phi_{(0)}^+ = V_t^+ - \angle I_{ref(0)}^+. \quad (6.40)$$

#### 6.4.5 Stage V. The Reference Positive-Sequence Current

The reference positive-sequence current, i.e.,  $I_{ref}^+$ , is determined to force  $\delta^+$  measured by the relay to be within the acceptable current-angle-based fault-type zone and maximize  $|I_{ref}^\pm|$  without violating the RCG requirements of the VDE-GC. Accordingly, the reference of the positive-reactive current injected by the IRES, i.e.,  $I_{q,ref}^+$ , is determined based on (6.4), i.e.,  $I_{q,ref}^+ = K|\Delta V_t^+|$ . Subsequently,  $|I_{ref}^+|$  is computed by

$$|I_{ref}^+| = \frac{I_{q,ref}^+}{\sin \phi^+} = \frac{K|\Delta V_t^+|}{\sin(\angle V_t^+ - \angle I_{ref}^+)} \quad (6.41)$$

where  $\phi^+$  is the phase shift between the positive-sequence voltage and current. By substituting (6.33), (6.40), and (6.41) into (6.38),  $K$  can be computed by

$$K = \frac{I_{Limit}}{\sqrt{\left(\frac{|\Delta V_t^+|}{\sin \phi_{(0)}^+}\right)^2 + \left(\frac{|V_t^-|}{\sin \phi^-}\right)^2 + \left(\frac{2|\Delta V_t^+||V_t^-|}{\sin \phi_{(0)}^+ \sin \phi^-}\right) \max\{\cos(\varphi_{a,b,c} + \angle I_{ref(0)}^+ - \angle I_{ref}^-)\}}}. \quad (6.42)$$

Thereafter, if  $K$  is between 2 and 6; thus, the three objectives can be achieved simultaneously, and  $\angle I_{ref}^+$  is determined by

$$\angle I_{ref}^+ = \angle I_{ref(0)}^+. \quad (6.43)$$

However, if  $K < 2$  in LLG faults,  $\phi^+$  is set at  $90^\circ$ ; then,  $K$  is updated by substituting  $\phi^+$  in (6.42). Otherwise, if  $K > 6$  in LLG faults, solution 2 will be selected to update  $\phi_{(0)}^+$ ; accordingly, the value of  $K$  will be updated by substituting the new value of  $\phi^+$  with  $\phi_{(0)}^+$

into (6.40), will be selected as the updated reference of  $\phi^+$ ; accordingly, the value of  $K$  will be updated by substituting the new value of  $\phi^+$  in (6.42). Thereafter,  $\angle I_{ref}^+$  is obtained by

$$\angle I_{ref}^+ = \angle V_t^+ - \phi^+. \quad (6.44)$$

On the other hand, if  $K$  is smaller than 2 in SLG faults,  $K$  will be set at 2 and  $\phi^+$  will be updated by rearranging (6.42) and substituting for  $K = 2$ . (6.42) is nonlinear; thus, by approximating (6.42) using  $\max\{\cos(\varphi_{a,b,c} + \angle I_{ref(0)}^+ - \angle I_{ref}^-)\} = 1$ , which ensures that the updated value of  $K$  will be higher than 2,  $\phi^+$  can be determined by

$$\phi^+ = \sin^{-1} \frac{K|\Delta V_t^+|}{I_{Limit} - \left| \frac{K|V_t^-|}{\sin \phi^-} \right|}. \quad (6.45)$$

Subsequently,  $\phi^+$  is compared with  $\phi_{(0)}^+ + \theta_{IBR,max}^0$ . If  $\phi^+ > \phi_{(0)}^+ + \theta_{IBR,max}^0$ ,  $\phi^+$  is set at  $\phi_{(0)}^+ + \theta_{IBR,max}^0$ . Otherwise,  $\phi^+$  determined from (6.45) is utilized. As a result,  $K$  is updated by substituting the new value of  $\phi^+$  in (6.42). However, if  $K$  is larger than 6 in SLG faults,  $K$  will be set at 6 and  $\phi^+$  will be updated by rearranging (6.42) and substituting for  $K = 6$ . By approximating (6.42) using  $\max\{\cos(\varphi_{a,b,c} + \angle I_{ref(0)}^+ - \angle I_{ref}^-)\} = 0.5$ , which ensures that the updated value of  $K$  will be less than 6,  $\phi^+$  can be determined by solving (6.46).

$$\left( \frac{K|V_t^-|}{\sin \phi^-} \right)^2 (\sin \phi^+)^2 + \left| \frac{(K|\Delta V_t^+|)(K|V_t^-|)}{\sin \phi^-} \right| \sin \phi^+ + (|\Delta V_t^+|^2 - I_{Limit}^2) = 0 \quad (6.46)$$

Accordingly,  $\phi^+$  is compared with  $\phi_{(0)}^+ - \theta_{IBR,max}^0$ . If  $\phi^+ < \phi_{(0)}^+ - \theta_{IBR,max}^0$ ,  $\phi^+$  is set at  $\phi_{(0)}^+ - \theta_{IBR,max}^0$ . Otherwise,  $\phi^+$  determined from (6.46) is utilized. Thereafter,  $K$  is updated by substituting the new value of  $\phi^+$  in (6.42). Thereafter,  $\angle I_{ref}^+$  is determined using (6.44). Lastly,  $I_{ref}^+$  given by

$$I_{ref}^+ = |I_{ref}^+| \angle (\omega t + \angle I_{ref}^+). \quad (6.47)$$

#### 6.4.6 Stage VI. The Reference Positive- and Negative-Sequence Currents in $dq$ Frame

This stage demonstrates the procedure for controlling the negative- and positive-sequence current references in the  $dq$  frame ( $I_{dq,ref}^\pm$ ). The negative-sequence current in the  $dq$  frame, i.e.,  $I_{dq,ref}^-$ , is determined based on the value of  $K$  and  $\phi^-$ , which are derived in Stages VI and II, respectively.  $I_{dq,ref}^-$  is calculated by

$$I_{q,ref}^- = K|V_t^-| \quad (6.48.a)$$

$$I_{d,ref}^- = |I_{ref}^-| \cos \phi^-. \quad (6.48.b)$$

Subsequently, a PI controller is utilized to determine the negative-sequence  $dq$  reference voltages, i.e.,  $E_{dq,ref}^-$ , using two decoupled controllers, as follows:

$$E_{d,ref}^- = V_{t,d}^- + \omega L_f I_q^- + PI(I_{d,ref}^- - I_d^-) \quad (6.49.a)$$

$$E_{q,ref}^- = V_{t,q}^- - \omega L_f I_d^- + PI(I_{q,ref}^- - I_q^-). \quad (6.49.b)$$

On the other hand, the  $dq$ -positive-sequence current, i.e.,  $I_{dq,ref}^+$ , is calculated according to the value of  $K$  and  $\phi^+$ , i.e., obtained in Stage VI.  $I_{dq,ref}^+$  is computed by

$$I_{q,ref}^+ = K|\Delta V_t^+| \quad (6.50.a)$$

$$I_{d,ref}^+ = |I_{ref}^+| \cos \phi^+. \quad (6.50.b)$$

Thereafter, the positive-sequence reference voltages in the  $dq$  frame, i.e.,  $E_{dq,ref}^+$ , are determined using two decoupled controllers, as given in (6.51).

$$E_{d,ref}^+ = V_{t,d}^+ - \omega L_f I_q^+ + PI(I_{d,ref}^+ - I_d^+) \quad (6.51.a)$$

$$E_{q,ref}^+ = V_{t,q}^+ + \omega L_f I_d^+ + PI(I_{q,ref}^+ - I_q^+). \quad (6.41.b)$$

## 6.5 Performance Evaluation

The effectiveness of the proposed DCC in fulfilling the current-angle-based PSM requirements as well as complying with recent GCs that impose injecting positive- and negative-sequence reactive currents are verified by executing extensive simulations. The proposed DCC was tested on the test system illustrated in Figure 4.13 using PSCAD/EMTDC. The tests were conducted at varying fault resistances, locations, and types, as well as different transmission line's  $X/R$  ratios.

### 6.5.1 Response under Different Fault Resistances

The accuracy of the proposed DCC is highlighted for each fault type separately, as follows.

#### A. SLG faults

Table 6.1 reports the values of  $\delta^+$ ,  $\delta^0$ ,  $k$ ,  $\phi^+$ ,  $\phi^-$ , and the difference between  $\angle I^+$  and  $\angle I^-$ . The results substantiate the effectiveness of the proposed DCC in achieving the current-angle-based PSM and recent GC requirements simultaneously.  $\delta^0$  is placed inside its correct fault-type zone with a maximum shift of  $8^\circ$  from its correct zone bisector without the need to inject negative-sequence active current, which is demonstrated by maintaining  $\phi^-$  equal to  $-90^\circ$ . This result matches the mathematical analysis in Section 6.2, which shows that  $R_g$  has a negligible effect on the zero-sequence current angle during SLG faults. Furthermore,  $\delta^+$  settles in its correct fault-type zone with a  $5^\circ$  margin with respect to its zone boundary. It is observed that increasing  $R_g$ , decreases  $\phi^+$  to compensate for the effect of the fault resistance on  $\delta^+$ ; hence, maintaining  $\delta^+$  at its zone bisector. This is achieved by keeping  $\angle I^+ - \angle I^-$  equal to  $300^\circ$ ,  $180^\circ$ , and  $60^\circ$  for AG, BG, and CG faults, respectively, which also represents the condition of injecting the maximum value of  $|I^+|$  and  $|I^-|$ . On the other hand, as  $R_g$  or the distance between the fault and the IRES increases, the required value of  $K$  increases to allow the IRES to inject the maximum current limit. This is because increasing  $R_g$  or the distance between the fault and the IRES, reduces the values of  $\Delta V^+$  and  $V^-$ , which requires a higher value of  $K$  to allow the IRES to continue injecting its maximum current during different fault conditions. For instance,  $K$  increases from 2.2 to 3.8, when  $R_g$  increases from 0 to  $50\ \Omega$  during an AG fault

Table 6.1 Performance of the proposed DCC during SLG faults at different fault locations

Fault Type	$R_g$	$R_{ph}$	Fault at 10% of $L_{25}$						Fault at 50% of $L_{25}$						Fault at 90% of $L_{25}$					
			$\delta^+$	$\delta^0$	$k$	$\phi^+$	$\phi^-$	$\angle I^+ - \angle I^-$	$\delta^+$	$\delta^0$	$k$	$\phi^+$	$\phi^-$	$\angle I^+ - \angle I^-$	$\delta^+$	$\delta^0$	$k$	$\phi^+$	$\phi^-$	$\angle I^+ - \angle I^-$
AG	0	0	-0.1	-7.3	2.2	88.3	-90	300	-0.2	-6.5	3.1	86.7	-90	300	-0.2	-5.8	4.4	85.5	-90	300
	10		-1.3	-7.2	2.3	69	-90	300	-1.2	-6.4	3.4	68.9	-90	300	-1.4	-5.4	5.1	63.9	-90	300
	20		-1.1	-7	2.5	54.4	-90	300	-1	-6	3.9	55.1	-90	300	-6	-4.1	5.5	40.9	-90	308.6
	30		-0.7	-6.7	2.8	44.1	-90	300	-0.6	-5.6	4.6	44.9	-90	300	-20.7	-5.3	5.0	22.8	-90	320.1
	40		-0.8	-6.4	3.3	36.6	-90	300	-0.5	-5	5.8	37.6	-90	300	-23.25	-5.4	5.0	15.04	-90	322.1
	50		-0.9	-6	3.8	31	-90	300	-10.7	-5.2	5.4	25.2	-90	308.5	-23.8	-5.4	5.2	10.45	-90	322.9
BG	0	0	120.1	-127.2	2.2	88.3	-90	180	120.9	-26.2	3.1	86.8	-90	180	121	-125.5	4.4	85.6	-90	180
	10		118.8	-127.1	2.3	69.1	-90	180	120	-126	3.4	69	-90	180	120.2	-125.1	5.1	64.1	-90	180
	20		119.1	-126.9	2.5	54.5	-90	180	119.9	-125.7	3.9	55.2	-90	180	114.7	-124.8	5.1	34.8	-90	196.6
	30		119.6	-126.6	2.8	44.1	-90	180	120.4	-125.3	4.7	45.1	-90	180	100	-125	5	22.5	-90	200.5
	40		119.5	-126.3	3.3	36.6	-90	180	120.1	-124.8	5.8	37.6	-90	180	97.6	-124.8	5	14.7	-90	203.1
	50		120.1	-125.7	3.9	31	-90	180	109.8	-125.4	5.2	22.7	-90	192.5	97.1	-124.5	5.1	10.11	-90	204.3
CG	0	0	-120	112	2.2	88.3	-90	60	-120.4	113.3	3.1	86.6	-90	60	-120.4	114	4.4	85.3	-90	60
	10		-121.5	112.8	2.3	69	-90	60	-122.1	113.4	3.4	68.8	-90	60	-122	114.5	5.1	63.9	-90	60
	20		-121.2	113	2.5	54.4	-90	60	-121.6	113.9	3.9	55.01	-90	60	-137.3	113.1	5.8	48.1	-90	60
	30		-120.9	113.2	2.8	44	-90	60	-121.3	114.3	4.6	44.86	-90	60	-140.9	114.6	5.0	22.8	-90	80
	40		-120.9	113.6	3.3	36.6	-90	60	-121.3	114.9	5.8	37.5	-90	60	-143.3	114.5	5	14.9	-90	82.3
	50		-121	114	3.8	31	-90	60	-130	114.8	5.3	24.2	-90	69.6	-143.8	114.6	5.2	10.4	-90	82.9

occurred at 10% of  $L_{25}$ . Moreover,  $K$  increases from 2.2 to 4.35 as the fault location changes from 10% to 90% of  $L_{25}$  during bolted AG faults. In addition, the proposed DCC allows the IRES to follow recent GC requirements by maintaining  $K$  between 2 and 6.

Figures 6.6–6.8 represent the dynamic response of an AG fault with  $R_g = 30 \Omega$  and occurred at 10% of  $L_{25}$ . Figure 6.6 illustrates that both  $\delta^0$  and  $\delta^+$  settle correctly around their zones' bisectors, in which,  $\delta^0$  settles at  $-6.7^\circ$ , while  $\delta^+$  settles at  $-0.7^\circ$ . Both  $\delta^0$  and  $\delta^+$  are placed in their correct-fault type zone in less than 0.025 seconds, which allows the relay to detect the faulted phase correctly in almost one cycle. Figure 6.7 depicts the phase currents measured at the IRES terminals, which have a maximum peak value equal to 1.5 p.u. This figure demonstrates the success of the proposed DCC in determining the value of  $K$  to inject phase currents with a peak value equal to or less than the maximum current

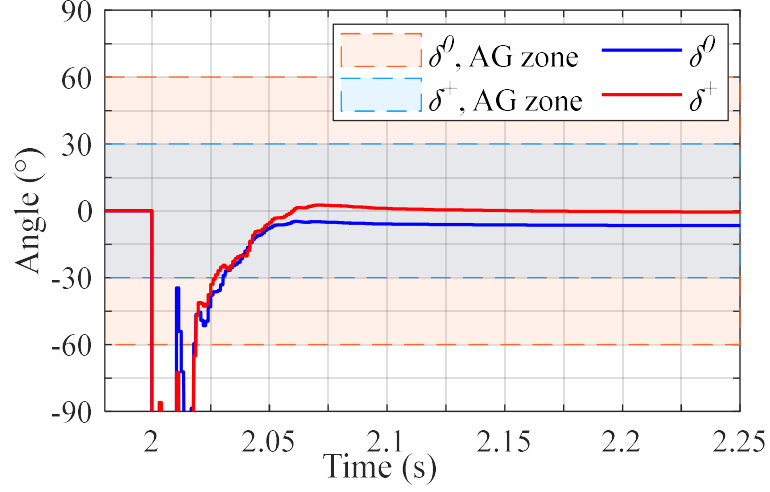


Figure 6.6. Measured  $\delta^0$  and  $\delta^+$  by  $R_{25}$  for an AG fault with  $R_g = 30 \Omega$  occurred at 10% of  $L_{25}$ .

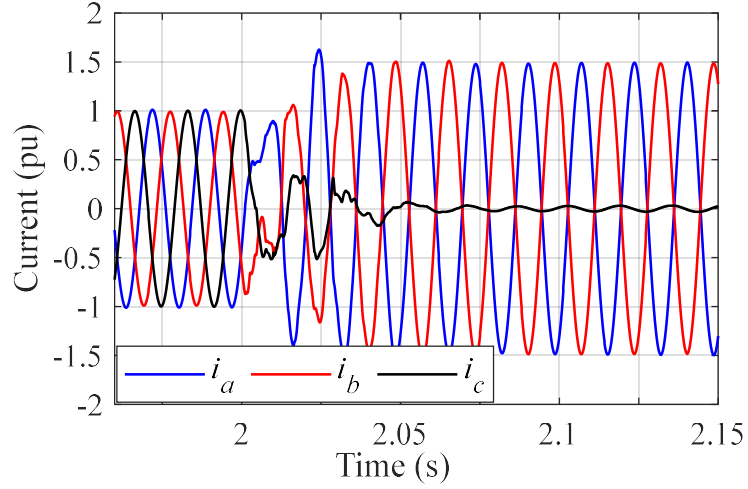


Figure 6.7. IRES's phase currents measurements during an AG fault occurred at 10% of  $L_{25}$  with  $R_g = 30 \Omega$ .

limit. Furthermore, Figure 6.8 reveals that  $|I^+|$  and  $|I^-|$  are equal to 0.879 and 0.845 p. u., respectively. These are the maximum values that can be set for  $|I^+|$  and  $|I^-|$ , where  $|I^+|^2 + |I^-|^2 + |I^+||I^-| = 1.5$  p. u. This results demonstrate the accuracy of the proposed DCC in determining  $\angle I^+$  that maximizes  $|I^+|$  and  $|I^-|$ .



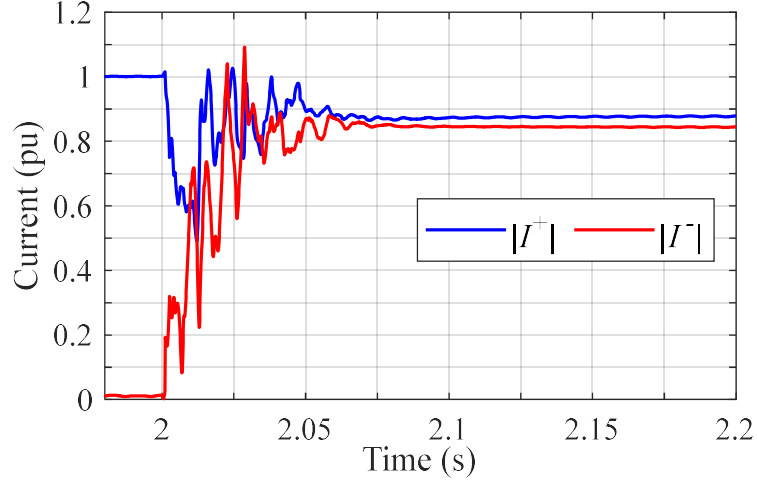


Figure 6.8. IRES's Positive- and negative-sequence currents magnitude during an AG fault occurred at 10% of  $L_{25}$  with  $R_g = 30 \Omega$ .

#### B. LLG Faults

Table 6.2 demonstrates the simulation results under various arc and ground resistances, as well as different fault locations. The results verify that the proposed DCC succeeds to determine  $\angle I_{ref}^+$  and  $\angle I_{ref}^-$  that meet both PSM requirements and RCG requirements as mandated by the VDE-GC. The calculated values of  $\delta^0$  measured at the relay location settle inside their correct fault-type zones with a minimum of  $5^\circ$  margin to guarantee a proper phase selection. The value of  $\phi^-$  demonstrates that the proposed DCC does not inject a negative-sequence active current, when  $R_g$  is small. However, as  $R_g$  increases,  $\delta^0$  will be continuously shifted from its zone bisector until violating the current-angle-based PSM requirements, when  $\phi^-$  is set equal to  $-90^\circ$ , as verified in Section 6.2. Thus,  $\phi^-$  varies to allow the IRES to absorb the minimum amount of negative-sequence active current that forces  $\delta^0$  to be within its correct fault type zone. For example, in a BCG fault occurred at 10% of  $L_{25}$  with  $R_{ph} = 0$ ,  $\phi^-$  changes from  $-90^\circ$  to  $-119^\circ$ , as  $R_g$  increases from 0 to  $50 \Omega$ , to keep  $\delta^0$  equal to or greater than  $-55^\circ$ , i.e., the maximum reduced zone limits. On the other hand,  $\delta^+$  settles inside its correct fault-type zone with a maximum shift of  $25^\circ$  from its zone bisector. It can be observed that the value of  $R_g$  has a marginal effect on the value of  $\delta^+$ ,  $\phi^+$ , and  $k$ . However, the value of  $R_{ph}$  has a considerable impact on controlling  $\angle I^+$  to determine the proper values of  $\delta^+$  and  $\phi^+$ . If  $R_{ph}$  is negligible, the

Table 6.2. Performance of the proposed DCC during LLG faults at different fault locations

Fault Type	$R_g$	$R_{ph}$	Fault at 10% of $L_{25}$						Fault at 50% of $L_{25}$						Fault at 90% of $L_{25}$					
			$\delta^+$	$\delta^0$	$k$	$\phi^+$	$\phi^-$	$\angle I^+ - \angle I^-$	$\delta^+$	$\delta^0$	$k$	$\phi^+$	$\phi^-$	$\angle I^+ - \angle I^-$	$\delta^+$	$\delta^0$	$k$	$\phi^+$	$\phi^-$	$\angle I^+ - \angle I^-$
ABG	0		62.5	110.5	1.6	90	-90	237	63.5	110.9	1.7	90	-90	237	64.8	111.6	1.8	90	-90	235
	20	0	78.2	64.8	1.6	90	-108.1	222	67	64.9	1.7	90	-94.7	233	69.4	65	1.8	90	-96.5	231
	40		84.7	64.8	1.5	88.5	-116.9	215	79.7	64.9	1.7	90	-109.4	220	81.7	65	1.8	90	-111.7	219
	0		84.7	89.2	2.0	73.4	-90	215	84.8	109.7	2.2	66.8	-90	215	85.3	120	3.1	57.4	-90	215
	20	20	84.9	65.1	2.0	79.6	-93	215	87.5	78.8	2.3	74	-90	215	85.5	88.9	3.3	63.4	-90	215
	40		84.7	65.1	2.0	75.1	-99.1	215	86.7	69.6	2.3	75.2	-90	215	85.6	80.1	3.2	64.2	-90	215
	0		84.6	89.3	2.7	61.5	-90	215	85.1	112.1	3.4	52.2	-90	215	85	123.3	5.6	42.3	-90	215
	20	40	84.7	75.5	2.7	65.3	-90	215	84.9	92.8	3.5	57.3	-90	215	84.8	102	5.8	50.6	-90	215
	40		84.6	71.4	2.6	65.6	-90	215	85.3	86	3.5	58.3	-90	215	85.5	95.1	5.7	51.4	-90	215
BCG	0		-177.7	-9.9	1.6	90	-90	117	-177.3	-9.7	1.7	90	-90	116	-176.1	-9	1.8	90	-90	115
	20	0	-161.7	-54.9	1.6	90	-108.1	102	-177	-56.1	1.7	90	-94.6	113	-172.1	-55.7	1.8	90	-96.3	111
	40		-155.6	-55.4	1.5	88.6	-116.8	95	-161.4	-55.7	1.7	90	-109.4	100	-159.6	-55.7	1.8	90	-11.5	99
	0		-155.8	-31.3	2	73.4	-90	95	-156.3	-10.9	2.2	66.8	-90	95	-156.1	-0.6	3.0	57.2	-90	95
	20	20	-155.5	-55.1	2	79.6	-93	95	-156.2	-41.8	2.3	73.9	-90	95	-156.2	-21.7	3.2	61.7	-90	95
	40		-155.6	-55.2	2	75	-99.1	95	-156.3	-51.1	2.3	75.1	-90	95	-156.6	-40.5	3.2	64.1	-90	95
	0		-155.8	-30.8	2.7	61.4	-90	95	-156.6	-8.6	3.4	52	-90	95	-156.5	2.7	5.5	44.9	-90	95
	20	40	-155.9	-44.7	2.7	65.3	-90	95	-156.4	-27.9	3.5	57.1	-90	95	-161.5	-17.7	5.4	50.5	-90	95
	40		-155.8	-48.8	2.6	65.6	-90	95	-156.4	-34.8	3.5	58.1	-90	95	-157	-24.7	5.9	50.6	-90	95
CAG	0		-57.5	-130	1.6	90	-90	-3	-57.5	-129.3	1.69	90	-90	-3.5	-55.6	-128.6	1.8	90	-90	-5
	20	0	-41.9	184.8	1.6	90	-108	-19	-53.7	184.7	1.7	90	-94.7	-7	-51.1	184.9	1.8	90	-96.5	-9
	40		-35.4	184.7	1.5	88.5	-116.8	-25	-40.8	184.9	1.7	90	-109.4	-20	-38.9	184.9	1.8	90	-111.7	-22
	0		-35.3	209.1	2.0	73.4	-90	-25	-35.5	-131	2.2	66.8	-90	-25	-35.5	-120.3	3.1	52.3	-90	-25
	20	20	-35.2	184.9	2.0	79.6	-92.9	-25	-35.3	198.7	2.3	74	-90	-25	-35.6	208.7	3.25	63.3	-90	-25
	40		-35.4	184.9	2.0	75.1	-99.1	-25	-35.5	189.4	2.3	75.2	-90	-25	-35.7	199.9	3.2	64.2	-90	-25
	0		-35.4	209.3	2.7	61.5	-90	-25	-35.2	-128	3.4	52.2	-90	-25	-35.8	-117.1	5.31	45.7	-90	-25
	20	40	-35.5	195.5	2.7	65.3	-90	-25	-37.4	212.8	3.5	57.3	-90	-25	-35.9	-138.2	5.8	50.5	-90	-25
	40		-35.5	191.3	2.6	65.6	-90	-25	-35.8	205.6	3.5	58.2	-90	-25	-35.9	214.8	5.7	51.3	-90	-25

value of  $\Delta V^+$  and  $V^-$  will be large, i.e., around 0.33 p.u. each. Thus,  $K$  should be lower than 2 to avoid exceeding the maximum current limit. Accordingly,  $\phi^+$  is set at  $90^\circ$  to ensure injecting the maximum allowable reactive current during this fault condition. However, increasing  $R_{ph}$  or increasing the distance between the fault and the IRES locations reduces the magnitude of  $\Delta V^+$  and  $V^-$ , which allows  $K$  to be higher than 2. Thus,

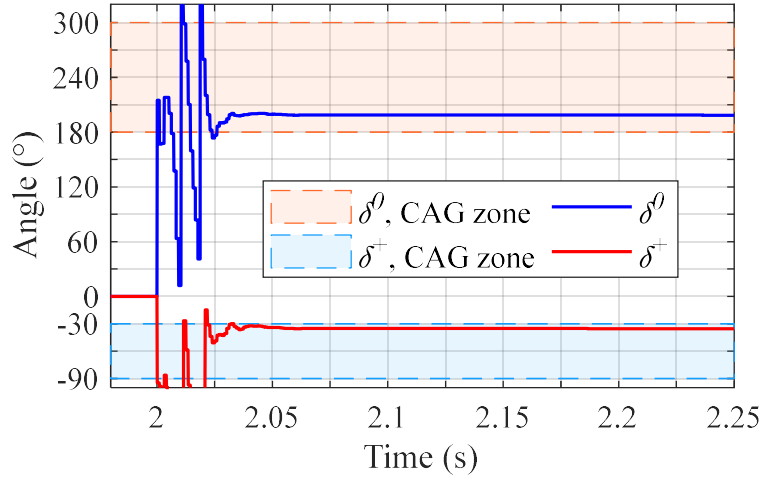


Figure 6.9. Measured  $\delta^0$  and  $\delta^+$  by  $R_{25}$  for a CAG fault occurred at 50% of  $L_{25}$  with  $R_g = R_{ph} = 20 \Omega$ .

$\angle I^+$  is controlled to inject the maximum allowable  $|I^+|$  and  $|I^-|$  without violating PSM requirements, which is achieved by making  $\delta^+$  equal to  $\delta_{F,bis}^+ \pm 25^\circ$ . For example,  $\delta^+$  approximately equals  $85^\circ$ ,  $-155^\circ$ , and  $-35^\circ$  for ABG, BCG, and CAG faults, respectively, when  $R_{ph}$  equals 20 and 40  $\Omega$ . The value of  $K$  is determined based on the chosen value of  $\angle I^+$  and  $\angle I^-$  to allow the IRES to inject the maximum current limit. For instance, during a BCG fault with  $R_{ph} = 20 \Omega$ ,  $K$  changes from 2 to 3.3 as the fault location changes from 10% to 90% of  $L_{25}$ . Moreover,  $K$  changes from 1.6 to 2.6, as  $R_{ph}$  changes from 0 to 40  $\Omega$ , during faults that occur at 10% of  $L_{25}$ .

Figures 6.9–6.11 demonstrate the dynamics of the highlighted fault scenario in Table 6.2, i.e., a CAG fault occurred at 50% of  $L_{25}$  with  $R_g = 20 \Omega$  and  $R_{ph} = 20 \Omega$ . Figure 6.9 illustrates the accuracy of the proposed DCC in controlling  $\angle I^+$  and  $\angle I^-$  to place  $\delta^+$  and  $\delta^0$  in their correct fault-type zones, where their values are  $-35.4^\circ$  and  $208.7^\circ$ , respectively. Also,  $\delta^+$  and  $\delta^0$  settle correctly within 0.02 seconds, allowing for fast and correct identification of the faulted phase by the relay. Moreover, Figure 6.10 illustrates the ability of the proposed DCC to calculate an accurate value of  $K$  that allow phase currents to reach their maximum allowable values, i.e., 1.5 p.u. Furthermore, Figure 6.11 depicts the values of  $|I^+|$  and  $|I^-|$ , which are equal to 0.83 and 0.7 p.u.; these magnitudes

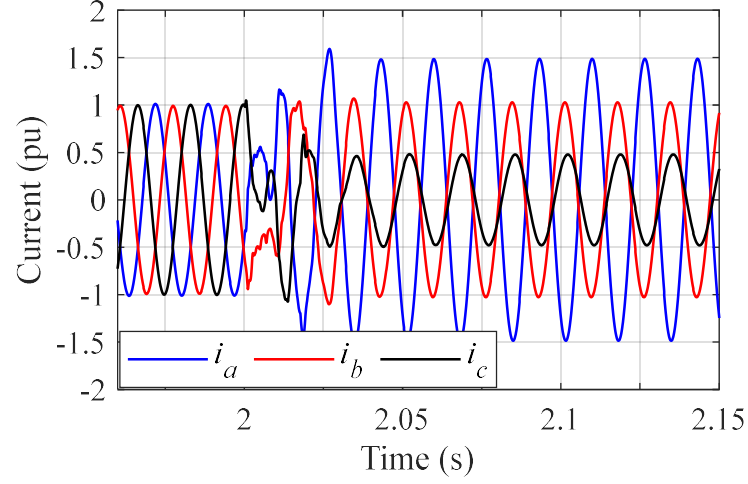


Figure 6.10. IIRES's phase currents measurements during a CAG fault occurred at 50% of  $L_{25}$  with  $R_g = R_{ph} = 20 \Omega$ .

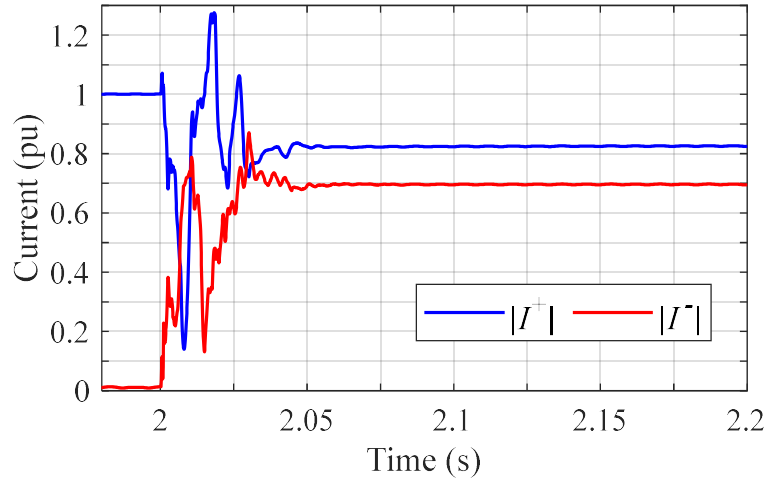


Figure 6.11. IIRES's Positive- and negative-sequence currents magnitude during a CAG fault occurred at 50% of  $L_{25}$  with  $R_g = R_{ph} = 20 \Omega$ .

are considered the maximum magnitudes that can be achieved for LLG faults, which are calculated using  $|I^+|^2 + |I^-|^2 + 1.813|I^+||I^-| = 1.5 \text{ p.u.}$

### C. LL Faults

The results for LL faults during different fault locations and resistances are listed in Table 6.3. During LL faults,  $\delta^+$  is the only decision parameter in determining faulty phase(s). Thus,  $\angle I^-$  is controlled to inject/absorb a zero value of the negative-sequence active

Table 6.3. Performance of the proposed DCC during LL faults at different fault locations

Fault Type	$R_g$	$R_{ph}$	Fault at 10% of $L_{25}$					Fault at 50% of $L_{25}$					Fault at 90% of $L_{25}$				
			$\delta^+$	k	$\phi^+$	$\phi^-$	$\angle I^+ - \angle I^-$	$\delta^+$	k	$\phi^+$	$\phi^-$	$\angle I^+ - \angle I^-$	$\delta^+$	k	$\phi^+$	$\phi^-$	$\angle I^+ - \angle I^-$
AB	0	0	61.2	1.58	90	-90	239	62.3	1.69	90	-90	238	63.3	1.8	90	-90	237
		10	78.9	1.7	90	-90	221	85.3	1.89	89.95	-90	215	86.2	2.24	80.04	-90	215
		20	85	1.88	82.4	-90	215	85.3	2.19	75.3	-90	215	85.4	3.02	64.1	-90	215
		30	84.9	2.09	72.3	-90	215	85.3	2.61	65.3	-90	215	85.3	4.27	54.8	-90	215
		40	84.9	2.36	64.8	-90	215	85.4	3.17	58.2	-90	215	75.2	5.62	47.4	-90	215
		50	84.8	2.71	59	-90	215	85.4	3.91	53	-90	215	53.2	4.52	18.7	-90	215
BC	0	0	-179.3	1.58	90	-90	118	-178.5	1.68	90	-90	118	-177.1	1.8	90	-90	116
		10	-161.6	1.69	90	-90	101	-155.5	1.89	89.9	-90	95	-156.8	2.24	79.9	-90	95
		20	-155.5	1.88	82.4	-90	95	-156.6	2.19	75.1	-90	95	-157.1	3.01	63.8	-90	95
		30	-155.7	2.1	72.3	-90	95	-156.1	2.6	65.1	-90	95	-158	4.25	54.6	-90	95
		40	-155.9	2.36	64.7	-90	95	-156.5	3.16	58	-90	95	-157.2	5.73	49.4	-90	95
		50	-156.4	2.7	58.9	-90	95	-156.8	3.89	52.7	-90	95	172.1	4.52	18.8	-90	95
CA	0	0	-59.5	1.58	90	-90	-1	-57.9	1.68	90	-90	-2	-56.9	1.8	90	-90	-3
		10	-41.5	1.69	90	-90	-19	-35.4	1.89	89.96	-90	-25	-35.4	2.24	80	-90	-25
		20	-35.3	1.88	82.4	-90	-25	-35.5	2.19	75.2	-90	-25	-35.6	3.02	64.1	-90	-25
		30	-35.6	2.09	72.3	-90	-25	-35.6	2.6	65.2	-90	-25	-35.9	4.27	54.7	-90	-25
		40	-35.5	2.36	64.7	-90	-25	-35.7	3.16	58.1	-90	-25	-35.5	5.82	49.7	-90	-25
		50	-35.7	2.7	59	-90	-25	-35.9	3.9	52.9	-90	-25	-67.2	4.52	18.6	-90	6.1

current, which is demonstrated in Table 6.3 by making  $\phi^- = -90^\circ$ . On the other hand,  $\angle I^+$  is controlled to allow the correct placement of  $\delta^+$  within its fault type zone and injecting the maximum combination of the positive-sequence active and reactive currents. With small values of  $R_{ph}$ ,  $\phi^+$  is set at  $90^\circ$  to inject the maximum allowable positive-sequence reactive current to maximize the value of  $K$  because its smaller than 2, e.g., 1.58, 1.69, and 1.8 for faults occurring at 10%, 50%, and 90% of  $L_{25}$  with  $R_{ph} = 20 \Omega$ , respectively. As  $R_{ph}$  increases or the distance between the fault and IIRES increases,  $\Delta V^+$  and  $V^-$  increases which allows  $K$  to be higher than 2. During these conditions,  $\angle I^+$  is controlled to allow  $\delta^+$  to be inside its zone limits with a  $5^\circ$  margin from its boundaries to maximize  $|I^+|$  and  $|I^-|$ . For instance,  $\delta^+$  equals  $85^\circ$ ,  $-155^\circ$ , and  $-35^\circ$  for AB, BC, and CA, respectively, when  $K$  is greater than 2. However, if the initial value of  $K$  is greater

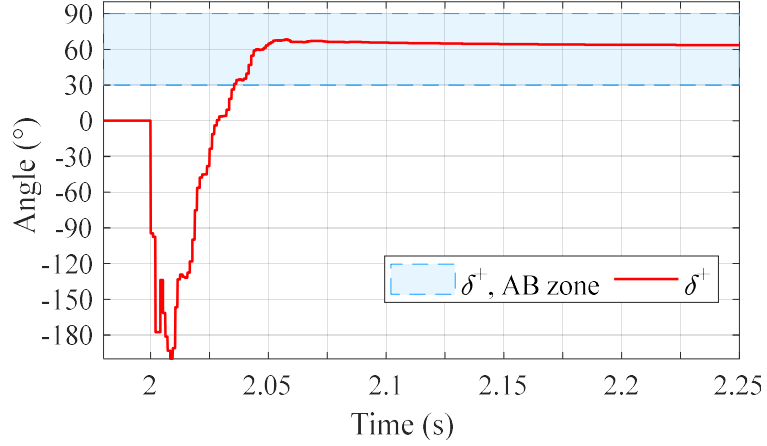


Figure 6.12. Measured  $\delta^+$  by  $R_{25}$  for a bolted AB fault occurred at 90% of  $L_{25}$ .

than 6, e.g., when a fault occurred at 50% of  $L_{25}$  with  $R_{ph} = 50 \Omega$ ,  $\phi^+$  and  $K$  are recalculated to be equal to  $18.6^\circ$  and 4.52, respectively; hence,  $K$  is prevented from exceeding its maximum limit, i.e.,  $K = 6$ , without violating the PSM requirements.

Figures 6.12–6.14 demonstrates the highlighted case study from Table 6.3, which is an AB fault that occurs at 90% of  $L_{25}$  with  $R_{ph} = 0 \Omega$ .  $\delta^+$  depicted in Figure 6.12 verifies the effectiveness of the proposed DCC in achieving the PSM requirements for LL faults, in which,  $\delta^+$  equals  $63.3^\circ$  and is located around the middle of its correct fault-type zone. Figure 6.13 represents the measured phase currents at the IRES terminals. The maximum peak of phase currents is equal to 1.5 p.u., which substantiates the accuracy of the proposed PSM in determining  $K$  without exceeding the maximum phase current limit. Lastly, Figure 6.14 illustrates the magnitudes of  $I^+$  and  $I^-$ , whose vector summation is equal to 1.5 p.u. In this case study,  $\angle I^+$  is controlled to force the IRES to inject only a reactive current component to follow the GC requirements that require injecting reactive current if  $K$  is smaller than 2. This prevents the IRES from injecting the allowable maximum values of  $|I^+|$  and  $|I^-|$ , which should be determined by forcing  $\angle I^+ - \angle I^-$  to be  $-145^\circ$ . Accordingly, the values of  $|I^+|$  and  $|I^-|$ , i.e., 0.734 and 0.763, respectively, shown in Figure 6.14 coincides with (6.38), i.e.,  $|I^+|^2 + |I^-|^2 + 2|I^+||I^-| = 1.5$  p.u. These results demonstrate the importance of selecting an adequate value of  $\angle I^+$  that maximize  $|I^+|$  and  $|I^-|$ , if  $K$  is between 2 and 6.

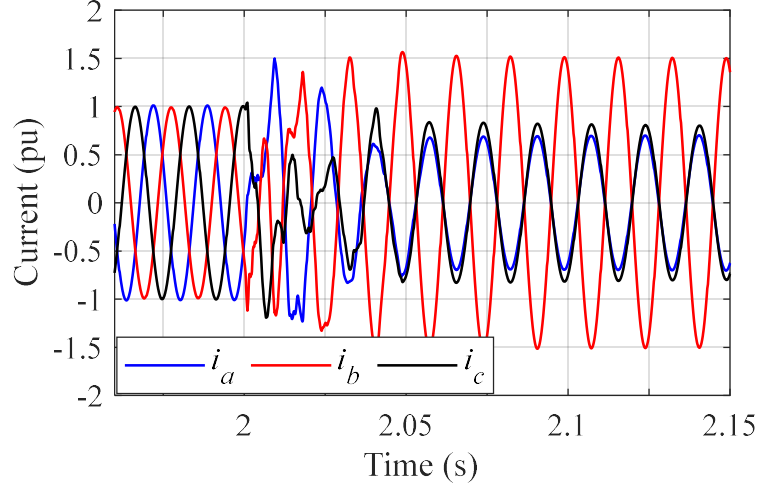


Figure 6.13. IIRES's phase currents measurements during a bolted AB fault occurred at 90% of  $L_{25}$ .

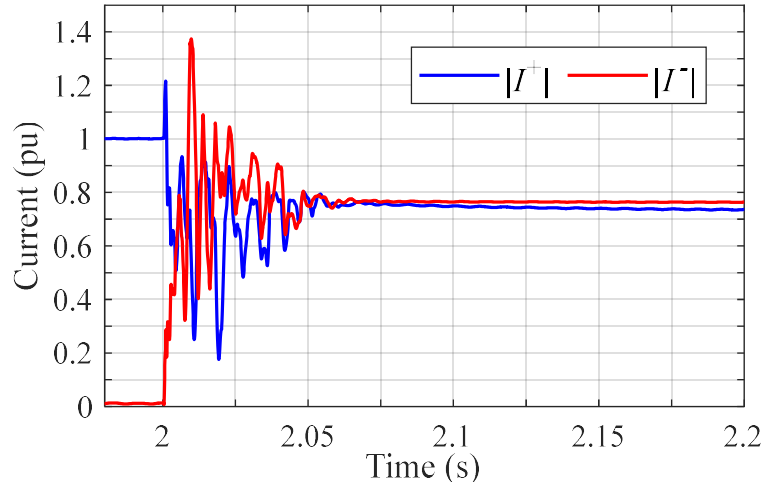


Figure 6.14. IIRES's Positive- and negative-sequence currents magnitude during a bolted AB fault occurred at 90% of  $L_{25}$ .

### 6.5.2 Compatibility with Various X/R Ratios of the Transmission Line

Table 6.4 demonstrates the accuracy of the proposed DCC at different fault types, fault resistances, and various transmission-line's  $X/R$  ratios during faults that occurred at 50% of  $L_{25}$ . Changing the  $X/R$  ratio of the transmission line has an impact on the value of  $\delta^0$  because the angle of the zero-sequence current is affected by the transmission-line impedance. Consequently, changing the  $X/R$  ratio can manipulate  $\delta^0$ . For instance, during

Table 6.4. Performance of the proposed DCC during faults at different transmission line's  $X/R$  ratio

Fault Type	$R_g$	$R_{ph}$	$X/R = 2$						$X/R = 5$						$X/R = 10$					
			$\delta^+$	$\delta^0$	k	$\phi^+$	$\phi^-$	$\angle I^+ - \angle I^-$	$\delta^+$	$\delta^0$	k	$\phi^+$	$\phi^-$	$\angle I^+ - \angle I^-$	$\delta^+$	$\delta^0$	k	$\phi^+$	$\phi^-$	$\angle I^+ - \angle I^-$
AG	0	0	0.4	-13.1	3.15	81.8	-90	-60	-0.2	-6.5	3.12	86.7	-90	300	-0.1	-4.7	3.12	87.9	-90	300
	40		-7.7	-11.2	5.36	30.8	-90	-50	-0.5	-5	5.77	37.6	-90	300	-0.87	-3.7	5.59	37.4	-90	300
BG	0	0	119.4	-133.5	3.15	81.7	-90	180	120.9	-26.2	3.12	86.8	-90	180	120.3	-124.6	3.12	88	-90	180
	40		117.2	-130.6	5.5	33.3	-90	187	120.1	-124.8	5.8	37.6	-90	180	119.6	-123.5	5.61	37.5	-90	180
CG	0	0	-120.2	106.6	3.15	81.7	-90	60	-120.4	113.3	3.12	86.6	-90	60	-120.4	115.1	3.12	87.9	-90	60
	40		-125.1	110	5.8	39.4	-90	60	121.3	114.9	5.75	37.5	-90	60	-121.4	116.2	5.58	37.4	-90	60
ABG	0	0	67.4	98.7	1.69	90	-90	172	63.5	110.9	1.68	90	-90	236	62.7	114.1	1.68	90	-90	237
	40		82.3	64.4	1.68	90	-110.9	216	79.7	64.9	1.67	90	-109.4	220	78.5	64.8	1.66	90	-109	221
	0	40	83.7	103.2	3.4	55.8	-90	215	85.1	112.1	3.36	52.2	-90	215	84.5	113.9	3.33	51.1	-90	215
	40		83.8	81.1	3.46	60.9	-90	215	85.3	86	3.46	58.3	-90	215	85.1	86.6	3.44	57.5	-90	215
BCG	0	0	-172.4	-21.1	1.69	90	-90	112	-177.3	-9.7	1.68	90	-90	116	-177.1	-5.4	1.68	90	-90	118
	40		-156.2	-55.1	1.68	90	-110.9	96	-161.4	-55.7	1.67	90	-109.4	100	-161.3	-54.8	1.66	90	-109	101
	0	40	-155.2	-16.1	3.41	56	-90	95	-156.6	-8.6	3.35	52	-90	95	-156.6	-6.4	3.32	51	-90	95
	40		-155.5	-38.6	3.46	61	-90	95	-156.4	-34.8	3.45	58.1	-90	95	-157.3	-33.7	3.44	57.4	-90	95
CAG	0	0	-51.5	219.5	1.69	90	-90	-8	-57.5	-129.3	1.69	90	-90	-4	-58.4	-127.1	1.69	90	-90	-3
	40		-36	185.1	1.68	90	-110.9	-24	-40.8	184.9	1.67	90	-109.4	-20	-41.8	184.5	1.67	90	-109	-19
	0	40	-35.1	-136.2	3.41	56	-90	-25	-35.2	-127.9	3.36	52.2	-90	-25	-35.5	-126.2	3.33	51.1	-90	-25
	40		-34.5	201.6	3.5	61	-90	-25	-35.8	205.6	3.46	58.2	-90	-25	-35.7	206.5	3.44	57.4	-90	-25
AB	0	0	64.7	.	1.69	90	-90	235	62.3	.	1.69	90	-90	238	61.7	.	1.68	90	-90	238
	40	94.1	.	3.33	250.1	-90	25	85.4	.	3.17	58.2	-90	215	84.4	.	3.13	57.3	-90	215	
BC	0	0	-175	.	1.69	90	-90	115	-178.5	.	1.68	90	-90	118	-178.1	.	1.69	90	-90	118
	40	-155.2	.	3.23	61.2	-90	95	-156.5	.	3.16	58	-90	95	-156.4	.	3.13	57.3	-90	95	
CA	0	0	-54.7	.	1.69	90	-90	-5	-57.9	.	1.68	90	-90	-2	-58.5	.	1.68	90	-90	1.6
	40	-34.5	.	3.24	61.2	-90	-25	-35.7	.	3.16	58.1	-90	-25	-35.9	.	3.13	57.3	-90	-25	

a bolted BG fault,  $\delta^0$  is equal to  $-133.5^\circ$ ,  $-126.2^\circ$ , and  $-124.2^\circ$  when the  $X/R$  ratio equals 2, 5, and 10, respectively. Thus, by increasing the  $X/R$  ratio,  $\delta^0$  tends to be nearer to its zone bisector. On the other hand, the value of  $X/R$  ratio of the transmission line has a minor impact on  $\delta^+$  and  $K$  quantities, because the voltage measured at the fault and the IRES locations are only shifted by a small angle when the IRES follows the recent GCs, as explained in Chapter 4. For example, during a CA fault with  $R_{ph} = 40 \Omega$ ,  $\delta^+$  changes



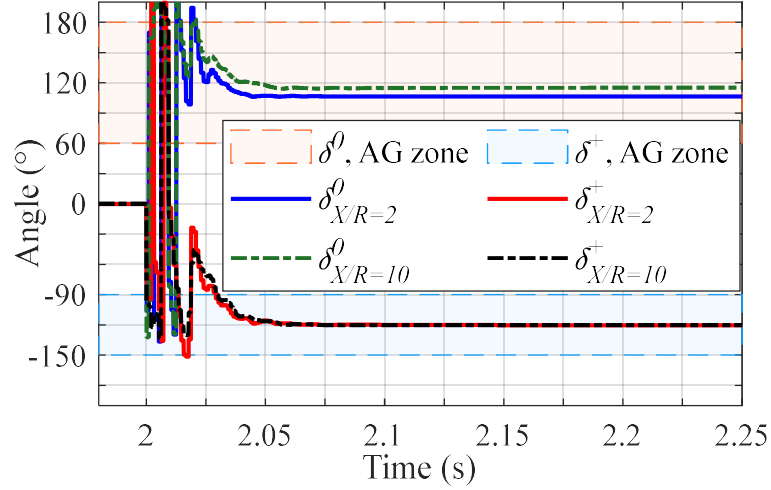


Figure 6.15. Measured  $\delta^0$  and  $\delta^+$  by  $R_{25}$  for a bolted CG when the transmission lines'  $X/R$  ratios equal to 2 and 10.

from  $-34.5^\circ$  to  $-35.9^\circ$ , as the  $X/R$  ratio changes from 2 to 10, while  $K$  changes from 3.24 to 3.13 to allow injecting the maximum phase current limit. Figure 6.15 demonstrates the value of  $\delta^0$  and  $\delta^+$  during a bolted CG fault at 50% of  $L_{25}$  when the  $X/R$  ratio is equal to 2 and 10. The results verify the accuracy of the proposed DCC in controlling both  $\delta^0$  and  $\delta^+$  at different  $X/R$  ratios. When the  $X/R$  ratio increases from 2 and 10,  $\delta^0$  changes from  $106.6^\circ$  to  $115.1^\circ$ , and  $\delta^+$  varies from  $-120.2^\circ$  to  $-120.4^\circ$ , respectively.

## 6.6 Conclusions

Recent GCs impose regulations for injecting positive- and negative-sequence currents during unbalanced faults. However, following these GCs without considering the principle of operation of protection relays may lead to improper operation of protective relaying functions, which adversely affects the power system's reliability and resiliency. In this chapter, a mathematical analysis was performed to understand the root causes behind the failure of the current-angle-based PSM when the fault currents are supplied from IIRESS that follow the recent GCs. Furthermore, a new DCC is proposed to achieve both current-angle-based phase selection and recent GC requirements. The DCC is designed in six stages. In the first two stages, the negative-sequence current is calculated by injecting the minimum negative-sequence active current that forces  $\delta^0$  to be within its correct fault-type

zone. In Stages III and IV, the positive-sequence current angle is calculated to allow  $\delta^0$  to be within its correct fault-type zone as well as injecting the maximum allowable positive-sequence active current. Accordingly, in Stage V,  $K$  is selected to meet the RCG requirements without exceeding the IRES maximum current. Lastly, the positive- and negative-sequence currents are controlled in the  $dq$  frame. Comprehensive simulation results verify the effectiveness of the proposed DCC in securing correct operation for the current-angle-based PSM and obeying the RCG requirements of the recent GCs during different fault types, resistances, and locations.

## **Chapter 7**

### **Conclusions**

This chapter presents the conclusions of the research work conducted in this dissertation, highlights its main contributions, and shows directions for future work.

#### **7.1 Conclusions**

The high penetration of IRESs in both transmission and distribution networks has an adverse effect on the main protection functions, which motivates researchers to find solutions to secure the correct operation of protection functions. The main objective of this dissertation was to ensure a secure operation of phase selection to enhance power system resiliency and protection reliability. The solutions proposed in this dissertation can be classified into two main categories (i) developing a new PSM algorithm that copes with different IRESs' controllers, fault resistances, and locations, and (ii) controlling the IRES to inject both positive and negative-sequence currents with phase angles that ensure proper operation of commercial PSMs. The first approach can be considered a long-term solution as it allows the IRES to support the grid during fault conditions without being limited by the conventional relay operation. However, replacing the deployed relays in the power grid is costly and needs to be done over a long-time interval. On the other hand, the second approach can be considered a short-term solution, in which the IRES is forced to inject currents that allow conventional relays to determine the faulty phase(s) precisely as well as to comply with the GC requirements; thus, it can be implemented instantly and secure the phase selection of existing relays in the grid. The conclusion of each chapter is highlighted as follows.

In Chapter 3, short circuit analysis is performed to understand the failure reasons of the current- angle-based PSM measured at a relay location as well as problems associated with voltage-angle-based PSM at relays near fault locations. Consequently, an adaptive current-angle-based PSM is developed, which adapts the PSM's zones by subtracting a compensation angle, i.e., the equivalent impedance angle measured at the relay side.

Besides, the conventional PSM's zones are modified to secure PSM operations at high resistive faults. Comprehensive simulation results verify the adequacy of the proposed method in both transmission and distribution networks for fault currents emanating from either IIREs or conventional SGs.

In Chapter 4, further analysis is performed to understand the effect of the transmission line impedance and IIREs'S controllers on the voltage-angle-based PSM. Consequently, the root causes of mis-operation of the voltage-angle-based PSM are determined for different fault locations. Thereafter, the voltage-angle-based PSMs are modified to determine the faulty phases accurately regardless fault locations, resistances, and types. PSCAD/ EMTDC simulations are utilized to verify the dependability of the proposed zones in determining the faulty phase(s) properly with various IIREs controllers and at different fault locations and resistances.

In Chapter 5, two DCCs are developed to ensure the proper operation of the PSM without violating positive-sequence RCG requirements. The two DCCs determine the initial angle of the positive- and negative-sequence currents to follow the RCG requirements and force the relative angle between the negative- and zero-sequence currents to match its zone bisector, respectively. However, they update these initial angles differently. DCC1 updates the negative-sequence current angle if only the relative angle between the negative-and positive-sequence currents falls outside its predefined zones. On the other hand, the relay security is enhanced in DCC2 by updating the angle of the negative-sequence current to ensure that both the relative angles between the negative- and zero-sequence currents and between the negative- and positive-sequence currents are equally shifted away from the bisectors of their respective zones. Extensive simulation results confirm the validity of these developed DCCs to preserve the proper operation of PSMs without violating RCG requirements under different ground and arc resistances, fault locations, and types. Moreover, a real-time simulation is conducted to validate the accurate operation of DCC.

In Chapter 6, mathematical analysis performed in Chapter 3 is extended to understand the root causes behind the failure of the current- angle-based PSMs, when the IIREs follows the VDE-GC that imposes requirements for both positive-and negative- sequence currents. Subsequently, a DCC is developed to ensure correct operation of the conventional

current-angle-based PSM under this GC's requirements and maximize the positive-sequence active current injection. First, negative-sequence current angle is designed to ensure injecting or absorbing the minimum negative-sequence active currents without violating PSM requirements. Then, the positive-sequence-current angle is determined to guarantee the correct operation of PSM and injecting the maximum available positive-sequence active current, subsequently, the positive- and negative-reactive currents magnitudes are obtained to follow the RCG requirements without exceeding the maximum IRES's current Limits. PSCAD/EMTDC simulation results verify the capability of the proposed DCC to guarantee proper PSM and follows RCG requirements, simultaneously, under different fault locations and resistances.

## 7.2 Contributions

The main contributions of this dissertation can be summarized as follows:

1. Investigating the root causes of the failure of the current-angle-based PSMs when fault currents emerge from IRESs,
2. Exploring the root causes behind the improper operation of the voltage-angle-based PSMs for faults near and away from the relay location.
3. Modifying the current-angle-based PSM zones boundaries to enhance phase selection dependability at high resistive faults in conventional grids,
4. Developing an adaptive current-angle-based PSM to determine fault type correctly for fault currents emanating from either IRESs or SGs without the need for communication,
5. Modifying the voltage-angle-based PSM zones boundaries to guarantee precise phase selection under various IRES controllers.
6. Developing two DCCs to guarantee precise PSM operation and follow the positive-sequence reactive-current requirements of GCs simultaneously, and
7. Developing a DCC to (i) ensure accurate PSM operation, (ii) follow positive- and negative-sequence-reactive current requirements of recent GCs, and (iii) inject the maximum allowable positive-sequence-active current concurrently.

### **7.3 Future Work**

The suggested future directions of this research can be summarized as follows:

1. Testing the proposed DCCs on industrial relays,
2. Determining the effect of inner loop controllers on the speed of the IIRESSs to track the positive- and negative-sequence current references,
3. Developing a DCC that ensures accurate PSM and achieves ancillary services during fault conditions, e.g., to enhance the system stability,
4. Investigating the root causes behind the failure of conventional PSMs when faults are supplied from voltage-controlled IIRESSs, and
5. Developing enhanced voltage-controlled converters that achieve power-sharing in microgrids and enable phase selection.

## Bibliography

- [1] A. S. Brouwer, M. van den Broek, A. Seebregts, and A. Faaij, “Operational flexibility and economics of power plants in future low-carbon power systems,” *Appl. Energy*, vol. 156, pp. 107–128, Oct. 2015, doi: 10.1016/J.APENERGY.2015.06.065.
- [2] C. Stockwell, G. Andreas, R. Deborah, M. Gidden, and B. Hare, “Climate summit momentum: Paris commitments improved warming estimate to 2.4°C.,” 2021. Accessed: Feb. 26, 2023. [Online]. Available: [moz-extension://5478b177-1a4a-4644-96d5-a794468a26b3/enhanced-reader.html?openApp&pdf=https%3A%2F%2Fclimateactiontracker.org%2Fdocuments%2F853%2FCAT\\_2021-05-04\\_Briefing\\_Global-Update\\_Climate-Summit-Momentum.pdf](moz-extension://5478b177-1a4a-4644-96d5-a794468a26b3/enhanced-reader.html?openApp&pdf=https%3A%2F%2Fclimateactiontracker.org%2Fdocuments%2F853%2FCAT_2021-05-04_Briefing_Global-Update_Climate-Summit-Momentum.pdf)
- [3] G. Barbose, “U.S. Renewables portfolio standards 2021 annual status update: early release,” California, 2021. Accessed: Feb. 26, 2023. [Online]. Available: [moz-extension://5478b177-1a4a-4644-96d5-a794468a26b3/enhanced-reader.html?openApp&pdf=https%3A%2F%2Feta-publications.lbl.gov%2Fsites%2Fdefault%2Ffiles%2Frp\\_status\\_update-2021\\_early\\_release.pdf](moz-extension://5478b177-1a4a-4644-96d5-a794468a26b3/enhanced-reader.html?openApp&pdf=https%3A%2F%2Feta-publications.lbl.gov%2Fsites%2Fdefault%2Ffiles%2Frp_status_update-2021_early_release.pdf)
- [4] D. Y. and X. W. F. Blaabjerg, Y. Yang, “Distributed power-generation systems and protection,” *Proc. IEEE*, vol. 105, no. 7, pp. 1311–1331, Jul. 2017, doi: 10.1109/JPROC.2017.2696878.
- [5] T. Zheng, L. Chen, Y. Guo, and S. Mei, “Comprehensive control strategy of virtual synchronous generator under unbalanced voltage conditions,” *IET Gener. Transm. Distrib.*, vol. 12, no. 7, pp. 1621–1630, 2018, doi: 10.1049/iet-gtd.2017.0523.
- [6] M. Nagpal and C. Henville, “Impact of power-electronic sources on transmission line ground fault protection,” *IEEE Trans. Power Deliv.*, vol. 33, no. 1, pp. 62–70, Feb. 2018, doi: 10.1109/TPWRD.2017.2709279.
- [7] K. W. C. and E. F. Haddadi, M. Zhao, I. Kocar, U. Karaagac, “Impact of inverter-based resources on negative sequence quantities-based protection elements,” *IEEE Trans. Power Del.*, vol. 36, no. 1, pp. 289–298, Feb. 2021.
- [8] S. Paladhi and A. K. Pradhan, “Adaptive distance protection for lines connecting converter-interfaced renewable plants,” *IEEE J. Emerg. Sel. Top. Power Electron.*, vol. 9, no. 6, pp. 7088–7098, Dec. 2021, doi: 10.1109/JESTPE.2020.3000276.
- [9] S. Paladhi, J. R. Kurre, and A. K. Pradhan, “Source-independent zone-1 protection for converter-dominated power networks,” *IEEE Trans. Power Deliv.*, 2022, doi: 10.1109/TPWRD.2022.3218615.
- [10] K. Jia, Z. Yang, Y. Fang, T. Bi, and M. Sumner, “Influence of inverter-interfaced renewable energy generators on directional relay and an improved scheme,” *IEEE Trans. Power Electron.*, vol. 34, no. 12, pp. 11843–11855, Dec. 2019, doi: 10.1109/TPEL.2019.2904715.

- [11] A. Hooshyar, E. F. El-Saadany, and M. Sanaye-Pasand, "Fault type classification in microgrids including photovoltaic DGs," *IEEE Trans. Smart Grid*, vol. 7, no. 5, pp. 2218–2229, Sep. 2016, doi: 10.1109/TSG.2015.2451675.
- [12] M. A. Azzouz, H. H. Zeineldin, and E. F. El-Saadany, "Selective Phase Tripping for Microgrids Powered by Synchronverter-Interfaced Renewable Energy Sources," *IEEE Trans. Power Deliv.*, vol. 36, no. 6, pp. 3506–3518, 2020, doi: 10.1109/TPWRD.2020.3044013.
- [13] P. M. Anderson, *Analysis of faulted power systems*. New York, NY, USA: IEEE Press, 1995.
- [14] J. Rocabert, A. Luna, F. Blaabjerg, and P. Rodríguez, "Control of power converters in AC microgrids," *IEEE Trans. Power Electron.*, vol. 27, no. 11, pp. 4734–4749, Nov. 2012, doi: 10.1109/TPEL.2012.2199334.
- [15] A. Yazdani and R. Iravani, *Voltage-Sourced Converters in Power Systems*. Hoboken, NJ, USA: Wiley, 2010.
- [16] R. P. Aguilera, P. Acuna, G. Konstantinou, S. Vazquez, and J. I. Leon, "Basic control principles in power electronics analog and digital control design," in *Control of Power Electronic Converters and Systems*, F. Blaabjerg, Ed. Academic Press, ELSEVIER, 2018.
- [17] W. W. Baker, "Control, modeling, and analysis of inverter-based resources," Auburn University, 2021.
- [18] R. W. Erickson and D. Maksimovic, *Fundamentals of power electronics*, Third. Springer, 2020.
- [19] L. Harnefors, M. Bongiorno, and S. Lundberg, "Input-admittance calculation and shaping for controlled voltage-source converters," *IEEE Trans. Ind. Electron.*, vol. 54, no. 6, pp. 3323–3334, Dec. 2007, doi: 10.1109/TIE.2007.904022.
- [20] M. Paolone *et al.*, "Fundamentals of power systems modelling in the presence of converter-interfaced generation," *Electr. Power Syst. Res.*, vol. 189, p. 106811, Dec. 2020, doi: 10.1016/J.EPSR.2020.106811.
- [21] P. Rodríguez, R. Teodorescu, I. Candela, A. V. Timbus, M. Liserre, and F. Blaabjerg, "New positive-sequence voltage detector for grid synchronization of power converters under faulty grid conditions," *PESC Rec. - IEEE Annu. Power Electron. Spec. Conf.*, 2006, doi: 10.1109/PESC.2006.1712059.
- [22] P. Rodríguez, J. Pou, J. Bergas, J. I. Candela, R. P. Burgos, and D. Boroyevich, "Decoupled double synchronous reference frame PLL for power converters control," *IEEE Trans. Power Electron.*, vol. 22, no. 2, pp. 584–592, Mar. 2007, doi: 10.1109/TPEL.2006.8900000.
- [23] M. Mirhosseini, J. Pou, B. Karanayil, and V. G. Agelidis, "Resonant versus conventional controllers in grid-connected photovoltaic power plants under unbalanced grid voltages," *IEEE Trans. Sustain. Energy*, vol. 7, no. 3, pp. 1124–1132, Jul. 2016, doi: 10.1109/TSTE.2016.2529679.



- [24] A. A. AbuEl-Naga, M. I. Marei, and H. S. K. El-Goharey, "Second order adaptive notch filter based wind power smoothing using flywheel energy storage system," *2017 19th Int. Middle-East Power Syst. Conf. MEPCON 2017 - Proc.*, vol. 2018-Febru, pp. 314–319, Feb. 2018, doi: 10.1109/MEPCON.2017.8301199.
- [25] G. Elhassan *et al.*, "Deadbeat current control in grid-connected inverters: a comprehensive discussion," *IEEE Access*, vol. 10, pp. 3990–4014, Jan. 2022, doi: 10.1109/ACCESS.2021.3138789.
- [26] M. Tsili and S. Papathanassiou, "A review of grid code technical requirements for wind farms," *IET Renew. Power Gener.*, vol. 3, no. 3, pp. 308–332, Sep. 2009, doi: 10.1049/iet-rpg.2008.0070.
- [27] "IEEE draft standard for interconnection and interoperability of inverter-based resources (IBR) interconnecting with associated transmission electric power systems," 2021.
- [28] "Technical standard for the supervision of the conformity of electricity generation modules according to EU Regulation 2016/631," 2020.
- [29] "Commission Regulation (EU) 2016/631 of 14 April 2016 establishing a network code on requirements for grid connection of generators," Brussels, 2016.
- [30] "Technical requirements for the connection and operation of customer installations to the high voltage network (TCR high voltage) VDE-AR-N 4120," 2018.
- [31] V. Valouch, M. Bejvl, P. Šimek, and J. Škramlík, "Power control of grid-connected converters under unbalanced voltage conditions," *IEEE Trans. Ind. Electron.*, vol. 62, no. 7, pp. 4241–4248, Jul. 2015, doi: 10.1109/TIE.2014.2384473.
- [32] Z. Yang, Z. Liu, Q. Zhang, Z. Chen, J. de J. Chavez, and M. Popov, "A control method for converter-interfaced sources to improve operation of directional protection elements," *IEEE Trans. Power Deliv.*, vol. 38, no. 1, pp. 642–654, Feb. 2023, doi: 10.1109/TPWRD.2022.3202988.
- [33] J. Jia, G. Yang, and A. H. Nielsen, "A review on grid-connected converter control for short-circuit power provision under grid unbalanced faults," *IEEE Trans. Power Deliv.*, vol. 33, no. 2, pp. 649–661, Apr. 2018, doi: 10.1109/TPWRD.2017.2682164.
- [34] S. F. Zarei, H. Mokhtari, M. A. Ghasemi, S. Peyghami, P. Davari, and F. Blaabjerg, "Control of grid-following inverters under unbalanced grid conditions," *IEEE Trans. Energy Convers.*, vol. 35, no. 1, pp. 184–192, Mar. 2020, doi: 10.1109/TEC.2019.2945699.
- [35] A. Camacho, M. Castilla, J. Miret, R. Guzman, and A. Borrell, "Reactive power control for distributed generation power plants to comply with voltage limits during grid faults," *IEEE Trans. Power Electron.*, vol. 29, no. 11, pp. 6224–6234, Nov. 2014, doi: 10.1109/TPEL.2014.2301463.
- [36] J. Miret, M. Castilla, A. Camacho, L. G. De Vicuña, and J. Matas, "Control scheme for photovoltaic three-phase inverters to minimize peak currents during unbalanced grid-voltage sags," *IEEE Trans.*

*Power Electron.*, vol. 27, no. 10, pp. 4262–4271, Oct. 2012, doi: 10.1109/TPEL.2012.2191306.

- [37] A. Banaieymoqadam, A. Hooshyar, and M. A. Azzouz, “A control-based solution for distance protection of lines connected to converter-interfaced sources during asymmetrical faults,” *IEEE Trans. Power Deliv.*, vol. 35, no. 3, pp. 1455–1466, Jun. 2020.
- [38] M. Salehi and F. Namdari, “Fault classification and faulted phase selection for transmission line using morphological edge detection filter,” *IET Gener. Transm. Distrib.*, vol. 12, no. 7, pp. 1595–1605, Mar. 2018, doi: 10.1049/iet-gtd.2017.0999.
- [39] SEL-651R Advanced recloser control,” SEL, Schweitzer Engineering Labs.. Accessed: Apr. 10, 2023. [Online]. Available: <https://selinc.com/products/651R/>.
- [40] J. R. Agüero, J. Wang, and J. J. Burke, “Improving the reliability of power distribution systems through single-phase tripping,” in *2010 IEEE PES Transmission and Distribution Conference and Exposition: Smart Solutions for a Changing World*, Apr. 2010, pp. 1–7. doi: 10.1109/TDC.2010.5484372.
- [41] R. M. Cheney, J. T. Thorne, G. Hataway, A. Power, and C. G. Hataway, “Distribution single-phase tripping and reclosing: overcoming obstacles with programmable recloser controls,” 2009, pp. 214–223.
- [42] M. Taberer and B. Jeremy, “Real-world troubleshooting with microprocessor-based recloser controls,” in *2009 62nd Annual Conference for Protective Relay Engineers*, May 2009, pp. 214–223.
- [43] “NOVA-TS Triple-Single Recloser,” *EATON Powering Business Worldwide*. <https://www.eaton.com/us/en-us/catalog/medium-voltage-power-distribution-control-systems/nova-ts-triple-single-recloser.html> (accessed Feb. 27, 2023).
- [44] T. Fahey and N. Burbure, “Single-phase tripping,” *IEEE Power Energy Mag*, vol. 6, no. 2, pp. 46–52, 2008.
- [45] S. Luo, X. Dong, S. Shi, and B. Wang, “A novel phase selection method based on instantaneous reactive power,” *IET Conf. Publ.*, vol. 2014, no. 626 CP, 2014, doi: 10.1049/CP.2014.0119.
- [46] A. K. Pradhan, A. Routray, S. Pati, and D. K. Pradhan, “Wavelet fuzzy combined approach for fault classification of a series-compensated transmission line,” *IEEE Trans. Power Deliv.*, vol. 19, no. 4, pp. 1612–1618, Oct. 2004, doi: 10.1109/TPWRD.2003.822535.
- [47] X. N. Lin, M. Zhao, K. Alymann, and P. Liu, “Novel design of a fast phase selector using correlation analysis,” *IEEE Trans. Power Deliv.*, vol. 20, no. 2 II, pp. 1283–1290, Apr. 2005, doi: 10.1109/TPWRD.2004.834298.
- [48] M. Mynam and Y. Gong, “Fault-type identification for electric power delivery systems,” U.S. Patent No. 8 791 704, 2014

- [49] “Technical manual: MiCOMho P446—fast multifunction distance protection relay,” U.K., 2011.
- [50] J. Zhang, B. Zhang, and C. Wang, “Improved schemes for traditional current-based phase selectors in wind power systems,” *IET Gener. Transm. Distrib.*, vol. 12, no. 21, pp. 5781–5788, Nov. 2018, doi: 10.1049/IET-GTD.2018.5873.
- [51] G. Song, C. Wang, T. Wang, M. Kheshti, and X. Kang, “A Phase selection method for wind power integration system using phase voltage waveform correlation,” *IEEE Trans. Power Deliv.*, vol. 32, no. 2, pp. 740–748, Apr. 2017, doi: 10.1109/TPWRD.2016.2577890.
- [52] T. Adu, “An accurate fault classification technique for power system monitoring devices,” *IEEE Trans. Power Deliv.*, vol. 17, no. 3, pp. 684–690, Jul. 2002, doi: 10.1109/TPWRD.2002.1022787.
- [53] “D90Plus line distance protection system,” Markham, ON, Canada, 2012.
- [54] D. Costello and K. Zimmerman, “Determining the faulted phase,” *2010 63rd Annu. Conf. Prot. Relay Eng.*, Mar. 2010, doi: 10.1109/CPRE.2010.5469523.
- [55] J. Roberts and E. Schweitzer, “Fault identification system for use in protective relays for power transmission lines,” 5 515 227, 1996
- [56] S. Fahim, S. K. Sarker, S. M. Mueen, S. K. Das, and I. Kamwa, “A deep learning based intelligent approach in detection and classification of transmission line faults,” *Int. J. Electr. Power Energy Syst.*, vol. 133, Dec. 2021.
- [57] A. Mukherjee, K. Chatterjee, and A. Kundu, Palash KumarDas, “Probabilistic neural network-aided fast classification of transmission line faults using differencing of current signal,” *J. Inst. Eng.*, vol. 102, pp. 1019–1032, 2021.
- [58] B. Vyas, B. Das, and R. P. Maheshwari, “An improved scheme for identifying fault zone in a series compensated transmission line using undecimated wavelet transform and Chebyshev Neural Network,” *Int. J. Electr. Power Energy Syst.*, vol. 63, Dec. 2014.
- [59] R. Godse and S. Bhat, “Mathematical morphology-based feature-extraction technique for detection and classification of faults on power transmission line,” *IEEE Access*, vol. 8, pp. 38459–38471, Feb. 2020.
- [60] A. Majd, G. Sahebi, M. Daneshtalab, and E. Troubitsyna, “Optimizing scheduling for heterogeneous computing systems using combinatorial meta-heuristic solution,” in *2017 IEEE SmartWorld*, 2017, pp. 1–8.
- [61] K. Xu, Z. Zhang, Q. Lai, and X. Yin, “Fault phase selection method applied to tie line of renewable energy power stations,” *IET Gener. Transm. Distrib.*, vol. 14, no. 13, pp. 2549–2557, 2020, doi: 10.1049/iet-gtd.2019.1472.
- [62] E. M. Carrasco, M. P. C. Moreno, M. T. V. Martínez, and S. B. Vicente, “Improved faulted phase

- selection algorithm for distance protection under high penetration of renewable energies,” *Energies*, vol. 13, no. 3, Jan. 2020, doi: 10.3390/en13030558.
- [63] M. A. Azzouz, A. Hooshyar, and E. F. El-Saadany, “Resilience enhancement of microgrids with inverter-interfaced DGs by enabling faulty phase selection,” *IEEE Trans. Smart Grid*, vol. 9, no. 6, pp. 6578–6589, Nov. 2018, doi: 10.1109/TSG.2017.2716342.
  - [64] M. A. Azzouz and A. Hooshyar, “Dual current control of inverter-interfaced renewable energy sources for precise phase selection,” *IEEE Trans. Smart Grid*, vol. 10, no. 5, pp. 5092–5102, Sep. 2019, doi: 10.1109/TSG.2018.2875422.
  - [65] A. Banaïmoqadam, A. Hooshyar, and M. A. Azzouz, “A Comprehensive Dual Current Control Scheme for Inverter-Based Resources to Enable Correct Operation of Protective Relays,” *IEEE Trans. Power Deliv.*, vol. 36, no. 5, pp. 2715–2729, 2021, doi: 10.1109/TPWRD.2020.3025878.
  - [66] GE Multilin, “D60 Line Distance Protection System,” 2008, [Online]. Available: <http://www.gedigitalenergy.com/products/manuals/d60/d60man-w1.pdf>
  - [67] Y. Fang, K. Jia, Z. Yang, Y. Li, and T. Bi, “Impact of Inverter-Interfaced Renewable Energy Generators on Distance Protection and an Improved Scheme,” *IEEE Trans. Ind. Electron.*, vol. 66, no. 9, pp. 7078–7088, Sep. 2019, doi: 10.1109/TIE.2018.2873521.
  - [68] G. Ziegler, *Numerical distance protection: principles and applications*, 4th ed. Erlangen, Germany: Publicis, 2011.
  - [69] and J. M. Bogdan Kasztenny, Bruce Campbell, “Phase selection for single-pole tripping–weak infeed conditions and cross country faults,” in *Proceedings of the 27th Annual Western Protective Relay Conference, Spokane, WA*, Oct. 2000.
  - [70] C. A. et al. K. Strunz, N. Hatziargyriou, “Benchmark systems for network integration of renewable and distributed energy resources,” *Cigre Task Force C*, vol. 6, no. 04–02, 2014.
  - [71] A. Hooshyar and R. Iravani, “Microgrid protection,” *Proc. IEEE*, vol. 105, no. 7, pp. 1332–1353, 2017, doi: 10.1109/JPROC.2017.2669342.
  - [72] R. Kabiri, D. G. Holmes, and B. P. McGrath, “Control of Active and Reactive Power Ripple to Mitigate Unbalanced Grid Voltages,” *IEEE Trans. Ind. Appl.*, vol. 52, no. 2, pp. 1660–1668, 2016, doi: 10.1109/TIA.2015.2508425.
  - [73] J. Glover, M. Sarma, and T. Overbye, *Power system analysis and design*, 5th ed. USA: GENAGE Learning, 2012.
  - [74] T. Gonen, *Modern power system analysis*, 2nd ed. U.S.: CRC Pres: Taylor & Francis Group, 2013.
  - [75] P. M. Anderson, *Power system protection*. USA: IEEE press, 1998.

- [76] D. W. Gao, E. Muljadi, T. Tian, M. Miller, and W. Wang, "Comparison of standards and technical requirements of grid connected wind power plants in China and the United States," 2016.
- [77] ERCOT, "Resource interconnection handbook Version 1.91," 2021. [Online]. Available: <https://www.ercot.com/services/rq/integration>
- [78] "PV ground referencing requirements and sample calculations," 2015. Accessed: Feb. 27, 2023. [Online]. Available: <moz-extension://5478b177-1a4a-4644-96d5-a794468a26b3/enhanced-reader.html?openApp&pdf=https%3A%2F%2Fwww.xcelenergy.com%2Fstaticfiles%2Fxe%2FPDF%2FFMN-SRC-Invertor-Based-Ground-Refrencing-Requirements-and-Sample-Calculations.pdf>
- [79] R. F. Arrit and R. C. Dugan, "Distributed generation interconnection transformer and grounding selection," *IEEE Power Energy Soc. 2008 Gen. Meet. Convers. Deliv. Electr. Energy 21st Century, PES*, Aug. 2008, doi: 10.1109/PES.2008.4596772.
- [80] Z. Xin, X. Wang, Z. Qin, M. Lu, P. C. Loh, and F. Blaabjerg, "An improved second-order generalized integrator based quadrature signal generator," *IEEE Trans. Power Electron.*, vol. 31, no. 12, pp. 8068–8073, Dec. 2016, doi: 10.1109/TPEL.2016.2576644.
- [81] R. Teodorescu, M. Liserre, and P. Rodriguez, *Grid converters for photovoltaic and wind power systems*. John Wiley & Sons, 2011.
- [82] D. N. Zmood and D. G. Holmes, "Stationary frame current regulation of PWM inverters with zero steady-state error," *IEEE Trans. Power Electron.*, vol. 18, no. 3, pp. 814–822, May 2003, doi: 10.1109/TPEL.2003.810852.
- [83] NERC, "Reliability guideline BPS-connected inverter-based resource performance," 2018. [Online]. Available: [https://www.nerc.com/comm/PC\\_Reliability\\_Guidelines\\_DL/Inverter-%0ABased\\_Resource\\_Performance\\_Guideline.pdf](https://www.nerc.com/comm/PC_Reliability_Guidelines_DL/Inverter-%0ABased_Resource_Performance_Guideline.pdf)
- [84] NERC, "Reliability guideline bulk power system reliability perspectives on the adoption of IEEE 1547-2018," 2020. [Online]. Available: [https://www.nerc.com/comm/PC\\_Reliability\\_Guidelines\\_DL/Guideline%0A\\_IEEE\\_1547-2018\\_BPS\\_Perspectives.pdf](https://www.nerc.com/comm/PC_Reliability_Guidelines_DL/Guideline%0A_IEEE_1547-2018_BPS_Perspectives.pdf)
- [85] "IEEE 39 bus system | PSCAD," 2022. <https://www.pscad.com/knowledge-base/article/28> (accessed Feb. 27, 2023).
- [86] "Baseline real-time target machine | Speedgoat." <https://www.speedgoat.com/products-services/real-time-target-machines/baseline-real-time-target-machine> (accessed Feb. 27, 2023).

## Appendices

### Appendix A

#### Data of Test Networks

The data of the test system shown in Figure 3.2 is as follows:

Table A.1. Sample test system parameters

Component	parameter	Value
Grid Source	$V_{Grid,nom}$	34.5 kV
	$Z_{th}$	$4\angle 80^\circ \Omega$
Load at Bus 2	$P_2$	4.5MW
	$Q_2$	0.6MVAR
Transmission Lines	$L_{12}, L_{32}$	8 km
	$Z_L^+$	$0.0178+j0.314 \Omega/\text{km}$
	$Z_L^0$	$0.29+j1.04 \Omega/\text{km}$
Transformer (Delta/Star-ground)	$P_{tr,nom}$	14-MW
	Turns ratio	34.5/4.16 kV
	$x$	0.1 p. u.
IIRES	$P_{IIRES,nom}$	9.2-MW
	$V_{IIRES,nom}$	4.16 kV
IIRES filter	$R_f$	$0.005 \Omega$
	$L_f$	0.918 mH
	$C_f$	61.3 $\mu\text{F}$

The data of the test system shown in Figure 4.13 is as follows:

Table A.2. Transmission system test system parameters

Component	parameter	Value
Voltages Sources' Impedances	$Z_{s1}^+$	$12.66\angle 83^\circ$
	$Z_{s1}^0$	$11.1\angle 83^\circ$
	$Z_{s3}^+$	$7.76\angle 81^\circ$
	$Z_{s3}^0$	$5\angle 81^\circ$
	$Z_{s4}^+$	$12.7\angle 84^\circ$
	$Z_{s4}^0$	$11.2\angle 84^\circ$
Transformer at Bus 2 (Delta/Star-ground)	$P_{tr,nom}$	100-MW
	Turns ratio	22/230 kV
Transmission lines	$Z_{TL}^+$	$0.08954 + j 0.5077 \Omega/\text{km}$
	$Z_{TL}^0$	$0.17908 + j 1.0154 \Omega/\text{km}$
	$L_{15}$	155 km
	$L_{25}$	100 km
	$L_{35}$	110 km
	$L_{45}$	120 km

## Appendix B

### Verification of the negative-sequence current magnitude equation

The relation between  $i_{t,\alpha\beta,ref}^-$  and  $i_{\alpha\beta,ref}^-$  can be determined by rearranging (2.16) as

$$\begin{cases} i_{t,\alpha,ref}^- = i_{\alpha,ref}^- - \omega C_f v_{t,\beta}^- \\ i_{t,\beta,ref}^- = i_{\beta,ref}^- + \omega C_f v_{t,\alpha}^- \end{cases} \quad (\text{B.1})$$

Squaring (B.1) yields

$$(i_{t,\alpha,ref}^-)^2 = (i_{\alpha,ref}^-)^2 + \omega^2 C_f^2 (v_{t,\beta}^-)^2 - 2\omega C_f I_{t,\alpha,ref}^- v_{t,\beta}^- \quad (\text{B.2})$$

$$(i_{t,\beta,ref}^-)^2 = (i_{\beta,ref}^-)^2 + \omega^2 C_f^2 (v_{t,\alpha}^-)^2 + 2\omega C_f I_{t,\beta,ref}^- v_{t,\alpha}^- \quad (\text{B.3})$$

Subsequently, the expression for  $(i_{t,\alpha,ref}^-)^2 + (i_{t,\beta,ref}^-)^2$  is deduced by adding (B.2) to (B.3) as

$$\begin{aligned} (i_{t,\alpha,ref}^-)^2 + (i_{t,\beta,ref}^-)^2 &= (i_{\alpha,ref}^-)^2 + (i_{\beta,ref}^-)^2 + \omega^2 C_f^2 \left( (v_{t,\beta}^-)^2 + (v_{t,\alpha}^-)^2 \right) \\ &\quad + 2\omega C_f (-i_{\alpha,ref}^- v_{t,\beta}^- + i_{\beta,ref}^- v_{t,\alpha}^-). \end{aligned} \quad (B.4)$$

On the other hand, the time-domain representation for the  $\alpha\beta$  current and voltage quantities are determined by replacing the arbitrary phasor ( $f$ ) in (2.14) with current and voltage quantities.

$$\begin{cases} i_{\alpha,ref}^- = I_{limit}^- \sin(\omega t + \angle I_{ref}^-) \\ i_{t,\alpha,ref}^- = I_{t,limit}^- \sin(\omega t + \angle I_{t,ref}^-) \\ v_{t,\alpha}^- = V_t^- \sin(\omega t + \angle V_t^-) \end{cases} \quad (B.5)$$

$$\begin{cases} i_{\beta,ref}^- = I_{limit}^- \cos(\omega t + \angle I_{ref}^-) \\ i_{t,\beta,ref}^- = I_{t,limit}^- \cos(\omega t + \angle I_{t,ref}^-) \\ v_{t,\beta}^- = V_t^- \cos(\omega t + \angle V_t^-). \end{cases} \quad (B.6)$$

Using (B.5) and (B.6),

$$\begin{cases} (i_{\alpha,ref}^-)^2 + (i_{\beta,ref}^-)^2 = (I_{limit}^-)^2 \\ (i_{t,\alpha,ref}^-)^2 + (i_{t,\beta,ref}^-)^2 = (I_{t,limit}^-)^2 \\ (v_{t,\alpha}^-)^2 + (v_{t,\beta}^-)^2 = (V_t^-)^2. \end{cases} \quad (B.7)$$

An expression for  $-i_{\alpha,ref}^- v_{t,\beta}^- + i_{\beta,ref}^- v_{t,\alpha}^-$  can be determined by

$$\begin{aligned} i_{\beta,ref}^- v_{f\alpha}^- - i_{\alpha,ref}^- v_{f\beta}^- &= I_{limit}^- V_t^- \sin(\omega t + \angle V_t^-) \cos(\omega t + \angle I_{ref}^-) \\ &\quad - I_{limit}^- V_t^- \cos(\omega t + \angle V_t^-) \sin(\omega t + \angle I_{ref}^-). \end{aligned} \quad (B.8)$$

(B.8) can be simplified by using the trigonometric identities, as given in (B.9).



$$i_{\beta,ref}^- v_{t,\alpha}^- - i_{\alpha,ref}^- v_{t,\beta}^- = I_{limit}^- V_t^- \sin(\angle V_t^- - \angle I_{ref}^-). \quad (B.9)$$

Substituting (B.7) and (B.9) into (B.4) yields

$$(I_{t,limit}^-)^2 = (I_{limit}^-)^2 + \omega^2 C_f^2 (V_t^-)^2 + 2\omega C_f I_{limit}^- V_t^- \sin(\angle V_t^- - \angle I_{ref}^-). \quad (B.10)$$

Thus,  $I_{t,limit}^-$  is calculated by

$$I_{t,limit}^- = \sqrt{\frac{(I_{limit}^-)^2 + \omega^2 C_f^2 (V_t^-)^2}{+2\omega C_f I_{limit}^- V_t^- \sin(\angle V_t^- - \angle I_{ref}^-)}}. \quad (B.11)$$

## **Vita Auctoris**

NAME: Abdallah Aboelnaga

PLACE OF BIRTH: Cairo, Egypt

YEAR OF BIRTH: 1991

EDUCATION: University of Windsor. Ph.D., in Electrical Engineering,  
Windsor, ON, 2023.

Ain Shams University, M.Sc. in Electrical Engineering,  
Cairo, Egypt, 2018.

Ain Shams University, B.Sc. in Electrical Engineering,  
Cairo, Egypt, 2014.

Omar-Ibn El Khattab High School, Cairo, Egypt, 2009.